NTNU
Norwegian University of
Science and Technology

Use of Battery Energy Storage for Power Balancing in a Large-Scale HVDC Connected Wind Power Plant

Marta Naasen Hellesnes

Master of Energy and Environmental Engineering
Submission date: June 2017
Supervisor: Elisabetta Tedeschi, IEL
Co-supervisor: Kamran Sharifabadi, Statoil ASA
Santiago Sanchez Acevedo, IEL

Norwegian University of Science and Technology
Department of Electric Power Engineering

Abstract

The increasing implementation of intermittent renewable energy sources into the power system brings challenges in terms of grid stability, power quality and security of supply. Traditionally, rotating reserves and thermal power plants based on fossil fuels have been used to provide balancing services in the grid, but due to an increased focus on sustainable solutions and increasingly demanding climate goals, more environmental friendly solutions must be considered. The main objective of this thesis is to study how battery energy storage can be used to provide the ancillary services of primary and secondary reserves to the grid, in order to help stabilize the grid and support integration of large scale offshore wind power.

The system studied in this project consists of an offshore wind farm connected to the grid onshore via a high voltage direct current (HVDC) transmission system. Battery energy storage is connected through a DC/DC converter to the DC-link of the HVDC system. The main focus of the work is related to the battery and the DC/DC converter. A number of battery technologies and DC/DC converter topologies have been studied. It is found that for the application in this project the lithium-ion (Li-ion) battery is the optimal choice of battery storage technology. The optimal DC/DC converter is found to be a galvanically bidirectional converter consisting of a modular multilevel converter (MMC) on the high voltage side and a two-level voltage source converter (2L-VSC) on the low voltage side of the medium frequency coupling transformer, which provides the galvanic isolation.

The scope of the thesis consists of two main parts; a design part and a simulation part. In the design part, the design of the different components of the system are discussed in terms of voltage levels, power ratings, number of components, type of components, size and cost. The battery is designed based on ABB's EssPro^{TM} Grid battery modules and an optimal design for the application in this project in terms of series and parallel connections of battery modules, is proposed. In terms of semiconductor devices for the DC/DC converter, it is found that the insulated-gate bipolar transistor (IGBT) press-pack devices are preferred over the integrated gate-commutated thyristor (IGCT) for both the MMC and the 2L-VSC for the converter design in this project. It is also found that for the galvanic isolation of the DC/DC converter, the optimal choice is to have a medium frequency transformer with a frequency of 300 Hz and a turns ratio of 1:3.

In the simulation part of the scope simulation models of the different parts of the system are developed. The models are implemented in MATLAB and Simulink. The different parts are modeled and verified separately before the final system is created by connecting the different parts. Two simulation cases are performed. In the first case a simulation of the DC/DC converter and the battery is performed. The power flow is controlled to be both positive and negative to verify that the converter provides bidirectional power flow so that the battery can be charged and discharged, depending on the state of charge (SOC). A battery SOC model has been included in the 2L-VSC model in order to verify that the battery is charging and discharging. The results show that the battery can be charged and discharged and that the proposed DC/DC converter provides bidirectional power flow.

The second simulation case also includes the simulation model of the HVDC transmission system, the offshore wind farm and the grid onshore. In this case the power flow of the HVDC system and the DC/DC converter is controlled so that when the wind power generation increases above the constant power consumption onshore of 0.82 pu, the battery system will charge, and when the wind power generation decreases below 0.82 pu, the battery system will discharge, in order to provide a constant power flow of 0.82 pu to the grid onshore. This is simulated to verify that the battery storage can provide balancing services in order to stabilize the grid and support integration of offshore wind power into the power system. The results show that the battery helps stabilize the grid by providing constant power flow to the onshore grid by charging in times when the wind power generation is higher than the power consumption onshore, and by discharging in times when the wind power generation is lower than the power consumption.

At the end of the thesis the results of the second simulation case is compared to the same simulation case of a similar system, where the battery storage is connected to the onshore AC-side through an MMC and a transformer. The results show that both DC-side and AC-side connection of the battery storage are possible, and in both cases the battery storage can stabilize the grid and support integration of offshore wind power into the power system.

Sammendrag

Økt implementering av fornybare energikilder som er varierende og ustabile av natur fører til utfordringer i kraftsystemet når det gjelder nettstabilitet, strømkvalitet og forsyningssikkerhet. Tradisjonelt sett har kraftproduksjon basert på fossile energikilder blitt brukt som balansekraft for å holde nettet stabilt, men på grunn av økt fokus på bærekraftige løsninger og stadig mer krevende klimamål, så må mer miljøvennlige løsninger vurderes. Hovedformålet med denne oppgaven er å studere hvordan batterilagring kan tilby balansetjenester i form av primær- og sekundærreserver for å bidra til å stabilisere nettet samt støtte integrasjon av storskala havvindkraft.

Systemet som studeres i denne oppgaven består av en havvindmøllepark som er koblet til nettet på land via et overføringssystem for høyspent likestrøm (HVDC). Batterilagringen kobles til på DC-siden av overføringssystemet via en likestrømsomformer (DC/DC). Hovedfokuset i oppgaven er relatert til batteriet og likestrømsomformeren. En rekke batteriteknologier og ulike likestrømsomformere er studert. For anvendelsen av batterisystemet i denne oppgaven er det optimale valget av batteriteknologi er å velge litium-ion (Li-ion) batterier. Det optimale valget av likestrømsomformer er å velge en med toveis effektflyt og galvanisk skille som er bygget opp av en modulær multinivå-omformer (MMC) på høyspenningssiden, og en to-nivå spenningskildeomformer (2L-VSC) på lavspenningssiden av en medium-frekvens koblingstransformator, som sørger for galvanisk skille.

Denne oppgaven består av to hoveddeler; en designdel og en simuleringsdel. I designdelen diskuteres utformingen av de forskjellige komponentene i systemet i forhold til spenningsnivåer, effektverdier, antall komponenter, komponenttyper, størrelse og pris. Batteriet er designet basert på ABB sine EssPro$^{\mathrm{TM}}$ Grid batterimoduler og det blir foreslått et optimalt design av batteriet med tanke på serie- og parallellkoblinger av batterimoduler. Når det gjelder halvlederkomponenter for likestrømsomformeren, så er det funnet at press-pack IGBTer (insulated gate bipolar transistor) foretrekkes over IGCTer (integrated gate-commutated thyristor) både for MMCen og for 2L-VSCen i omformerdesignet som benyttes i dette prosjektet. Det er også funnet at for det galvaniske skillet i likestrømsomformeren så er det optimale valget å bruke en medium-frekvens koblingstransformator med frekvens på 300 Hz og et viklingsforhold på 1:3.

I simuleringsdelen av oppgaven blir det utviklet simuleringsmodeller av de forskjellige komponentene i systemet. Modellene er implementert i MATLAB og Simulink. De forskjellige modellene blir først simulert og verifisert hver for seg før de kobles sammen for å simulere hele systemet. Det utføres to simuleringscaser. I den første casen blir systemet av likestrømsomformeren og batteriet simulert for å verifisere toveis strømflyt gjennom omformeren, slik at batteriet kan opplades og utlades. Dette gjøres ved å kontrollere effektflyten til å være både positiv og negativ. En SOC-modell (state of charge) av batteriet er inkludert i 2L-VSC-modellen av systemet for å kontrollere at batteriet kan opplades og utlades. Resultatene viser at batteriet kan opplades og utlades, og at den foreslåtte modellen av likestrømomformeren har toveis strømflyt.

I den andre simuleringscasen er også modellen av overføringssystemet, havvindparken og

nettet på land tatt med. I denne casen simuleres hele systemet og strømmen til HVDC-systemet og likestrømsomformeren kontrolleres. Når strømmen i HVDC-systemet er styrt slik at vindkraftproduksjonen overstiger det antatte konstante forbruket på land på 0.82 pu, så må batterisystemet lades opp og når vindkraftproduksjonen faller under 0.82 pu, så må batterisystemet lades ut for å gi en kontant strømflyt, og dermed også effektflyt til nettet på land. Denne casen simuleres for å verifisere at batterilagring kan brukes for å stabilisere nettet og støtte integrasjonen av havvindkraft i kraftsystemet. Resultatene av denne casen viser at batteriet bidrar til å stabilisere nettet ved å sørge for konstant effektflyt til nettet på land ved å lade seg opp når vindkraftproduksjonen overstiger forbruket, og ved å lade seg ut når vindkraftproduksjonen er lavere enn forbruket.

I slutten av denne masteroppgaven sammenlignes resultatene fra den andre simuleringscasen mot resultatene for den samme simuleringscasen for et lignende system, der batterisystemet er koblet til på AC-siden av overføringssystemet på land via en MMC og en transformator. Resultatene viser at batterilagring er mulig både ved AC- og DC-tilkobling, og i begge tilfeller kan batterilagringen bidra til å stabilisere nettet og støtte integrasjon av havvindkraft.

Preface

This Master's Thesis was written during the spring semester of 2017 to complete my Master of Science degree in Energy and Environmental Engineering at the Norwegian University of Science and Technology (NTNU), Trondheim. The thesis was written at the Department of Electric Power Engineering at NTNU in cooperation with Statoil ASA.

The objective of the work was to study how battery energy storage can be used to stabilize the grid and support integration of large scale offshore wind power into the grid by providing services of primary and secondary reserves. My main motivation for this thesis and for the study program in general was to be able to work with renewable energy and to be able to contribute to development of more sustainable solutions for future power systems. The work with this thesis has given me valuable knowledge about electric power engineering, energy storage and power electronic converters.

I would like to thank my supervisor Professor Elisabetta Tedeschi at NTNU for excellent guidance and for her availability throughout the work of both the specialization project and the Master's Thesis. Her feedback and advises have been very valuable. In the same manner, I would like to thank my co-supervisor Kamran Sharifabadi at Statoil ASA for sharing his knowledge about this field and for his availability to answer my questions. I would also like to thank my co-supervisor Post Doctor Santiago Sanchez Acevedo at NTNU for his help and guidance. I really appreciate his help with the simulation models.

Furthermore, I would like to thank fellow student Ida Pria Reite and her supervisor Associate Professor Dimosthenis Peftitsis at NTNU. Ida and I have been working on similar Master's Theses and it has been great to have someone to discuss system design and modeling with, and not least someone to share the frustration with when the simulations did not run correctly. I would like to thank Dimosthenis Peftitsis for his guidance and for answering my questions.

Regarding the simulation models I would also like to thank Postdoctoral Fellow Gilbert Bergna-Diaz at NTNU for his help. In addition, I would like to thank Professor Arne Nysveen at NTNU for sharing his knowledge regarding transformers.

Last but not least, I would like to thank my friends and family for their support.

Marta Naasen Hellesnes
Trondheim, June 2017

Contents

List of Figures

List of Tables

Nomenclature

Superscripts and subscripts

$*$	Complex conjugate
	Reference value
α,β	Alpha (α) and beta (β) components of the synchronous $\alpha\beta0$ reference frame
a,b,c	Phases a, b, c
b	Base value
CL	Closed Loop
d,q	Direct (d) and quadrature (q) components of the synchronous dq0 reference frame
i	Submodule index
	Current index
k	Phase index
n	Harmonic order
OL	Open Loop
pu	Per unit value
u,l	Upper (u) and lower (l) arm
v	Voltage index

Variables, parameters and functions

θ	Angular position
λ	Tip speed ratio
ρ	Air density
τ_{pu}	Per unit time constant of the system in the inner control loop of the 2L-VSC
Φ_M	Phase margin
$\omega = 2\pi f$	Fundamental angular frequency
ω_b	Base angular frequency
ω_d	Crossover frequency
$\Re$	Real part

A	Area
B	Flux density
C	Capacitance
C_b	AC-side base capacitance
C_{dcb}	DC-side base capacitance
C_{eq}	Equivalent capacitance of the AVM-MMC
$C_p(\lambda)$	Power coefficient
C_{pu}	Per unit capacitance
f	Fundamental frequency
f_s	Sampling frequency
f_{sw}	Switching frequency

E $= E_d + j \cdot E_q$	Voltage driving the AC grid current
E	Battery energy [Wh]
H	Inertia constant
i $= i_d + j \cdot i_q$	AC current in dq0 reference frame
I_b	Peak of the base AC phase current
$i_c = (i_u + i_l)/2$	Circulating current
i_{cz}	Zero-sequence circulating current
I_C	DC collector current
$i_{d,q}$	Direct and Quadrature components of the AC current
i_{dc}	DC-bus current
$I_{dc,b}$	Base DC-side current
i_k	Phase current
$i_s = i_u$ - i_l	Output current
i_{SM}	Submodule current
I_{TGQM}	Maximum controllable turn-off current
$i_{u,l}$	Arm current
K_i	Integral gain of the PI-controller
K_p	Proportional gain of the PI-controller
L	Inductance
L_a	Arm inductance
L_b	AC-side base inductance
L_{dc}	DC-side equivalent inductance
L_{dcb}	DC-side base inductance
L_f	Filter inductance
L_{pu}	Per unit inductance
L_T	Transformer inductance
m_a	Modulation index
N	Number of turns in a transformer winding
	Number of DC-link capacitors in a converter
	Number of submodules per arm of the MMC
n_{arms}	Number of arms per leg of the MMC
n_i	Insertion index of submodule i
N_{series}	Number series connected semiconductors in each valve of the 2L-VSC
P	Active output power
p	Pulse number
$P_{DC,transf.}$	DC power rating
Q	Reactive output power
	Battery capacity [Ah]
Q_{pu}	Per-unit energy capacity of the battery
R	Resistance
R_a	Arm resistance
R_{dc}	DC-side equivalent resistance
R_f	Filter resistance
R_{pu}	Per unit resistance
R_T	Transformer resistance
R_{trafo}	Resistance of the resistor connected to the secondary side of the transformer to verify the
R_1	Resistance of the resistor connected to the AC-side of the 2L-VSC to verify the stand-alon
S	Apparent power

S_b	Base apparent power
T_a	Time delay due to the switches in the converter
T_i	Time constant of the PI-controller
T_{sw}	Switching time of the converter switches
U	Wind speed
u_{cz}	Zero-sequence voltage driving the zero-sequence circulating current, i_{cz}
v $= v_d + j \cdot v_q$	AC voltage in dq0 reference frame
V_1	RMS-value of the fundamental harmonic component
$V_{blocking}$	Rated blocking voltage of a semiconductor device
V_b	Peak of the base AC phase voltage
v_C	Capacitor voltage
v_c	Voltage driving the circulating current i_c
$\hat{V}_{carrier}$	Peak amplitude of the modulation carrier signal
V_{CE}	Collector emitter voltage
$\hat{V}_{control}$	Peak amplitude of the control reference signal
v_{dc}	DC voltage
$V_{dc,b}$	Base DC-side voltage
V_{DRM}	Maximum repetitive voltage in the forward direction
v_k	Phase voltage
V_n	RMS-value of the harmonic component of order n
V_{ratio}	Voltage ratio
v_s	Voltage driving the output current i_s
v_{SM}	Submodule voltage
W_z	Zero-sequence energy
$w^k_{u,l}$	Energy stored in the upper (u) or lower (l) arm of phase k of the MMC
$w^k_\Sigma = w^k_u + w^k_l$	Sum energy
$w^k_\Delta = w^k_u - w^k_l$	Energy difference
Z_b	Base impedance
$Z_{dc,b}$	Base DC-side impedance

Abbreviations

2L	Two-level
2Q	Two-quadrant
3L	Three-level
4Q	Four-quadrant
4L	Four-level
5L	Five-level
AC	Alternating Current
AVM	Average Value Model
BES	Battery Energy Storage
BESS	Battery Energy Storage System
BJT	Bipolar Junction Transistor
CAES	Compressed Air Energy Storage
CE	Coloumbic Efficiency
CSC	Current Source Converter

CTB	Controlled Transition Bridge converter
CTL	Cascaded Two-Level converter
DAB	Dual Active Bridge
DC	Direct Current
DHB	Dual Half Bridge
DoD	Depth of discharge
EES	Electric Energy Storage
EMF	Electromotive Force
FACTS	Flexible AC Transmission System
FBES	Flow Battery Energy Storage
FES	Flywheel Energy Storage
FLC	Flying Capacitor clamped converter
FRT	Fault-Ride-Through
FSWT	Fixed Speed Wind Turbine
GHG	Greenhouse Gas
GTO	Gate Turn-Off Thyristor
GWEC	Global Wind Energy Council
HV	High Voltage
HVAC	High Voltage Alternating Current
HVDC	High Voltage Direct Current
IEEE	Institute of Electrical and Electronics Engineers
IEGT	Injection-Enhanced Gate Transistor
IGBT	Insulated Gate Bipolar Transistor
IGBT-PP	Insulated Gate Bipolar Transistor Press-Pack
IGCT	Integrated Gate-Commutated Thyristor
KCL	Kirchhoff's Current Law
KVL	Kirchhoff's Voltage Law
LA	Lead-acid
LCC	Line-Commutated Converter
Li-ion	Lithium-ion
LV	Low Voltage
MMC	Modular Multilevel Converter
MOSFET	Metal-Oxide-Semiconductor Field-Effect Transistor
MOV	Metal Oxide Varistor
NaS	Sodium-sulfur
NiCd	Nickel-cadmium
NiMH	Nickel-metal hybrid
NPC	Neutral Point Clamped converter
O&M	Operation and Maintenance
OPWM	Optimal Pulse-Width Modulation
PCC	Point of Common Coupling
PCS	Power Conversion System
PHS	Pumped Hydro Storage
PI	Proportional-Integral
PLL	Phase-Locked Loop
PSB	Polysulfide Bromide flow battery
PSC	Phase-Shifted Carrier
PV	Photo Voltaic

PWM	Pulse-Width Modulation
RES	Renewable Energy Source
SC	Super Capacitor
SCR	Short-Circuit Ratio
SHE	Selective Harmonic Elimination
SM	Sub-Module
SMES	Superconducting Magnetic Energy Storage
SOC	State Of Charge
SPWM	Sinusoidal Pulse-Width Modulation
STATCOM	Static Synchronous Compensator
SVC	Static Var Compensator
SVM	Space Vector Modulation
TAC	Transition Arm Multilevel Converter
THD	Total Harmonic Distortion
TSO	Transmission System Operator
VBR	Vanadium Redox flow battery
VSC	Voltage Source Converter
VSI	Voltage Source Inverter
VSWT	Variable Speed Wind Turbine
XLPE	Extruded cross-bound polyethylene
ZEBRA	Sodium nickel chloride battery
ZnBr	Zinc Bromine flow battery
ZVS	Zero Voltage Switching

Chapter 1

Introduction

The global demand for electricity and energy has grown rapidly over the last decades. In 2014 the global annual electricity production was 23 816 TWh [29]. According to REN21 [30], the share of electricity produced by renewables was 24.5% in the end of 2016, and the remaining 75.5 % were produced from non-renewables where fossil fuels like oil, natural gas and coal had the biggest share. At the same time as there is this increasing demand for electricity, there is an increasing focus on increasing the share of renewable energy sources for electricity production in order to reduce environmental consequences of power generation.

The Kyoto Protocol is a driving force towards reducing greenhouse gas (GHG) emissions by having national emission targets and by providing international emissions trading [31]. The parties of the protocol have committed to reduce GHG emissions by at least 18 % below the 1990 levels in the period from 2013 to 2020. In November 2016, the Paris Agreement was enacted, and the main aim is to keep the global temperature rise in this century well below $2°C$ and to increase the ability of countries to deal with the impacts of climate change [32].

In Europe, the EU Directives on Renewable Energy is also an important driving force towards a more sustainable future, and on 30 November 2016, a proposal for a revised Renewable Energy Directive was published by the Commission [33]. The main goal of this directive is to make sure that the 2030 targets are met, and to make EU a global leader in renewable energy. The 2030 targets include a goal of at least a 27 % share of renewable energy consumption, which is an increase from the 20 % goal in the 20-20-20 goals that were enacted in 2009 [34]. To achieve these goals of an increased share of renewable energy generation, wind power is considered as a promising solution, and especially offshore wind power is considered as its potential is enormous since the wind is more stable and blows stronger offshore. According to the Global Wind Energy Council [35], the potential of offshore wind energy in the United States is four times the energy demand, and in Europe is as high as seven times the energy demand.

An increased implementation of intermittent renewable energy sources, like wind and solar, will bring challenges to the power system in terms of uncertainty, security of supply, grid reliability and stability. Traditionally, rotating reserves and thermal power plants based on fossil fuels have been used to provide balancing power in the grid. In order to reach the climate goals described above, more environmental friendly solutions for balancing power have to be considered. Electrical energy storage (EES) is seen as a promising solution since this type of storage technology can support the integration of renewables by providing a number of power and energy services to the grid [21].

In this project battery energy storage will be used to help stabilizing a grid with large scale integration of offshore wind power. In case of an imbalance in frequency in the grid, primary reserves are used to stabilize the frequency and secondary reserves are used to bring the frequency back to the system frequency [36], which is 50 Hz for this project. These control actions require quick response times and since quick response time is one of the advantages of battery energy storage, it is seen as a promising solution compared to using traditional rotating reserves, which have longer start-up and response times. After the battery system has provided these control actions and the system frequency is restored, a tertiary control will replace the primary and secondary, and provide congestion management. This tertiary control can have longer response times since it does not have to provide balancing power before the secondary control has restored the frequency, which can take up to 15 minutes [36]. Therefore, traditional rotating reserves or other power plants can be started to provide these further control actions. This project will however not study the long term balancing of the grid, but it will look at short time balancing and how battery energy storage can provide the ancillary services of primary and secondary reserves to the grid.

1.1 Objective

The objective of this work is to study how battery energy storage can be used to stabilize the grid and support integration of large scale offshore wind power into the grid. In this project it is assumed that the battery storage has a capacity of 10 - 20 % of the wind farm capacity in order to support the grid with ancillary services for a duration of up to 15 minutes. If the wind power generation decreases and/or the consumption increases, the system frequency will decrease and the battery must discharge to supply power to grid in order to stabilize and restore the frequency. In the opposite scenario when the frequency increases, power must be drawn from the grid in order to stabilize and restore the system frequency, and then the battery must charge to provide the balancing service.

A one-line diagram of the system used in this project is shown in figure 1.1. It consists of a 1 GW offshore wind farm which is connected to the grid onshore through a high voltage direct current (HVDC) transmission system. The HVDC system is built up of two two level (2L) voltage source converters (VSCs) and 200 km DC subsea transmission cables. Battery energy storage with a capacity of 180 MW is connected to the system to provide the ancillary services of primary and secondary reserves. It is connected to the DC-link of the HVDC system through a galvanically isolated DC/DC converter. The DC/DC converter is built up of a 2L-VSC and a modular multilevel converter (MMC) connected by a medium frequency transformer. The voltage levels of the different components of the system are shown in figure 1.1.

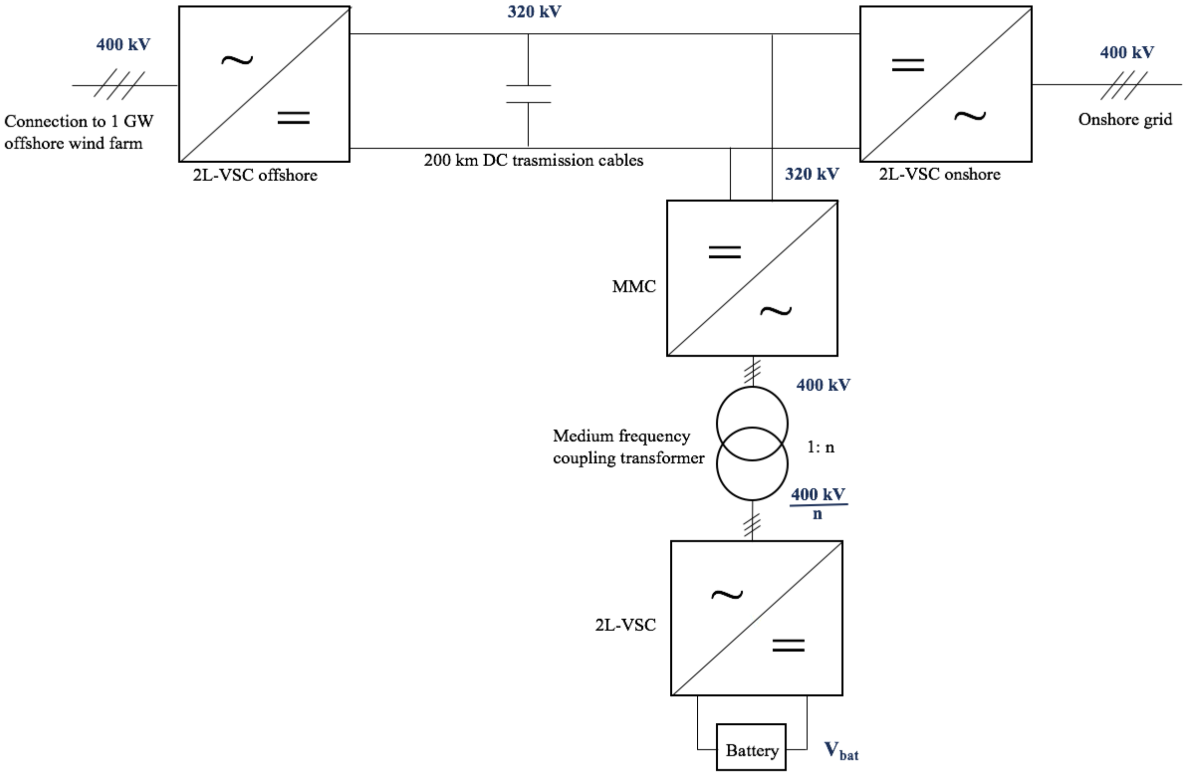

Figure 1.1: One-line diagram of the system

1.2 Scope and limitations of work

This Master's Thesis is a continuation of the work done in the specialization project [3]. The scope of the specialization project was to find an optimal battery storage technology and an optimal DC/DC converter topology for the project. The scope of the Master's Thesis include:

- A design part:
  Perform an analysis and discuss the design of the different components of the system. This includes design of the battery system in terms of size, power and voltage levels and design of the DC/DC converter including choice of semiconductor devices, power and voltage levels, capacitances and inductanes of the converters, and turns ratio and operating frequency of the coupling transformer. The design of the HVDC transmission system, the offshore wind farm and onshore grid are outside the scope of this project since the main focus is on the battery and the DC/DC converter.

- A simulation part:
  Make a simulation model of the system in MATLAB and Simulink and study different test cases to verify the application of the battery. The test cases include verifying that the DC/DC converter provides bidirectional power flow so that the battery can be charged and discharged, depending on the state of charge (SOC), and verifying that the battery can provide grid support when the power generation of the wind farm varies. As mentioned in the preface, parts of this project has been done in cooperation with Ida Pria Reite since the system of her project is similar [19]. In her project the battery system is connected through a MMC to the AC grid side of the HVDC transmission system as shown in figure 1.2. A

part of the scope when it comes to the simulations is to compare the simulations of the battery providing grid support when it is connected to the AC-side compared to when it is connected to the DC-side.

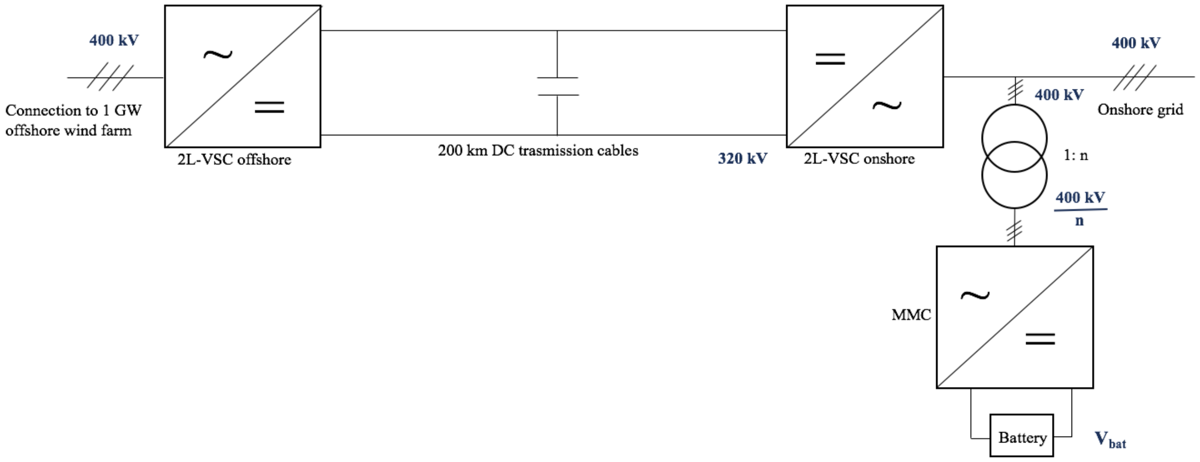

Figure 1.2: One-line diagram of the system with the battery system connected to the AC-side of the HVDC transmission system

The limitations of work in this project include:

- Design of the components used in the system with connection of the battery system on the AC-side of the HVDC system is outside the scope of this project. Detailed descriptions regarding design and modeling of this system can be found in [19].
- The design and modeling of the 2L-VSCs used in the HVDC transmission system is outside the scope.
- Detailed study of other components than the battery and the DC/DC converter is left outside the scope due to limited time. Other topics of the system it could be relevant to study are the onshore grid, the transformers used in the system, the wind farm construction and construction of the single wind turbines within the wind farm, protection system in the grid like AC and DC circuit breakers, etc.
- Other storage technologies than battery storage are mentioned, but they are not studied in detail in this project.
- Detailed modeling of the offshore wind farm and the onshore grid is left outside the scope. As will be seen in the design and modeling chapter, the modeling of these two components are very simplified.
- Simulations to verify that the battery can stabilize the grid in case of faults. For simplicity, circuit breakers and other fault protection equipment have not been considered in the design part of this thesis. Nor has it been implemented in the modeling part. Fault handling and protection is a very important, but also very large topic, and due to the limitation of time for this project, it has been excluded.
- Detailed modeling of the converters that the DC/DC converter is built up of is left outside the scope. As will be seen later in the design and modeling chapters, there are a number of different models that can be implemented in order to simulate the MMC. In this project

both the MMC and the 2L-VSC are based on average value models where the switches in the converters are not modeled explicitly since the objective of the simulations is to look at the overall system and study how the battery can charge and discharge to support and stabilize the grid. If the objective of the simulations had been to study performances of the converters in terms of losses, harmonics etc, more detailed models of the converters must have been used, but this is a totally different objective of the project that is left outside the scope for this Master's Thesis.

- Detailed modeling of the battery is also left outside the scope. As will be seen in the modeling chapter, the modeling of the battery is very simplified consisting only of an ideal DC voltage source in series with a small resistor. A more detailed representation should have been implemented in order to study the performance of the battery in terms of efficiency, lifetime, losses, etc., but this is left outside the scope due to the limited time for this Master's Thesis.

1.3 Relation to specialization project

As mentioned in the previous subchapter, this Master's Thesis is a continuation of the work done in the specialization project [3]. The main objectives of the specialization project was to study battery storage technologies and DC/DC converter topologies, and based on a set of criteria for the application in the project, an optimal battery technology and an optimal DC/DC converter topology were proposed. This is briefly summarized in chapter 2 in this report along with other relevant theoretical background for this Master's Thesis. Appendices E and F provide excerpts from the battery energy storage chapter and DC/DC converter chapter of the specialization project.

Chapters 3 and 4 in this thesis describes the structure, operation and control of the 2L-VSC and the MMC, respectively. These converter topologies were briefly described in the specialization project. They are important for the project in this thesis since they are considered as the converters used in the design of the optimal DC/DC converter in this project, and therefore they are described in detail in chapters 3 and 4.

The tasks of this Master's Thesis include using the results from the specialization project to study the battery storage and the DC/DC converter more in detail by defining an optimal system design for this project. The tasks also include to develop a simulation model of the system in order to run simulations to verify the application of the battery storage system when it is connected to the HVDC-link.

1.4 Literature review

The main source for finding relevant literature for this Master's Thesis has been Oria. It is the online search engine of the University Library of NTNU, and it searches in all databases that NTNU has access to. It has been used to find relevant books and research articles on the topics of this project. In addition, databases such as IEEE and Elsevier have been used to find publications regarding specific research topics.

In the advanced search in Oria one can search using the logical search operators AND, OR and NOT to optimize the search. Key search phrases used to find literature for this project include:

- HVDC AND Battery energy storage
- High voltage DC/DC converters
- HVDC AND offshore wind
- Modular multilevel converter
- Two-level voltage source converter
- MMC AND battery storage
- Design of modular multilevel converter
- Number of submodules AND modular multilevel converter
- Average value modeling AND MMC
- Submodule design AND MMC
- 2L-VSC AND control
- MMC AND control

Since the topics of this project include relatively new technologies and technologies that are fast developing, especially two things have been kept in mind when looking for references for this project:

1. To use as new references as possible for converter and battery technologies since those technologies are quickly developing and being improved.
2. To use references that have many citations since that can indicate a good and reliable source. However, this can be tricky since it is also desired to use as new references as possible and since some of the references used in this project are from 2017, they have not been cited much yet. To find the number of citations, Google Scholar has been used.

Google Scholar has also been used to get BibTex codes for the different books, articles and papers used in this project. The reference list in the end of this thesis is made based on the BibTex codes.

The DOE Global Energy Storage Database[37] has been used regarding energy storage. The manufacturers web sites have been used to find information and characteristics about different products that they offer such as semiconductor devices, storage solutions and converters. In addition these web sites have been used to find information about projects that they have participated in regarding energy storage and/or HVDC transmission. The web sites that have been used include:
`www.abb.com`
`www.alstom.com`
`www.siemens.com`
`www.gegridsolutions.com`

`www.mitsubishielectric.com`
`www.westcode.com`
`www.toshiba.semicon-storage.com`

1.5 Structure of report

The report is written in LaTeX, and the simulations are performed in MATLAB® and Simulink®. The scripts and the Simulink models are provided in Appendices C and D, respectively. Sections are enumerated on the form X.Y.Z, where X is the number of the chapter, Y is the number of the section and Z is the number of the subsection within section Y. Figures and tables are enumerated on the form X.Y, where X is the number of the chapter and Y is the number of the figure or table in chapter X. Equations are enumerated using the same notation, but in round brackets (X.Y). The references can be found in the Bibliography chapter in the end of this report. They are made according to the Institute of Electrical and Electronics Engineers (IEEE) citation style, and the references are shown in square brackets, [X], in the text.

This report consists of ten chapters, including this introduction chapter. The main content of each of the remaining nine chapters is described below:

Chapter 2
This chapter provides the theoretical background for this thesis. It starts with a brief introduction to offshore wind power and the challenges related to large scale integration of wind power into the power system. Further, an introduction to battery energy storage is provided and the optimal storage technology for this project is decided. Next, there is a section regarding HVDC transmission systems, and both LCC-HVDC and VSC-HVDC are discussed. A brief introduction to the most common VSCs is included since the DC/DC converter in this project is built up of the same type of VSCs that is used for HVDC. The last part of this chapter provides an introduction to DC/DC converters and the optimal DC/DC topology for this project is decided. As mentioned in subchapter 1.3, this chapter is based on the specialization project [3].

Chapter 3
Chapter 3 provides a more detailed description of the 2L-VSC than what is provided in chapter 2. This converter is important in this project since it is used in the HVDC transmission system and it is used on the low voltage-side of the DC/DC converter. In addition, it forms the building block of the half-bridge submodule, which is the type of submodules used in the MMC, which is the other converter that the DC/DC converter consists of. This chapter describes the structure, operation, modulation techniques and control of the 2L-VSC.

Chapter 4
The MMC is the other important converter topology in this project and as for the 2L-VSC, this chapter provides a more detailed description of the converter than what is provided in chapter 2. The chapter starts with an introduction to distributed batteries in MMCs, which is an important advantage of the MMC when it comes to battery applications. Further, the structure, operation and control of the MMC is provided. The last subchapter briefly introduces the modulation

techniques of this converter.

Chapter 5
This chapter provides the first part of the main scope of this thesis, namely the system design. The chapter is divided into subchapters based on the different components of the system and in each subchapter the design of the component is discussed and an optimal design for the project in this thesis is proposed. The subchapters include HVDC system design, MMC design, 2L-VSC design, coupling transformer design and battery design. The design is discussed based on voltage levels, power rating, size of components, type of components (i.e. which type of semiconductor switches to use in the converters, etc.), number of different components and cost.

Chapter 6
Chapter 6 is called simulation model and in this chapter the simulation models of the different parts of the system are described. The models are described in detail with references to the MATLAB scripts and Simulink models provided in appendices so that the reader also should be able to built the same simulation models, if desired. Compared to the design described in chapter 5, the simulation models are simplified models of the different parts of the system. The simplifications are discussed and argued for in this chapter and the models are implemented and verified as stand-alone models. In the end of the chapter the models are connected to form the final model of the whole system.

Chapter 7
The first part of this chapter describes the simulation cases and describes why the cases are interesting to study. It also discusses assumptions and simplifications that are made. The second part of this chapter provides the simulation results of the simulation cases.

Chapter 8
This chapter provides the discussion of the thesis. This chapter is also divided into two parts, where the first part is a summary of the discussions regarding system design, which is discussed in chapter 5. The report is structured to include this in even though it is discussed in chapter 5. This is done because it is more structured to provide the discussions in one separate chapter in case the reader wishes to jump right to the discussions. This chapter also contains discussions regarding the limitations of the simulation models used.

Chapter 9
In this chapter the simulation results of simulation case 2 in chapter 7 is compared to the results of the same simulation case of Ida's simulation model [19]. The difference between the two simulation models compared in this chapter is that one of them have battery storage connected to the DC-link of the HVDC system while the other has battery storage connected to the onshore AC-side of the HVDC system.

Chapter 10
This chapter provides the conclusions of this Master's Thesis and proposals for further work.

This report also contain six appendices:

Appendix A
This appendix provides equations regarding harmonic components.

Appendix B
In this appendix Clark's and Park's transformations are described in terms of their transformation matrices. The appendix also includes a figure which shows the relation between the abc, the $\alpha\beta0$ and the $dq0$ reference frames.

Appendix C
In this appendix the MATLAB scripts used in this thesis are provided. The script in C.1 is used to calculate the system parameters for the design part. The script in C.2 is used to set the parameters for the simulation model and it is used both for verifying the different simulation models described in chapter 6 and for the two simulation cases in chapter 7. The script in C.3 is used to calculate the pu-values of the parameters used for the MMC in the script in C.2. The function in C.4 is the function used to calculate the parameters and the controller gains of the 2L-VSCs of the HVDC system, and this function is also used in the script in C.2.

Appendix D
Appendix D provides figures of the different parts of the Simulink models used for the simulation part in this thesis. These are the figures referred to in chapters 6 and 7 where the simulation models are described.

Appendix E
This appendix provides an excerpt from the battery energy storage chapter in the specialization project [3]. This is referred to in chapter 2 for more detailed information regarding the different battery storage technologies and for the discussion regarding the choice of battery storage technology for the project in this thesis.

Appendix F
Appendix F provides an excerpt from the DC/DC converter chapter in the specialization project [3]. Dedicated converters and differnet configurations of DAB converters are described more in detail in this appendix. In addition, the discussion regarding choice of DC/DC converter topology for the specialization project is provided in the end of the appendix.

Chapter 2

Background

This chapter provides some background information of the system of this project. It starts with offshore wind power and challenges with large scale integration of wind power into the grid. Further, information about battery energy storage systems is provided, since this is seen as a possible solution to the challenges with large scale integration of wind power. Some information regarding HVDC transmission systems are included since the transmission system in this project is a HVDC system. Finally DC/DC converters are discussed since a DC/DC converter is required in this project in order to connect the battery to the DC-link of the HVDC transmission system. This chapter is based on the work done in the specialization project [3].

2.1 Offshore wind energy

As mentioned in the introduction, offshore wind energy is a renewable energy source with an enormous potential as the wind blows stronger and is more stable offshore. A wind turbine can produce electricity by the conversion of wind power to mechanical power on the rotating shaft of the turbine, and by further conversion of mechanical power to electricity using a generator [38]. The power output of a wind turbine is calculated using equation 2.1:

$$P = \frac{1}{2}\rho C_p(\lambda) A U^3 \tag{2.1}$$

where ρ is the air density, C_p is the power coefficient which is dependent on λ, the tip speed ratio, A is the rotor blade area, and U is the wind speed. The theoretical maximum value of C_p is known as the Betz limit and its value is 59.3 % [38].

According to Global Wind Energy Council (GWEC), the total global installed capacity of wind power by the end of 2016 was 486 749 MW [39]. Globally, China has installed the largest share with 168 690 MW of installed capacity. This is more than the total installed capacity of Europe which was 161 330 MW by the end of 2016. In Europe Germany is the leading country with a total installed capacity of 50 018 MW.

Although offshore wind power has an enormous potential, it today only represents about

3 % of the total installed wind power capacity worldwide [35]. The total global installed capacity of offshore wind power was 14 384 MW by the end of 2016 [39], where UK has the largest share and accounts for about 36 % of the total installed capacity worldwide. According to IRENA [40], the operating capacity of global offshore wind power is expected to grow to roughly 400 GW in 2045.

2.2 Challenges with integration of wind power into the power system

Large scale integration of renewable energy sources (RES) into the power system presents challenges for grid owners and operators in terms of geographical distribution and transmission [41]. Existing AC grids were designed for transmission from centralized power plants that were located near the consumers. Offshore wind power, on the other hand, is a type of RES that is located far away from both the consumers and the existing AC grid. Therefore, large scale integration of this type of renewable energy source requires development and reinforcement of transmission and distribution grids. In addition, with the distributed power generation of offshore wind power, there is a risk of congested or overloaded transmission and distribution lines. Therefore, large scale integration of offshore wind power will also require development and reinforcement when it comes to system operation and balance management.

There must be a continuously maintained balance between generation and consumption in the power system [42]. The system frequency will change if an imbalance occurs; if the generation exceeds consumption, the frequency will increase, and if the consumption exceeds generation, the frequency will decrease. Since wind power is intermittent and fluctuating, a system with large scale integration of wind power will require a large amount balancing power from available conventional power plants and/or storage technologies such as electrochemical battery storage, which will be discussed later in this chapter.

As mentioned, the intermittent fluctuations and variability of the resource is a challenge when it comes to wind power compared to conventional power plants. In addition, it is challenging that a wind turbine can only produce power when the wind resource is available [38]. Figure 2.1 shows the variability in system load and wind power generation over a time period of 400 hours in Denmark. It shows that the load has a similar repeating pattern as the load will be quite similar on a day-to-day and week-to-week basis, but it may be more seasonably variant. The figure also shows that the wind power generation, on the other hand, fluctuates a lot and it does not always match with the load. This is due to the intermittent wind resource, and it shows that energy planning and energy dispatching is hard in a system where wind turbines are integrated.

Other challenges with wind power is that it is not possible to store the wind power for later use and the wind is not transportable as the conversion from wind energy to electricity has to be done where the wind is blowing [38]. These challenges are however somehow overcome in modern power systems as the power lines and cables for power transmission reduce the challenge of not being able to transport the wind power. In addition, expanded research and use of energy storage systems reduces the challenge of not being able to store the wind power for later use. On the other hand, the use of improved and smarter grids in addition to energy storage systems to

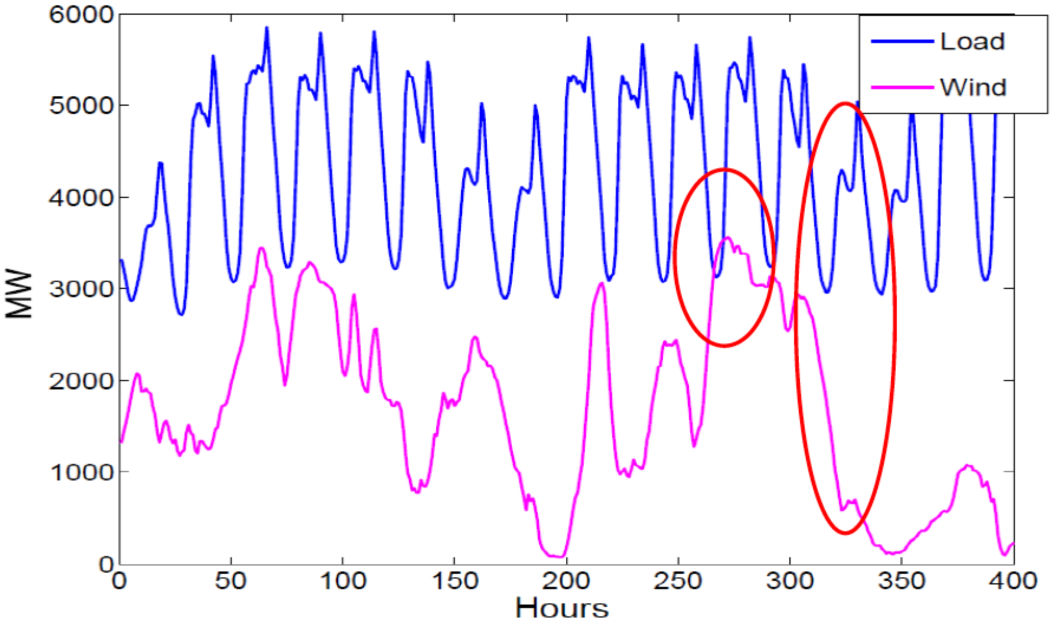

Figure 2.1: Wind power generation and load over a 400 hours period in Denmark[1]

overcome the challenges caused by increased implementation of such intermittent renewable energy sources, will however add to the complexity of the power system.

According to O. Anaya-Lara [43], there are two types of impacts on power system operation caused by wind generation:

1 **System wide impacts:** These include variability in forecasting, generation, stability and system inertia, and balancing of the power system [43]. Inertia will be described further in the next subsection.

2 **Local impacts:** These include power quality issues in terms of harmonics, flicker, voltage steps and dips [43]. Flicker can be seen as a noticeable brightness and it is caused by voltage disturbances with a small magnitude at low frequencies. Harmonics are AC currents or voltages at an integer multiple of the fundamental frequency that can affect components in the power system and reduce the power quality and the efficiency of the system[38].

2.2.1 Inertia

All types of rotating loads or generators connected to the grid has energy stored in their inertia that damps frequency changes in the grid that is caused by imbalances between generation and consumption [44]. For a wind turbine the inertia is defined as its resistance to changes in its speed of rotation [45]. In a grid with conventional synchronous generators connected to it, the generators can be controlled to increase or decrease the energy in the system and in that way stabilize the system in case of a change in frequency [46]. However, for a modern grid with large scale integration of renewables like wind and solar this might not be the case since photo voltaics (PVs) and modern wind turbines are connected to the grid through power electronic interfaces that decouples them from the grid. In this way the system cannot ”see” the inertia from the wind turbines or PVs [43]. For a wind turbine this problem can be solved in two ways:

1. Deloading the wind turbine: This is done by not supplying the maximum available power during normal operation of the wind turbine, leaving a margin so that it can increase the production in case of a decrease in frequency in the system [46].
2. Emulate synthetic inertia: This is done by adding extra control loops to the control of the wind turbine to emulate inertia and support frequency control [45, 46]. This control manipulates the torque of the wind turbine and is able to temporarily slow down the wind turbine in order to extract kinetic energy which can be stored and used later for frequency control.

In modern power systems with large scale integration of renewable energy sources that are connected through power electronic interfaces and interconnections of systems using HVDC, a key concern is reduction in system inertia [47]. In order to solve this problem, these power systems will require faster frequency response that can emulate inertia. Similarly to the wind turbines with power electronic interfaces that can emulate synthetic inertia, control loops can also be added to the power electronic converters of HVDC transmission systems to provide synthetic inertia and in that way increase the system inertia [2, 10, 47]. This so-called inertia emulation control uses the energy stored in the DC-link capacitors of the VSC-HVDC to emulate inertia. It uses the grid frequency as inputs, and as the output it produces a DC voltage reference that is used in the voltage control loop. The controller is included in the VSC-HVDC controller as shown in figure 2.2 and it is based on equation (2.2) [2]. The VSC controller for a 2L-VSC will be described in more detail in chapter 3.

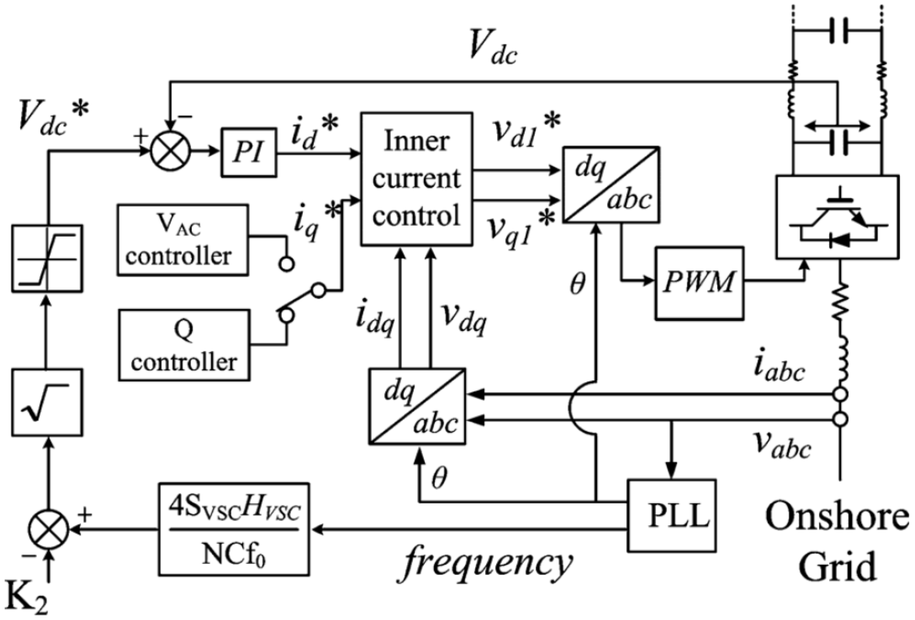

Figure 2.2: Inertia emulation controller included in the control system of a VSC-HVDC [2]

$$V_{DC}^{*} = \sqrt{\frac{4S_{VSC}H_{VSC}}{NCf_0} \cdot f - K_2} \tag{2.2}$$

where

$$K_2 = \frac{4S_{VSC}H_{VSC}}{NC} - V_{DC0}^2 \tag{2.3}$$

where S_{VSC} is the rated power of the VSC, C is the DC-link capacitance of the converter and N is the number of DC-link capacitors in the converter (i.e in a 3L-NPC converter, N = 2, which will be shown later in this chapter). V_{DC}^* is the DC voltage referene which varies with the AC grid frequency f. H_{VSC} is the inertia constant of the VSC which determines the response of angular speed to the changes in input power and f_0 is the nominal frequency.

Since the DC/DC converter that connects the battery to the DC-link of the HVDC system in this project is built up of VSCs, i.e. the same type of converters that are used in modern HVDC systems, it is also possible to include this extra control loop to the converter connecting the battery. Hence it is possible that battery storage connected to the grid can provide synthetic inertia and also in that way help stabilizing the grid. This solution will not be discussed further in the design and modeling chapters, but it is an aspect to consider and it is included as a proposal for further work of this project in chapter 10.

2.2.2 Voltage dips

One of the local impacts on power system operation caused by grid faults is voltage dips. Conventional generation can supply reactive power to the grid to restore the voltage level. However, with large scale integration of wind power, compensation might be needed. In case of a variable speed wind turbine (VSWT) with power electronic interfaces, the wind turbine can control reactive power and provide voltage control if the wind turbine stays connected during the fault [48]. A problem with this type of wind turbine is namely that it is sensitive to over-currents caused by the voltage dips and it can easily disconnect. In order to ensure safe operation of electrical grids, technical regulations which include specifications for operation of the grid have been developed [49]. These technical regulations are known as grid codes and they vary from country to country depending on the requirements stated from the Transmission System Operator (TSO) of each country. Depending on the magnitude and duration of the voltage dip, grid codes require wind turbines to stay connected during the voltage dip, which is know as Fault-Ride-Through (FRT) capability.

The other type of wind turbine, the fixed speed wind turbine (FSWT), also has a problem during faults; it accelerates due to the imbalance between the mechanical power from the turbine and the electrical power that is supplied to the grid, and when the fault is cleared the generator absorbs reactive power, which is further depressing the voltage level [48]. This problem can be solved by using power electronic shunt compensators, which reduce the reactive power drawn from the grid. Integration of battery storage can also be used to supply the grid with reactive power in case of a voltage dip since the VSCs that are used to connect the battery to the grid can control active and reactive power independently, as will be shown later in this thesis.

2.3 Battery energy storage system (BESS)

The use of energy storage has increased over the last years and today there is a total of 168.61 GW of energy storage in operation worldwide [37]. The different types of electrical energy storage (EES) technologies can be classified based on the form the energy is stored in the system [21] and figure 2.3 shows an overview over these.

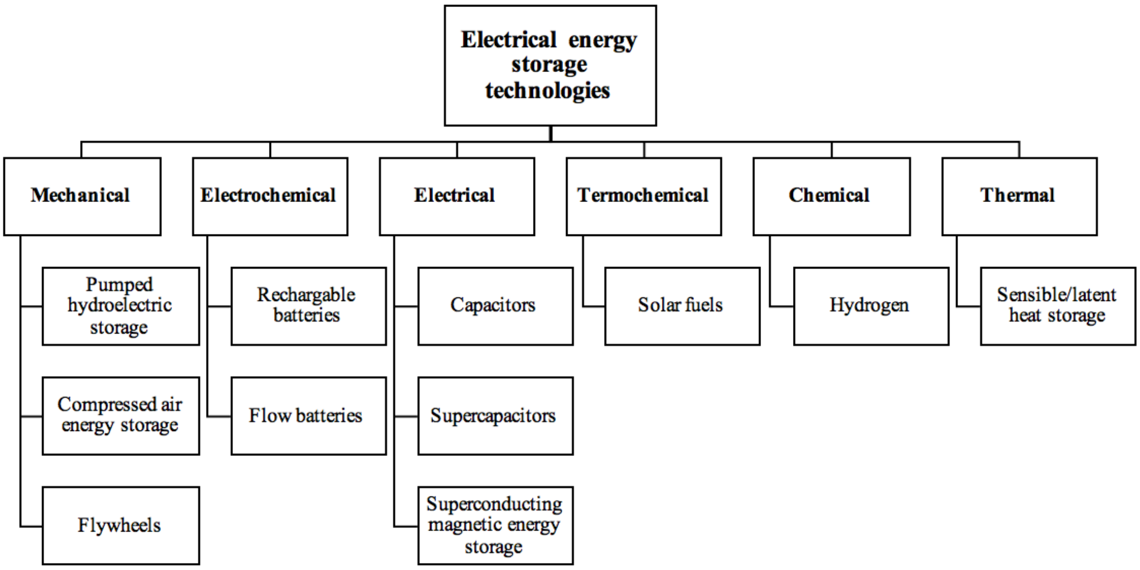

Figure 2.3: Electrical energy storage (EES) technologies [3]

According to H. Zhao et. al [26], pumped hydro storage (PHS), flywheel energy storage (FES), compressed air energy storage (CAES), superconducting magnetic energy storage (SMES), battery energy storage systems (BESSs) and super-capacitors (SCs) are technologies that are commonly used for wind power integration support. PHS has been the dominating energy storage technology due to its many advantages, and today it represents 99 % of the bulk energy storage in the world [21]. BESSs is of the type electrochemical energy storage, and it has had increasing growth in installations over the last years [4] as shown in figure 2.4[1]. The market of battery technologies are expected to increase in the coming years due to increased research and development of battery storage technologies as well as incentives from governmental support [50]. BESS is the type of energy storage technology which will be used in this project.

---

[1] This figure is based on electrochemical storage technologies that are in operation, under construction and storage projects that have been contracted. Here, electrochemical storage includes electrochemical capacitors and a variety of conventional batteries and flow batteries

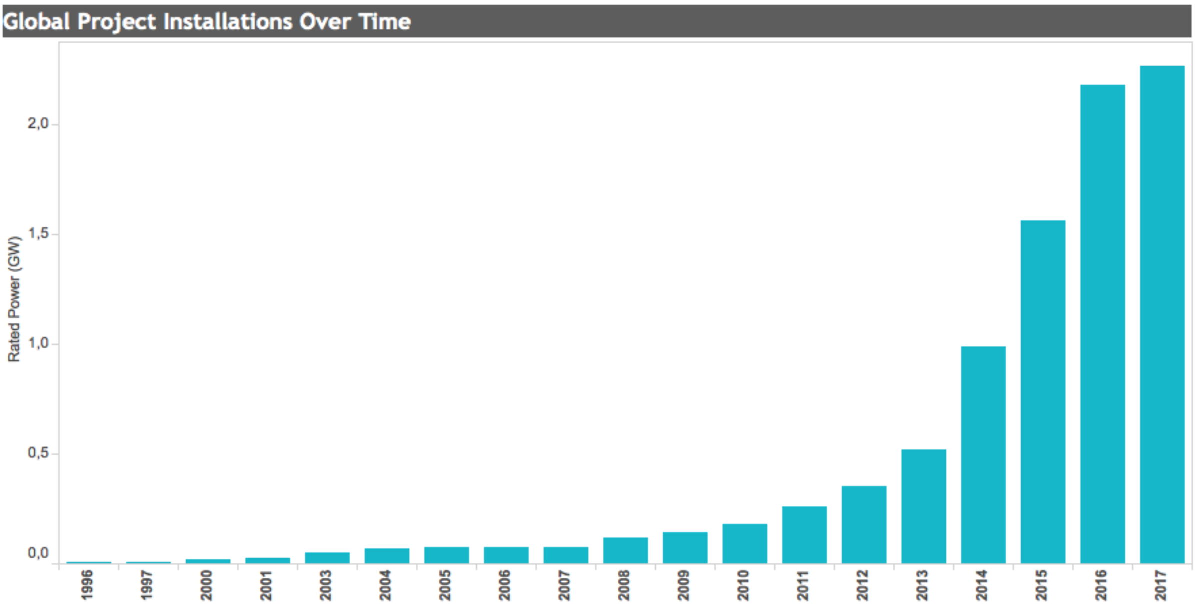

Figure 2.4: Global project installations of electrochemical energy storage systems [4]

2.3.1 Services that energy storage systems can provide

Energy storage systems can provide a number of services at different levels of the power system. The services can benefit different stakeholders and have positive impacts on the system in terms of technical, environmental and economic aspects [51]. Battery storage services can be divided into five umbrella groups; bulk energy services, ancillary services, transmission infrastructure services, distribution infrastructure services and customer energy management services [50]. Figure 2.5 [2] shows these groups including their subcategories.

The application of the battery storage system in this project is to provide ancillary services to the grid in terms of primary and secondary reserves. Therefore, only the subcategories under the ”Ancillary services” group in the figure will be described in this report. Ancillary services are here defined as ”facilities that enhance the security and reliability of the electricity system as well as servicing the normal production and consumption of electricity” [50]. The other subcategories are discussed in literature [21, 26, 27, 50, 52].

Regulation:

As mentioned in subchapter 2.2, it is important that there is a continuously maintained balance between generation and consumption in the power system in order to maintain stability in the system. If an imbalance occurs, the frequency will deviate from the system nominal frequency, which is normally 50 or 60 Hz, depending on geographical area [50]. There are regulation services to help restore the system frequency in case of imbalances in the grid and they are often categorized according to the time frame they use to provide or take away power in the system. The definitions of time frames vary according to geographical area. In Norway the primary control is deployed over a few seconds and up to two minutes, the secondary control over a period of 2-15 minutes, and the tertiary control over a duration of more than 15 minutes [36]. The primary control use primary reserves and the objective is to stabilize the frequency as fast as

---

[2] This figure is based on a figure in the IRENA Battery storage report [50]

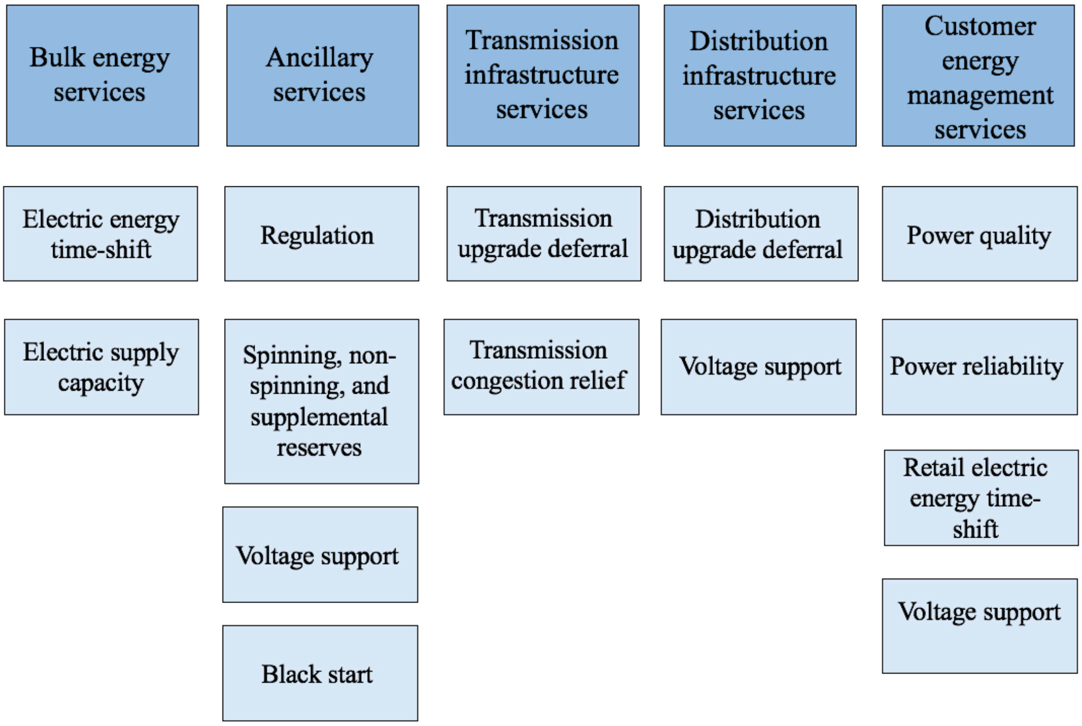

Figure 2.5: Services that battery storage can provide

possible after the imbalance occurs. Therefore it is important that the primary reserve is able to respond immediately, and a battery with a quick response time is well suited for this service [50]. The objective of the secondary and tertiary controls are to restore the frequency back to the system frequency (secondary control) and to replace primary and secondary controls and provide congestion management (tertiary control) [36]. Battery energy storage systems can be used to provide the fast acting control of frequency regulation as both primary and secondary reserves, and this is also the application of the battery storage system in this project. The frequency is regulated by adjusting the power output to fit the demand fluctuations. If the frequency increases, there is more generation than consumption in the system, and then the battery can consume power by charging. If the opposite situation occurs and the frequency decreases, the battery can discharge and in that way provide power to the grid and increase the generation. These regulating services are called ramping and load following [21].

Spinning, non-spinning, and supplemental reserves:
A spinning reserve is defined as a generation capacity that is online and that can respond instantaneously to an unexpected change in generation or demand in the grid [50, 52]. A non-spinning reserve, on the other hand, is not instantaneously available, but it can respond within a short time period (typically in less than 10 minutes) to the same types of unexpected events. The battery system is suited to provide this service of a spinning reserve due to its quick response time. It can be used as a capacity reserve which can be used to maintain contingency in the power system in times of unexpected events.

Voltage support:
The voltage level in the grid must comply with the existing grid codes for the area where the grid is operated. The voltage can be regulated to stay within those boundaries in order to ensure

continuous electricity flow in the grid [52]. Battery energy storage and its converter to connect it to the grid can be used to help the system maintain a specific voltage level [26].

Black start:
Black start generation support the power system in case of a grid outage and helps the system to restore operation and bring the grid back online [52]. A battery storage system can provide this service of starting a system from shut-down condition.

2.3.2 BESS for this project

A BESS is built up of electrochemical cells that are connected in parallel and series in order to achieve the desired power and voltage level of the battery system. Electricity is produced from bi-directional chemical reactions in the cells [21]. In the specialization project [3] a number of conventional and flow batteries were discussed and compared to a set of requirements in order to find the optimal storage technology to use in this project. The following conventional battery technologies were discussed: Lead-acid (LA), Lithium-ion (Li-ion), Sodium-sulfur (NaS), Nickel-cadmium (NiCd), Nickel-metal hybrid (NiMH) and Sodium nickel chloride (ZEBRA). In addition, the vanadium redox flow battery (VRB), the zinc bromine flow battery (ZnBr) and the polysulfide bromine flow battery (PSB) were discussed. The work resulted in table 2.1 which provides different characteristics which are important to consider when choosing a battery technology for the purpose of this project.

It was found that the optimal choice of battery technology for this project is the Li-ion [3]. That is because among the technologies compared, it has best performances on most the criteria that were set for the choice of battery technology for the application in this project, namely high efficiency, quick response time, long lifetime, and relatively low costs. The costs aspect does not show in the table since some of the references used in this table have references that are quite old and the Li-ion battery has improved in terms of performances and costs over the last years [23].

Quick response time is important since the battery must be able to provide ancillary services to the grid in case of a sudden imbalance in the grid. Small size is achieved by having high specific power and energy and this is an important aspect, especially if the battery is to be connected offshore where size and weight are critical parameters when it comes to costs [25]. Long lifetime is also an important aspect as it can reduce the need for frequent replacement or maintenance of the battery, which will add to the cost. The operating conditions of the battery affect its performance, and hence its lifetime and costs [50]. These conditions include the cycle lifetime and efficiency, the depth of discharge (DoD) and the operating temperature, and they are described in Appendix E along with the discussion of choice of battery technology from the specialization project [3].

The design of the Li-ion battery used in this project is discussed in chapter 5.6.

Table 2.1: Characteristics of different battery storage technologies [3]

	LA	Li-ion	NaS	NiCd	NiMH	ZEBRA	VRB	ZnBr	PBS
Power rating [MW][1]	0-20	0.005-50	0.05-8	0-40	-	-	0.03-3	0.05-2	1-15
Energy density [Wh/L][1]	50-80	200-400	150-300	60-150	170-420	150	25-35	30-65	20-30
Power density [W/L][1]	90-700	1500-10,000	140-180	80-600	-	-	0.5-2	25	2
Specific energy [Wh/kg][1]	30-50	75-200	150-240	50-75	70-100	94-120	10-30	30-50	15-30
Specific power [W/kg][1]	75-300	150-315	150-230	150-300	-	150-170	166	100	-
Unit voltage [V][1]	2.0	3.7	2.08	1.0-1.3	1.0-1.3	2.58	1.4	1.8	1.5
Response time[2]	ms	ms	ms	ms	-	-	ms	1/4 cycle	ms
Lifetime [cycles][1]	200-1800	1000-10,000	2500-4500	2000-2500	-	-	12,000+	2000	-
Daily self-discharge [%][1]	0.1-0.3	0.1-0.3	~ 0	0.03-0.6	5-20	-	very low	low	~ 0
Cycle efficiency [%][3]	70-80	90-97	75-90	60-83	-	90	75-85	65-75	60-75
Capital cost [$/kWh][4]	200-400	600-2500	300-500	800-1500	-	-	150-1000	150-1000	-
O&M costs [$/kWh/year][1]	50	-	80	20	-	-	70	-	-

---

[1] Power rating, energy density, power density, specific energy, specific power, unit voltage, lifetime, daily self-discharge and operation and maintenance cost characteristics found in [21]

[2] Response time characteristics found in [21, 27]

[3] Cycle efficiency characteristics found in [21, 51]

[4] Capital cost characteristics found in [26]

2.4 HVDC transmission systems

High voltage power transmission is used for electric power transmission over long distances because the high voltage lowers the current, and that results in lower losses. There are two types of systems, based on using high voltage alternating current (HVAC) or high voltage direct current (HVDC) transmission lines or cables. There are many advantages of HVDC compared to HVAC, including:

- The line construction of a DC-system is simpler and has a smaller footprint than an AC-system for the same power rating [53].
- In HVAC systems the reactive power flow limits the maximum transmission distance [54] due to the large cable capacitance, which increases the capacitive component of the charging current with increasing length of the cable. This is not the case for HVDC since there are no charging currents in DC-systems and hence no reactive power flow [55].
- The cost of HVDC is lower than the cost of HVAC above the critical distance (i.e the distance of the transmission system at which the cost of HVAC is equal to that of HVDC). This distance depends on the technology used in the transmission system. For overhead lines this distance is around 700-800 km [56]. For long distance submarine cables however, the critical distance is at around 100 km [55].
- The power transmission capability per conductor is higher for HVDC than for HVAC due to the fact that there are no skin or proximity effects associated with DC currents [53].
- HVAC systems require synchronous operation for interconnection, but HVDC on the other hand, can interconnect asynchronous systems and also systems of different frequencies [55]. Since the HVDC-link can decouple frequencies of the two ends of the link, a variation in frequency at one end will not be reflected at the other end of the HVDC-link.

In addition to connection of asynchronous systems and connection of systems at different frequencies, applications of HVDC systems include offshore power transmission, bulk power transmission over long distances, power delivery to large urban areas, multiterminal HVDC systems and integration of renewable energy into the power systems [57]. It is also foreseen that flexible AC transmission systems (FACTS) controllers can be installed in combination with HVDC systems to realize smart grids [58]. In this project a HVDC transmission system is used for offshore power transmission over long distances and for integration of renewable energy into the power system by connecting an offshore wind farm to the grid onshore.

There are two types of HVDC technologies, a mature technology using line-commutated (LCC) current source converters (CSC), and a newer technology based on voltage source converters (VSC). Most of the HVDC systems in operation today are based on the LCC technology [53], and since the commission of the first LCC-HVDC scheme in 1954, more than 100 LCC-HVDC schemes have been installed worldwide [41]. The first VSC-HVDC scheme was commissioned in 1999 [41], and this HVDC technology is also known as HVDC light, named by ABB [59], or HVDC Plus, named by Siemens [60]. The structures of the two technologies are shown in figure 2.6.

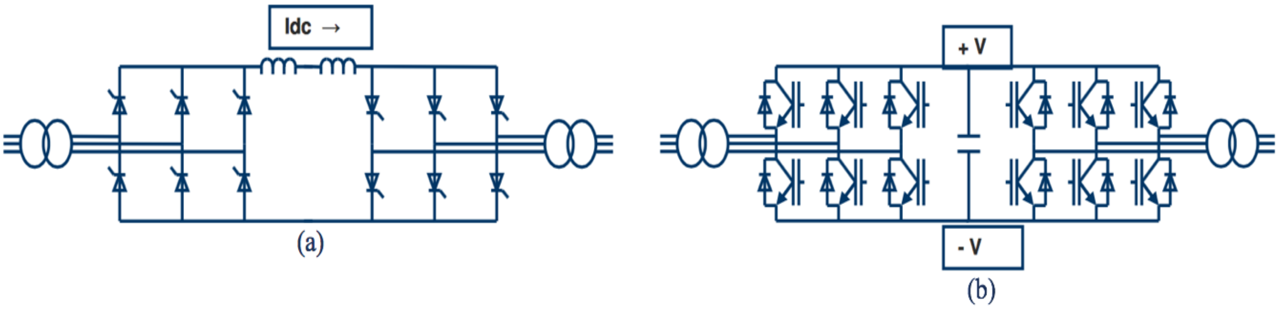

Figure 2.6: HVDC technologies: LCC-HVDC (a) and VSC-HVDC (b) [5]

2.4.1 LCC-HVDC

The LCC-HVDC utilizes thyristor semiconductors which require a synchronous voltage source in order to operate [57]. The thyristors conduct current in one direction only, namely when the thyristor is forward-biased and switched on by the gate signal [41].

The LCC technology has a number of drawbacks, including [6, 41, 58]:

- **Reactive power consumption:** The LCC always consumes reactive power in all operating modes since the current is always lagging behind voltage [41]. Hence shunt capacitor banks or other reactive support devices are required, and this adds to the size, weight and cost of the converter.
- **No black-start capability:** The tyhristors in the CSCs can only provide turn-on control while the turn-of is dependent on the zero-crossing of the current, and hence black-start is not possible with this type of converter.
- **Harmonic filter requirements:** Since the converter generates AC and DC harmonics, harmonic filters are required, and this adds to the size and cost of the converter.
- **Requirement of connection to a strong AC grid:** In order for the LCC to ensure the commutation, i.e the transfer of current from one phase to the next between the thyristor valves, and to avoid operation instability of the converters, the LCC requires connection to a strong AC grid. An AC grid is considered strong if the value of the short-circuit ratio (SCR) is higher than 2-3 [41]. If this is not the case, then the AC grid is weak and then the LCC must be supplemented by reactive power compensation equipment, such as a static var compensator (SVC) or static synchronous compensator (STATCOM), in order to ensure commutation when connected to a weak AC grid.
- **Commutation failures:** A commutation failure is the situation when the commutation voltage reverses before the current is commutated from one phase to the next. Then the valve that previously conducted the current will continue to conduct and this creates a short-circuit on the DC-side, so that power transmission will be prevented during the commutation fault [41]. The commutation failures are more likely to happen at the inverter end since they are most likely caused by AC voltage sags, caused by a fault in the AC- side grid.
- **Not possible to use high-voltage extruded cross-bound polyethylene (XLPE) cables**

for LCC-HVDC: This is due to the limitation of commutation failures in LCC in addition to the fact that reversal of the power flow direction is achieved by changing the polarity of DC-side voltage and not by current reversal. The reason for this is the use of thyristor valves in LCC, which can conduct current in one direction only. The XLPE cables are lighter, cheaper, have a higher transmissible power per conductor and have a smaller environmental impact compared to the mass-impregnated cable technologies that have to be used for LCC-HVDC since XLPE cannot be used [41].

2.4.2 VSC-HVDC

The VSC-HVDC utilizes voltage source semiconductors with both turn-on and turn-off capability such as the Insulated Gate Bipolar Transistor (IGBT) and the Gate Turn-Off Thyristor (GTO) [6].

The VSC-HVDC technology has many advantages compared to the LCC-HVDC technology [41, 53, 57]:

- **Black start capability:** Since the VSC-HVDC is self-commutated, it can be switched both on and off in response to the gate signal. Hence both turn-on and turn-off can be controlled, which makes this converter able to provide black-start capability.
- **No commutation failures due to AC disturbances:** In VSC-HVDC, commutation failures will not occur in the event of an AC fault, as it would in the case of LCC-HVDC.
- **Independent control of active and reactive power:** As will be shown later in this section when discussing the operation of the VSCs, it can be shown that active and reactive power can be controlled independently due to the decoupling of the direct (d) and quadrature (q) components of the current in the control system.
- **Smaller footprint:** According to [41], the VSC-HVDC technology has a 40-60 % smaller footprint compared to the LCC-HVDC technology. The compact dimensions make it ideal for use offshore where the reduced size will give a drastic reduce in cost.
- **Fast reversal of power flow:** Since the power flow can be reversed by controlling the current direction and not by revering DC voltage polarity, as for LCC-HVDC, VSC-HVDC provides fast power reversal.
- **It can utilize XLPE cables:** Since the power reversal does not require reversal of the DC voltage, XLPE cables can be used for this technology. As mentioned earlier, that reduces footprint, reduces the costs and increases the power transmission per cable pair [41] compared to using the mass-impregnated cables that are the only option for LCC-HVDC.

The VSC-HVDC also have some disadvantages compared LCC-HVDC, namely that the converter losses are higher (about 1.5-2 % per converter for VSC-HVDC compared to 0.6-0.8 % per converter for LCC-HVDC) and that the converter costs are higher [41]. The converter losses can be reduced to around 1 % using MMCs, but as will be seen later in this section, that is a more complex and expensive technology.

Despite the disadvantages, due to the many advantages and to the fact that VSC-HVDC can support AC grids with a number of ancillary services and are able to meet the most demanding grid-code requirements, the VSC-HVDC technology is the preferred solution for future DC grids [41]. The HVDC transmission system used in this project is also based on the VSC technology.

The converters used for VSC-HVDC can be divided into three categories:

1 **Two-level converters (2L):**
The structure of the 2L converter is shown in figure 2.7, and as shown it consists six semiconductor valves, consisting of an IGBT with an anti-parallel diode in this figure, but other semiconductors can also be used. The 2L-VSC also consists of a DC-side capacitor and three pairs of series connections of a resistor and an inductor, one for each phase on the AC-side of the converter. The DC-side capacitor smooths the output voltage ripple on the DC-side and in this way, regardless of the AC-side currents, the DC-side voltage will remain approximately constant for a fraction of a fundamental cycle [41]. The AC-side inductors are used to filter out undesired low-order harmonics [61]. As described earlier in this chapter, harmonics are AC voltages or currents at an integer multiple of the fundamental frequency. They are caused by, among others, switch mode inverters, which is the case here. ”Low order harmonics” means that the harmonics appear at low integers multiples of the fundamental frequency.

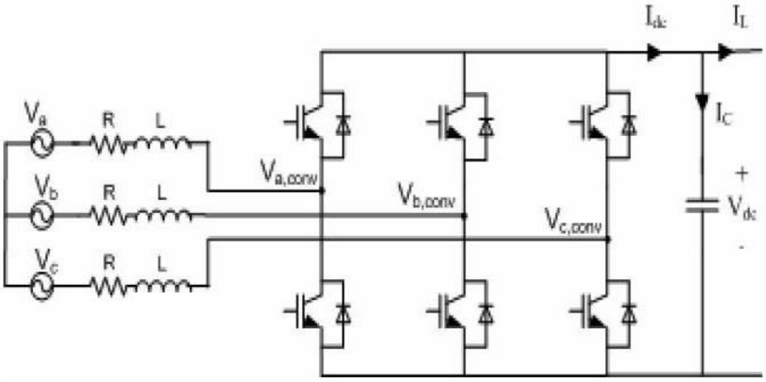

Figure 2.7: Structure of the two-level (2L) converter [6]

This converter can, as the name implies, generate two AC voltage levels, $\frac{1}{2}$ V_{dc} and $\frac{-1}{2}$ V_{dc}. The semiconductor devices (IGBTs in the figure) are series connected in order to achieve the desired operating voltage. A further explanation of the operation and control of this converter is provided in chapter 3.

Advantages of this converter is that the structure is simple and it contains few components, which makes the footprint of the converter smaller and the cost lower compared to alternative multilevel converters [41, 62]. However, this converter topology suffers from a number of disadvantages:

- Harmonics: The AC-side voltages will contain harmonic components of multiples of the switching frequency [41]. This problem can be reduced by increasing the switching frequency since that will cause the harmonics to appear at higher frequencies and reduce the low order harmonics. This will however increase another disadvantage of the 2L-VSC, namely the switching losses.

- Switching losses: The 2L-VSC suffers from high switching losses caused by the high frequency hard switched pulse-width modulation (PWM) control [63].
- High voltage stress: High dv/dt is caused by the series connection of IGBTs [63] and this will impose stress on the insulation of equipment connected to the AC-side of the converter[41].

2 **Multilevel converters:**

The disadvantages of the 2L-VSC can be reduced by using a multilevel converter. Multilevel converters can generate more than two voltage levels since they have more than one DC-link capacitor [41]. The higher number of levels used, the more low-order harmonics are reduced and the closer the AC output voltage will be to a sinusoidal wave. There are two main types of multilevel converters:

Diode clamped converters:

The structure of a three-level (3L) diode clamped converter is shown in figure 2.8 (a). This topology is also called the 3L neutral-point clamped (NPC) converter since the clamping diodes are connected to the midpoint or neutral point of the DC-link [41]. As the name implies, this converter can generate three voltage levels, $\frac{1}{2}$ V_{dc}, 0 V and $\frac{-1}{2}$ V_{dc}. In each phase leg of the converter there are two complementary switch pairs (i.e S_{1a} and S_{3a}, and S_{2a} and S_{4a} in figure 2.8 (a)), and these must be controlled in a complimentary manner [48]. Similarly to the 2L-VSC, the switch in each semiconductor valve consists of a series connection of switches in order to achieve the desired operating voltage [64].

$\frac{1}{2}$ V_{dc} is produced by turning on the two series connected upper valves of the converter. The 0 V voltage level is obtained by switching the two middle valves in each leg so that the extra diodes are connected. $\frac{-1}{2}$ V_{dc} is produced by turning on the two series connected lower valves. The upper DC capacitor charges when the output phase currents are positive and discharges when they are negative [48].The lower DC capacitors has the opposite charging/discharging sequence.

Flying capacitor converters:

The structure of a 3L flying capacitor converter (FLC) is shown in figure 2.8 (b). The structure and operation of this converter is similar to the diode clamped converter, but in this converter the 0 V voltage step is obtained by applying a DC capacitor in each phase [64]. These capacitors have no connection to a common DC-link and therefore they are called flying capacitors [41]. The voltage of these capacitors should be maintained at $\frac{V_d}{2}$.

Also in this topology there are two switch pairs in each leg which need to be switched in a complimentary manner. The 0 V voltage level can be achieved by two switching states; when S1 and S3 are on or when S2 and S4 are on [41]. In these two cases the current is forced through the flying capacitor and the terminal voltage will be 0 V.

The number of levels in a commercial multilevel converter is generally not very high due to the increasing number of components of the converter when the number of levels is increased, and the increasing cost and the complex mechanical design of the converter that causes [41]. According to D. Krug et. al. [7], the 3L-NPC converter is the most widely used topology in industry out of the 2L, 3L-NPC, 3L-FLC and 4L-FLC topologies. That

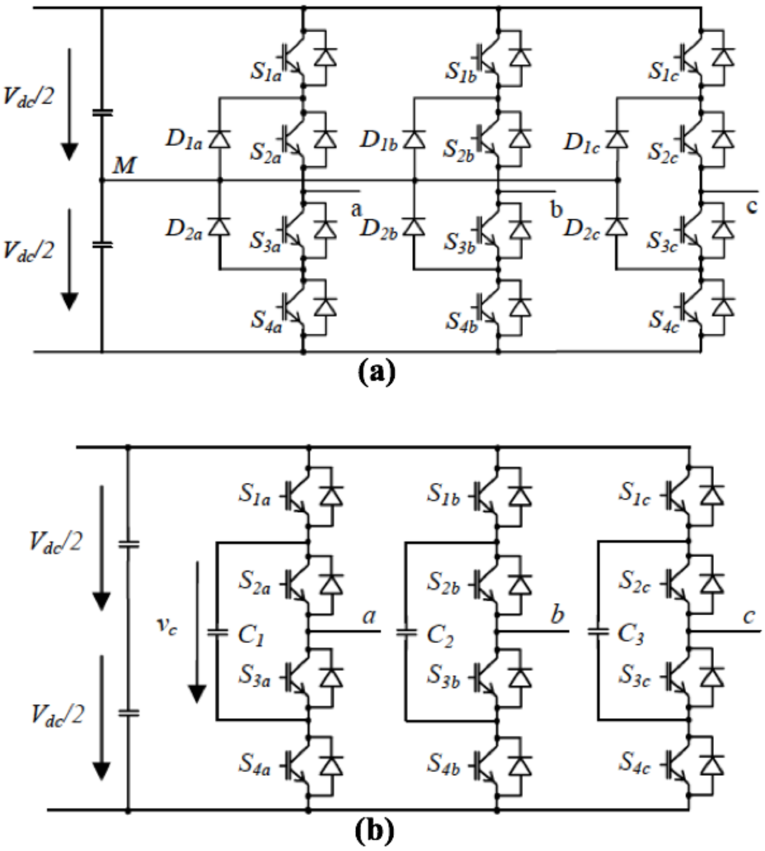

Figure 2.8: (a) 3L-NPC converter (b) 3L-FLC converter [7]

is because it has lower losses, costs, size and weight compared to the other topologies. According to K. Sharifabadi et. al [41], the only diode clamped converter that has had significant commercial success is the 3L-NPC, and the 3L-FLC has met limited success compared to the 3L-NPC. Compared to the 2L converter, the 3L has lower voltage stress, lower switching losses and lower harmonic content [64].

3 **Cascaded multilevel converters:**
Earlier Two-Level (2L) and Three-Level (3L) converters were used in VSC-HVDC schemes, but today the preferred technology is based on Modular Multilevel Converters (MMC) due to its many advantages. The MMC is a type of cascaded multilevel converters which are converters based on series connection of submodules (SMs) [41]. The SMs contain the VSC-DC capacitors and semiconductor valves, and this is a modular approach where more SMs are added to increase the number of levels in the converter. Figure 2.9 (a) shows the structure of the MMC and 2.9 (b) shows the most popular SM for the MMC, namely the half-bridge SM [8]. There are a number of different types of SMs that could be used for the MMC, and they will be discussed further in chapter 4 which describes the structure, operation and control of the MMC more in detail. As seen in figure 2.9 (a), the three-phase MMC consists of three phase legs with an upper and a lower arm in each leg. The arms consist of a number of SMs, where each of them is operating as a controllable voltage source [64].

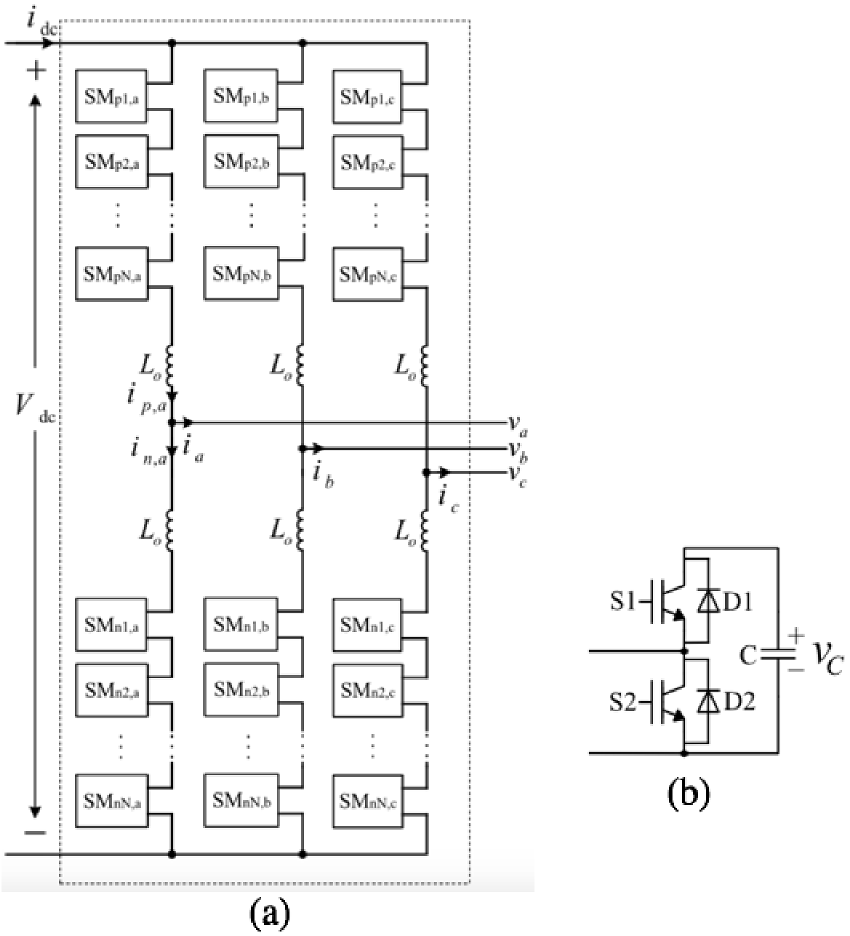

Figure 2.9: (a) Structure of the MMC (b) Half-bridge SM [8]

The MMC has a number of advantages compared to the 2L- and 3L-VSCs. Since the output waveform can be based on a large number of small voltage steps, the semiconductor valves in the SMs can be operated at a lower switching frequency and this results in lower switching losses, lower voltage stress dv/dt and less audible noise [63, 65]. In addition, with the increasing number of levels, the output waveform will become more sinusoidal and the harmonic content of the output will be reduced, which reduces the need for filters. An advantage when it comes to using the MMC for integration of battery storage is that the SM structure provides modularity and easy scalability and the battery storage cells can be placed inside each SM [66]. This concept of distributed batteries in MMC will be described further in chapter 4. The disadvantages of the MMC, on the other hand, are the complex circuit and its control in addition to a higher cost due to an increased count of semiconductor components.

2.4.3 HVDC configurations

HVDC transmission systems can have different configurations based on the application. In this project a point-to-point HVDC system is used, which means that two terminals are interconnected with a single HVDC-link. This configuration is used for most HVDC-systems [55]. Since there are two converters for each line, the DC power flow and voltage can be fully controlled, and since each line can be operated at a different voltage level, this configuration can be used to connect existing DC-links into a DC grid [58]. However, disadvantages with this configuration in a DC grid include high costs and losses due to the large number of converters required. For DC grids, a meshed configuration is a better solution due to use of fewer converters, which reduces the losses and costs compared to using point-to-point systems for the same system. In addition, the meshed configuration has an advantage in terms of security of supply, as the power can flow in a different path in case of a fault.

2.4.4 Fault handling and protection

In a power system it is important to have protection equipment installed so that faults can be handled quickly in order to maintain system stability and to comply with grid codes. If faults are not detected and isolated quickly, they will propagate through the grid and finally the voltage will collapse and power transmission will be lost. In worse cases, faults can lead to blackouts of large parts of a power system. Since the HVDC system used in this project is a point-to-point configuration, the AC-side circuit breakers can be used for protection [58]. In addition the DC/DC converter is galvanically isolated, so even though the MMC is not built up of full-bridge SMs which provide fault protection, the DC/DC converter is protected. However, as discussed in the previous subsection, a meshed configuration is a better solution for a multiterminal DC grid when it comes to fault protection. If the bigger picture is to be studied in terms of a multiterminal HVDC system, DC grids fault handling and protection must be taken into consideration.

In DC grids fault propagate rapidly since DC grids have low impedance and are almost inertia-less [41], meaning that the fault currents increase very quickly to high values and hence the fault propagates rapidly. Therefore the short circuit currents are high in DC systems and fast switching actions are required. A number of solutions have been developed:

- **Electronic switches:** One solution to interrupt the flow of uncontrolled currents into the DC grid is to connect IGBTs or another electronic switch in series with the DC pole of the converter [41]. When the switch has been opened, the converter can exchange reactive power with the AC system. However, this switch introduces additional losses to the converter.

- **Converters:** An alternative is to use converters with inherent DC fault current blocking capability such as full-bridge converters where the fault can be cleared using the AC-side circuit breakers [41].

- **AC-side circuit breakers:** The basis for the AC circuit breaker technologies in use today is the zero crossing of currents and voltages. This is the main challenge of DC circuit breakers, as there are no zero crossing of voltages and currents in DC systems, and hence the AC circuit breaker technology cannot be used to turn off large DC currents [67]. However, in a point-to-point HVDC system the AC-side circuit breakers can be employed to clear DC faults [58]. The AC breaker will disconnect the HVDC-link from the AC terminals so that the power will no longer be able to flow to the AC-side, and the DC voltage will be brought down to zero. However, for a multiterminal HVDC system this is not a good solution as the power flow in the DC grid is interrupted for every DC fault, and re-energizing the DC grid after the fault is cleared takes a considerable time [61].

- **DC circuit breakers:** The increasing use of HVDC technologies for transmission and DC grids has caused an increased investigation of DC circuit breakers, and a number of DC breaker solutions have been developed in industry and academia [41, 67, 68]. The DC current can only be extinguished by inserting a counter electromotive force (EMF) that exceeds the driving EMF of the DC network [41]. A DC circuit breaker can insert this voltage in parallel or series and a metal oxide varistor (MOV) can be used to provide this EMF. When the inserted EMF exceeds the driving voltage source of the DC grid, the fault current will decrease.

As shown in this subsection, there are a number of ways protection systems can be included in a DC grid. When choosing protection equipment it is important to consider is that it can add size, losses and costs to the total system, so the type of protection equipment should be chosen carefully considering these aspects in addition to the configuration of the system and the converter technologies used in the system.

The fault handling and protection concepts discussed in this subsection will not be treated more in the design or simulation parts of this project, since as discussed in the beginning of this subsection, the AC-side breakers and the galvanic isolation will be used for protection in this project. However, these are important aspects to consider when designing a multiterminal DC grid, which the system used in this project potentially could be a part of in the future. Therefore these aspects were included in this subsection.

2.5 DC/DC converters

A DC/DC converter is required in order to connect the battery to the DC-link of the HVDC transmission system. The battery has has a lower DC voltage than the DC-link and the battery must have bidirectional power flow capability in order for it to be able to charge and discharge to provide the ancillary services of primary and secondary reserves to the grid. Therefore the DC/DC converter must be able to step up the battery voltage to the voltage level of the DC-link when the power flow is from the battery to the DC-link, namely when the battery is discharging and provides power to the grid, and vice versa when the power flow is reversed. All DC/DC converters discussed in this chapter provide bidirectional power flow.

DC/DC converters can be classified based on their power rating and voltage ratios as shown in table 4.1 [25]. The voltage ratio is defined as the ratio between the DC voltage on the high voltage (HV) side and the DC voltage on the low voltage (LV) side according to equation 2.4:

$$V_{ratio} = \frac{V_{DC,HV}}{V_{DC,LV}} \tag{2.4}$$

The DC/DC converter in this project has a medium voltage ratio. As will be discussed in the design of the system in chapter 5, the high voltage side of the converter is connected to the HVDC-link, and hence has the DC-voltage of the HVDC-link, namely 320 kV. The low voltage side of the converter is connected to the battery, and since the coupling transformer steps down the voltage with $\frac{1}{3}$ (as also discussed in chapter 5), the battery voltage is found to be 108.87 kV in this project. In terms of power rating the power of the DC/DC converter in this project is 180 MW since the power flow to the battery is through this converter and it was stated in the objectives of this project that the battery power is supposed to be 10 - 20 % of the total wind farm power, which is 1 GW.

Table 2.2: Power ratings and voltage ratios for DC/DC converters [25]

High power			$P_{DC,transf.}$	$\geq$	500 MW
Medium power	50 MW	$\leq$	$P_{DC,transf.}$	$\leq$	500 MW
Low power	0 MW	$\leq$	$P_{DC,transf.}$	$\leq$	50 MW
High voltage ratio			V_{ratio}	$\geq$	5
Medium voltage ratio	1.5	$\leq$	V_{ratio}	$\leq$	5
Low voltage ratio			V_{ratio}	$\leq$	1.5

2.5.1 Galvanic isolation

Galvanic isolation is defined as a prevention of a direct current path between the two ends of the converter [25] and a coupling transformer is often used to provide the galvanic isolation. The structure of a front-to-front DC/AC/DC converter without galvanic isolation is shown in figure 2.10 (a). The DC/DC converter consists of a front-to-front connection of two AC/DC converters. As will be discussed in the next subsections, these converters can be different types of the VSCs discussed in chapter 3. In case of a fault in the DC-system at one of the converter ends, using this configuration without galvanic isolation, the fault will be transferred to the other end and affect the DC system there. The DC/DC converter with galvanic isolation (shown in figure 2.10 (b)), on the other hand, will prevent the fault transfer from the first DC system to the second due to the fact that the galvanic isolation prevents fault transfer.

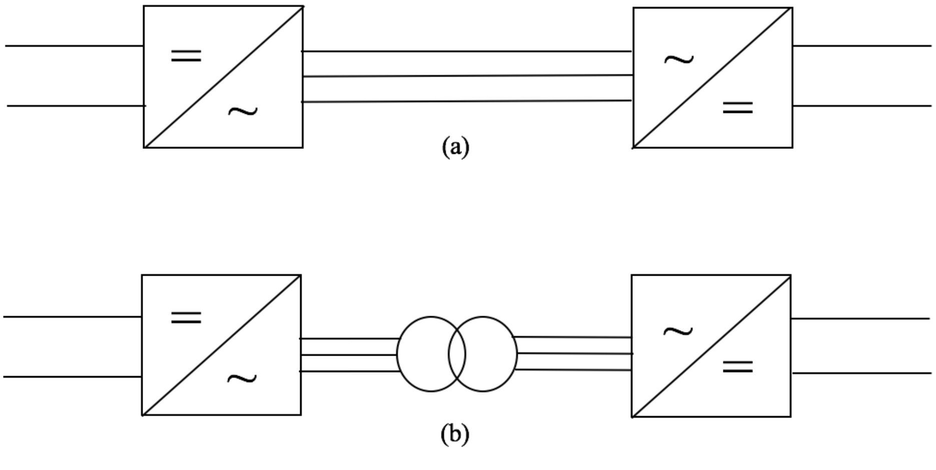

Figure 2.10: (a) DC/DC converter without galvanic isolation
(b) DC/DC converter with galvanic isolation [3]

In addition to providing galvanic isolation, the coupling transformer provides voltage matching, noise reduction, improves personnel safety and it ensures correct operation of protection systems [9]. On the other hand, introducing this extra component makes the converter more complex and it adds to the cost and size of the converter. Especially if the converter is to be placed offshore, size and weight are crucial and should be kept to a minimum in order to reduce costs [25]. In order to reduce the size and weight of the core of the transformer, the transformer can be designed for a operating frequency that is higher than the grid frequency [69]. Both three-phase and single-phase transformers can be used for the AC-link, but three-phase is the preferred solution since it limits the required current rating per phase. High frequency transformers and the design and modeling of the coupling transformer used in this project will be described further in chapters 5 and 6.

2.5.2 Front-to-front connected DC/AC/DC converters

A DC/DC converter can be created by connecting two VSCs in a front-to-front configuration as shown in figure 2.10. The DC/AC inverter and the AC/DC rectifier can be based on different types of the VSCs discussed in chapter 2.4.2. This type of DC/AC/DC converters can be with (figure 2.10 (b)) or without (figure 2.10 (a)) galvanic isolation. For converters with lower voltage ratios the DC/DC converters can be designed without galvanic isolation since the fault transfer can be inhibited by using very fast control response [25]. This works as long as the valves of the converter of the DC-system without fault, are rated for maximum voltage difference. However, for higher voltage ratios it is preferred to use DC/DC converters with galvanic isolation in order to avoid fault transfer [24, 25].

The DC/AC/DC converter has the same advantages and disadvantages as the VSCs it is made up of, which is described in subsection 2.4.2. However, if the DC/AC/DC converter is designed with galvanic isolation, it will provide additional advantages in terms of voltage matching and fault prevention. On the other hand, this extra component will add complexity, size and cost to the converter.

2.5.3 Resonant converters

Resonant converters have switching strategies which result in switching at zero-voltage and/or zero-current [70]. In most cases an LC resonant circuit in the converter is employed to achieve the soft switching and this control strategy reduces the switching losses. A type of zero-voltage switching (ZVS) bidirectional DC/DC converter that has gotten attention by researchers in the recent years is the dual active bridge (DAB)[24, 63].

Dual active bridge (DAB)
The three-phase DAB converter consist of two full-bridge cells that is connected with a transformer circuit [71, 72]. A single-phase DAB converter (shown in figure 2.11) will be used to explain the operation of the DAB converter. The converters that this DAB consist of have voltage-fed structures, and since they have capacitors with stiff voltage characteristics at the terminals, the converters will act like conventional buck or step-down converters at the input terminals [9].

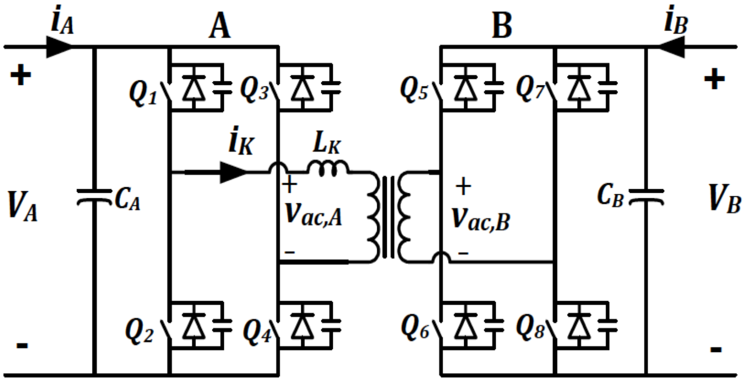

Figure 2.11: Single-phase dual active bridge [9]

The control strategy of the DAB is based on soft switched phase-shift modulation. ZVS is obtained when the current leaving the leg lags the voltage pole of the leg [9]. This implies that the zero-crossing of the current occurs after the zero-crossing of the voltage. This soft swithing modulation is possible over the entire power range when the voltage conversion ratio is equal to one [9, 73]. The voltage conversion ratio is defined as:

$$d = \frac{V_B}{nV_A} \tag{2.5}$$

where n is the transformer turns ratio and V_A and V_B are the DC-side voltages of the DC/DC DAB converter. The power flow is controlled by applying an appropriate phase shift between the AC voltages $V_{ac,A}$ and $V_{ac,B}$, imposed by the bridges on both sides of the transformer [9, 73]. The leakage inductance of the transformer L_k decides the amount of transferable power for a given frequency [9]. Hence, a high power density converter an be achieved by designing the transformer with low leakage inductance. Table 2.3 describes the power flow of the converter.

Table 2.3: DAB converter power flow [3]

AC voltage	Phase shift	Power flow direction
$V_{ac,A}\ leads\ V_{ac,B}$	Positive	$A \rightarrow B$
$V_{ac,A}\ lags\ V_{ac,B}$	Negative	$B \rightarrow A$

Due to the soft switching, the DAB has lower switching losses than the hard-switched PWM converters discussed in chapter 2. However, the conduction losses are higher for the DAB, but since the switching losses are kept low, the overall losses are lower in the DAB converter [9]. This also implies that the efficiency is higher. Other advantages of the DAB converter is that it has low device and component stresses [72], limited voltage stress and almost equal current stress on all the switches on each side of the converter [9].

There are also some disadvantages of this converter. Due to high current ripple in the DC buses, filtering circuits are required, which increases the size and cost of the converter. Three-phase DABs also have higher costs and size due to the use of more magnetic devices and the requirements of higher power [74]. Other disadvantages of the DAB includes loss of the soft-switching capability in light-load conditions, the converter is highly sensitive to variations in phase shift, and as there is no inherent DC current blocking capability for the transformer windings, good control systems is required to prevent dc saturation [9].

Further information about and comparisons of different types of DAB converters can be found in Appendix F.

Dual half-bridge (DHB)
Another DC/DC converter topology using ZVS soft switching control is the DHB. This converter can be used when the voltage on the low voltage side is a few tens of volts and the voltage on the high voltage side is a few hundreds of volts [9]. Also for this converter topology the single-phase structure (shown in figure 2.12) will be used to explain the operation of the converter. The DHB is different from the DAB by the fact that it is made up of two half-bridges instead of full-bridges, connected by a transformer. In the DAB both full-bridges are voltage-fed, but in the DHB, one half-bridge is voltage fed while the other is current-fed. As mentioned, the voltage-fed structure acts like a conventional buck or step-down converter. The current-fed structure acts like a conventional boost or step-up converter since it has an inductor with stiff current characteristics at the terminals [9]. Since smooth current with low ripple is desired for the battery, the current-fed half-bridge (side A on the figure) is placed on the low voltage side for battery applications.

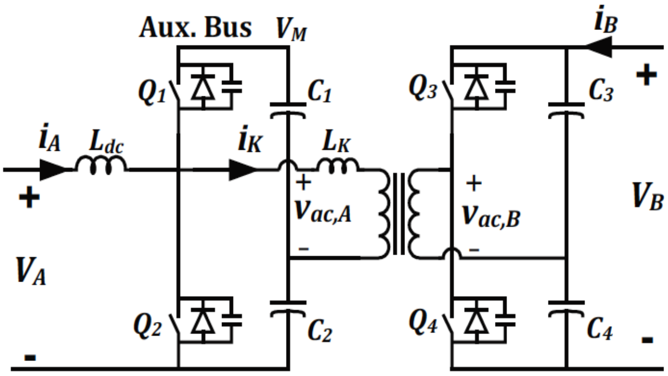

Figure 2.12: Single-phase dual half bridge [9]

The operation of the DHB converter is also based on soft switched phase-shift modulation. Also for this converter the power flow is determined by the inductance, which for the DHB consist of the leakage inductance of the transformer in addition to the series inductance on side A. According to H. R. Karshenas [9] the bidirectional power flow can be controlled over the whole range when the phase shift is controlled in the range -90° to +90°.

Advantages of the DHB include low current ripple on the current-fed side, simple phase-shift modulation control and a relatively wide range of ZVS operation [9]. In addition, when compared to the DAB, the switch count is low and the total device rating of active elements is the same as for a DAB with the same power. A disadvantage of this converter is that there is a large current ripple in the splitting capacitors on the low voltage side and that there is unbalanced stress in current between the switches.

2.5.4 Choice of DC/DC converter technology for this project

In the specialization project [3], two quadrant (2Q) and four quadrant (4Q) dedicated converters, 2L-, 3L- and MMC VSCs, in addtion to DHBs and DABs where discussed and compared to a set of criteria in order to find the optimal DC/DC converter for this project. The work resulted in table 2.4 which provides different characteristics for the different converter topologies which are important to consider when choosing a converter topology for this project. Further information about the different DC/DC converters can be found in Appendix F.

The criteria that these characteristics were compared to include low converter losses, low costs, ability to provide fault tolerance and bidirectional power flow, operation at medium voltage ratio and medium power level. In addition it was mentioned that the complexity of the converter and its control should be taken into consideration since it on the one hand could improve the converter in terms of lower losses and better performances, but on the other hand it could add to the size and cost of the converter. The discussion of the choice of optimal DC/DC converter topology is provided in Appendix F. The results shows that ideally the best choice would be to have soft switched DAB converter, but when choosing among the converter topologies that are in use in industry today it was concluded that the optimal choice is a galvanically isolated front-to-front connected DC/DC converter based on MMC [3].

In the specialization project [3] it was assumed that the same converter topology would be used as both the DC/AC inverter and the AC/DC rectifier in the front-to-front connected DC/DC converter. It is however possible to use two different topologies. Since the optimal DC/DC converter should provide galvanic isolation, a coupling transformer will be used which also will be able to provide voltage matching. Hence, the voltage levels of the two converters that make up the DC/DC converter will differ and it can be discussed whether the MMC is the optimal choice for the converter with the lowest voltage rating (i.e the converter connected to the battery).

According to G. P. Adam et. al [24], the use of series connected IGBTs is limited to 200 kV. The high voltage side of the DC/DC converter is connected to the DC-link of the HVDC transmission system with a voltage of 320 kV, hence an MMC, which utilizes series connections of SMs instead of series connection of single switching devices, will be the best choice of the DC/AC inverter in the DC/DC converter. The transformer providing galvanic isolation will step down the voltage on the battery side, and hence the voltage can be stepped down so much that 2L or 3L converters with series connected IGBTs can be used instead if a small increase in losses can be accepted for the price of a converter at a much lower cost.

However, if better performances are more important than lower costs and complexity, having a DC/DC converter made up of two MMCs will definitely be the best choice. In addition, it has been shown that the MMC has an advantage when it comes to battery connection since it can provide distributed batteries. This is also a motivation to use a DC/DC converter made up of two MMCs. A description of the MMC technology including a section on distributed batteries in MMCs is provided in chapter 4.

The main objective of this project is to show that a battery connected to the DC-link of an HVDC transmission system transferring power from an offshore wind farm to the grid onshore can provide ancillary services of primary and secondary reserves to stabilize the grid. Hence, since it is possible that this battery connected AC/DC converter can be a 2L-VSC and for simplicity when it comes to simulations, a 2L-VSC will be chosen so that the DC/DC converter will consist of a MMC on the high voltage side and a 2L-VSC on the low voltage side, connected by a coupling transformer. The topology chosen for the DC/DC converter in this project is therefore not the topology that optimally is the best solution, but it is a topology that is much simpler to implement in terms of simulation models and simulation times. It also used because it is able to represent the system for the simulation cases of interest in this project and the choice of this topology compared to the optimal topology does not affect the results much when the objective is to show that the battery can support the grid and that the DC/DC converter provides bidirectional power flow for this purpose. The design of the DC/AC/DC converter for this project is discussed in chapter 5.3.

Table 2.4: Characteristics of different DC/DC converter topologies [3]

Topology	**2Q**	**4Q**	**2L**	**3L**	**MMC**	**DHB**	**DAB**
Switching frequency [Hz]	–[i]	–[i]	1950[61], 1150[75][ii]	1350[61][iii] 1500[61][iv]	150[61], 89-765[71][v]	–[i]	Depends[vi]
Converter losses [%] (at power)[vii]	–[i]	–[i]	3[61]	1.8-2.2[61]	1(1000MW)[61][viii]	–[i]	0.8-1.01(1.2GW)[71]
Scalability	–	–	–	–	Easy	–	Easy
Complexity of controller	Low	Low	Low	Medium	High	Low	Low
Fault tolerance	No	No	If isolated	If isolated	If isolated	Yes	Yes
Voltage ratio	Low	Low	Low-High[ix]	Low-High[ix]	Low-High[ix]	High	High
Voltage level [V]	Low	Low[x]	±200000[xi]	High	High	10s-100s[xii]	Depends[24][xiii]
Number of valves[xiv]	2	4	6	12	12n[xv] 24n[xvi]	2[xvii]	Depends[xviii]
Number of extra components[xix]	0	0	0	6[xx] 3[xxi]	Depends[xxii]	0	Depends[xxii]
Cost[xxiii]	Low	Low	Medium, $13,260 [7]	Medium, $15,499[xxiv]or $16,311[xxv]	High	Low	Depends[xxvi]
Bidirectional power flow	Yes[xxvii]	Yes	Yes	Yes	Yes	Yes	Yes

---

[i] Numerical values for switching frequency was not found for the 2Q, 4Q or DHB converter. Based on the structure of these converters it can be assumed that the 2Q and DHB will have similar characteristics in terms of switching frequencies and converter losses, and that the 4Q and the DAB converters will have similar characteristics in terms of switching frequencies and converter losses.

[ii] Switching frequency for the 350 MW 2L optimal pulse-width modulation (OPWM) switched converter used in the Estlink HVDC Light® Transmission System

[iii] For the 3L active NPC [61]

[iv] For the 3L diode NPC [61]

[v] Different switching frequencies for the upper and lower arms for different operating scenarios of the MMC described in [71]

[vi] According to [76] the switching frequency is 20 000 Hz for a power of 1 MW, and for increasing power, the switching frequency decreases. The paper does not say anything about power levels as high as 200 MW, but for 5 MW the switching frequency is 1000 Hz. According to [71], a switching frequency of 1000 Hz is used for powers of 15 MW and 1.2 GW

[vii] Typical losses per converter. This includes both switching losses and conduction losses

[viii] Close to 1 % losses per station for converter stations of up to 1000 MW [60]

[ix] Low for 2L/3L/MMC based front-to-front DC/DC converter without galvanic isolation and and higher voltage ratios for 2L/3L/MMCs with transformer/galvanic isolation if assumed that the 2L and 3L converters with galvanic isolation can operate at higher voltage ratios similarly to the MMC in [25]

[x] Higher than for the 2Q converter

[xi] Assuming that it has the same voltage level as the 2L based DAB in [24]

[xii] Characterized as: voltage level on low voltage side - voltage level on high voltage side. I.e. 10s of volts on the LV side and 100s of volts on the HV side.

[xiii] 2L based: up to ±200 kV, MMC based: higher than for the 2L based

[xiv] Number of valves per converter. The front-to-front connection of VSCs and the DHB and DAB converters consist of two converters per DC/DC converter.

[xv] For a three-phase MMC with n half-bridge sub-modules (2 valves per submodule)

[xvi] For a three-phase MMC with n full-bridge sub-modules (4 valves per submodule)

[xvii] For a single-phase DHB

[xviii] 4 for a single-phase DAB, 6 for a 2L-based DAB, 12n for a MMC based DAB with half-bridge sub-modules, 24n for a MMC based DAB with full-bridge sub-modules, 6+6n for the TAC based DAB, 6+12n for the CTB based and the hybrid cascaded 2L based DABs and 6+24n for the alternative arm MMC based DAB. n is the number of sub-modules.

[xix] Number of extra diodes or extra capacitors per converter. The front-to-front connection of VSCs and the DHB and DAB converters consist of two converters per DC/DC converter.

[xx] Extra diodes for the 3L-NPC, the 3L-FLC does not have any extra diodes

[xxi] Extra capacitors for the 3L-FLC, the 3L-NPC does not have any extra capacitors

[xxii] Depends on the type of sub-module used in the MMC and MMC-based configurations of the DAB.

[xxiii] According to [71], the power electronics account for a major part of the total cost of the converter. Therefore the cost to a great extent depends on the number of power electronic components that the converter consists of. For some of the converter topologies it was possible to find a numerical cost value, so then that is given in this table in addition to a cost evaluation of low, medium or high costs.

[xxiv] For the 3L-NPC from [7]

[xxv] For the 3L-FLC from [7]

[xxvi] Depends on the structure of the DAB, but in general the cost of a DAB compared to a similar MMC is lower due to the fact that the DAB consists of fewer semiconductor components [71]

[xxvii] But it can only step up the voltage in one direction and step it down in the other [9]

Chapter 3

Two-level voltage source converter (2L-VSC)

3.1 Introduction

According to K. Sharifabadi et. al. [41], the 2L-VSC is the most used VSC for applications with DC-side voltages up to 1.8 kV. There is a wide variety of applications for this converter including automotive drive systems, industrial drives, low-voltage grid-connected converters and home appliances. In addition, the 2L-VSC is important since it is the basic building block for cascaded converters. In this project the 2L-VSC is used in the HVDC transmission system and it is also used in the front-to-front connected DC/DC converter used to connect the battery system to the DC-link of the HVDC system. In addition, it forms the building block for the half-bridge submodules used in the MMC, which is the other converter used in the DC/DC converter. The MMC is described in chapter 4.

The structure of the converter and its advantages and disadvantages compared to the other types of VSCs mentioned in this report, was discussed in chapter 2. This chapter will describe the operation, control and mathematical model of the 2L-VSC. This will further be used in chapters 5 and 6 to discuss the design of the converter and to develop the simulation model of the converter.

3.2 Operation

Figure 3.1 shows the operation of a phase leg of the 2L-VSC. In order to maintain safe operation of the converter, the semiconductor valves of the same phase leg must be operated in a complementary manner. If they are not, over-currents can occur, which can lead to damages of the system [48]. Since they operate in a complimentary manner, each of the switching devices must be rated to fully tolerate the DC link voltage. The relationship between the AC-side and DC-side voltages is described by equation (3.1) [41]:

$$V_{AC,ph} = s \cdot \frac{V_{DC}}{2} \tag{3.1}$$

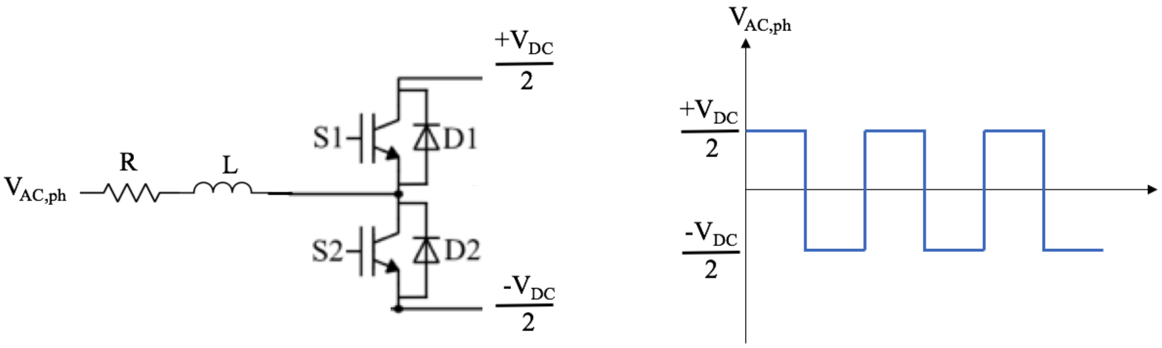

Figure 3.1: 2L-VSC phase leg operation

Where s = +1 when the upper valve is ON and s = -1 when the lower vale is ON. Depending on the current direction, the switch (S) or the diode (D) is conducting when a valve is ON. The operating states of a phase leg of the 2L-VSC are summarized in table 3.1. The different operating states are switch conduction (S), diode conduction (D), commutation from switch to diode (C1) and commutation from diode to switch (C2).

Table 3.1: Operating states of a phase leg of the 2L-VSC

Operating state	**S1**	**S2**	**D1**	**D2**	$v_{AC,ph}$	**Current direction**
S	1	0	0	0	$\frac{+V_{DC}}{2}$	DC to AC
$C1$	1	0	0	1	Change from $\frac{+V_{DC}}{2}$ to $\frac{-V_{DC}}{2}$	DC to AC
D	0	0	0	1	$\frac{-V_{DC}}{2}$	DC to AC
$C2$	1	0	0	1	Change from $\frac{-V_{DC}}{2}$ to $\frac{+V_{DC}}{2}$	DC to AC
D	0	0	1	0	$\frac{+V_{DC}}{2}$	AC to DC
$C2$	0	1	1	1	Change from $\frac{+V_{DC}}{2}$ to $\frac{-V_{DC}}{2}$	AC to DC
S	0	1	0	0	$\frac{-V_{DC}}{2}$	AC to DC
$C1$	0	1	1	0	Change from $\frac{-V_{DC}}{2}$ to $\frac{+V_{DC}}{2}$	AC to DC

The semiconductor devices of each valve are connected in series in order to increase the operating voltage:

$$V_{DC} = N_{series} \cdot V_{blocking} \tag{3.2}$$

Where V_{DC} is the operating voltage on the DC-side of the converter and N_{series} is the number of series connections of semiconductor devices with rated bloking voltage of $V_{blocking}$.

3.3 Mathematical model

Figure 3.2 shows the structure of the 2L-VSC and it will be used to develop the mathematical model of the converter.

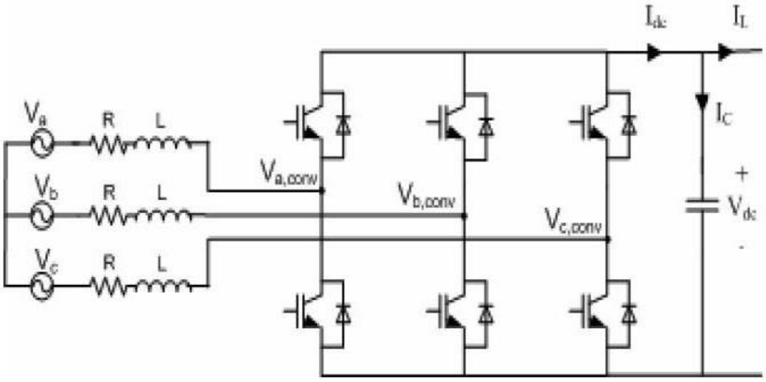

Figure 3.2: Structure of the two-level converter [6]

Using Kirchhoff's voltage law (KVL) on the AC-side, the voltages and currents of each phase $k \in a, b, c$ of the 2L-VSC can be described by [6]:

$$V_k = R \cdot i_k + L\frac{di_k}{dt} + V_{k,conv} \tag{3.3}$$

where V_k is the phase voltage, i_k is the phase current, R is the filter resistance, L is the filter inductance and $V_{k,conv}$ is the converter input voltage.

Using Clake's and Park's transformations given in Appendix B, equation (3.3) in the three-phase reference frame can be expressed in the $dq0$ reference frame which is synchronously rotating at a given AC frequency ω:

$$L\frac{di_d}{dt} = -R \cdot i_d + \omega \cdot L \cdot i_q - V_{d,conv} + V_d \tag{3.4}$$

$$L\frac{di_q}{dt} = -R \cdot i_q - \omega \cdot L \cdot i_d - V_{q,conv} + V_q \tag{3.5}$$

Using Kirchhoff's current law (KCL) on the DC-side, the DC-side current is described by [6]:

$$i_{dc} = C \cdot \frac{dv_{dc}}{dt} + i_L \tag{3.6}$$

The active power balance between the AC- and DC-sides of the circuit is described by the power balance equation [6]:

$$P = \frac{3}{2}(v_d \cdot i_d + v_q \cdot i_q) = v_{dc} \cdot i_{dc} \tag{3.7}$$

The reactive power at the AC-side is described by [77]:

$$Q = \frac{3}{2}(v_q \cdot i_d - v_d \cdot i_q) \tag{3.8}$$

If the d-axis is aligned to the AC voltage vector, $v_q = 0$ and the equations for the active and reactive power on the AC-side reduce to [6]

$$P = \frac{3}{2}v_d \cdot i_d \tag{3.9}$$

$$Q = \frac{3}{2}v_d \cdot i_q \tag{3.10}$$

Equations (3.9) and (3.10) show that active and reactive power of the converter can be controlled independently; active power can be controlled by controlling i_d and reactive power can be controlled by controlling i_q. The angular position of the voltage vector is given by the angle $\omega t = \theta$, shown in figure B.1 in Appendix B.

$$\theta = \tan^{-1}(\frac{u_\alpha}{u_\beta}) \tag{3.11}$$

where u_α and u_β are voltage components in the stationary $\alpha\beta0$ reference frame, described in Appendix B. θ is obtained from the phase-locked loop (PLL) in the controller, which will be discussed further in the next subchapter.

3.4 Control

Figure 3.3 shows an overview of the 2L-VSC controllers. As shown, the control of the 2L-VSC consists of an outer control loop where the power or voltage of the converter is controlled to generate the reference signals i_d^* and i_q^*, which are inputs to the inner controller loop which controls the current of the converter. Since the voltages and currents are transformed to the synchronous $dq0$ reference frame, the signals become signals with balanced sinusoidal conditions that are perfect synchronized, and hence proportional-integral (PI) controllers can be used in the control loops to ensure zero steady state error [6]. As seen in equations (3.4) and (3.5), the model in the synchronous rotating $dq0$ reference frame is coupled due to the cross-coupling terms $\omega \cdot L \cdot i_q$ and $\omega \cdot L \cdot i_d$. The control system requires a decoupled control of i_d and i_q, and a decoupling of equations (3.4) and (3.5) can be obtained by feed-forward compensation, as described in [78]. In the Laplace domain the decoupled equations are on the form:

$$(Ls + R)I_{d,q}(s) = V_{d,q}(s) \tag{3.12}$$

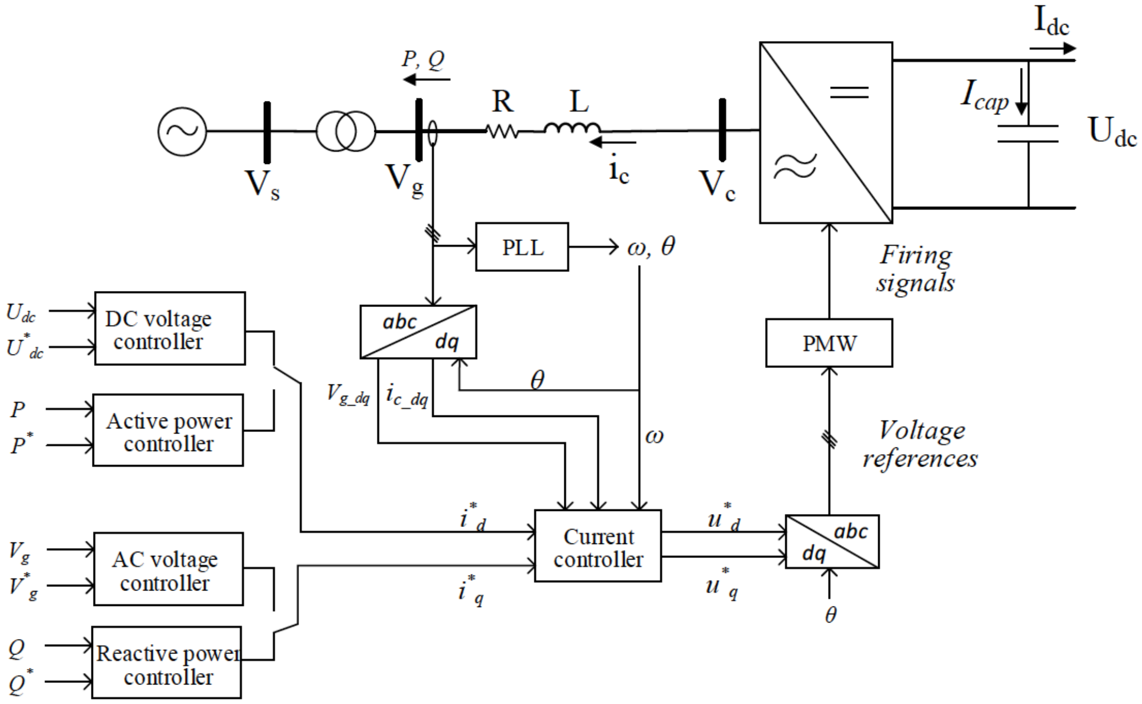

Figure 3.3: 2L-VSC controllers [10]

In the simulation model, the circuits are modelled using SI units while the controllers are modelled using pu-values for easy scalability. The system can be represented in pu using the following equations and base values [78]

$$Z_b = \frac{V_b}{I_b} \tag{3.13}$$

$$Z_{dc,b} = \frac{V_{dc,b}}{I_{dc,b}} \tag{3.14}$$

$$S_b = \frac{3}{2} V_b I_b = V_{dc,b} \cdot I_{dc,b} \tag{3.15}$$

$$V_{dc,b} = 2 \cdot V_b \tag{3.16}$$

Where Z_b is the base impedance, V_b is the peak of the base phase AC voltage, I_b is the peak of the base AC phase current, $Z_{dc,b}$ is the DC-side base impedance, $V_{dc,b}$ is the base DC-side voltage, $I_{dc,b}$ is the base DC-side current and S_b is the base three-phase power on the AC-side. In addition the base angular frequency of the AC quantities, w_b, is introduced. The SI-values can now be represented as pu-values using the base values and the equation:

$$X_{pu} = \frac{X_{SI}}{X_b} \tag{3.17}$$

In pu-values the filter resistance and inductance are represented as

$$R_{pu} = \frac{R}{Z_b} \tag{3.18}$$

and

$$L_{pu} = \frac{w_b L}{Z_b} \tag{3.19}$$

And the DC-side capacitance is represented as

$$C \cdot Z_{dc,b} = \frac{1}{\omega_b C_{pu}} \tag{3.20}$$

Equation (3.12) can now be represented in pu:

$$V_{d,q,pu}(s) = I_{d,q,pu}(s)(\frac{L_{pu}}{w_b}s + R_{pu}) \tag{3.21}$$

Using equations (3.6), (3.7) and (3.9), the DC-side dynamics can be represented in pu [79]

$$\frac{1}{\omega_b C_{pu}} \cdot \frac{dV_{dc}}{dt} = \frac{V_{d,pu}}{dt} \cdot I_{d,pu} - I_{L,pu} \tag{3.22}$$

3.4.1 Inner control loop

Figure 3.4 shows a block diagram of the inner current control loop. The AC-side currents are measured in the circuit and θ is obtained from the PLL, which is used to synchronize the converter to the grid voltage at the point of common coupling (PCC) [2] and to track the grid frequency [80]. The measured AC-side current and θ are used as inputs to the acb/dq block (as shown in figure 3.3) which transforms the signal into the $dq0$ reference frame. The input to the current controller is this measured current in the $dq0$ reference frame and the reference current, obtained from the outer control loop. The PI-controller controls the current to follow its reference. This controller is tuned using the modulus optimum criteria, which will be described in the next subsection. The output of the PI-controller is a voltage component that is sent to the PWM converter, which creates the gate signals that are sent to the converter to control the switching. PWM modulation is described in chapter 3.5. The PWM converter and the system are represented by the transfer functions Y(s) and G(s) as shown in the block diagram [78].

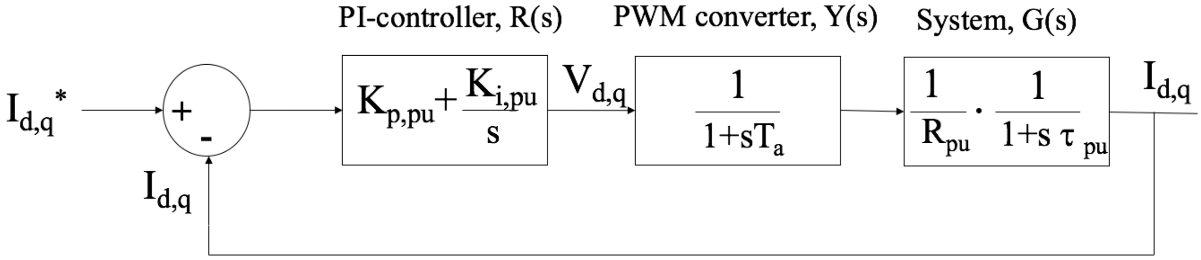

Figure 3.4: Inner current controller loop

3.4.2 Modulus optimum

The inner control loop is designed to have fast response and it is tuned according to the modulus optimum condition [6]. The goal is to achieve a closed loop transfer function which should be higher than unity for as high frequencies as possible [6, 78]. In other words, it is desirable to have a closed loop transfer function that follows the 0 dB-line of the bode plot for as long as possible (i.e. for as high frequencies as possible). The open loop transfer function of the inner controller loop is described by equation (3.23).

$$G_{i,OL} = R(s) \cdot Y(s) \cdot G(s) = K_{p,pu} \cdot \frac{1+sT_i}{sT_i} \cdot \frac{1}{1+sT_a} \cdot \frac{1}{R_{pu}} \cdot \frac{1}{1+s\tau_{pu}} \tag{3.23}$$

where

$$K_{i,pu} = \frac{K_{p,pu}}{T_i} \tag{3.24}$$

$K_{p,pu}$ and $K_{i,pu}$ are the integral and proportional gains of the PI-controller, respectively. T_i is the time constant of the PI-controller and τ_{pu} is the per unit time constant of the system [6]. T_a is the delay caused by the switches in the converter and in this project digital PWM modulation is assumed, and hence $T_a = 1.5T_{sw} = \frac{1.5}{f_{sw}}$, where f_{sw} is the switching frequency of the converter [78]. PWM modulation is described in subchapter 3.5.

The closed loop transfer function of the inner controller can be found using equation

$$G_{i,CL} = \frac{1}{1+\frac{1}{G_{i,OL}}} \tag{3.25}$$

The modulus optimum tuning criteria says that "the control system transfer function for the modulus optimum is achieved by cancelling the largest time constant, while the closed loop gain should be larger than unity for as high frequencies as possible" [6]. Using this tuning criteria, the following parameters are obtained [6, 78]:

$$T_i = \tau_{pu} = \frac{L_{pu}}{\omega_b R_{pu}} \tag{3.26}$$

$$K_{p,pu} = \frac{\tau_{pu} R_{pu}}{2 \cdot T_a} = \frac{L_{pu}}{\omega_b \cdot 2 \cdot T_a} \tag{3.27}$$

$$K_{i,pu} = \frac{K_{p,pu}}{\tau_{pu}} = \frac{R_{pu}}{2 \cdot T_a} \tag{3.28}$$

And the obtained open loop and closed loop transfer functions of the system are described by equations (3.29) and (3.30), respectively [6].

$$G_{i,OL} = \frac{1}{2 \cdot T_a} \cdot \frac{1}{s \cdot (1+sT_a)} \tag{3.29}$$

$$G_{i,CL} = \frac{1}{2 \cdot s^2 \cdot T_a^2 + 2 \cdot s \cdot T_a + 1} \tag{3.30}$$

3.4.3 Outer control loop

As shown in figure 3.3 the outer control loop can control either DC voltage or active power, creating i_d^* which is the input current reference to the current controller. To create i_q^* the outer controller can control either AC voltage or reactive power. In this project the 2L-VSC will be connected to the battery side of the DC/DC converter. The battery must be able to charge and discharge, so the converter must provide bidirectional power flow. Hence, the DC voltage (i.e the battery voltage) or the active power flow must be controlled in addition to the current. As will be seen in the simulation model later $i_q^* = 0$, so this outer control part of the 2L-VSC chapter will focus on an outer DC voltage controller. Also the 2L-VSCs used in the HVDC transmission system in this project are based on controlling the DC-link voltage to maintain a balance between the DC-link power and the AC power supply, as described by equation (3.7). A block diagram of the controller is shown in figure 3.5. The PI-controller controls the DC voltage to follow its reference. The dynamics of the DC-side are represented in pu in equation (3.22). This equation is non-linear which is a problem when designing a linear PI-controller. Therefore the equation is linearized around the operating point, as shown in [6, 79]. As shown in figure 3.5 a feed-forward reference is included ($\frac{V_{d,pu}}{V_{dc,pu}} \cdot I_{L,pu}$). This is because a cascaded control system like this consisting of two controller loops is likely to respond slowly, and therefore a feed-forward can be included to minimize this slow response [6]. In addition, the second order closed loop transfer function of the inner current controller is approximated by a first order equivalent transfer function as shown in the figure, where

$$T_{eq} = 2 \cdot T_a \tag{3.31}$$

This is found by equating the error functions of the two transfer functions and it is described further in [79].

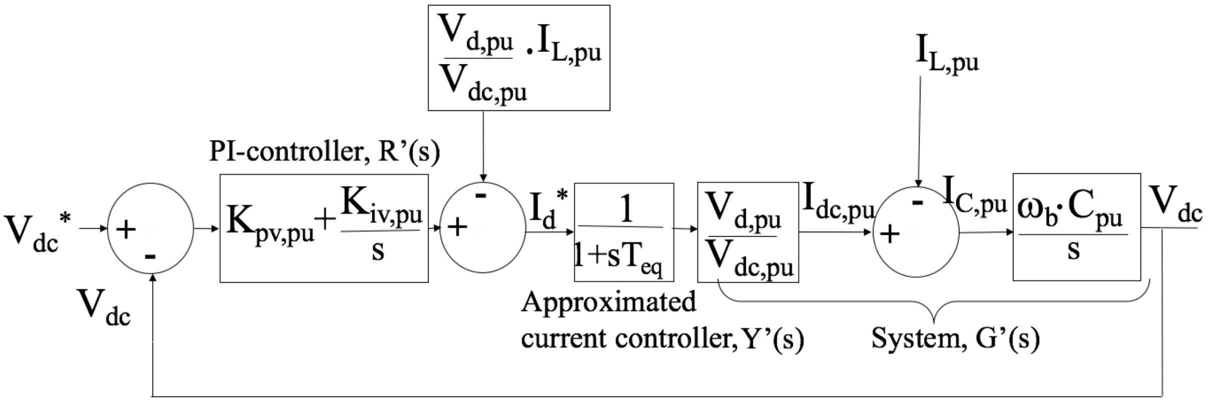

Figure 3.5: Outer DC voltage controller loop

3.4.4 Symmetrical optimum

In order to ensure stability, the outer control loop must be slower acting than the inner control loop [2]. The open loop transfer function of the outer DC voltage controller is given by equation (3.32).

$$G_{v,OL} = R'(s) \cdot Y'(s) \cdot G'(s) = K_{pv,pu} \cdot (\frac{1 + sT_{iv}}{sT_{iv}}) \cdot \frac{1}{1 + sT_{eq}} \cdot (\frac{V_{d,pu}}{V_{dc,pu}} \cdot \frac{\omega_b \cdot C_{pu}}{s}) \tag{3.32}$$

The tuning of this controller cannot be based on the modulus optimum criteria since the open loop transfer function has two poles in origo, which can be seen from equation (3.32). Therefore the symmetrical optimum design criterion is used which aims at having the crossover frequency at the maximum of the phase margin [79]. When the phase margin is maximized, the system can tolerate longer delays without stability loss [6]. The tuning criteria is obtained using the Nyquist criteria of stability [6]:

$$|G_{v,OL}(j\omega)| = 1 \tag{3.33}$$

and

$$\angle G_{v,OL} = -180^\circ + \Phi_M \tag{3.34}$$

where Φ_M is the phase margin. Using the criteria in equation (3.34) it can be found that the open loop frequency characteristic will have a maximum Φ_M at the crossover frequency ω_d [6]:

$$\omega_d = \frac{1}{\sqrt{T_{iv} \cdot T_{eq}}} \tag{3.35}$$

This crossover frequency is symmetric about $\frac{1}{T_{iv}}$ and $\frac{1}{T_{eq}}$, so the time constant of the controller is given by equation (3.36) [6].

$$T_{iv} = T_{eq} \cdot (\frac{1 + \sin \Phi_M}{1 - \sin \Phi_M}) = a^2 \cdot T_{eq} \tag{3.36}$$

where a is the symmetrical distance between ω_d and $\frac{1}{T_{iv}}$, and ω_d and $\frac{1}{T_{eq}}$.

Using the criteria in equation (3.33) the proportional gain of the PI-controller is found to be [6]:

$$K_{pv,pu} = \frac{T_c}{K \cdot \sqrt{T_{iv} \cdot T_{eq}}} = \frac{T_c}{a \cdot K \cdot T_{eq}} \tag{3.37}$$

where

$$K = \frac{V_{d,pu}}{V_{dc,pu}} \tag{3.38}$$

and

$$T_c = \frac{1}{\omega_b \cdot C_{pu}} \tag{3.39}$$

The integral gain of the PI-controller can be found using equation (3.40):

$$K_{iv,pu} = \frac{K_{pv,pu}}{T_{iv}} \tag{3.40}$$

The obtained open loop and closed loop transfer functions are described by equations (3.41) and (3.42) [6].

$$G_{v,OL} = \frac{1}{a^3 \cdot s^2 \cdot T_{eq}^2} \cdot (\frac{1 + a^2 \cdot sT_{eq}}{1 + sT_{eq}}) \tag{3.41}$$

$$G_{v,CL} = \frac{1 + a^2 \cdot sT_{eq}}{1 + a^2 \cdot sT_{eq} + a^3 \cdot s^2 T_{eq}^2 + a^3 \cdot s^3 T_{eq}^3} \tag{3.42}$$

3.5 Modulation techniques

3.5.1 Control algorithm based on PWM

The purpose of the PWM control is to control the output voltage and the harmonic content in the voltage and current waveforms. By switching a direct voltage between two discrete voltage levels, the PWM method is used to synthesize the reference voltage in the output for the 2L-VSC [41]. For multilevel converters it is switched between a higher number of levels to create the desired number of levels in the output waveform.

In order to produce a sinusoidal waveform at the desired frequency, a control reference signal at the desired frequency is compared to a modulation carrier signal [70]. The modulation signal has a frequency f_{sw}, which establishes the switching frequency of the converter. The reference signal has the frequency f_1, which is the desired fundamental frequency of the output of the converter. Since the output of the converter will not have a perfect sinusoidal waveform (as discussed in chapter 2, more levels will provide an output closer to a perfect sinusoidal wave), the output will contain harmonic components at harmonic frequencies of f_1. As mentioned in chapter 2, the harmonics can affect components in the power system and reduce efficiency and power quality of the system. Therefore it is desired to move the harmonics to higher frequencies where they can more easily be filtered out and where their negative effects have less impact on the system [41]. Total harmonic distortion (THD) is used to characterize the harmonic distortion [38, 41]:

$$THD = \frac{1}{V_1}\sqrt{\sum_{n=2}^{\infty} V_n^2} \tag{3.43}$$

where V_1 is the RMS value of the fundamental harmonic component and V_n is the harmonic component of order n. n = 1 represents the fundamental frequency. The equations of the harmonic components are provided in Appendix A.

The modulation index or amplitude modulation ratio relates the amplitude of the reference and modulation signals [41, 70]:

$$m_a = \frac{\hat{V}_{control}}{\hat{V}_{carrier}} \tag{3.44}$$

where $\hat{V}_{control}$ is the peak amplitude of the control reference signal and $\hat{V}_{carrier}$ is the peak amplitude of the modulation carrier signal. For the 2L-VSC the output signal fluctuates between $\frac{1}{2}v_{DC}$ and $-\frac{1}{2}v_{DC}$, as described earlier in this chapter. It can be shown that the fundamental frequency component of the output signal of the converter is described by equation (3.45) [70].

$$\hat{v}_{s,1} = m_a \frac{v_{DC}}{2} \tag{3.45}$$

where m_a is normally a value between zero and one. The performance of a PWM-VSC can be improved by increasing the frequency of the modulation since the higher number of pulse number provides a broader spectrum of harmonics that can be eliminated, and the pulse number is given by equation (3.46) [11]

$$p = \frac{f_{sw}}{f_1} \tag{3.46}$$

As described before, f_{sw} is the modulation signal frequency or the switching frequency of the converter. It depends on the semiconductor devices used in the converter [11]. f_1 is the fundamental frequency of the output of the converter.

The most widely use PWM techniques include sinusoidal pulse-width modulation (SPWM), selective harmonic elimination (SHE) and space vector modulation (SVM) [11]:

Sinusoidal pulse-width modulation (SPWM):
In this strategy a low-frequency reference signal $v_{control}$ is compared to a high-frequency carrier signal $v_{carrier}$ [48], as shown in figure 3.6. The switches of the upper and lower valves of the 2L-VSC phase leg are turned on and off in a complimentary manner when the reference and carrier signals cross. When the reference signal exceeds the carrier signal, the upper switch is turned on while the lower switch is turned off. The opposite switching sequence occurs when the carrier signal exceeds the reference signal. For a three-phase 2L converter, three reference signals are required, one for each phase, but they are all compared to the same high-frequency carrier signal [11, 48].

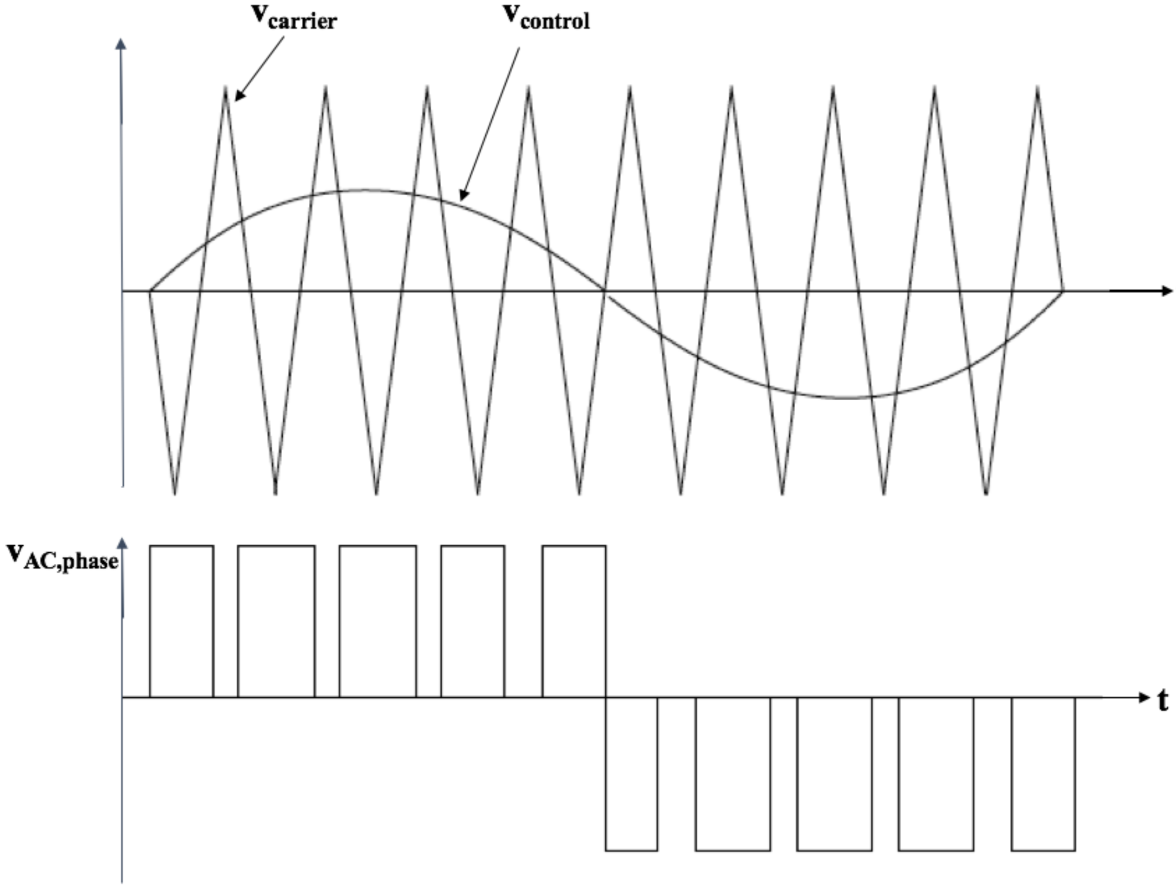

Figure 3.6: SPWM waveforms [11]

Selective harmonic elimination (SHE):
This technique is based eliminating low order harmonics selectively by reversing the phase voltage a few times during each half cycle [11]. The method explicitly defines the switching

angles of the phase voltage that are required to eliminate specific harmonics in the output [48]. This control strategy helps improving the quality of output voltage as it reduces the harmonic content of the output. However, the high order harmonics may increase in magnitude [11]. **Space vector modulation (SVM):**
In this control strategy all possible switching combinations of the converter is plotted in the $\alpha\beta$-plane [48]. Using equation (3.47) the output voltages of each phase of the converter can be transformed into the equivalents v_α and v_β. This is done for all possible combination of switching pattern. Using equations (3.48) ad (3.49), the space vector diagram can be plotted.

$$\begin{bmatrix} v_\alpha \\ v_\beta \end{bmatrix} = \begin{bmatrix} 1 & \frac{-1}{2} & \frac{-1}{2} \\ 0 & \frac{\sqrt{3}}{2} & -\frac{\sqrt{3}}{2} \end{bmatrix} \begin{bmatrix} v_a \\ v_b \\ v_c \end{bmatrix} \tag{3.47}$$

$$|v| = \sqrt{{v_a}^2 + {v_b}^2} \tag{3.48}$$

$$\theta = \tan^{-1} \frac{v_\beta}{v_\alpha} \tag{3.49}$$

As described earlier, PWM modulation is used for calculating the gains of the controllers of the 2L-VSCs in the HVDC system. The calculations are provided in the MATLAB script in Appendix C.2. However, as will be seen later in this thesis, the simulation models of the 2L-VSCs in this project are based on average value models of the converter, so the switches are not modeled explicitly, and hence there is no modeling of the PWM modulation. The output of the controllers (which use PI-controllers with gains calculated based on PWM modulation) are creating the reference signal that is sent to the average value model of the switches, so it is somehow included, but it is not modeled explicitly.

3.5.2 Control algorithm based on square wave operation

According to T. M. Undeland et. al [70], there are two types of three-phase switch-mode voltage source inverters (VSI); PWM inverters, based on PWM modulation as described in the previous subsection, and square-wave inverters, based on square wave operation, which will be described briefly in this subsection.

In the square-wave switching scheme, the inverter controls only the frequency of the output AC voltage since the input DC voltage is controlled to control the magnitude of the output AC voltage [70]. Each switching valve of the converter leg is on for half a cycle of the desired output frequency, and hence the output AC voltage has square-waveform, as shown in figure 3.7.

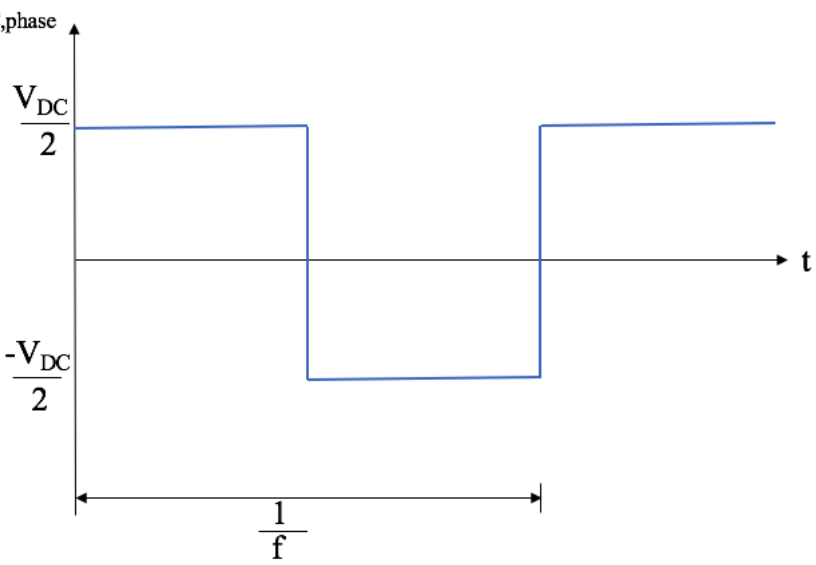

Figure 3.7: Square wave AC output

This type of switching scheme is a special case of the SPWM switching when m_a becomes so large that $v_{control}$ only intersects with $v_{carrier}$ at the zero-crossings of $v_{control}$ [70]. Hence, this type of switching scheme can be used to provide a type of soft-switching. This is shown in figure 3.8 were $v_{AC,1}$ is the fundamental frequency component in the inverter output.

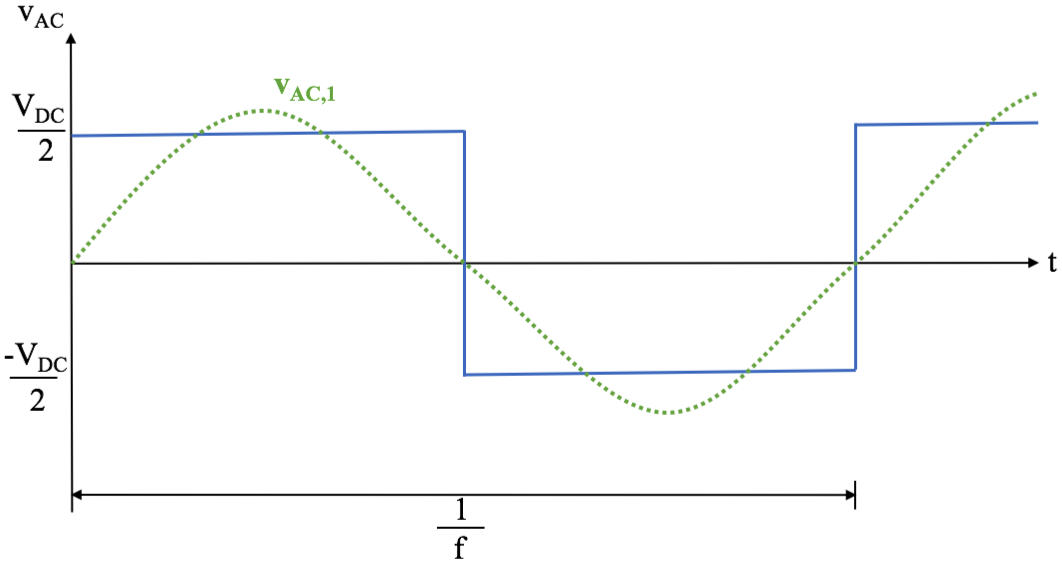

Figure 3.8: Square wave operation

An advantage with this type of operation is that the switches change state only twice per cycle [70]. At very high power levels this is desired since the switches generally have lower turn-on and turn-off speeds at these power levels. A disadvantage is that the AC-side voltage output must be regulated by controlling the DC input voltage and it is not controlled in the inverter with this type of operation.

Chapter 4

Modular multilevel converter (MMC)

4.1 Introduction

The MMC is a relatively new technology and it was introduced by R. Marquardt [81] in 2002. As seen in chapter 2, the MMC has some great advantages compared to more traditional VSC technologies such as the 2L and 3L converters. There has been a rapid adoption of this technology within industry [41] and a number of HVDC transmission systems using MMCs are already in operation. The first HVDC transmission project using this technology was the Trans Bay Cable project [82] in 2010, which was manufactured by Siemens. Other manufacturers have also commercialized the MMC technology. ABB has introduced the cascaded two-level converter (CTL) in their existing HVDC Light$^{\text{TM}}$ technology [83], Mitsubishi use MMCs in their SVC-Diamond$^{\text{TM}}$ Static Synchronous Compensator [84], and Altsom use MMCs in their HVDC MaxSine$^{\text{TM}}$ technology [85].

This chapter starts with an introduction to the concept of distributed batteries in MMCs, which was discussed as one of the advantages of this converter topology in chapter 2. After that, the MMC topology and different types of submodules (SMs) are discussed, before the mathematical model, operation and control of a three-phase MMC with half-bridge SMs is described.

4.2 Distributed batteries in MMCs

A BESS consists of battery storage units and a power conversion system (PCS) [86]. Using conventional 2L- or multilevel VSCs as the PCS, the battery units are connected in series to achieve the desired voltage and the total battery is connected on the DC-side of the converter. Disadvantages of this configuration include reduced lifetime of the batteries due to overcharging unless an equalization method is used, and disconnection of an entire string if a fault occurs in one battery module due to the series connections. These disadvantages negatively impact the system in terms of cost, efficiency and reliability. In addition, since the energy must be transferred bidirectionally through the battery, the round trip efficiency of the BESS is the square of the converter efficiency [86]. Hence, in terms of efficiency an MMC with losses of around

1 % (see table 2.4) would have much better performances for battery connection than a 2L-VSC with around 3 % converter losses. Therefore, an MMC with centralized batteries would have better performances in terms of losses compared to 2L- and multilevel VSC, but it would still require long battery strings and it would not utilize the modularity of the converter.

As mentioned in chapter 2, an advantage of the MMC for battery storage applications is that the battery cells can be placed inside the SMs of the MMC instead of having one centralized battery that the converter is connected to. Figure 4.1 shows how a BESS can be connected to an MMC with half-bridge SMs. The storage elements can be connected directly to the DC-link (as shown in figure 4.1 (a)) or they can be connected in a distributed manner in the SMs that the MMC is built up of (as shown in figure 4.1 (b)). According to G. Wang et. al [12] the latter is the best option for MMCs used in battery storage applications. Also T. Soong et. al [86] concludes this. [86] provides a comparison of the performances of an MMC with distributed batteries and an MMC with centralized batteries. The results show that the MMC with distributed batteries requires a larger number of semiconductor devices for a given power level, but also that this is the most efficient, reliable and versatile solution for integration of battery storage.

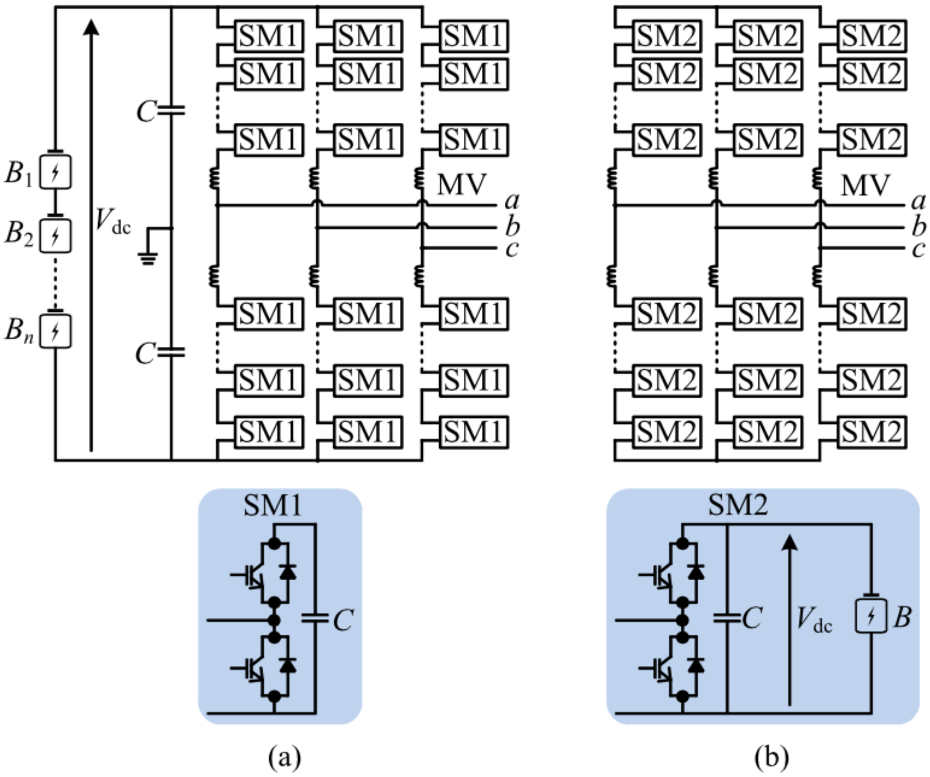

(a) (b)

Figure 4.1: (a) MMC with centralized batteries on the DC-link (b) MMC with distributed batteries in the SMs [12]

In the MMC with distributed batteries the battery modules can be connected in the SMs in two ways; they can be connected directly across the capacitor in the SM as shown in figure 4.2 (a), or they can be connected through a DC/DC converter as shown in figure 4.2 (b). When the battery is directly connected across the capacitor, the battery is directly exposed to harmonics, and a large SM capacitance is required to minimize this exposure [86]. Using a DC/DC converter to connect the battery to the SM, the battery is decoupled from the SM capacitor, and this allows for a decrease in SM capacitance. In addition, using this topology provides better conditions for the battery since it is increasing the battery lifetime.

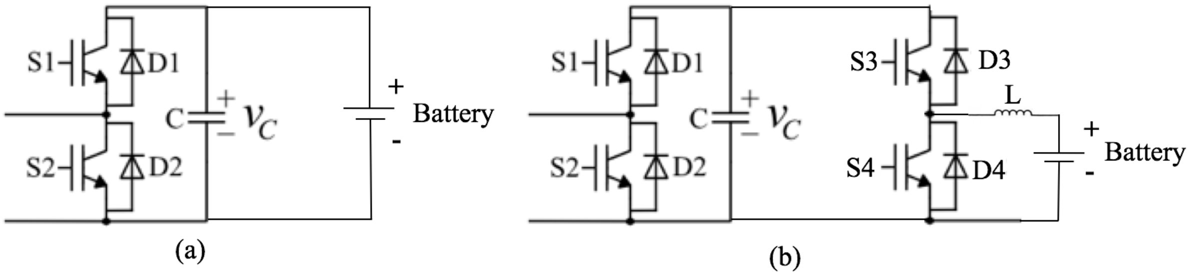

Figure 4.2: (a) MMC half-bridge submodule with battery directly connected across the capacitor (b) MMC half-bridge submodule with battery connected through a DC/DC converter

As described by equations (4.4), (4.5) and (4.8), the arm currents in the MMC consist of half the output AC phase current and a circulating current which consist of one third of the DC-link current of the MMC. The MMC with distributed batteries operates differently than a regular MMC [86] and since each SM includes battery modules, the power transfer between the legs does not need to be delivered through the DC-link via the circulating current. Therefore, in case of an MMC with distributed batteries, the arm current of the MMC only consist of half the output AC phase current. This reduces the conducting losses of this topology.

For the design and simulations parts of this thesis, centralized batteries will be used since it was concluded in chapter 2 that the DC/DC converter for this project is designed to have a 2L-VSC at the battery-side of the DC/DC conerter.

4.3 MMC topology

The three-phase MMC consists of three legs and six arms (two per leg), which each consist of a number of SMs, as shown in figure 4.3. The SMs consist of converters of different structures as shown in figure 4.4, and each of the SMs operates as a controllable voltage source [64]. In each arm, the SMs are controlled to generate the phase voltage [8]. The MMC generates staircase voltage waveforms, where the size of the voltage steps depend on the number of SMs used in the configuration. The more SMs that are used, the more sinusoidal the shape of the output waveform will be. In figure 4.3 the three phases are denoted by the superscripts a,b and c, and the upper and lower arms of each phase leg are denoted by the subscripts u and l, respectively.

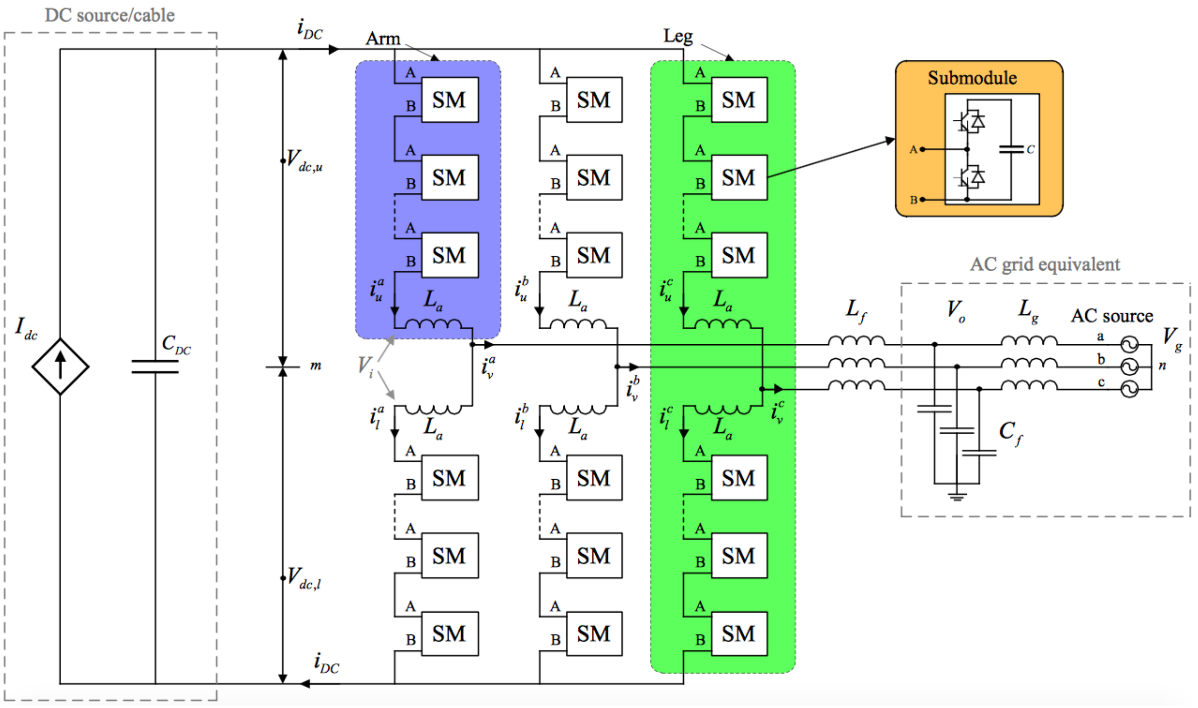

Figure 4.3: Structure of modular multilevel converter [13]

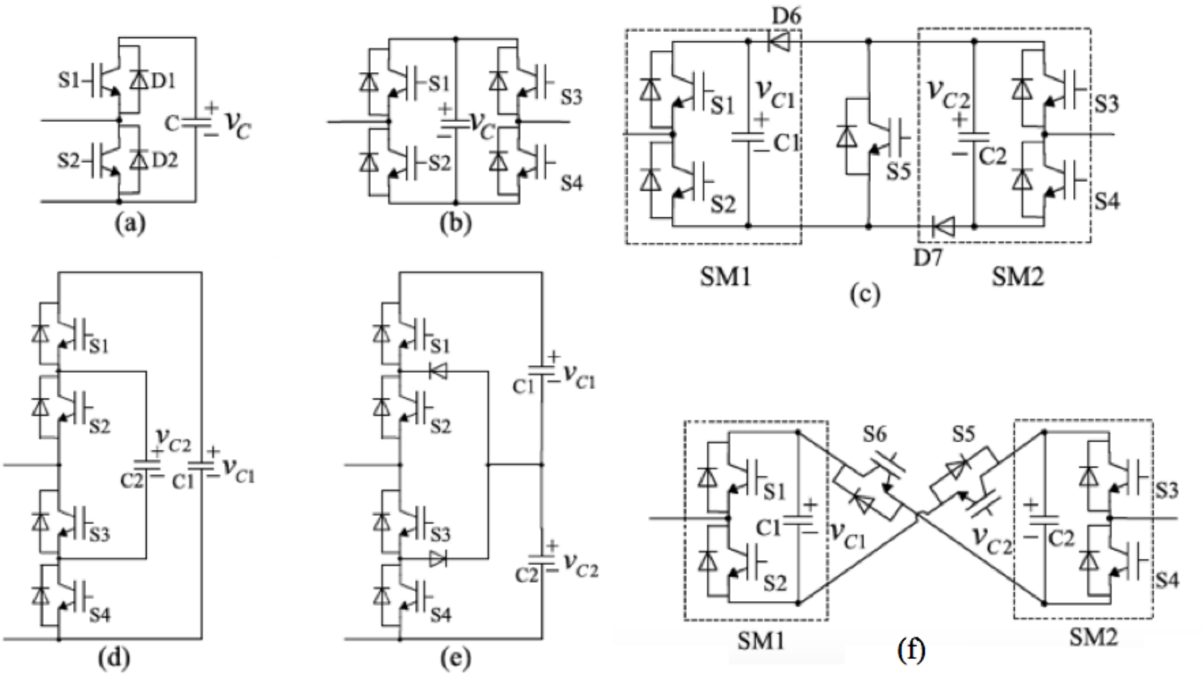

Figure 4.4: Submodule topologies for MMCs [8]

There are no common DC-link capacitors in the MMC since each SM has its own capacitor (D_{DC} shown in the figure is the capacitance of the DC cable). The arm inductances (L_a in the figure) are included to reduce the current ripple in the output.

The different SMs shown in figure 4.4 are the half-bridge (a), the full-bridge (b), the clamp-double (c), the 3L-FLC (d), the 3L-NPC (e), and the five-level (5L) cross-connected (f). Characteristics of the mentioned types of SMs are provided in table 4.1. The most common SMs are the half-bridge and the full-bridge. An advantage of the full-bridge SM is that it can reverse the cell capacitor voltage in order to block the switch, and in that way it can handle DC faults by forcing the fault current to be zero [87]. However, the half-bridge SM is the most popular SM for the MMC configuration due to the fact that it consists of only two switches which result in a less complex MMC topology in terms of number of components, and it also provides higher efficiency and lower switching losses than the other SM topologies [8]. Therefore, the half-bridge SM will be used in this project, and when describing submodule operation in the next subchapter, the half-bridge SM is considered.

Table 4.1: Characteristics of different submodules [8]

Submodule	**Number of valves**	**Voltage levels**	**Losses**	**DC fault handling**
Half bridge (a)	2	0, v_c	Low	No
Full bridge (b)	4	0, $+v_c$	High	Yes
Clamp-double (c)	5	0, v_{c1}, v_{c2}, (v_{c1}+v_{c2})	Moderate	Yes
3L FLC (d)	4	0, v_{c1}, v_{c2}, (v_{c1}-v_{c2})	Low	No
3L NPC (e)	4	0,v_{c2}, (v_{c1}+v_{c2})	Moderate	No
5L cross-connected (f)	6	0, v_{c1}, v_{c2}, +(v_{c1}+v_{c2})	Moderate	Yes

4.4 Submodule operation

Figure 4.5 shows the current direction and SM voltage, v_{SM}, for the different operating states of the half-bridge SM and table 4.2 summarizes the characteristics of the different operating states. Here, the SM current, i_{SM}, entering the SM from left to right, is defined as the positive current direction. For the valves in the table, 1 means that the valve is on/active, meaning that either the switch in that valve is on or that the diode in that valve is conducting. Similarly, 0 means that the valve is off/bypassed, meaning that either the switch is off or the diode is blocking the current. If both valves are on/active at the same time, the capacitor will be shortened. If both valves are off/bypassed at the same time, the result is a blocked state where current an be conducted in the freewheeling diodes, dependent on the voltage across and current through the diodes. If the current is positive in the blocked state, the diode in the upper valve conducts and the SM is inserted. If the current is negative (so that the lower diode D2 conducts), the SM is bypassed, and otherwise the reversed biased diodes will chop the current.

The SM voltage of the i^{th} SM is defined by equation (4.1) [14]:

$$v_{SM,i} = n_i \cdot v_{C,i} \tag{4.1}$$

where

$$n_i = \begin{cases} 1 & \text{, when the upper valve is ON and the lower valve is OFF} \\ 0 & \text{, when the upper valve is OFF and the lower valve is ON} \end{cases}$$

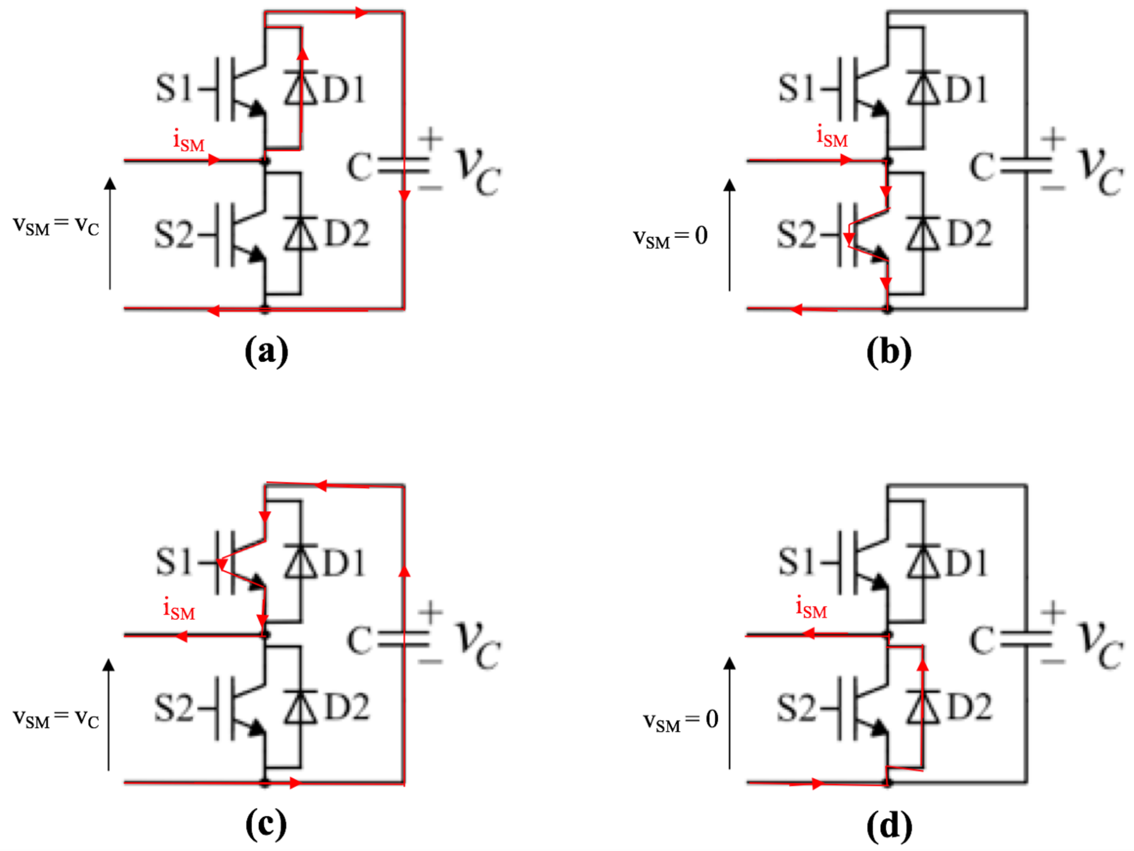

Figure 4.5: Operating states of the half-bridge submodule.
(a): Active state with positive current (b): Bypassed state with positive current (c): Active state with negative current (d): Bypassed state with negative current

Table 4.2: Operating states of the half-bridge submodule

Operating state	**Upper valve**	**Lower valve**	v_{SM}	**Current direction**	**Capacitor status**
Active	1	0	v_C	+	Charging
Active	1	0	v_C	-	Discharging
Bypassed	0	1	0	+	Bypassed
Bypassed	0	1	0	-	Bypassed

4.5 Mathematical model

Each phase $k \in a, b, c$ of the three-phase MMC can be described by the equations given in this subchapter. Figure 4.6 shows phase k of an MMC, and it will be used to derive the mathematical model of a phase of the MMC.

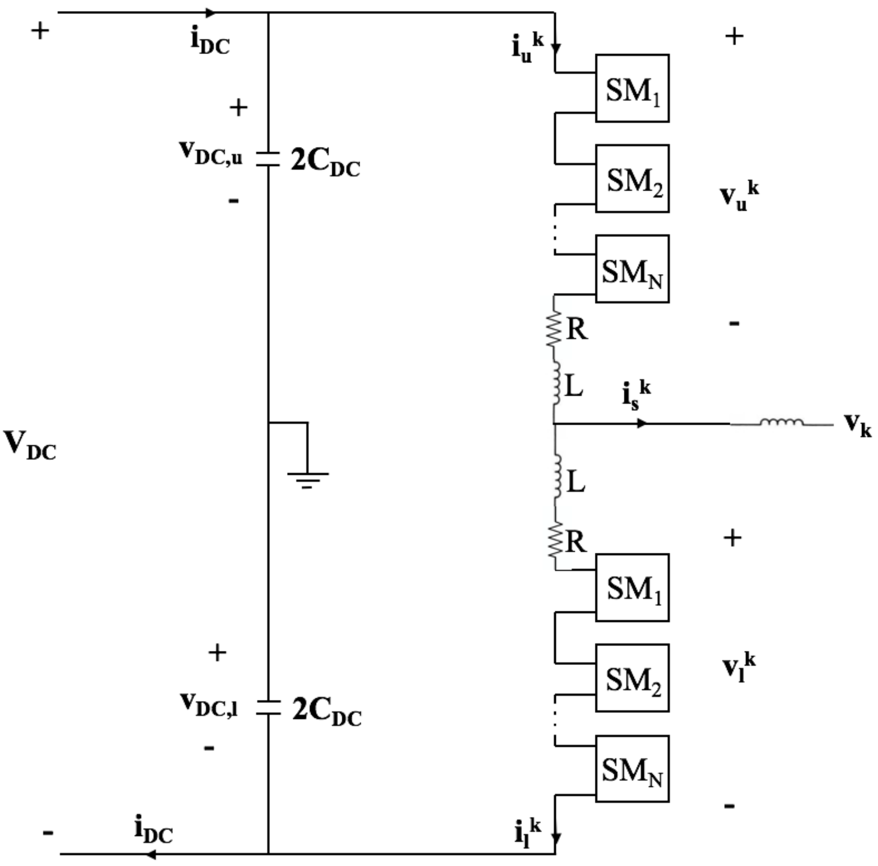

Figure 4.6: One phase of the MMC

Currents

Using KCL, the AC-side output current can be defined as [13]:

$$i_s^k = i_u^k - i_l^k \tag{4.3}$$

Where the subscripts u and l denote upper and lower arm, respectively.
The currents in the upper and lower arms are defined as [41]:

$$i_u^k = \frac{i_s^k}{2} + i_c^k \tag{4.4}$$

$$i_l^k = -\frac{i_s^k}{2} + i_c^k \tag{4.5}$$

Where i_c^k is the circulating current, defined as [13, 41]:

$$i_c^k = \frac{i_u^k + i_l^k}{2} \tag{4.6}$$

There are 3 upper arms and 3 lower arms. In order for the DC-bus current, V_{DC} to remain constant, the mean value of the arm currents must add up to i_{DC} [41]:

$$\sum_{i=1}^{3} \overline{i_{u,l}^{k}} = i_{DC} \tag{4.7}$$

Under balanced AC-side conditions the DC component in the arm currents are given by [41]:

$$\overline{i_u^k} = \overline{i_l^k} = \overline{i_c^k} = \frac{i_{DC}}{3} \tag{4.8}$$

Voltages

Looking at figure 4.6 and using KVL on the upper and lower arms give:

$$\frac{V_{DC}}{2} - v_u^k - Ri_u^k - L\frac{di_u^k}{dt} = v_k \tag{4.9}$$

$$-\frac{V_{DC}}{2} + v_l^k + Ri_l^k + L\frac{di_l^k}{dt} = v_k \tag{4.10}$$

Here it is assumed that the DC bus is balanced, i.e:

$$v_{DC,u} = v_{DC,l} = \frac{V_{DC}}{2} \tag{4.11}$$

The voltages driving the currents i_s and i_c are defined by equations (4.12) and (4.13) [13].

$$v_s^k = \frac{v_l^k - v_u^k}{2} \tag{4.12}$$

$$v_c^k = \frac{v_l^k + v_u^k}{2} \tag{4.13}$$

Using equations (4.3), (4.6), (4.12) and (4.13), adding equations (4.9) and (4.10) results in [41]

$$\frac{L}{2}\frac{di_s^k}{dt} = v_s^k - v_k - \frac{R}{2}i_s^k \tag{4.14}$$

and subtracting equations (4.9) from (4.10) results in [41]

$$L\frac{di_c^k}{dt} = \frac{V_{DC}}{2} - v_c^k - Ri_c^k \tag{4.15}$$

It is desirable that the circulating current is pure DC to keep the RMS arm currents and the converter losses at a minimum [41]. That implies having $\frac{di_c^k}{dt} = 0$, meaning that the right-hand side of equation (4.15) must be zero. That implies that the voltage driving the circulating current is

$$v_c^k = \frac{V_{DC}}{2} - Ri_c^k \approx \frac{V_{DC}}{2} \tag{4.16}$$

Averaged dynamic model

As seen in subchapter 4.4, the SM voltage is equal to the capacitor voltage of the SMs if the SM is in the active operating state. The sum capacitor voltages are defined by [13]:

$$v_{C,u,l}^{k,\Sigma} = \sum_{i=1}^{N} v_{C,u,l}^{k,SM_i} \tag{4.17}$$

Where $v_{u,l}^{k,SM_i}$ is the voltage of SM i in the upper u or lower l arm of phase k. The sum capacitor voltage is the sum of all N such voltages in the upper u or lower l arm of phase k. If the MMC includes a control algorithm that ensures that the voltages on the individual SM capacitors of an arm are equal, the arm voltage of phase k is defined by equation (4.18) [13] where $n_{u,l}$ is the insertion index. Such a balancing algorithm is described in figure 4.7. The insertion index has a value between 0 and 1; if it is 0 it means that all SMs in the arm are bypassed and if it is 1 it means that all SMs are inserted. The sum of insertion indexes of the upper and lower valve should equal 1 [88].

$$v_{u,l}^{k} \approx n_{u,l}^{k} \cdot v_{C,u,l}^{k,\Sigma} \tag{4.18}$$

where

$$n_{u,l}^{k} = \frac{1}{N} \sum_{i=1}^{N} n_{u,l,i}^{k} \tag{4.19}$$

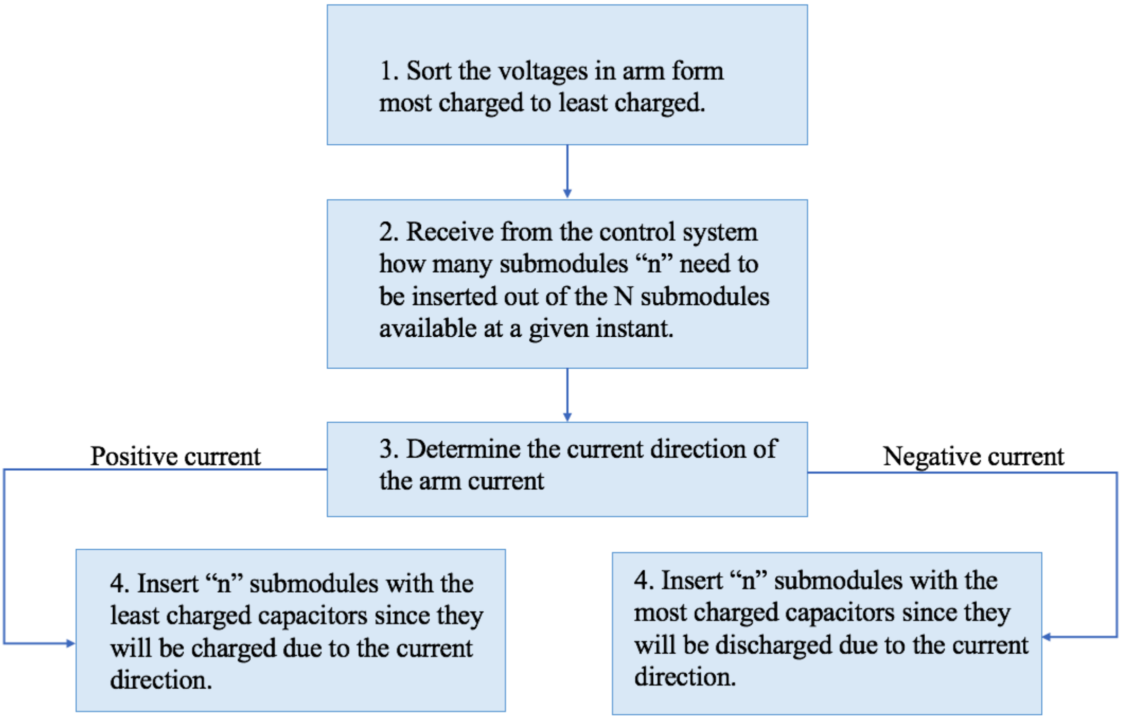

Figure 4.7: MMC balancing algorithm [14]

Equations (4.12) and (4.13) now become [13]:

$$v_s^k = \frac{v_l^k - v_u^k}{2} \approx \frac{n_l^k \cdot v_{C,l}^{k,\Sigma} - n_u^k \cdot v_{C,u}^{k,\Sigma}}{2} \tag{4.20}$$

$$v_c^k = \frac{v_l^k + v_u^k}{2} \approx \frac{n_l^k \cdot v_{C,l}^{k,\Sigma} + n_u^k \cdot v_{C,u}^{k,\Sigma}}{2} \tag{4.21}$$

And equations (4.14) and (4.15) can now be written as

$$\frac{L}{2}\frac{di_s^k}{dt} = \frac{n_l^k \cdot v_{C,l}^{k,\Sigma} - n_u^k \cdot v_{C,u}^{k,\Sigma}}{2} - v_k - \frac{R}{2} i_s^k \tag{4.22}$$

$$L\frac{di_c^k}{dt} = \frac{V_{DC}}{2} - \frac{n_l^k \cdot v_{C,l}^{k,\Sigma} + n_u^k \cdot v_{C,u}^{k,\Sigma}}{2} - Ri_c^k \tag{4.23}$$

From equations (4.22) and (4.23) it can be seen that the maximum output voltage can be obtained when all SMs in the lower arm are inserted and all SMs in the upper arm are bypassed. Using equations (4.12) and (4.17), that gives [41]

$$v_s^{k,max} = \frac{v_{C,l}^{k,\Sigma}}{2} \tag{4.24}$$

It can also be seen that the minimum output voltage can be obtained when all SMs in the upper arm are inserted and all SMs in the lower arm are bypassed:

$$v_s^{k,min} = -\frac{v_{C,u}^{k,\Sigma}}{2} \tag{4.25}$$

To get $v_s^{k,min} = -v_s^{k,max}$, there should be a charge balance between the upper and lower arms [41]. In order to at the same time maintain having a circulating current that is pure DC (equation (4.16)), the mean value of the sum capacitor voltages should equal the DC bus voltage:

$$\overline{v_{C,u,l}^{k,\Sigma}} = V_{DC} \tag{4.26}$$

If the distribution of the sum capacitor voltages is balanced over the N SMs per arm, the mean value of each SM capacitor voltage is given by [41]

$$\overline{v_{C,u,l}^{k,SM_i}} = \frac{\overline{v_{C,u,l}^{k,\Sigma}}}{N} = \frac{V_{DC}}{N} \tag{4.27}$$

Figure 4.5 shows the operation of the half-bridge SM and equation (4.1) defines the SM voltage. The capacitor voltage dynamics are given by [14]:

$$C\frac{dv_{C,u,l}^{k,SM_i}}{dt} = n_{u,l}^{k,SM_i} \cdot i_{u,l}^{k,SM_i} \tag{4.28}$$

Where $v_{C,u,l}^{k,SM_i}$ is the capacitor voltage of the capacitor in SM i in the upper u or lower l arm of phase k, $i_{u,l}^{k,SM_i}$ is the current and $n_{u,l}^{k,SM_i}$ is the insertion index in that SM. Taking the sum of all N SMs in an arm and using equations (4.4), (4.5), (4.17) and (4.19), equations (4.29) and (4.30) can be obtained:

$$\frac{C}{N}\frac{dv_{C,u}^{k,\Sigma}}{dt} = n_u^k \cdot (\frac{i_s^k}{2} + i_c^k) \tag{4.29}$$

for the upper arm of phase k, and

$$\frac{C}{N}\frac{dv_{C,l}^{k,\Sigma}}{dt} = n_l^k \cdot (-\frac{i_s^k}{2} + i_c^k) \tag{4.30}$$

for the lower arm of phase k.

Equations (4.22), (4.23), (4.29) and (4.30) comprise the averaged dynamic model of the MMC. Equations (4.22) and (4.23) describe the grid current and circulating current dynamics, while (4.29) and (4.30) describe the upper and lower arm aggregated voltage dynamics.

Energy dynamics

Equations (4.29) and (4.30) can be multiplied by $v_{C,u}^{k,\Sigma}$ and $v_{C,l}^{k,\Sigma}$, respectively:

$$v_{C,u}^{k,\Sigma} \cdot \frac{C}{N}\frac{dv_{C,u}^{k,\Sigma}}{dt} = v_{C,u}^{k,\Sigma} \cdot n_u^k \cdot (\frac{i_s^k}{2} + i_c^k) = \frac{dw_u^{k,\Sigma}}{dt} \tag{4.31}$$

$$v_{C,l}^{k,\Sigma} \cdot \frac{C}{N}\frac{dv_{C,l}^{k,\Sigma}}{dt} = v_{C,l}^{k,\Sigma} \cdot n_l^k \cdot (-\frac{i_s^k}{2} + i_c^k) = \frac{dw_l^{k,\Sigma}}{dt} \tag{4.32}$$

Where $w_u^{k,\Sigma}$ and $w_l^{k,\Sigma}$ are the energy stored in the capacitors of the upper (u) and lower (l) arm of phase k and are defined by [41]:

$$w_{u,l}^{k,\Sigma} = \frac{C}{2N}(v_{u,l}^{k,\Sigma})^2 \tag{4.33}$$

The sum energy and energy difference are defined by equations (4.34) and (4.35) [13], respectively:

$$w_\Sigma^k = w_u^k + w_l^k \tag{4.34}$$

$$w_\Delta^k = w_u^k - w_l^k \tag{4.35}$$

Power is defined as the derivative of the energy, so by taking the derivative of the sum energy and the energy difference, the power balance equations can be defined [13, 41]:

$$\frac{dw_\Sigma^k}{dt} = 2v_c^k \cdot i_c^k - v_s^k \cdot i_s^k \tag{4.36}$$

$$\frac{dw_\Delta^k}{dt} = v_c^k \cdot i_s^k - 2v_s^k \cdot i_c^k \tag{4.37}$$

From equations (4.22), (4.23), (4.36) and (4.37) it can be seen that the AC-side current i_s^k can be used to control the active and reactive powers (similarly to the 2L-VSC), while the circulating current i_c can be controlled to regulate the energy (sum and difference) and to stabilize the converter [14]. Control of the MMC will be discussed further in the next subchapter.

4.6 Control of the MMC

4.6.1 Output AC-current control

This control is based on equation (4.22). Using Clarke's and Park's transformations (see Appendix B) it can be represented in the dq reference frame as [14]:

$$\frac{L}{2}\frac{di_s^d}{dt} = -\frac{R}{2}i_s^d + v_s^d - v_k^d + \omega\frac{L}{2}i_s^q \tag{4.38}$$

$$\frac{L}{2}\frac{di_s^q}{dt} = -\frac{R}{2}i_s^q + v_s^q - v_k^q - \omega\frac{L}{2}i_s^d \tag{4.39}$$

Where equation (4.38) represents the active current dynamics and equation (4.39) represents the reactive current dynamics. A PI-controller is used for the output AC-current control and it is shown in figure 4.8 for the d-axis and q-axis components.

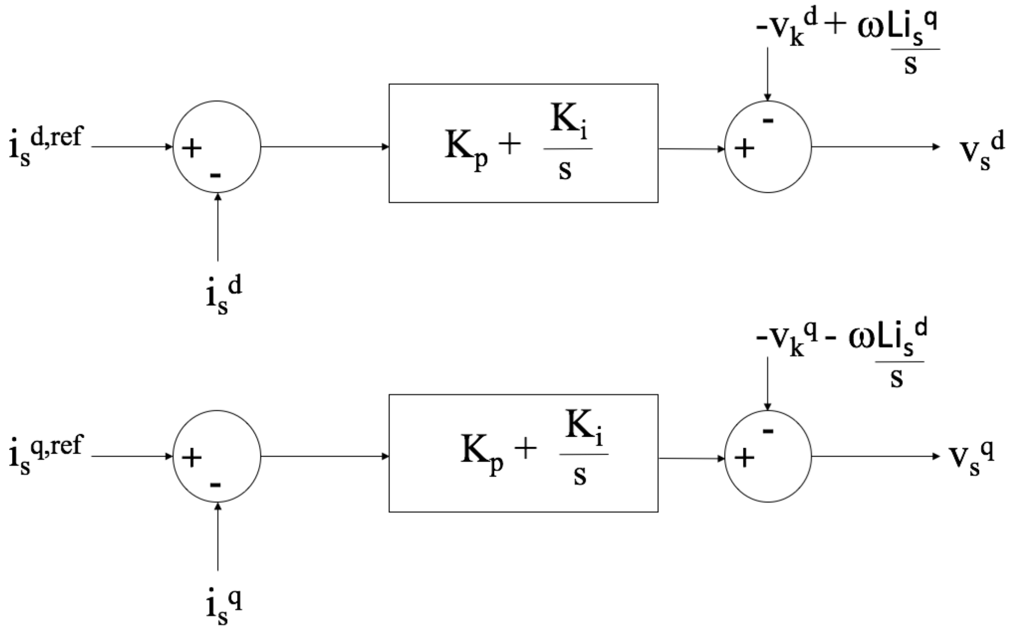

Figure 4.8: Block diagram of the output AC-current control of the MMC

4.6.2 Circulating current control

The circulating current control is based on equation (4.23) and also for this control a PI-controller is used [14] as shown in figure 4.9. The input to the circulating current control is the output of the energy controller, which is described in the next subsection.

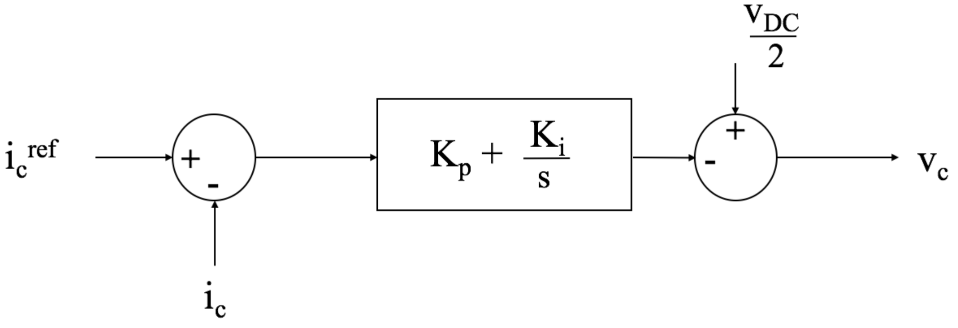

Figure 4.9: Block diagram of the circulating current control of the MMC

4.6.3 Energy sum and energy difference control

The power balance equations (equations (4.36) and (4.37)) have non-linear terms. These equations can be made linear by assuming

$$n_u^k + n_l^k \approx 1 \tag{4.40}$$

and assuming that equation (4.26) is valid. Then (4.21) becomes

$$v_c^k \approx \frac{(n_u^k + n_l^k)}{2} V_{DC} \approx \frac{V_{DC}}{2} \tag{4.41}$$

And hence equations (4.36) and (4.37) can be written as

$$\frac{dw_\Sigma^k}{dt} \approx 2\frac{V_{DC}}{2} \cdot i_c^k - v_s^k \cdot i_s^k \tag{4.42}$$

$$\frac{dw_\Delta^k}{dt} \approx \frac{V_{DC}}{2} \cdot i_s^k - 2v_s^k \cdot i_c^k \tag{4.43}$$

The energy sum control is based on equation (4.42) and the energy difference control is based on equation (4.43). The block diagram of the two controllers and how their output creates the input to the circulating current controller are shown in figure 4.10 [14].

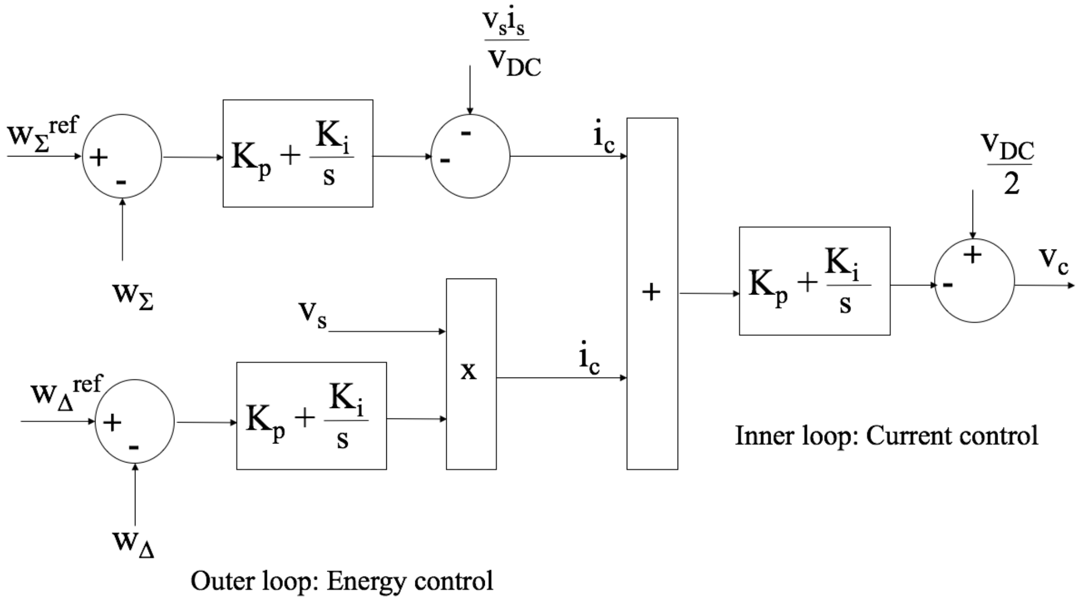

Figure 4.10: Block diagram of the energy sum, energy difference and circulating current controllers of the MMC

4.7 Modulation techniques

This subchapter includes a brief introduction modulation techniques for the MMC. As will be shown later, the MMC used in the simulations in this project is based on a simplified average value model, where the switches are not modeled explicitly, and hence the modulation creating signals to switches is not modeled either. For more information regarding the different modulation techniques, the reader is suggested to read the literature in the references of the different methods mentioned in this subchapter.

The modulation techniques presented in chapter 3.5 for the 2L-VSC can also be applied to MMCs. There are three categories for PWM modulation methods for multilevel converters [15]:

1 **Carrier-based modulation**
This is the same types of modulation as described in chapter 3.5 for the 2L-VSC, but for multilevel converters the multilevel waveform is split in to a number of 2L PWM waveforms, each having its own carrier [41]. All carrier signals are compared to the same reference signal. There are two types of carrier-based modulation:

- Phase-shifted carrier (PSC) modulation:
  The carrier signals in this type of modulation consist of a number 2L PWM waveforms which have the same magnitude and are symmetrically phase shifted [41]. In this type of modulation there are reference signals for the upper and lower arm of each SM.

- Level-shifted carrier modulation:
  In this type of modulation the multilevel the carrier signals have the same magnitude and frequency, but they are stacked on top of each other so that they have different offset values [41]. In this type of modulation there is only one reference waveform

that spans the entire voltage range of all carrier signals.

2. **Space vector modulation (SVM)**
   This technique was described in chapter 3.5 for the 2L-VSC. However, for a multilevel converter the number of switching states will be largely increased, so this type of modulation is more complex for an MMC. A detailed description of SVM of an n-level converter is provided in [15].

3. **Nearest-level modulation**
   The idea of this modulation technique is to sample the reference signal at a high frequency and approximate it with the nearest level available [41]. The sample frequency must be high in order to avoid having steps that exceed one level. Figure 4.11 shows the principle of this technique. For each switching cycle there are two switching states of phase h: K_h and $K_h + 1$ with duty cycles $1 - D_h$ and D_h, respectively. The reference voltage is approximated by the two nearest voltage levels shown i the figure [15]:

$$V_h^* = (1 - D_h) \cdot \frac{K_h V_{dc}}{n-1} + D_h \cdot \frac{(K_h + 1) V_{dc}}{n-1} = \frac{(K_h + D_h) V_{dc}}{n-1} \tag{4.44}$$

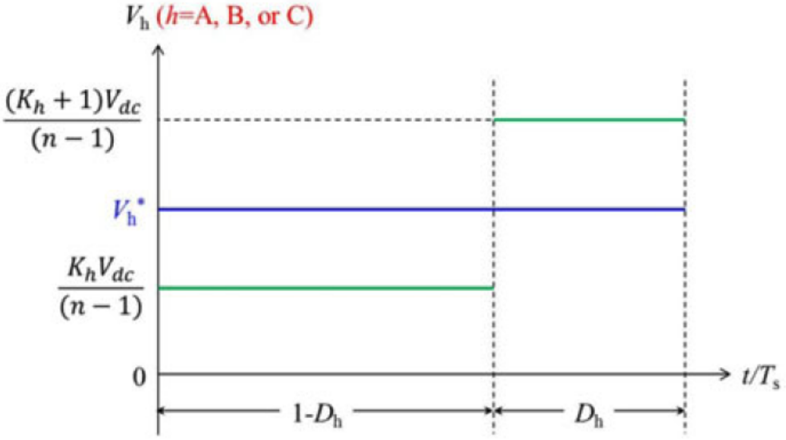

Figure 4.11: Nearest-level modulation method [15]

It as advantageous to use this type of modulation when the number of SMs is high, since the other two modulation methods described above will become more complex when the number of levels of the output increases [15, 89]. This method, on the other hand, does not use carrier signals, so it is simple to implement even when the number of levels of the converter increases to a very high value.

Chapter 5

System design

Figure 5.1 shows a one-line diagram of the system used in this project. This chapter provides a discussion regarding design of the different components in the system. A MATLAB script used to calculate all the parameters of the system based on the equations used to discuss the design of the components in this chapter, is provided in Appendix C.1. The results for the different parts of the system are presented in tables in the end of each subchapter.

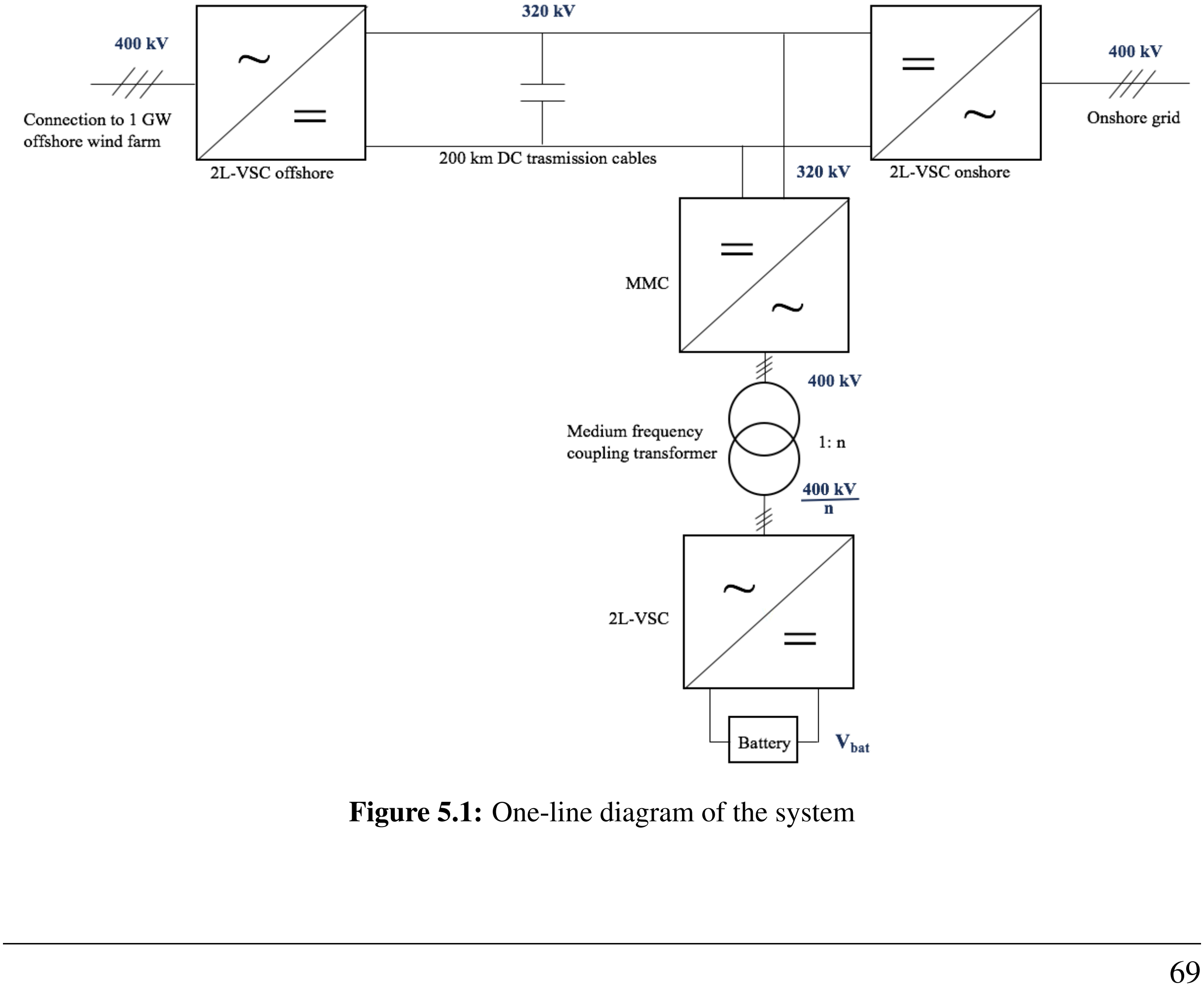

Figure 5.1: One-line diagram of the system

5.1 HVDC transmission system

Figure 5.2 shows the one-line diagram of the HVDC transmission system used in this project. As mentioned in chapter 1, the design of the components of the HVDC transmission system is outside the scope of this thesis. However, since a HVDC transmission system was given[i] for the simulations part of this project, a short description of the system parameters will be discussed in this subchapter and the simulation model and its operation will be explained in chapter 6.1.

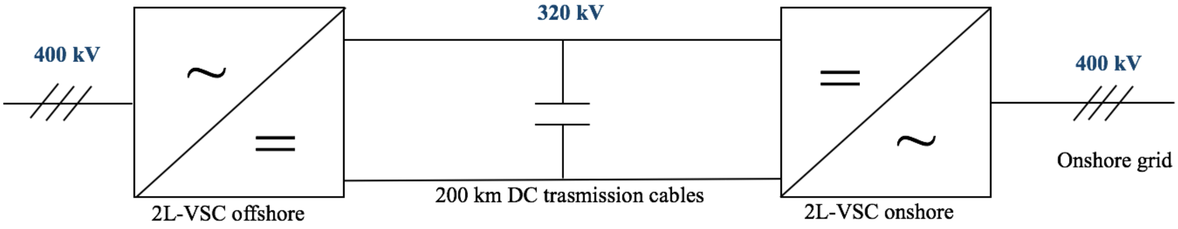

Figure 5.2: One-line diagram of the HVDC transmission system

The HVDC transmission system connects a 1 GW offshore wind farm to the grid onshore. Therefore the power rating is set to 1000 MW. The HVDC system is made in a point-to-point configuration and it consists of two 2L-VSCs and two 200 km DC transmission cables. The DC voltage of the DC-cables are chosen to be 320 kV since this is the highest voltage level available for HVDC transmission cables in use in industry today [41]. The AC-side RMS line voltage is found to be 400 kV using equation (5.1) [56]:

$$V_{AC,line,RMS} = \sqrt{\frac{3}{2}}V_{DC} \tag{5.1}$$

In chapter 2 it was mentioned that the critical distance for subsea transmission cables is at around 100 km, so for transmission distances longer than this, HVAC is no longer an option and HVDC transmission will be used. In this project an offshore wind farm is connected to the grid onshore, so it is clear that subsea cables must be used. In this project it is assumed that HVDC transmission is the only feasible option, and hence the length of the transmission cables must be longer than 100 km.

An argument for choosing HVDC and a long transmission distance is that an offshore wind farm of 1 GW requires a very large footprint and in chapter 2 it was mentioned that the wind conditions are better offshore. So in order to have a wind farm that operates more stable, it is desirable to place it quite far offshore and hence HVDC will be the only feasible solution in terms of losses and cost. For the design and simulations of the HVDC system in this project, HVDC cables with a length of 200 km are used since that was given in the given model of the HVDC system.

---

[i] The model is made in MATLAB and Simulink by Santiago Sanchez Acevedo, Post Doctor at the Department of Electric Power Engineering, NTNU.

Table 5.1 provides the parameters of the HVDC transmission system used in this project.

Table 5.1: Parameters of the HVDC transmission system

Parameter	Value
Power rating	1000 MW
AC voltage	400 kV
DC voltage	320 kV
Length of transmission line	200 km

5.2 DC/DC converter design

The choice of DC/DC converter for this project was discussed in chapter 2, and chapter 3 and 4 describes the 2L-VSC and the MMC topologies, respectively. The next subchapters contain discussions regarding the design of the two converters and the coupling transformer that the DC/DC converter is built up of. A one-line diagram of the DC/DC converter is shown in figure 5.3.

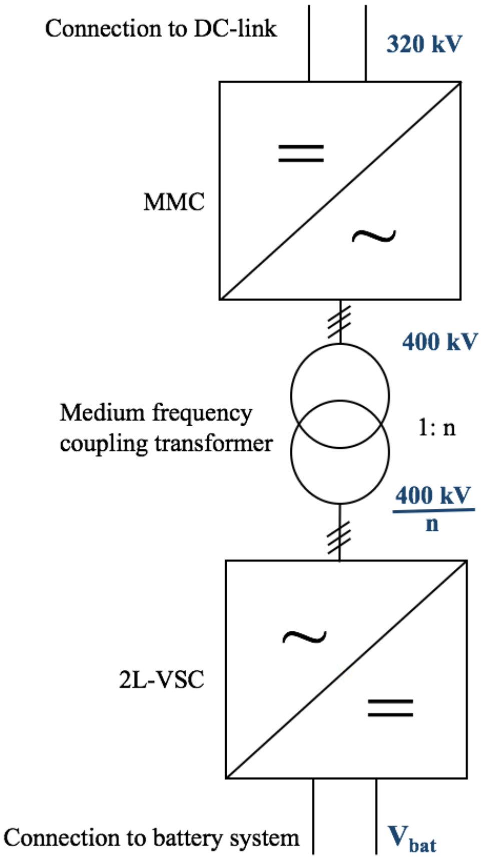

Figure 5.3: One-line diagram of the DC/DC converter

5.3 MMC design

5.3.1 Power rating and voltage levels

Since the MMC is a part of the DC/DC converter and since the DC/DC converter connects the battery to the DC-link of the HVDC transmission system, the power rating of the converters that the DC/DC converter is made up of, is decided by the power rating of the battery. This is set to be 180 MW, and will be described further in subsection 5.6.4. Hence, the power rating of the MMC is also 180 MW.

When it comes to voltage levels, the MMC is connected to the DC-link. Therefore, the DC-side of the MMC has the same DC voltage as the DC-link, namely 320 kV. The voltage on the AC-side of the MMC can be calculated using equation (5.1), and it is found to be 400 kV.

5.3.2 Arm current

The arm current of an MMC can be calculated using equation (5.2).

$$I_{arm} = \frac{I_{DC}}{3} + \frac{i_a}{2} + 0.15 \cdot i_a \tag{5.2}$$

Where 0.15 accounts for the circulating current and is a margin that is included to ensure safe operation. The DC-side current, I_{DC}, is calculated using equation (5.3):

$$I_{DC} = \frac{P}{V_{DC}} \tag{5.3}$$

The AC phase-current i_a is defined as[90]:

$$i_a = \frac{S}{3 \cdot v_a} \tag{5.4}$$

where i_a is the RMS AC-side phase current, S is the apparent power and v_a is the RMS AC-side phase voltage:

$$v_a = \frac{V_{AC,line,RMS}}{\sqrt{3}} = V_{AC,phase,RMS} \tag{5.5}$$

The apparent power can be calculated using equation (5.6)

$$S = \frac{P}{pf} \tag{5.6}$$

Where pf is the power factor, and for this project it is given to be pf = 0.95. Using the power and AC and DC voltages found in the subsection above, it can be found that i_a = 273.48 A and that I_{DC} = 562.5 A. Therefore, using equation (5.2) it is found that the arm current that the semiconductors of the SMs must be able to withstand is $I_{arm} \approx$ 365.26 A.

5.3.3 Semiconductors

The semiconductor devices used in the converters affect the total losses in the system, and in addition to SM capacitors, the semiconductors in the SMs affect a large part of the total cost of the MMC due to the large number of required SMs in the converter [41]. Therefore the choice of semiconductors for the converters is a critical part of the design of the MMC.

Power semiconductor devices consist of a variety of transistors, thyristors and diodes [16]. The three symbols used for these three types of semiconductor devices are shown in figure 5.4. The diode conducts in the forward direction and blocks in the reverse direction, and it does not have a gate to control the conduction. This device is often added to power devices that are designed without the capability to block current in the reverse direction. The transistor conducts in the forward direction when the collector is positive with respect to the emitter and when a turn-on signal is applied to the base electrode. The thyristors also have a gate to control the turn-on and they can be designed to also control the turn-off. Thyristors can be designed to block in both the forward and reverse direction (symmetrical device) or to block only in the forward direction (asymmetrical device).

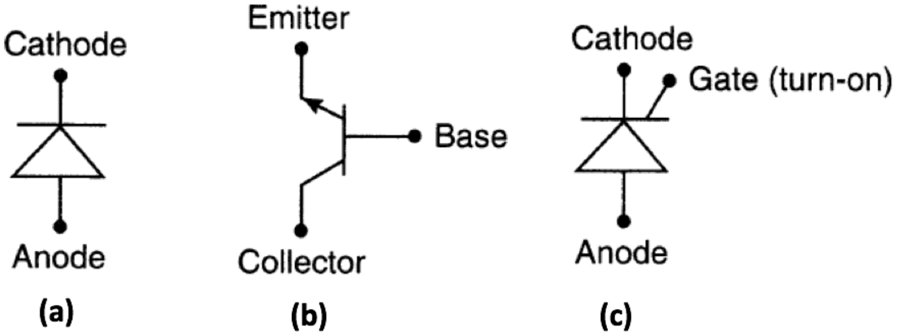

Figure 5.4: (a) Diode (b) Transistor (c) Thyristor [16]

The choice of semiconductors is dependent on the arm current of the MMC. The semiconductors used in the SMs of the MMC must be able to withstand the arm current discussed in subsection 5.3.2. When deciding upon a semiconductor device to use in the MMC in this project, the insulated-gate bipolar transistor (IGBT) and the integrated gate-commutated thyristor (IGCT) will be compared since these devices are discussed in literature as most suitable for MMCs [41, 91]. Asymmetrical IGBTs and IGCTs can be used in VSCs together with an anti-parallel diode [92], so from now on only asymmetrical devices will be treated.

IGBTs

The IGBT is a type of transistor semiconductor device. It was developed as attempts to combine the best qualities of the bipolar junction transistor (BJT) and the metal-oxide-semiconductor field-effect transistor (MOSFET) [70]. The MOSTFET has advantages of fast switching speed, but it is not suitable for high power applications, as it can only be used for kilowatt power applications [16]. Another disadvantage is that the on-state conduction losses are higher in devices rated for higher blocking voltages [70]. BJTs have lower on-state conduction losses, but suffers from lower switching speed. Combining these two devices to create the IGBT would therefore lead to a device with advantages of both high switching speed and low switching losses.

IGCTs

The IGCT is a type of thyristor semiconductor device with both turn-on and turn-off capability [16] and it is a further development and improvement of the gate turn-off (GTO) thyristor [41]. Disadvantages of the GTO include slow turn off-times, bulky gate drivers, high power required to control the GTO and costly snubber circuits, which are required due to an in-homogeneous turn-off transient [16, 93]. Compared to the IGBT, the IGCT has advantages of lower on-state losses (i.e. conduction losses) and it can be used for applications where higher blocking voltages and currents are required [91].

According to K. Sharifabadi et. al [41] the IGBT has been the dominating semiconductor device for MMCs. However, it has been questioned whether it could be replaced by the IGCT. That is because besides the semiconductor structure and operation, the main difference between the IGBT and IGCT is in terms of losses. As mentioned above, the IGBT has lower switching losses than the IGCT, but the IGCT has lower conduction losses than the IGBT. As described i chapter 2, the MMC can be operated at lower switching frequencies and therefore the main contribution to the power losses in an MMC is the conduction losses and not the switching losses. Therefore IGCTs can be preferred over IGBTs in MMCs.

In order to choose the type of semiconductors to be used as the semiconductor valves of the SMs in the MMC, characteristics of different semiconductor devices from different manufacturers have been compared. The types of semiconductors that have been compared are the IGCT and IGBT press-pack devices since the press-pack type of packaging provides safe operation for high power and high voltage applications [92], which is the application of the semiconductor devices used in the DC/DC converter in this project. From Toshiba, the injection-enhanced gate transistor (IEGT) is used for the comparisons, which is their type of IGBT. The comparisons of semiconductor devices in this subchapter will be used to decide the type of semiconductor device for the MMC in this subsection and for the 2L-VSC in subsection 5.5.3. However, for the 2L-VSC, the choice will be made among the IGBTs since this converter operates at higher switching frequencies than the MMC, and hence switching losses account for a large part of the total losses and therefore the IGBT will be the best choice of semiconductor device. The results are presented in table 5.2 and figure 5.5. The characteristics are found in data sheets from the different manufacturers, and they are provided references in the ”Manufacturers” column of the table. The voltage is the blocking voltage of the semiconductor devices which is found as the collector emitter voltage V_{CE} for the IGBTs and as the maximum repetitive voltage in the forward direction V_{DRM} for the IGCTs. The current is given as the DC collector current I_C for the IGBTs and as the maximum controllable turn-off current I_{TGQM} for the IGCTs.

Table 5.2: Characteristics of different semiconductor devices

Semiconductor	Voltage [V]	Current [A]	Manufacturers
IGBT	2500	360	Westcode [94]
IGBT	2500	750	Westcode [94]
IGBT	2500	1000	ABB [95]
IGBT	2500	1200	Westcode [94]
IGBT	2500	1300	ABB [95]
IGBT	2500	2000	ABB [95]
IGBT	3300	1200	Toshiba [96]
IGBT	4500	160	Westcode [94]
IGBT	4500	340	Westcode [94]
IGBT	4500	600	Westcode [94]
IGBT	4500	750	Toshiba [96]
IGBT	4500	800	Westcode [94]
IGBT	4500	900	Westcode [94]
IGBT	4500	1200	Toshiba [96]
IGBT	4500	1300	ABB [95]
IGBT	4500	1500	Toshiba [96]
IGBT	4500	1600	Westcode [94]
IGBT	4500	1800	Westcode [94]
IGBT	4500	2000	ABB [95]
IGBT	4500	2100	Toshiba [96]
IGBT	4500	3000	ABB [95]
IGBT	6500	258	Westcode [94]
IGBT	6500	600	Westcode [94]
IGBT	6500	900	Westcode [94]
IGBT	6500	1290	Westcode [94]
IGCT	4500	3600	ABB [97]
IGCT	4500	4000	ABB [97]
IGCT	4500	5000	ABB [97]
IGCT	6500	400	Mitsubishi Electric [98]
IGCT	6500	800	Mitsubishi Electric [98]
IGCT	6500	1500	Mitsubishi Electric [98]
IGCT	6500	3800	ABB [97]

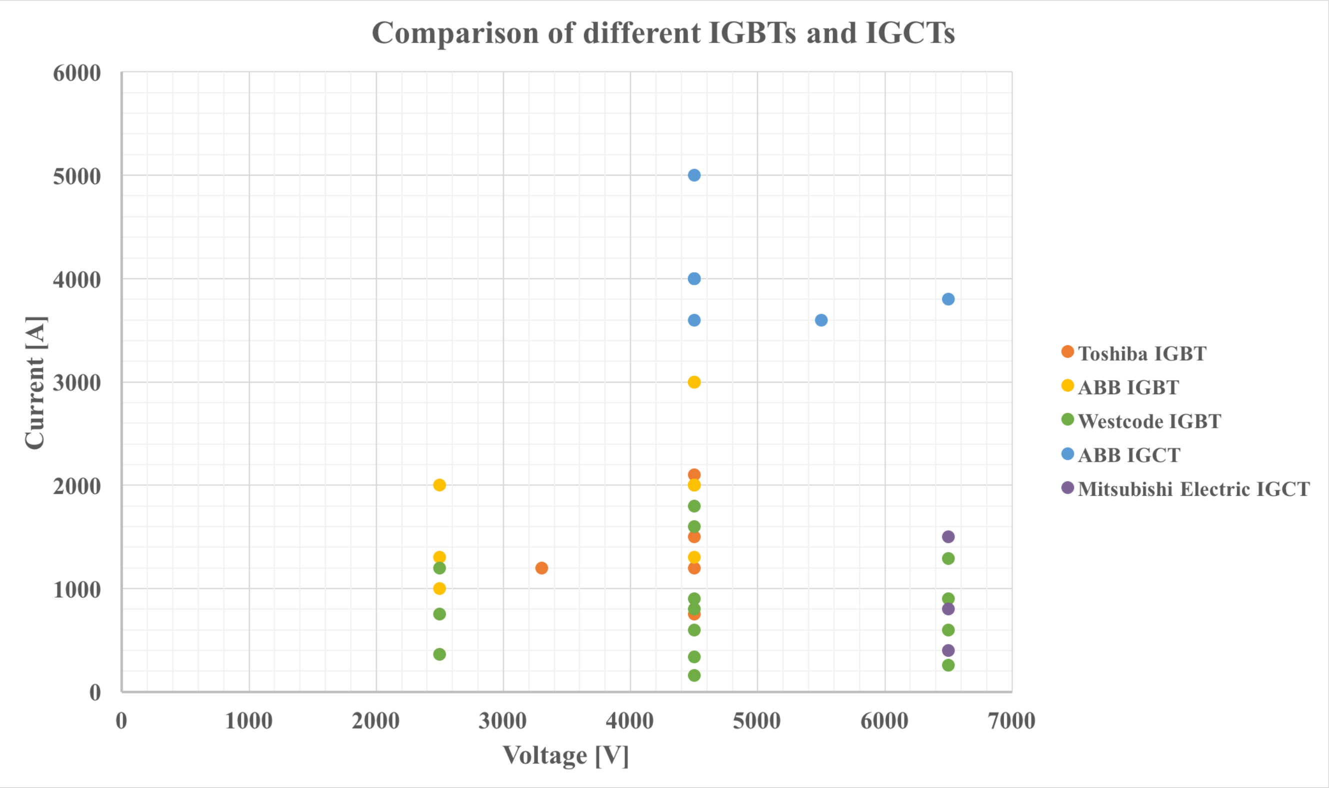

Figure 5.5: Comparison of different types of press-pack IGBTs and IGCTs

The criteria for the choice of type of semiconductor device to use in the converter is that the rated current of the device must be higher than the arm current of the MMC for the choice of semiconductor device for the MMC, and higher than the phase current for half a period for the choice of semiconductor for the 2L-VSC. A higher current capability of the semiconductor device implies a larger diameter of the device [16]. Cost is also related to the current capability and a semiconductor device with higher current capability will require a larger chip area and it will be more costly. Therefore the choice of semiconductor device in terms of current capability should be chosen as close to the arm current for the MMC, and phase current for the 2L-VSC, as possible.

The number of SMs in each arm of the MMC are decided by the chosen blocking voltage of the semiconductor switch used in the SMs, as shown by equation (5.7). More SMs are required to be series connected in the MMC in order to achieve the desired voltage level of the converter if semiconductors with lower blocking voltages are used in the design. This implies increased cost of the converter. On the other hand, if semiconductors with a higher blocking voltage are used, fewer SMs are required per arm of the MMC. But in this case the voltage steps of the AC-output of the converter will be larger since the higher number of SMs used, the more close to a perfect sinusoidal wave the AC-output will be. Therefore the choice of semiconductor device in terms of blocking voltage must be a trade-off between cost and performance of the converter.

The results in table 5.2 and figure 5.5 show that most of the available IGCTs are rated for high voltages and high currents. In subsection 5.3.2 the arm current of the MMC used in the DC/DC converter in this project was calculated to be $I_{arm} \approx 365A$. Hence, as seen from the table, an option if an IGCT is going to be chosen is to use Mitsubishi Electric's IGCT with

$V_{DRM} = 6500$ and $I_{TGQM} = 400A$ in order to minimize over-dimensioning of the current capability and keeping it as close to the arm current as possible. On the other hand, an option if an IGBT is going to be chosen is to use Westcode's press-pack IGBT with $V_{CE} = 4500V$ and $I_C = 600A$.

When it comes to rated current of the chosen semiconductor, it is obvious that the IGCT should be chosen. However, the rated voltage should also be considered, and if an IGCT is to be chosen, as seen from table 5.2 and figure 5.5, an IGCT with rated voltage of 6.6 kV is the only option unless it is desired to increase the rated current to 3.6 - 5.0 kA. According to F. Filsecker [92], IGBTs are preferred over IGCTs in very high voltage applications because they have lower gate driving power requirements and for high voltage applications many devices need to be connected in series in order to achieve the desired voltage of the converter. In addition, the press-pack IGBT offers advantages like simple series and parallel connection, short circuit current limitation and short-circuit turn-off capability.

The IGBT is more used in industry and it is more mature than the IGCT technology. A number of manufacturers offer IGBTs at different rated voltages and currents, while the variety of IGCTs commercially available is smaller and this technology is offered by fewer manufacturers. This is another motivation for choosing the IGBT instead of the IGCT for this project.

Another motivation for choosing the press-pack IGBT instead of the IGCT when it comes to voltage is that, as seen from table 5.2 and figure 5.5, lower rated voltages with lower rated currents is possible if this type of semiconductor is chosen. As seen from the figure, semiconductors of mainly three blocking voltage levels are produced in industry; 2.5 kV, 4.5 kV and 6.5 kV. As discussed earlier, in terms of achieving a more perfect sinusoidal output waveform, connecting a high number of SMs consisting of semiconductors of lower rated voltage is preferred. On the other hand, this would increase the total converter cost since more semiconductor devices are required. Having fewer SMs connected, but with semiconductor devices at higher rated voltages, would decrease the cost, but also decrease the output waveform quality. The type of semiconductor in terms of voltage rating is therefore chosen as a trade-off between performances and cost of the converter. The choice of semiconductor used for the MMC in this project is therefore the IGBT from Westcode with $V_{CE} = 4500V$ and $I_C = 600A$ in order to chose a rated voltage that could be a trade-off between performance and cost of the converter considering the three voltage levels discussed above. Based on this choice of rated voltage, the IGBT is the only option. In addition, the IGBT is chosen due to its advantages mentioned above.

5.3.4 Number of submodules

As found in chapter 4, the optimal choice of type of SMs for the MMC was the half-bridge type. Therefore this type will be chosen for this project, and the other types will not be investigated further in this project.

The number of SMs per arm of the MMC can be decided by equation (5.7):

$$N_{SM,arm} = \frac{V_{DC}}{f_{safetymargin} \cdot V_{blocking}} \tag{5.7}$$

Based on the choice of modulation technique for operation of the MMC, some over-voltages are expected to occur and therefore a safety margin is included to make sure that the MMC has enough SMs to ensure safe operation. In case of hard-switched PWM the MMC is normally designed with a safety margin of $\frac{1}{3} = 33\%$ in industry, while the margin can be smaller for modulation methods where less over-voltages can be assumed, i.e using soft-switched modulation schemes. Since hard-switched PWM is used for this project, $f_{safetymargin} = 0.67$ is assumed so that the safety margin is 33%. $V_{blocking}$ is the blocking voltage of the switches in the semiconductor valves and this can be found in data sheets from the manufacturer providing the semiconductors used in the converter. V_{DC} is the DC-side voltage of the MMC.

In the previous subsection the press-pack IGBT from Westcode with V_{CE} = 4500 V and I_C = 600 A [94] was chosen as the semiconductor device to be used for the MMC in this project. It consists of one IGBT and one diode in anti-parallel, so for each half-bridge SM, two such semiconductor valves are required. However, since the semiconductor valves of the SM operate in a complimentary manner and only one of them are ON at a time, one semiconductor valve must be able to handle the full current through it and voltage across it. The current it must handle is the arm current found in subsection 5.3.2 to be I_{arm} = 365.26 A. The number of SMs connected in series per arm of the MMC can be found to be $N \approx 107$ using equation (6.14) with $V_{bloking}$ = 4500 V and V_{DC} = 320 kV. The total number of SMs in the MMC can be calculated using equation (5.8)

$$N_{SM,tot} = N_{arm} \cdot N_{SM,arm} \tag{5.8}$$

where N_{arm} is the number arms in the MMC, which is 6 for the three-phase MMC used in this project. This gives a total of $N_{SM,tot} = 642$ SMs in the MMC used in this project when it is designed for the voltage level and power rating provided in table 5.3, and when the specific type of semiconductor device also provided in this table, is used.

5.3.5 Submodule capacitance

The SM capacitors are one of the most important components of the MMC since it is the voltage across these capacitors that is inserted or bypassed in the operation of the MMC, and each time a SM is inserted, it is these capacitors that absorb the charge pulses generated by the arm current [41]. Therefore it is important that they are reliable and that a suited capacitance is chosen. A too high capacitance increases the cost of the MMC since the SM cost is a large part of the total cost of the MMC due to the high number of SMs in the converter. A too low SM capacitance will cause a high voltage ripple. According to K. Sharifabadi et. al [41] there are two steps of choosing the SM capacitance:

1. An initial value of the SM capacitance is chosen within an interval where the total stored energy in all SM capacitors of the converter is 30 - 40 kJ/MVA.
2. The cost of the SM capacitors is optimized against the cost of power semiconductor devices (which also contributes to a large part of the total MMC cost) and it is compared to capacitor voltage ripples for different capacitances. The capacitance is decided as a trade-off between acceptable voltage ripple and total MMC cost.

The topic of SM capacitance will not be treated further in this chapter. In chapter 6 the simulation model of the MMC used for the simulations in this project is discussed. The capacitance used in that model is based on a CIGRE test grid [99], which will be discussed in chapter 6.2.

5.3.6 Arm inductance

According to K. Sharifabadi et. al [41] the arm inductance of the MMC can be dimensioned in three different ways, depending on how the converter is designed and how DC-side short-circuits are handled.

1. If the SMs are equipped with separate power modules with diodes or if it is equipped with bypass thyristors, the current coming from the AC-side which is fed into the fault on the DC-side does not need to be limited in order to protect the anti-parallel diodes of the SMs. In this case the inductance can be chosen in the order of 0.05 pu.
2. If the SMs are not equipped as described above, the SMs must be protected against the high currents that are fed into the fault on the DC-side. The magnitude of the current must be limited by the arm inductors in order to protect the antiparallel diodes in the SMs. In this case the inductance is typically chosen in the order of 0.10-0.15 pu.
3. Another design option to increase the current capability on the AC-side by increasing the sum of capacitor voltages per arm $\overline{v_{C,u,l}^{k,\Sigma}}$ beyond the DC-side voltage V_{DC}. The arm inductance will have to be increased compared to the first case in order to design the converter in the way explained in this case.

The topic of arm inductance will not be treated further in this chapter. In chapter 6 the simulation model of the MMC used for the simulations in this project is discussed and as will be shown there, the arm inductance used in the simulations is calculated to be $L = 0.1496pu$. According to the descriptions of the second case above this can be reasonable to assume since the SMs are not equipped with protection for DC-side short-circuits in the simulation model. The arm inductance used in that model is based on a CIGRE test grid [99], which will be discussed in chapter 6.2.

Table 5.3 provides the parameters of the MMC designed for this project.

Table 5.3: Parameters of the MMC

Parameter	**Value**
Power rating	180 MW
AC voltage	400 kV
DC voltage	320 kV
Arm current	365.26 A
Type of semiconductor device	T0600TB45A press-pack IGBT [94]
Blocking voltage of IGBTs	4.5 kV
DC collector current	600 A
Number of submodules per arm	107
Total number of submodules	642

5.4 Coupling transformer design

As mentioned in chapter 2, a front-to-front coupled DC/DC converter with galvanic isolation is the best choice of DC/DC converter for this project. A coupling transformer will be used to provide the galvanic isolation.

According to W. Shen et. al [100], the magnetic components are among the bulkiest components in switch-mode converters. By increasing the operating frequency, the size of the magnetic components can be reduced. However, higher frequencies cause higher switching losses in the converter and increase the losses in the core and the windings of the transformer. In addition, leakage inductances and parasitic winding capacitances in the transformer can cause current and voltage spikes at high frequencies. This is undesirable as that will lead to increased switching and snubber losses and reduce the overall converter efficiency. Therefore, the operating frequency of the transformer should be chosen based on a trade-off between component size and losses .

The use of a coupling transformer at a higher operating frequency also provides other advantages. In addition to reduced size of the transformer, the use of a medium frequency transformer in an MMC based DC/DC converter is beneficial for the converter design as it leads to size reduction of the passive elements, such as arm reactors and cell capacitors [24]. The size of the transformer is related to the operating frequency by equation (5.9) [101]:

$$EMF = 4.44fNBA \tag{5.9}$$

where EMF is the value of the electromotive force (EMF) induced in the transformer windings, f is the operating frequency, N is the number of turns, B is the flux density and A is the cross sectional area of the core. This equation shows that the size of the transformer is inversely proportional to the operating frequency.

According to G. P. Adam et. al. [24] the operating frequency of the transformer should be constrained to $<$1 kHz for a multiterminal HVDC network with operating pole-to-pole voltages of up to 800 kV. That is because the size and weight reduction obtained by increasing the frequency is limited by the increased switching losses. In addition, the increased $\frac{dv}{dt}$ obtained by increasing the operating frequency makes transformer design more challenging. The operating voltage of the DC-link is 320 kV, corresponding to a voltage of around 400 kV on the AC side of the converter (using equation 5.1), which will be the voltage applied to the primary windings of the transformer. Therefore, an operating frequency of the converter lower than 1 kHz can be reasonable to assume.

The AC voltage at the secondary windings of the transformer can be calculated using equation (5.10):

$$V_{secondary} = \frac{V_{primary}}{n} \tag{5.10}$$

Where 1:n is the turns ratio of the transformer.

The active power to be transferred to/from the DC-link through the DC/DC converter is dependent on the power of the battery, and as mentioned earlier in this chapter, it is found to be 180 MW. Since a power factor of pf = 0.95 is used in this project, using equation (5.6) to calculate the apparent power, it will be found that a medium frequency transformer with a power rating of around 190 MVA will be required in this project.

In order to choose an operating frequency and a turns ratio for the transformer in this project, characteristics of different transformers found in papers are compared. The characteristics are provided in table 5.4 and the papers that they are taken from are presented in the column ”Reference”.

Table 5.4: Medium and high frequency transformer design

Power	$V_{primary}$	$V_{secondary}$	Turns ratio	Frequency	Reference
30 MW	25 kV	15 kV	5:3	350 Hz	[65]
30 kW	280-325 V	max 10 kV	1:11	79-200 kHz	[100]
6.7 kVA	3800 V	400 V	19:2	3 kHz	[102]
166 kW	2000 V	400 V	5:1	20 kHz	[103]
25 kW	2400 V	400 V	6:1	4 kHz	[104]
1000 MVA	400 kV	350 kV	8:7	500 Hz	[24]
600 MVA	330 kV	400 kV	33:40	250 Hz	[105]
63 MVA	55 kV	110 kV	1:2	250 Hz	[106]
1.6 MVA	1.5 kV	13.5 kV	31:375	500 Hz	[107, 108]
0.8 MVA	0.6-0.7 kV	13.5 kV	16:375	500 Hz	[107, 108]

According to the results provided in table 5.4, it seems like higher operating frequencies are used for lower voltage levels and power ratings. As discussed above, the converter to be used in this project has a power rating of around 190 MVA and it needs to step down the MMC AC-side voltage of 400 kV to the AC-side voltage of the 2L-VSC that corresponds to the desired battery voltage. When comparing this to the projects in the table, it can be reasonable to assume an operating frequency between 250 and 500 Hz. Therefore, an operating frequency of 300 Hz will be used for the transformer in this project.

When it comes to turns ratio, it looks like quite small ratios are used for the projects in table 5.4 with similar voltage and power ratings as for this project. When choosing a turns ratio it is also important to consider that the whole system is connected and that the design of one component affects the design of another component in the system. I.e, if a large turns ratio is chosen for the transformer, that implies a higher current in the battery since the battery voltage will decrease with an increasing turns ratio of the transformer, while the power rating is constant at 180 MW or 190 MVA for the battery and the DC/DC converter (and the converters and transformer that it is made of). A high battery current will imply that the semiconductors switches in the 2L-VSC connected to the battery, must be able to withstand a high current. As discussed earlier, semiconductor devices that can withstand higher currents require a larger conducting area, and this increases the cost of the semiconductor device. An option is to parallel connect semiconductor switches in order to increase the current capability, but again this would increase the cost as more semiconductor switches would be required. Another option is to decrease the turns ratio of the transformer so that the battery voltage will be higher and the battery current lower, implying that semiconductor devices with a lower current capability (and with a lower cost) can be applied. Since quite low turns ratios are used in the projects in table 5.4, a low turns ratio of 1:3 is chosen for this project. In order to make sure that the turns ratio chosen is low enough, equations (5.4), (5.5) (where $V_{AC,line}$ = $V_{secondary}$) and (5.10) can be used to calculate the AC-side phase current of the 2L-VSC for chosen turns ratio. By comparing this to the maximum current capabilities of the discussed semiconductor devices in the MMC design part in table 5.3, it can be found that a number of these semiconductor devices can be used in the 2L-VSC connected to the battery if the turns ratio is 1:3.

When it comes to the parameters used to represent the winding losses of the transformer in this project, assuming an equal impedance on the primary side representing the losses in both the primary and secondary windings, the resistance and inductance are set to R_T = 0.005 pu and L_T = 0.15 pu. These values are chosen since they are close to values used in transformers in industry today [109]. Also A. Hassanpoor [110] has used these parameters for a transformer connected to an MMC with V_{AC} = 400 kV, V_{DC} = 320 kV and P = 1 GW. This also motivates the choice of using these parameters since the HVDC system in this paper has an MMC rated for the same voltages as the MMC in this project.

Table 5.5 presents the parameters of the coupling transformer for this project.

Table 5.5: Parameters of the transformer

Parameter	Value
Apparent power rating	190 MVA
Voltage on primary winding	400 kV
Voltage on secondary winding	133.33 kV
Turns ratio	1:3
Operating frequency	300 Hz
Resistance pu-value, R_T	0.005 pu
Inductance pu-value, L_T	0.15 pu

5.5 2L-VSC design

5.5.1 Power rating and voltage levels

The AC-side voltage level of the 2L-VSC depends on the turns ratio of the transformer. As found in the subchapter above, the AC voltage on the secondary side of the transformer is 133.33 kV and therefore this will be the line voltage at the AC-side of the 2L-VSC. Similarly to the calculations earlier in this chapter, the DC-side voltage of the converter can be found using equation (5.1). This gives $V_{DC} = 108.87kV$ for this converter. The power rating is still 180 MW since this converter is also a part of the DC/DC converter connecting the 180 MW battery to the DC-link of the HVDC transmission system.

5.5.2 Current

The AC-side phase current of the 2L-VSC can be found using equation (5.4) and (5.5). Using (5.5) the AC phase voltage is calculated to be $V_{AC,phase,RMS} = 76.98kV$ and inserting this into (5.4), the phase current is found to be $i_a = 820.45A$. The DC-side current is found using equation (5.3) and it is $I_{DC} = 1653.4A$. For the semiconductors used in the 2L-VSC it is i_a that must be lower than the rated current of the semiconductor device used. In the MMC, the SMs that are series connected in each arm to achieve the desired voltage level of the converter, but for the 2L-VSC it is the semiconductor switches that are series connected in each valve to achieve the desired voltage level. Next subsection will discuss the choice of semiconductors for this converter.

5.5.3 Choice of semiconductors

As mentioned in subsection 5.3.3, the choice of semiconductors for the 2L-VSC will be among the IGBT press pack devices in table 5.2. The voltage and current ratings of these IGBT semiconductor devices are shown graphically in figure 5.6.

For the 2L-VSC, the number of series connected semiconductor switches in each valve is decided by the blocking voltage of the semiconductor, as shown by equation (3.2). Since the 2L-VSC also is based on hard-switched PWM modulation, the same safety margin of 33 % which was used when calculating the number of SMs in each arm of the MMC, is included in this case, so equation (3.2) becomes (5.11). By using semiconductors with lower blocking voltages, more semiconductor devices have to be series connected in order to achieve the desired voltage level of the converter. As mentioned in subsection 5.3.3, the cost of the semiconductor devices is mostly dependent on the current rating and therefore also the size of the conduction area of the semiconductor. Therefore, for the 2L-VSC where the semiconductors are series connected in order to achieve the desired operating voltage of the converter, choosing semiconductors with as high blocking voltages as possible would be desirable in order to reduce costs.

The number of series connected semiconductors per valve of the 2L-VSC can be calculated using equation (5.11)

$$N_{series,valve} = \frac{V_{DC}}{f_{safetymargin} \cdot V_{blocking}} \tag{5.11}$$

where V_{DC} is the DC-side voltage of the 2L-VSC, $V_{safetymargin}$ is the safety margin which is set to $\frac{2}{3}$ and $V_{blocking}$ is the blocking voltage of the semiconductor switches used in the converter.

As mentioned in subsection 5.3.3, a semiconductor device with a current rating as close as possible to the phase current of the 2L-VSC should be chosen in order to minimize costs. The phase current of the 2L-VSC used in this project was calculated in subsection 5.5.2 to be $i_a = 820.45A$. Comparing this to the results of different semiconductor devices offered commercially, shown in figure 5.6, it can be found that the IGBT press-pack from Westcode

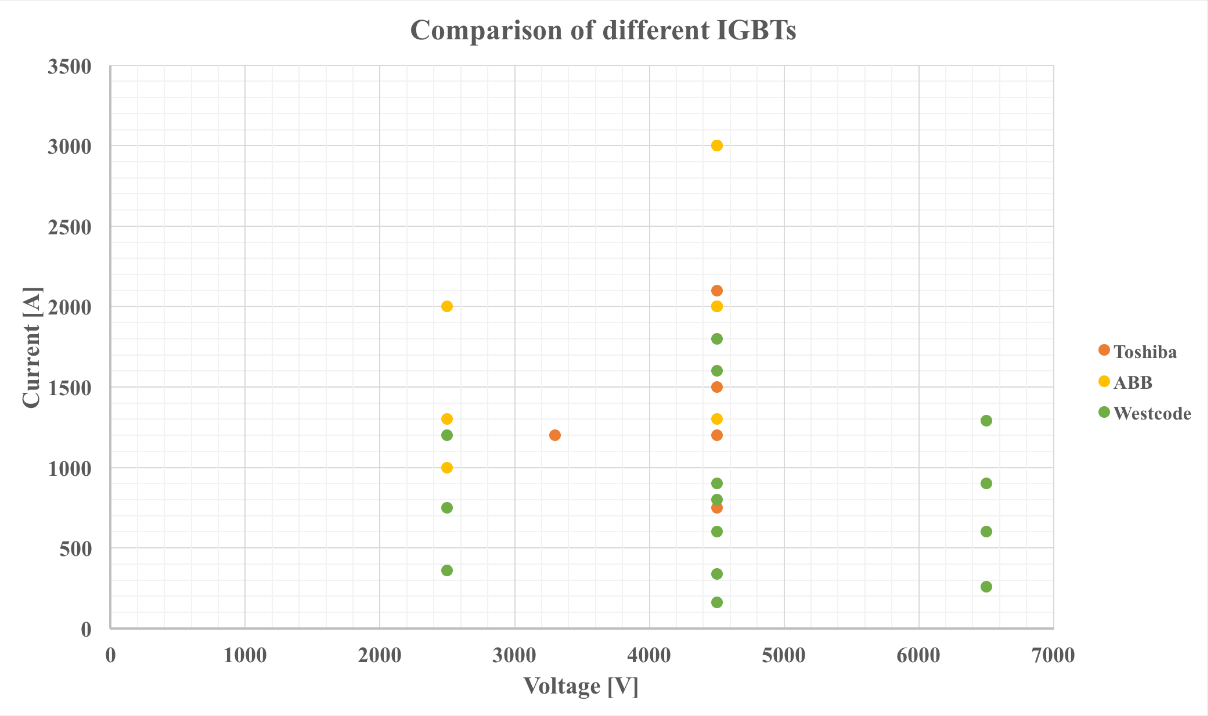

Figure 5.6: Comparison of different types of press-pack IGBTs

with $V_{CE} = 6500V$ and $I_C = 900A$ should be chosen. This is the T0900DF65A IGBT press-pack in the brochure from Westcode [94]. Using equation (5.11) with $V_{DC} = 108.87kV$, $f_{safetymargin} = 0.67$ and $V_{blocking} = 6.5kV$ the number of series connected semiconductors per valve of the 2L-VSC is found to be $N_{series,valve} = 24.99 \approx 25$.

Table 5.6 provides the parameters of the 2L-VSC chosen for the design of the 2L-VSC in this project.

Table 5.6: Parameters of the 2L-VSC

Parameter	Value
Power rating	180 MW
AC line - voltage	133.33 kV
AC phase - voltage	76.98 kV
DC voltage	108.87 kV
Phase current	820.45 A
DC current	1653.4 A
Type of semiconductor device	T0900DF65A Press-pack IGBT [94]
Blocking voltage of IGBTs	6.5 kV
DC collector current	900 A
Number of series connections of semiconductor devices per valve	25

5.6 Battery design

In industry, different battery storage systems have been developed by different manufacturers. These storage systems consist of the battery module or battery container, DC/AC converters and transformers in order to connect the battery to the AC grid, and protection- and control-systems for safe operation. Some of the developed battery storage systems in industry include the EssPro™ Grid [17] developed by ABB, SIESTORAGE [111] by Siemens and the MaxSine™ eStorage [85] developed by Altsom.

5.6.1 ABB EssPro™ Grid

The design of the battery to be used in the battery system in this project will be based on the information provided by the manufacturers and their battery storage systems mentioned above, but only looking at the battery module or battery container part of the total battery system. Since most information in terms of technical data is provided in the ABB solution, their EssPro™ Grid system will be used as the base of the battery design part of this project. Figure 5.7 shows the layout of a 1 MW, 15 min EssPro™ Grid from ABB.

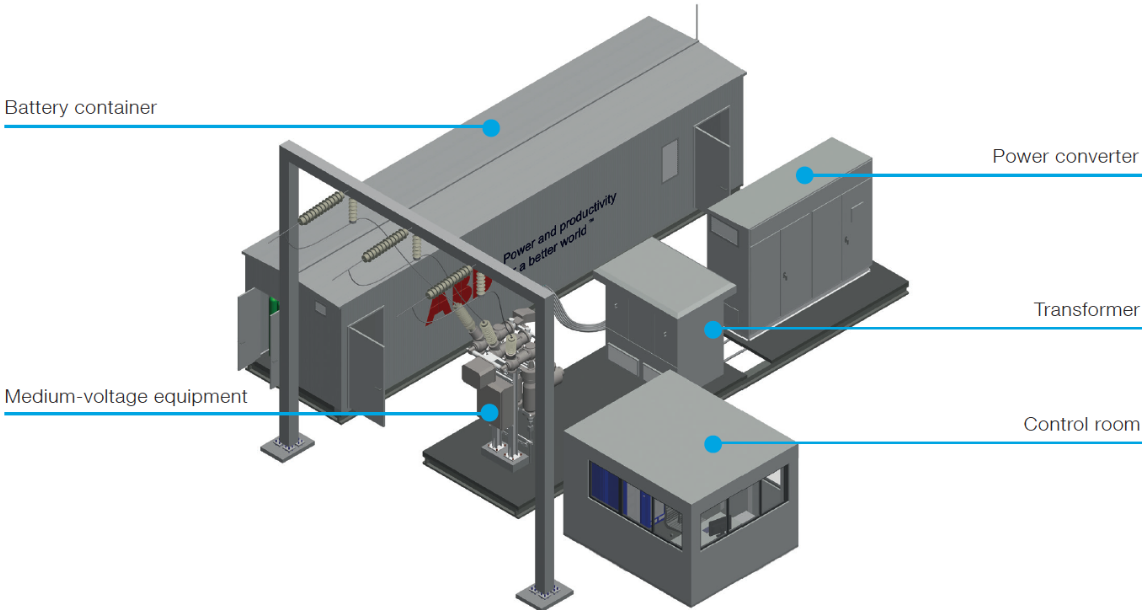

Figure 5.7: Battery energy storage systems layout of a 1 MW, 15 min EssPro™ Grid layout[17]

5.6.2 Battery voltage

Different battery technologies can be used in the EssPro™ Grid, including NaS, LA, Li-ion, NiCd and flow batteries. The choice of battery technology is based on the application of the battery storage system, and as found in chapter 2, the Li-ion battery technology will be used in this project. ABB's brochure on the EssPro^{TM} Grid [17] also provides information regarding voltage and power rating of the system. The DC side battery voltage can be up to 1.2 kV per battery module or container, and the power and energy can be up to 30 MW and 7.2 MWh per module. The battery modules can be connected in series and parallel in order to achieve the desired voltage and power rating of the system.

For this design part of the thesis it is assumed that the voltage of one EssPro^{TM} Grid battery module is $V_{module} = 1.2\ kV$. This is because the battery system will be quite large since it is going to have a capacity of 180 MW, and in addition the battery modules are costly. Therefore it is desirable to have a voltage as high as possible per module so that less modules have to be connected in order to achieve the total battery voltage and power, and in that way both size and costs of the battery system can be minimized.

The battery system is going to be connected to a 2L-VSC that makes up the LV-side of the front-to-front connected galvanically isolated DC/DC converter, and hence the battery voltage is dependent on the voltage of the 2L-VSC. In subsection 5.2.6 it was found that the DC-side voltage of the 2L-VSC, i.e the battery voltage, is $V_{bat} = 108.87\ kV$. The number of series connections of EssPro Grid battery modules can now be calculated using

$$N_{series} = \frac{V_{bat}}{V_{module}} \tag{5.12}$$

Using this equation and the battery and module voltages mentioned above, it is found that $N_{series} = 91$.

5.6.3 Battery current

The total battery current is equal to the DC-side current of the 2L-VSC and it can be calculated using equation (5.13) or (5.14):

$$I_{bat} = \frac{P_{bat}}{V_{bat}} \tag{5.13}$$

$$I_{bat} = \frac{E_{bat}}{V_{bat} \cdot t_{discharge}} \tag{5.14}$$

As discussed, the battery power is $P_{bat} = 180\ MW$, and using this and $V_{bat} = 108.87\ kV$, it can be found that the battery current is $I_{bat} = 1653.4\ A$. The number of battery modules connected in series can be found using equation (5.15)

$$I_{bat} = N_{parallel} \cdot I_{string} \tag{5.15}$$

where I_{string} is the current per string of battery modules connected in series and $N_{parallel}$ strings are connected in parallel to achieve the total battery voltage I_{bat}.

$$I_{string} = \frac{P_{string}}{V_{string}} = \frac{N_{series} \cdot P_{module}}{V_{bat}} \tag{5.16}$$

As shown by equation (5.16), the number of parallel connections of battery strings depends on the power of an EssPro^{TM} Grid battery module. A higher value of P_{module} implies a higher

I_{string}, and hence fewer battery connections, and fewer battery modules in total to achieve the total battery power. However, the EssPro^{TM} Grid brochure [17] does not provide information about maximum current capability of a battery module. This is probably because a number of different battery technologies can be used in the EssPro^{TM} Grid and they all have different current capabilities. In addition, the current capability of one module depends on how the battery cells are connected in series and parallel within the battery module, and there is not provided information about this in the brochure. The battery power is discussed in the next subsection and as will be shown, a power rating of the battery module is chosen based on a discussion regarding how high current it is assumed that the battery can handle.

5.6.4 Battery power

As described in chapter 1, the battery storage system used in this project should have a rated power of 10-20 % of the rated power of the wind farm. That is because the battery system is to be used to provide the ancillary services of primary and secondary reserves in case of change in frequency in the power system , meaning that the battery will charge or discharge for a short time period (up to 15 minutes if it also provides secondary reserves) in order to stabilize the frequency in the system. In case of a large change in frequency, the battery will help stabilize the system for a short time of period until other generators in the system that have longer response time are able to be ramped up/down to continue the stabilization. 10-20 % of the wind farm rated power, meaning 100-200 MW, is assumed as an appropriate power rating for the battery system for this purpose. For this reason, a battery power of $P_{bat} = 180MW$ has been chosen for this project.

As mentioned in subsection 5.6.3, the power of an EssPro^{TM} Grid battery module has to be chosen for this project in order to calculate the number of parallel connections of modules. In the brochure [17] from ABB the power of one module can be chosen to be between 100 kW and 30 MW. The higher the value that is chosen, the less battery modules are required in total and the less parallel connections of battery strings will be included. However, the higher the value for P_{module}, the higher the current capability must be for each module. In addition having more strings in parallel provide an advantage of redundancy and in case of a fault in one module, the whole string that it is connected to will be decoupled. In case of few parallel connections, a fault can lead to disconnection of a large part of the total battery capacity. Since the battery in this project is used to provide ancillary services to the grid and must have a size of 10-20 % of the wind farm capacity, having few parallel connections can be critical. I.e. if the battery only consist of two parallel connections a fault occurs in one of them, only half of the total battery will be available to provide the ancillary services to the grid, meaning that the available battery power is less than 10-20 % of the wind farm capacity. Therefore, when having a battery with a capacity of 18 % of the wind farm capacity, it is decided to have at least 3 parallel connections of battery stings so that if one is disconnected due to i.e a fault in one module, a battery capacity of 12 % of the wind farm capacity will still be available to provide ancillary services, which is within the acceptable range of battery capacity between 10-20 %. Using equations (5.15) and (5.16) with $N_{parallel} = 3$ gives $I_{string} = 551.14A$ and $P_{module} = 660kW$ Based on the assumptions discussed above and assuming that the battery module is designed so that it can handle this current calculated above, $P_{module} = 660kW$ is used in this project.

The battery power is described by equation (5.17)

$$P_{bat} = N_{series} \cdot N_{parallel} \cdot P_{module} \tag{5.17}$$

The total energy capacity of the battery system is found multiplying the battery power with its discharge time, which is $t_{discharge} = 0.25h$ for this project since the battery system is going to provide ancillary services for a time duration of up to 15 min.

$$E_{bat} = P_{bat} \cdot t_{discharge} \tag{5.18}$$

The results obtained from using these equations with the parameters discussed in this subsection, are provided in table 5.7.

5.6.5 Size of the battery

The total number of EssPro^{TM} Grid battery modules required in the construction of the battery can be found using equation (5.19):

$$N_{tot} = N_{series} \cdot N_{parallel} \tag{5.19}$$

Using $N_{series} = 91$ and $N_{parallel} = 3$, it is found that N_{tot} = 273. In addition to these 273 battery modules, protection equipment and control-systems will be required in the battery system, and hence it is clear that the final battery system will require quite a large footprint. Since weight and size are critical parameters when it comes to costs of offshore placement of equipment [25], it can be concluded that it will be advantageous to place the battery onshore.

Table 5.7 presents the battery parameters calculated in this subchapter.

Table 5.7: Battery parameters

Parameter	Value
Power rating	180 MW
Battery voltage	108.87 kV
Battery energy	45 MWh
Discharge time	15 min
Battery current	1653 A
Battery capacity	413.25 Ah
EssPro^{TM} Grid battery module voltage	1.2 kV
EssPro^{TM} Grid battery module power	660 kW
Number of EssPro^{TM} Grid battery modules used in the battery	273

Chapter 6

Simulation model

In this chapter the simulation model used for the simulations in this project is described. It consists of models of the different components of the system that are modeled and tested separately before they are connected to form the final system. The simulation models are made in Simulink and the scripts and functions required to run the simulation models are made in MATLAB. The Simulink models and MATLAB scripts for all the simulation models described in this chapter are provided in Appendices C and D in the end of this report.

6.1 HVDC system

The Simulink model of the HVDC system is shown at the top of figure D.6 and a closer look at the different components that it is built up of are shown in figures D.7-D.13. As mentioned in chapter 5, this model was given for this project. However, it will be described why the simplifications that have been made to the model is applicable for this project and why this model can be used for the test cases in this thesis without affecting the results. In the end of this subchapter the simulation model is verified.

For simplicity, and since modeling of the offshore wind farm and the onshore grid is outside the scope of this project, both the wind farm and the onshore grid are modeled as three-phase sources without impedance that are star (Y)-connected to an internally grounded neutral. The transmission lines are modelled using a PI-line model as shown in figure D.13 where the impedances of the lines are calculated as shown in the script in Appendix C.2.

A subsystem of the CIGRE B4 DC grid test system [112] has been used to set the parameters for the HVDC transmission system model. For the 2L-VSCs, the pu-values of the parameters in the ”AC-DC converter pole in CIGRE test grid” section have been used (table 7 in [112]), and based on the base values used for the system, the SI values of the parameters are calculated in the script using equations (3.13)-(3.20). For the transmission lines, the values for a DC cable of +/- 400 kV from table 9 in [112] have been used, and the SI values of the parameters are calculated in the same way as for the parameters of the 2L-VSCs. The parameters used for the HVDC transmission system are provided in table 6.1. The reason why the pu-value of the capacitor is expressed in ms and not $\%$ or pu is that it represents the DC-side capacitance and the system frequency of the DC-system is zero. The ms value of the capacitor expresses the time it takes for the capacitor to charge to a reference voltage with a reference current [112]

The modeling of the 2L-VSCs are based on the mathematical model described in chapter 3.3. However, a simplified representation of the model is used in the simulations; the representation of the semiconductor valves in the model are simplified using the universal bridge block in Simulink with average-model based VSCs as the power electronic devices. It can be used in this project since the main objective is to look at the ”bigger picture” of the system and to verify that the battery system can help stabilizing the grid. Detailed modeling of the converters of the HVDC system is not required in order to simulate this, since the focus is not on the performance of the semiconductor valves in terms of losses etc., but rather on the operation of the whole system. Simplifications of the modeling of the HVDC system also leads to faster simulations without affecting the results, so this is another motivation to use a simplified model.

In the simulation models used in this project, all the circuits are modelled using SI units while all the controllers are modelled using pu-values for easy scalability. The control of the 2L-VSCs of the HVDC system is based on the controllers described in chapter 3.4 and the Simulink models of the converters and their control loops are provided in figures D.7, D.8, D.9, D.10, D.11 and D.12. In this model the 2L-VSC connected to the wind farm side of the HVDC link is a slave configuration and its controller controls the power to be transferred from the wind farm to the grid onshore. This is done by controlling the d-axis and q-axis current components. By regulating the step functions shown in figure D.11, which are added to create the d-axis reference current in pu, i_d^*, the d-axis current can be controlled. The transfer function $\frac{1}{0.2s+1}$ is included in order to create a reference signal that provides smoother transitions when the steps are changed. This is done for all reference signals that are created from step functions in this project, and it is done to have a smoother signal which will lead to less oscillations in the results. The smaller the term multiplied with s is, the faster the response. The PI-controllers in this figure are both tuned using the modulus optimum criteria described in chapter 3.4.2. The upper control loop controls the q-axis current to follow its reference which is set to 0. The lower loop controls the d-axis current to follow its reference. The outputs of the current controller is transformed to an abc-signal as shown in figure D.9, using the angle found in the PLL as shown in figure D.10. This signal, Cmd is used as the reference input in the universal bridge block in the circuit, as shown in figure D.8.

The 2L-VSC connected to the onshore grid side of the HVDC system is a master configuration and its controller controls both the power to be transferred onshore and the voltage at the point of connection. The controller is shown in figure D.12. The q-axis current is controlled in the same way as it is for the slave converter; it is controlled to follow its reference which is 0. The reference that the d-axis current is controlled to follow is in this converter set to be the output of the voltage control loop. The PI-controllers for the current control loop are tuned using the modulus optimum criteria, as for the slave converter. In the voltage control loop the square of the DC-voltage is controlled to follow its reference which is set to 1. This means that the controller controls the voltage to be constant at 1 pu and this is done in order to control the power flow of the DC-link by controlling the currents of the converters. The PI-controller for the voltage control loop is tuned using the symmetrical optimum criteria as described in chapter 3.4.4. Similarly to the slave converter, the output of the control loops C_q and C_d are transformed to a three-phase abc-signal which is used as the reference signal to the universal bridge block.

The gains of the controllers are given in table 6.1. They are written on the form $K_{p,x}$ and $K_{i,x}$ where $x = v$ for the voltage controller and $x = i$ for the current controller.

Table 6.1: Parameters used in the simulation model of the HVDC transmission system

Parameter	**Value**
Power rating	1000 MW
AC voltage	400 kV
DC voltage	320 kV
Switching frequency	2500 Hz
Filter resistance pu-value	0.01
Filter inductance pu-value	0.255
DC-side capacitance pu-value	60 ms
Length of transmission line	200 km
Line capacitance, C	0.1906 $\mu F/km$
Line conductance, G	0.048 $\mu S/km$
Line resistance, R	0.0095 Ω/km
Line inductance, L	2.1120 mH/km
Gains of the PI-controllers	
$K_{p,v}$	0.0650
$K_{i,v}$	9.0243
$K_{p,i}$	0.6764
$K_{i,i}$	8.3333

6.1.1 Verification of the 2L-VSC HVDC system

The model of the HVDC system can be verified by running a simulation of the model shown in the top of figure D.6, commenting out the PI-line model connecting the DC/DC converter, the DC/DC converter and the battery. The script in Appendix C.2 is run to set the parameters of the circuit in the Simulink model and to calculate the gains of the PI-controllers. The bode plot of the closed loop transfer functions of the two controllers are shown in figure 6.1 where the purple line indicates the closed loop transfer function of the voltage controller and the blue line indicates the closed loop transfer function of the current controllers. As shown in the figure, the current controllers are faster than the voltage controller (since the blue line is constant at the 0 dB line for a longer time and for higher frequencies than the purple), which was discussed in chapter 3 as an important characteristic of the the controllers of the 2L-VSC.

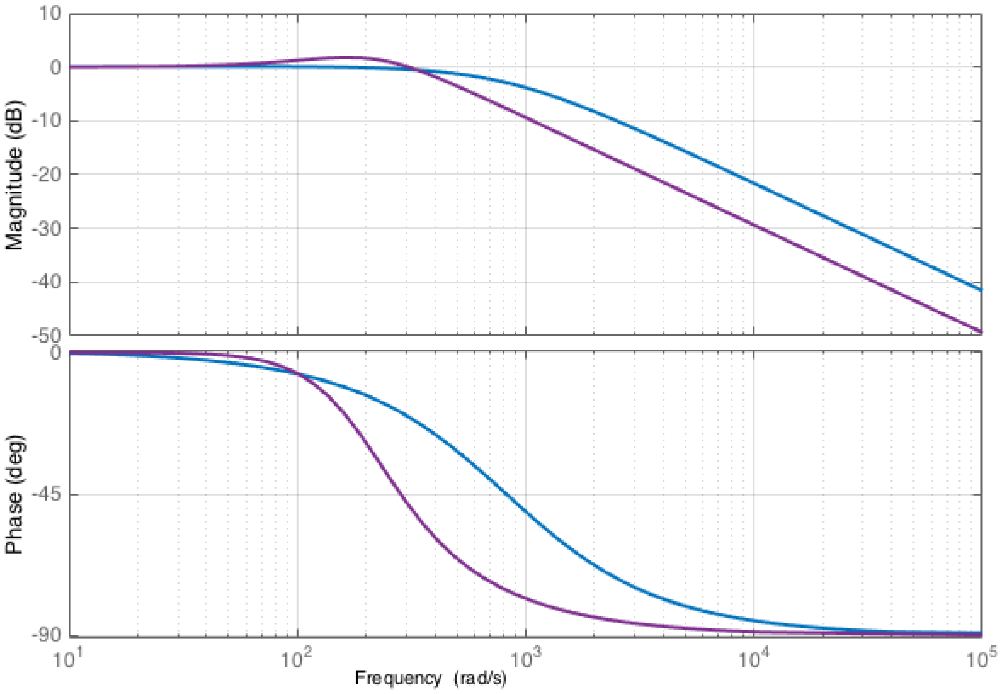

Figure 6.1: Bode plot of the closed loop transfer functions of the current and DC voltage controllers of the HVDC system

As discussed above, the DC-side voltage of the master converter is controlled to follow its reference of 1 pu. Hence, by controlling the current on the DC-link, the power flow is controlled. The current is controlled, as discussed, by controlling the reference value step functions of the current controller on the slave converter. To verify that the HVDC model works, the d-axis current reference value step functions are set to the values shown in table 6.2, and DC-side currents, voltages and powers are measured at the DC-side of the two converters. The resulting reference signal after the transfer function is added, is shown in figure 6.2.

Table 6.2: Step functions for the d-axis reference current of the slave 2L-VSC

Time [s]	Step from [pu]	Step to [pu]
3	0.20	0.60
7	0.60	0.50
12	0.50	0.80

The results of this verification are shown in figures 6.3 and 6.4, where figure 6.3 shows the power, current and voltage on the DC-link measured at the slave 2L-VSC and figure 6.4 shows the same parameters measured at the master 2L-VSC. The current direction is defined so that positive DC-current is flowing from the AC-side to the DC-side of the converter, and hence the simulations show that current is flowing from the slave to the master configuration. The current is controlled in the slave converter, and when comparing the DC-current of figure 6.3

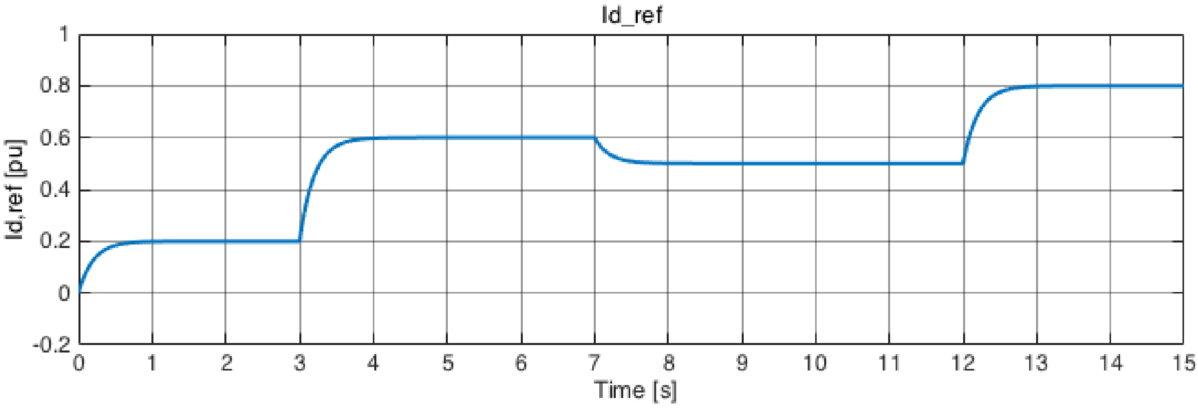

Figure 6.2: Reference current for the slave 2L-VSC current controller of the HVDC system, used to control the power flow on the DC-link

to the current reference in figure 6.2 the results show that the current is controlled to follow its reference. In the same manner, the voltage is controlled at the master configuration to a constant value of 1 pu and the results in figures 6.3 and 6.4 show that the voltage is kept constant at 1 pu. Hence, it can be verified that this simulation model works properly.

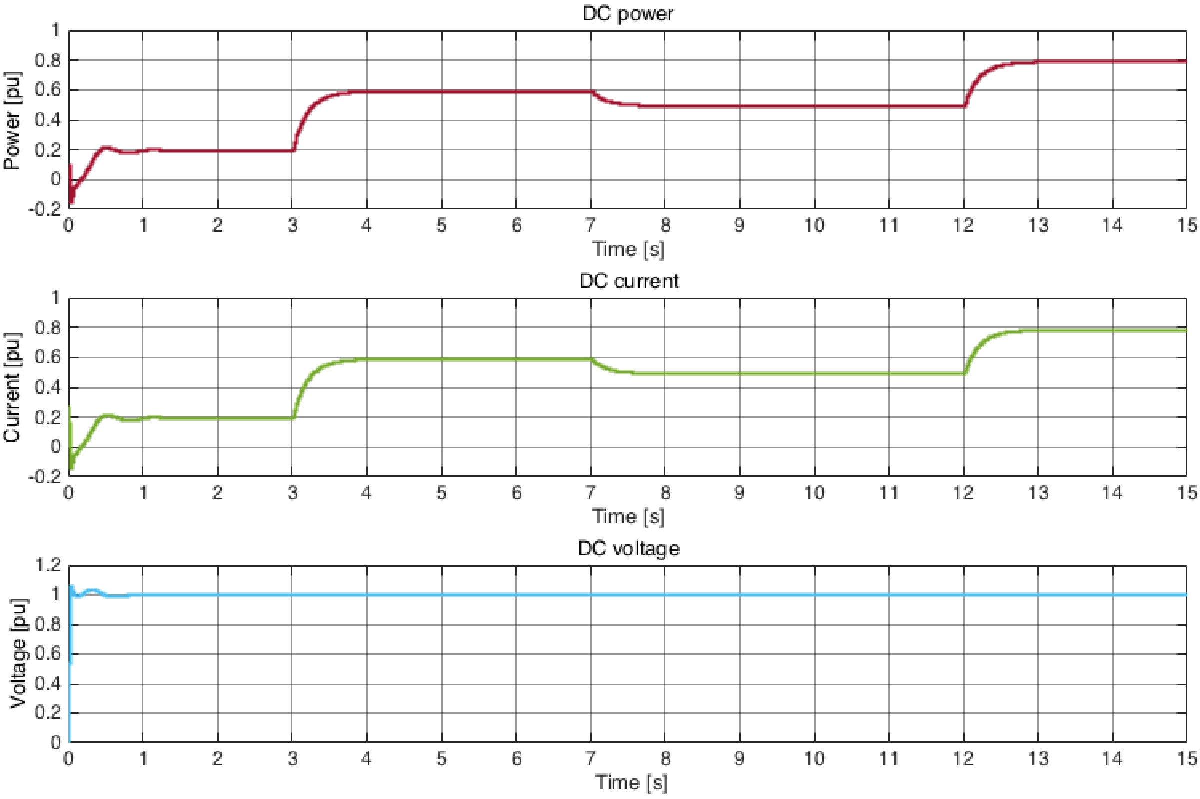

Figure 6.3: DC-side voltage, current and power measured at the slave 2L-VSC of the HVDC system

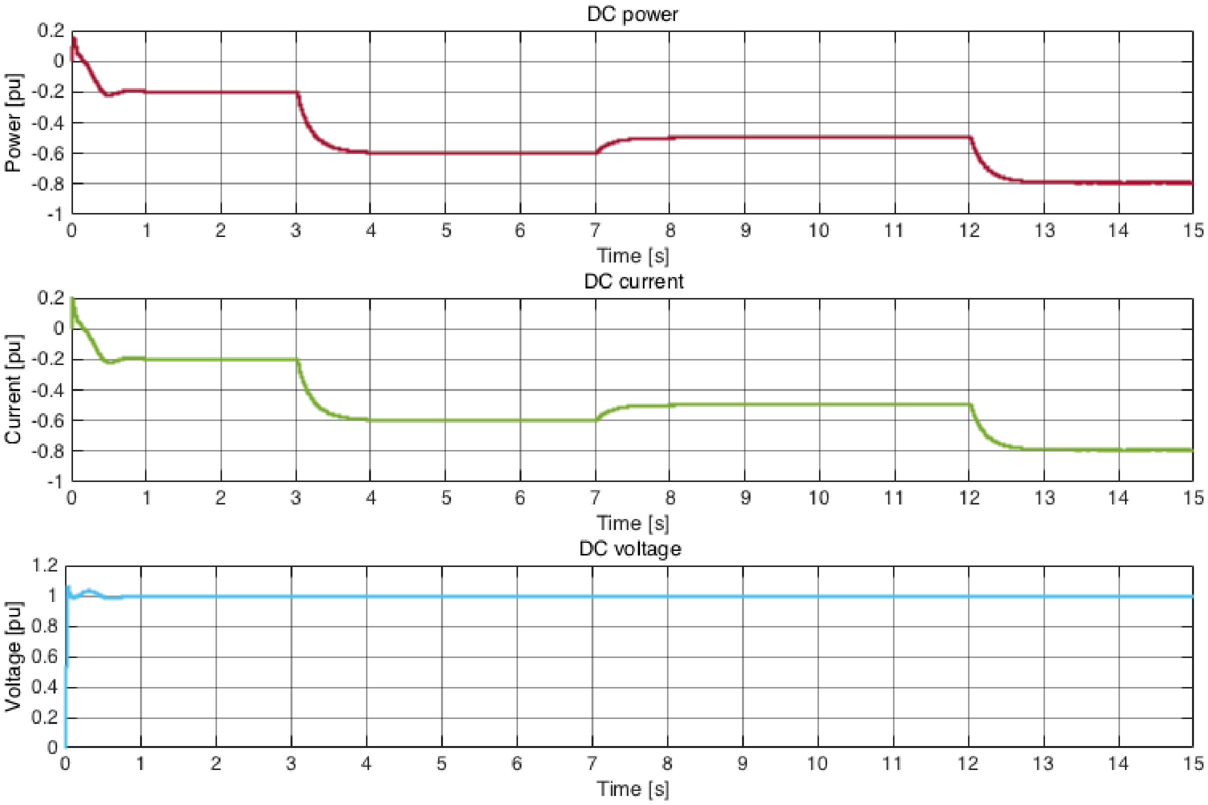

Figure 6.4: DC-side voltage, current and power measured at the master 2L-VSC of the HVDC system

6.2 MMC model

When making a simulation model for a converter the objectives of the study should be taken into consideration when deciding upon the degree of detail of the model. As mentioned in the previous subchapter, it is possible to use a simplified model of the 2L-VSCs of the HVDC system in this project since the objective of this project is to study the ”bigger picture” of the system and verify that integration of battery energy storage can provide support and stabilize the grid when sudden changes occur in the grid. For MMCs a number of models have been developed for different types of studies. In this subchapter different types of MMC models will be described before one topology is chosen for the simulations part of this project.

6.2.1 MMC models

Different MMC models with different levels of detail can be used for simulations depending on the the case that is to be studied. When voltage or current stress or losses within the converter is to be studied, a detailed model of the MMC is required since the individual SMs must be studied [41]. On the other hand, when studying power system related issues such as i.e. load changes in power system that the MMC is connected to, a simplified model where each SM is not modelled explicitly can be used. Detailed models of the MMC can be very complex since a large number of elements must be represented in the circuit and controlled by the controllers. These type of simulations require a large computational effort and long simulation times. This is a motivation to simplify the model as much as possible without affecting the results, especially for this project with a limited time frame.

A number of MMC models have been discussed in literature, including:

1 **Full physics-based model:** This is the most detailed model which is described by partial differential equations. This model provides great accuracy, but on the other hand it also require excessive computational times. This type of models are normally not used for power system simulations [18].

2 **Detailed model:** This is a simplified version of the model described above. It is based on simplified non-linear IGBT modules using an ideal controlled switch, a snubber circuit and two anti-parallel diodes [18, 99], as shown in figure 6.5. This model is suited for modeling details in the SMs and internal converter faults and it can also be used to simulate blocked states [18].

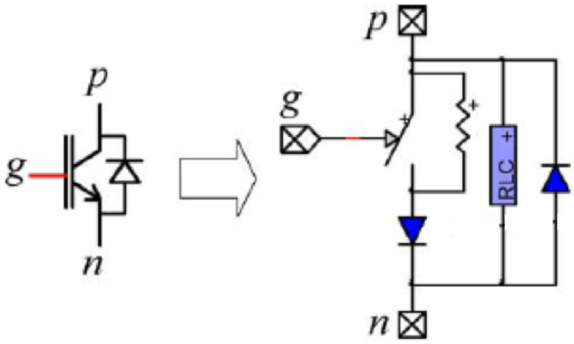

Figure 6.5: Representation of the non-linear IGBT used in the detailed MMC model [18]

3 **Equivalent circuit-based model:** This model is a simplified version of the models described above. In this model the SM is represented by a two-state resistor [18, 113]. The simplified SM is shown in figure 6.6. R1 and R2 depend on the capacitor voltage, current direction and gating signal. The ”switch” of the half-bridge SM is ON when R has a low, conductive resistance, and it is OFF when it has a large open-circuit resistance. By using a Thevenin equivalent, the model is simplified to having one Thevenin equivalent SM per arm [99]. This model can be used for most electromagnetic transient studies such as fault conditions, over-voltages and short-circuit studies [114].

4 **Average value model (AVM):** In this model the AC and DC sides of the converter are represented by controllable current and voltage sources [99]. Each arm of the MMC is modelled as a controllable voltage source in series with an inductor and the DC-side is modeled using two controllable current sources in anti-parallel, an equivalent capacitor and a switch in parallel with a diode (for DC fault control) as shown in [18, 113]. An assumption for this type of model is that the capacitor voltages are balanced. This type of model has faster computational times than the models described above due to reduced complexity [99]. Since this model is not representing the switches and the SMs explicitly, this model cannot be used for detailed study of the SMs, etc., but it is better suited for power system related simulation cases.

5 **Simplified AVM model:** The AVM model described above can be even more simplified

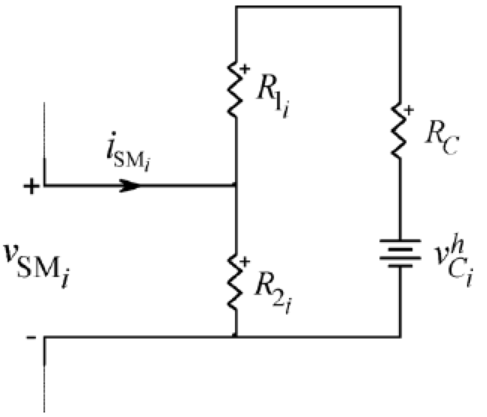

Figure 6.6: Representation of the simplified half-bridge submodule used in the equivalent circuit-based MMC model [18]

by representing the the MMC by the AC- and DC-side circuits as shown in figure 6.7 [115]. This model can also be used for power system related simulation cases, and compared to the AVM model described above, this AVM model is simpler and hence requires less simulation time.

The MMC model used for the simulations in this project is the simplified AVM based MMC (5). That is because it can simplify the simulation model in terms of complexity of the circuit and its controllers, and it can reduce the simulation time, whilst not affecting the simulation cases of interest. The AVM-MMC model used in the simulations is described and its operation is verified in the next subsections.

6.2.2 Mathematical model of the AVM MMC

This subsection presents a simplified mathematical model compared to the one presented in chapter 4. That is because, as discussed in the previous subsection, a simplified AVM-MMC model is used for the modeling of the MMC in this project.

The simplified AVM-MMC is shown in figure 6.7 [i]. It consists of separate AC- and DC-sides, connected by an energy balance equation, and it is based on the model in [115]. The dynamics of this model are represented in the synchronous reference frame by the following equations [13][115]:

$$L\frac{d\mathbf{i}}{dt} = \mathbf{E} - \mathbf{v} - R\mathbf{i} - j \cdot \omega L\mathbf{i} \tag{6.1}$$

$$L_{dc}\frac{di_{dc}}{dt} = -R_{dc}i_{dc} + v_{dc} - 2u_{cz} \tag{6.2}$$

$$\frac{dW_z}{dt} = (2u_{cz}\frac{i_{dc}}{3} - \frac{1}{2}\Re\{\mathbf{E}^*\mathbf{i}\}) \tag{6.3}$$

---

[i] The figure is based on the model presented in [115]

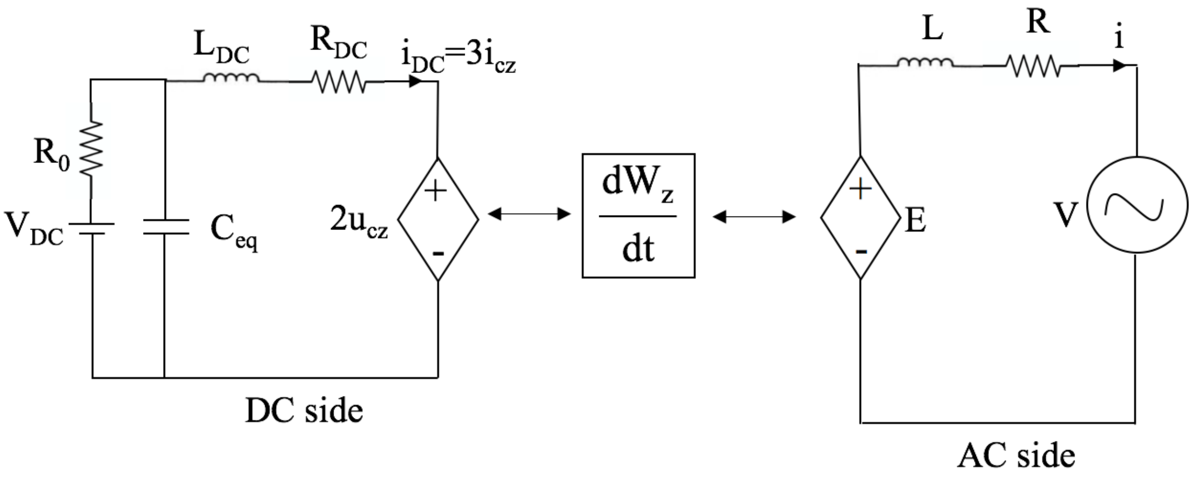

Figure 6.7: Simplified energy based AVM-MMC

Equation (6.1) represents the AC side of the model, (6.2) represents the DC side, and (6.3) represents the energy balance that couples the two systems together.

The AC current is represented by

$$\mathbf{i} = i_d + j \cdot i_q \tag{6.4}$$

The voltage driving the AC grid current is represented by

$$\mathbf{E} = E_d + j \cdot E_q \tag{6.5}$$

The voltage at the point of common coupling, **v**, is represented by

$$\mathbf{v} = v_d + j \cdot v_q \tag{6.6}$$

R and L are the AC equivalent resistance and inductance, respectively, and they are defined as

$$R = R_f + \frac{R_a}{2} \tag{6.7}$$

$$L = L_f + \frac{L_a}{2} \tag{6.8}$$

where R_f and L_f are the AC output filter resistance and inductance, while R_a and L_a are the MMC arm resistance and inductance, respectively.

The DC side equivalent resistance and inductance are defined as

$$R_{dc} = \frac{2}{3} R_a \tag{6.9}$$

$$L_{dc} = \frac{2}{3} L_a \tag{6.10}$$

u_{cz} is the zero sequence voltage driving the zero sequence circulating current, i_{cz}, which is defined as

$$i_{dc} = 3i_{cz} \tag{6.11}$$

Equations (6.1)-(6.3) can be represented in a pu system by defining the following base values [115]:

$$S_b = \frac{3}{2} \cdot v_b \cdot i_b \tag{6.12}$$

$$\omega_b = 2\pi f_b \tag{6.13}$$

$$Z_b = \frac{v_b}{i_b} \tag{6.14}$$

$$L_b = \frac{Z_b}{\omega_b} \tag{6.15}$$

$$C_b = \frac{1}{Z_b \omega_b} \tag{6.16}$$

$$P_{dcb} = S_b \tag{6.17}$$

$$v_{dcb} = 2v_b \tag{6.18}$$

$$i_{dcb} = \frac{3}{4} i_b \tag{6.19}$$

$$Z_{dcb} = \frac{v_{dcb}}{i_{dcb}} \tag{6.20}$$

$$L_{dcb} = \frac{Z_{dcb}}{\omega_b} \tag{6.21}$$

$$C_{dcb} = \frac{1}{Z_{dcb} \omega_b} \tag{6.22}$$

where v_b is the AC side base voltage, i_b is the AC side base current, S_b is the base apparent power, ω_b is the base electrical speed based on the base frequency, f_b. Equations (6.12)-(6.16) represent the AC side base values of impedance, inductance and capacitance, respectively. Equations (6.17)-(6.22) represent the DC side base values of power, voltage, current, impedance, inductance and capacitance, respectively. By knowing the value of two of these parameters (in this case v_b and i_b) the rest of the base values can be calculated.

The pu parameters are calculated by the following equation

$$X_{pu} = \frac{X}{X_{base}} \tag{6.23}$$

The resulting equations (6.1)-(6.3) in pu become [13, 115]:

$$\frac{L_{pu}}{\omega_b}\frac{d\mathbf{i}_{pu}}{dt} = \mathbf{E}_{pu} - \mathbf{v}_{pu} - j\omega_{pu}L_{pu}\mathbf{i}_{pu} - R_{pu}\mathbf{i}_{pu} \tag{6.24}$$

$$\frac{L_{dcpu}}{\omega_b}\frac{di_{dcpu}}{dt} = -R_{dcpu}i_{dcpu} + v_{dcpu} - 2u_{czpu} \tag{6.25}$$

$$\frac{dW_{zpu}}{dt} = \frac{\omega_b}{8C_{eqpu}}(2u_{czpu}i_{dcpu} - \Re\{\mathbf{E^*_{pu}i_{pu}}\}) \tag{6.26}$$

6.2.3 Controller design and tuning strategies

There are three control loops of the AVM-MMC; two inner loop controllers controlling the AC and DC currents, respectively, and an outer loop controller controlling the energy. The outer loop consists of an energy balance controller which controls the energy W_z to follow its reference W_z^* in addition to calculating i_d^*, the reference of the direct component of the AC grid current [115]. The AC current controller controls both the direct and the quadrature components of the AC current, i_d and i_q, to follow their reference values and the output of the controller is the gating signals controlling the voltage driving the AC-grid current. The DC current controller controls the DC current, i_{dc}, to follow its reference value and it produces the voltage driving the zero sequence circulating current in the DC side of the AVM-MMC. The controllers are similar to those described in chapter 4.6, but they will also be described here using the same nomenclature for the parameters as in the model described in the previous subsection. Figure 6.8 shows a block diagram of the control loops of the AVM-MMC. It shows the inputs and the outputs of the different controllers and how they interact with the circuits. The PLL block is the same as in the 2L-VSC model, described in chapter 3, and the abc to dq0 transformations are based on Clarck's and Park's transformations, which are provided in Appendix B.

As described in chapter 4.6, the control loops are based on PI controllers and the structure of the controllers are shown by means of a block diagram in the Laplace domain in figure 6.9. Y_{ref} is the reference value that the controller controls Y, the output of the system, to follow. U is the output of the controller and D is a disturbance term. The PI controller has the transfer function

$$K_p + \frac{K_i}{s} \tag{6.27}$$

where K_p is the proportional gain and K_i is the integral gain.

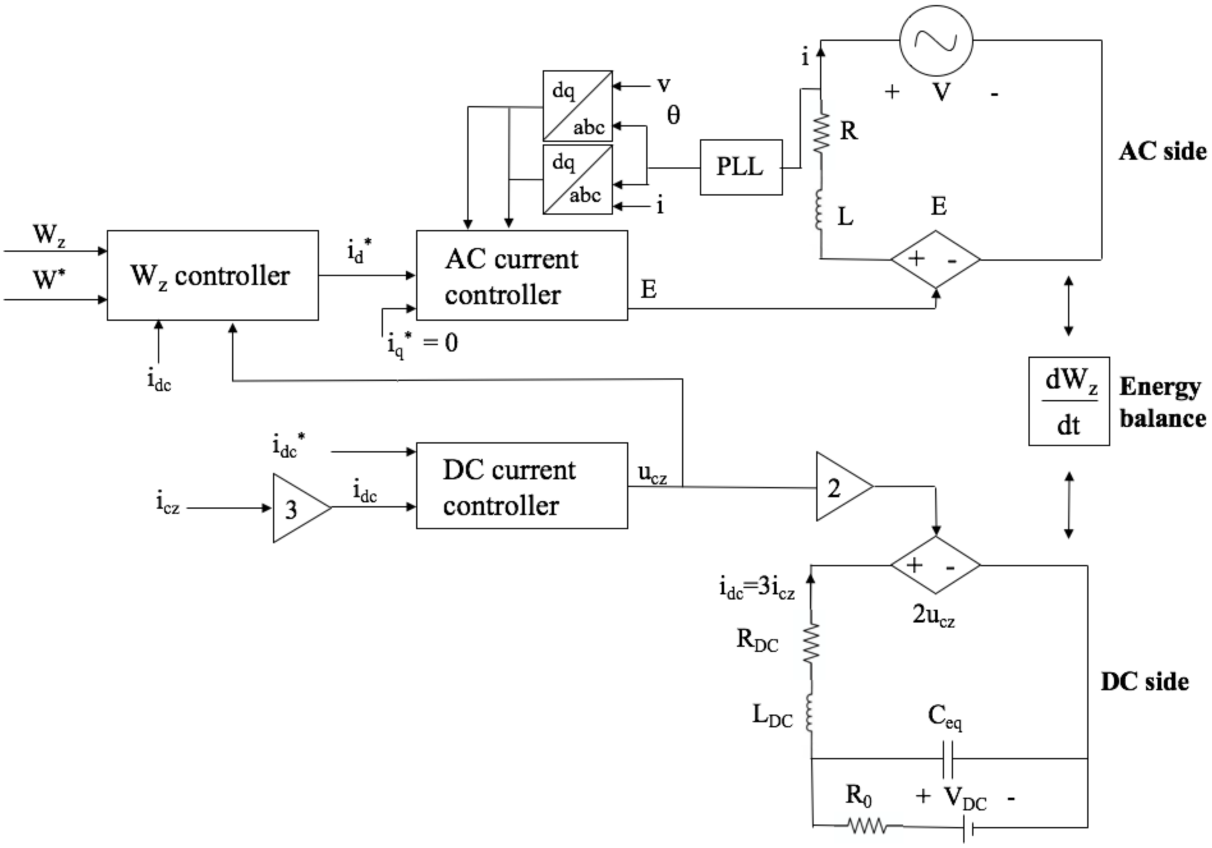

Figure 6.8: Block diagram of the control loops of the AVM-MMC

Table 6.3 provides the values of the parameters for the different controllers used for the AVM-MMC.

Table 6.3: Parameters of the different controllers of the AVM-MMC

Controller	$\mathbf{Y_{ref}}$	Y	D	U
AC_d	i_d^*	i_d	$-v_d+\omega Li_q$	E_d
AC_q	i_q^*	i_q	$-v_q-\omega Li_d$	E_q
DC	i_{dc}^*	i_{dc}	v_{dc}	$2u_{cz}$
W_z	W_z^*	W_z	$2u_{cz}i_{dc}$	i_d^*

The following reference values are used in the model: i_q^* is set to 0, i_d^* is the output of the energy controller and i_{dc}^* is set so that it controls the current through the MMC. As shown in figure D.1, it is set by three step functions. The values of these will be described further in the subsection on verification of the stand-alone MMC model and in the simulation cases in chapter 7. The energy reference is calculated using equation (6.28) [115]:

$$W_z^* = 2 \cdot n_{arms} C_{eq} v_b^2 \tag{6.28}$$

where n_{arms} is the number of arms per leg of the MMC and C_{eq} is the equivalent capacitance of the AVM-MMC. In this project n_{arms} = 2 is used.

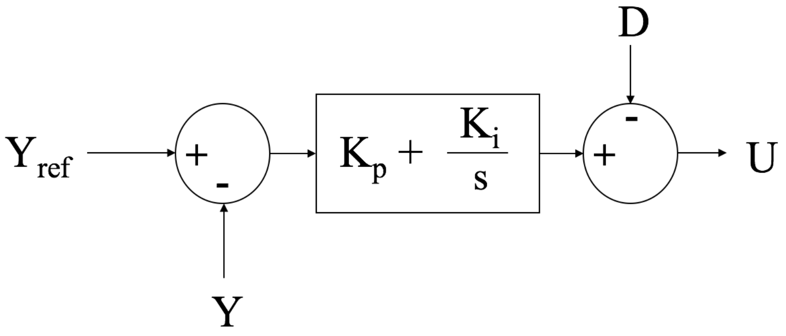

Figure 6.9: Block diagram of the control system in the Laplace domain

The inner loop current controllers are tuned using the modulus optimum criteria and the outer loop energy balance controller is tuned using symmetrical optimum, described in chapters 3.4.2 and 3.4.4, respectively. The equations used to calculate the gains of the controllers are provided in the MATLAB script in Appendix C.2, and the resulting gains of the controllers are given in table 6.4, along with the other parameters used for the simulations of the AVM-MMC in this project.

6.2.4 AVM-MMC simulation model

The Simulink model of the AVM-MMC is shown in figure D.1. This is the same MMC that is used in the final system in figure D.6, but since the MMC is modeled as a stand-alone model in this verification, the AC-side is connected to a three-phase AC source without impedance that is star (Y)-connected to an internally grounded neutral, and the DC-side is connected to an ideal DC voltage source in series with a small resistor (R_0 in figure 6.7), as shown in figures D.2 and D.3, respectively. The small resistor is included in the DC-side circuit to make the model run. If it had not been included, an ideal voltage source would have been connected in parallel to the capacitor at the DC-side of the 2L-VSC, and the the model would not run since a capacitance cannot have sudden changes in voltage across it [90]. The value of the resistor is very low in order to not influence the results of the simulation.

As mentioned in the previous subsection, the only controller reference value that is set externally in this model is the step functions that are used to create the reference value of the DC current controller. As shown in D.1 a transfer function of $\frac{1}{0.2s+1}$ is included for smoother transitions of the reference signal, similarly to what is done in the 2L-VSC current reference of the HVDC system. The inputs to the DC current controller, i_{dcpu} and v_{dcpu} are measured in the DC-circuit and in the transformation subsystem (shown in figure D.18) they are transformed to pu-values. In the DC current controller, the DC-current is controlled to follow this reference, and the output of the controller u_{cz}, the zero sequence voltage, is used as input in the DC-side circuit and as input to the energy balance controller, as shown in figure 6.8. In the energy balance controller, shown in figure D.20, the energy is controlled to follow its reference of 1 pu. The input W_{ref} is the output of the energy balance circuit, shown in figure D.16, which is based on equation (6.3). As shown in figure D.20, the energy controller is not turned on before the switch in the figure is turned on. That is because it takes some time to energize the circuits, so the AC- and DC-side circuits are running for a few seconds first so that current flows properly in them, and then they are connected by the energy balance. In the simulations the switch for turning on the energy controller is turned on after 4 seconds. Also here a transfer function is included for the same reason as described earlier in this section. As shown in figure 6.8, the output of the energy controller is the d-axis reference value used in the AC current controllers.

As described earlier, and as shown in figure D.20, the q-axis current is controlled to follow its reference of 0, while the d-axis current is controlled to follow the reference value which is the output of the energy controller. The inputs to these currents controllers are I_{dpu}, I_{qpu}, v_{dpu} and v_{qpu} which are obtained by measuring the AC voltage and current of the AC-side circuit and then using the transformation subsystem (as shown in figure D.18) to transform these values into the dq reference frame and to calculate the pu-values which are used in the controllers. The outputs of the AC current controllers, E_{qpu} and E_{dpu} are transformed back to the abc-system and used as input to the controlled voltage sources in the AC-side circuit, as shown in figure D.2.

The parameters of the AVM-MMC model used for the simulations are provided in table 6.4. The resistances, inductances and capacitance are based on the values used in [115] which again are based on the CIGRE B4 test grid [99]. In table 6.4 these parameters are given in pu-values which are calculated based on the SI-values in [115] and the base power and base voltage used in that paper. The calculation of the pu-values is provided in Appendix C.3. The other parameters and gains for the controllers are calculated using the MATLAB script in Appendix C.2.

Table 6.4: Parameters of the AVM-MMC

Parameter	Value
Base active power, P_b	180 MW
Power factor, pf	0.95
Base apparent power, S_b	189.47 MVA
AC base phase voltage, v_b	230.94 kV
Number of submodules per arm, $N_{SM,arm}$	107
Single phase reference energy, W_{ref}	$4.2442 \cdot 10^6$ J
AC-side equivalent resistance, R	0.0047 pu
AC-side equivalent inductance, L	0.1469 pu
DC-side equivalent resistance, R_{dc}	$7.5215 \cdot 10^{-4}$ pu
DC-side equivalent inductance, L_{dc}	0.0120 pu
Equivalent capacitance, Ceq	0.0042 ms
Gains of the PI-controllers	
$K_{p,DC}$	0.2400
$K_{i,DC}$	4.7257
$K_{p,AC}$	2.9380
$K_{i,AC}$	29.5310
$K_{p,W}$	0.2743
$K_{i,W}$	287.2912

6.2.5 Verification of the AVM-MMC simulation model

The stand-alone model of the simplified AVM-MMC can be verified by running a simulation of the model described in the previous subsection. The script in Appendix C.2 is run to set the parameters of the circuit in the Simulink model and to calculate the gains of the PI-controllers. The bode plot of the closed loop transfer functions of the controllers are shown in figure 6.10 where the red and blue lines indicate the closed loop transfer function of the current controllers (the red indicates the DC-current controller and the blue, the AC-current controller) and the yellow line indicates the closed loop transfer function of the energy balance controller. As shown in the figure, the inner loop current controllers are faster than the outer loop energy balance controller.

As discussed above, the energy is controlled to follow its reference of 1 pu. This means that the power on the AC- and DC-sides of the converter are balanced, as shown in equation (6.26). The current can be controlled by controlling the step functions to set the reference value of the DC-current controller, since the output of this control is further used in the energy

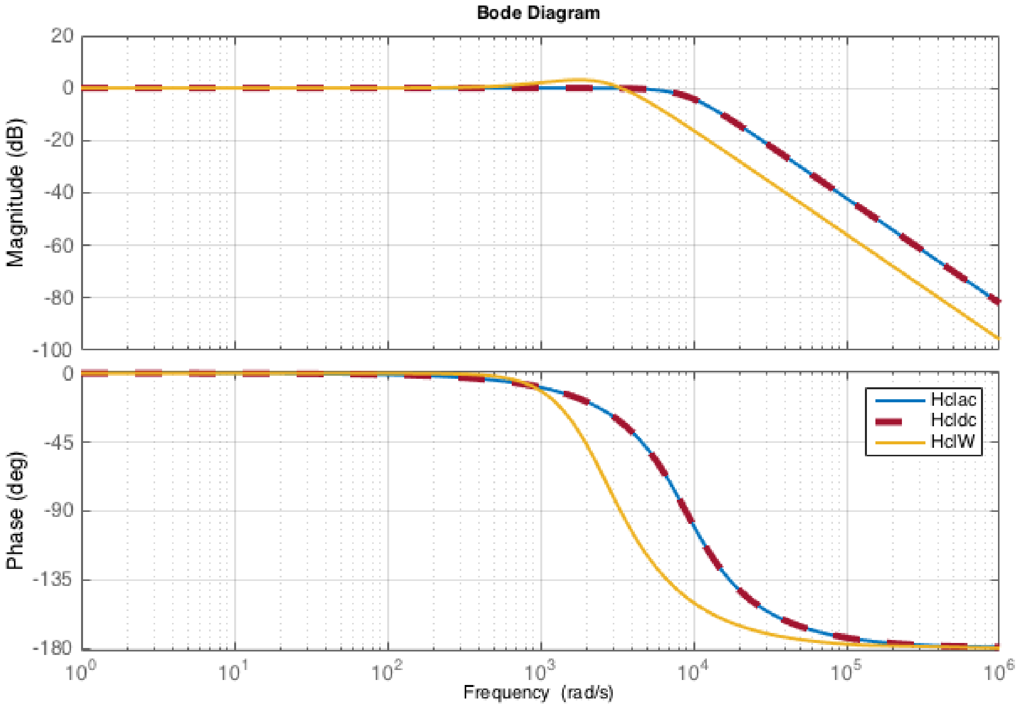

Figure 6.10: Bode plot of the closed loop transfer functions of the AC and DC current and energy balance controllers of the simplified AVM-MMC

controller and the output of that controller again is used in the AC-current controllers. Hence, by controlling the reference value of the DC-current controller, the current, and power flow of the converter can be controlled. To verify that the stand-alone simplified AVM-MMC model works, the step functions are set to the values shown in table 6.5 and the AC-side energy, currents, and active and reactive power are measured in addition to the DC-side power. The resulting DC-current reference is shown in figure 6.11.

Table 6.5: Step functions to control the DC-current reference of the simplified AVM-MMC

Time [s]	Step from [pu]	Step to [pu]
5	0.50	1.00
7	1.00	- 1.00
12	- 1.00	0.50

The results of this verification are shown in figures 6.12 - 6.14. Figure 6.12 shows the zero sequence energy, the d-axis and q-axis currents, and their references. As shown and described above, the energy controller is turned on at 4 seconds, so that is the reason why the energy is zero before this time. Since everything that happens before 4 seconds is out of interest for the simulation results since that is before the MMC is properly connected, the simulation results provided in chapter 7 will start at 4 seconds. The middle graph shows that the d-axis current follows its reference perfectly once the energy controller is turned on and that is follows the

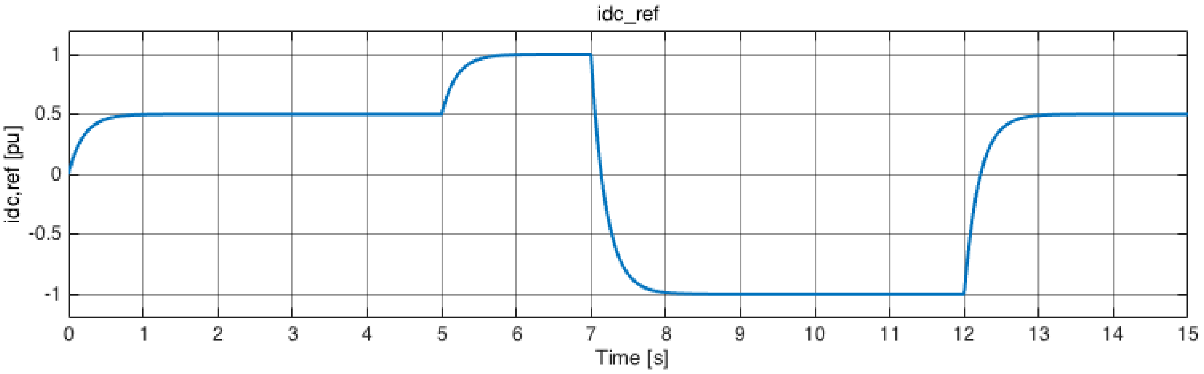

Figure 6.11: Reference current for the slave 2L-VSC current controller of the HVDC system, used to control the power flow on the DC-link

same pattern as the DC-current reference in figure 6.11. The lower graph shows that the q-axis current does not perfectly follow its reference. This indicates that the PI-controller for the q-axis current may not be tuned correctly and it may not respond fast enough. The disturbance term (D in figure 6.9) is added after the the PI-controller has controlled i_q to follow its reference i_q^*, and since the current does not perfectly follow its reference the controller might not be acting fast enough so that this disturbance term impacts the results. However, as seen in the figure, the deviation from the reference is small (only a few percent), so the model will be used the way it is in the simulations in the next chapter. A further discussion regarding the q-axis results in the context of the simulation cases are provided in the discussions in chapter 8.

Figure 6.14 shows the active and reactive power flow of this AVM-MMC. It verifies that the active power of the converter is controlled by controlling the DC-current reference. The reactive power is not constantly zero due to the small deviations from zero in the q-axis current. Figure 6.13 shows that the DC-power follows the same pattern as the AC-side active power and the DC-current reference value, hence it can be concluded that the DC-current reference can be controlled to control the power flow of the simplified AVM-MMC.

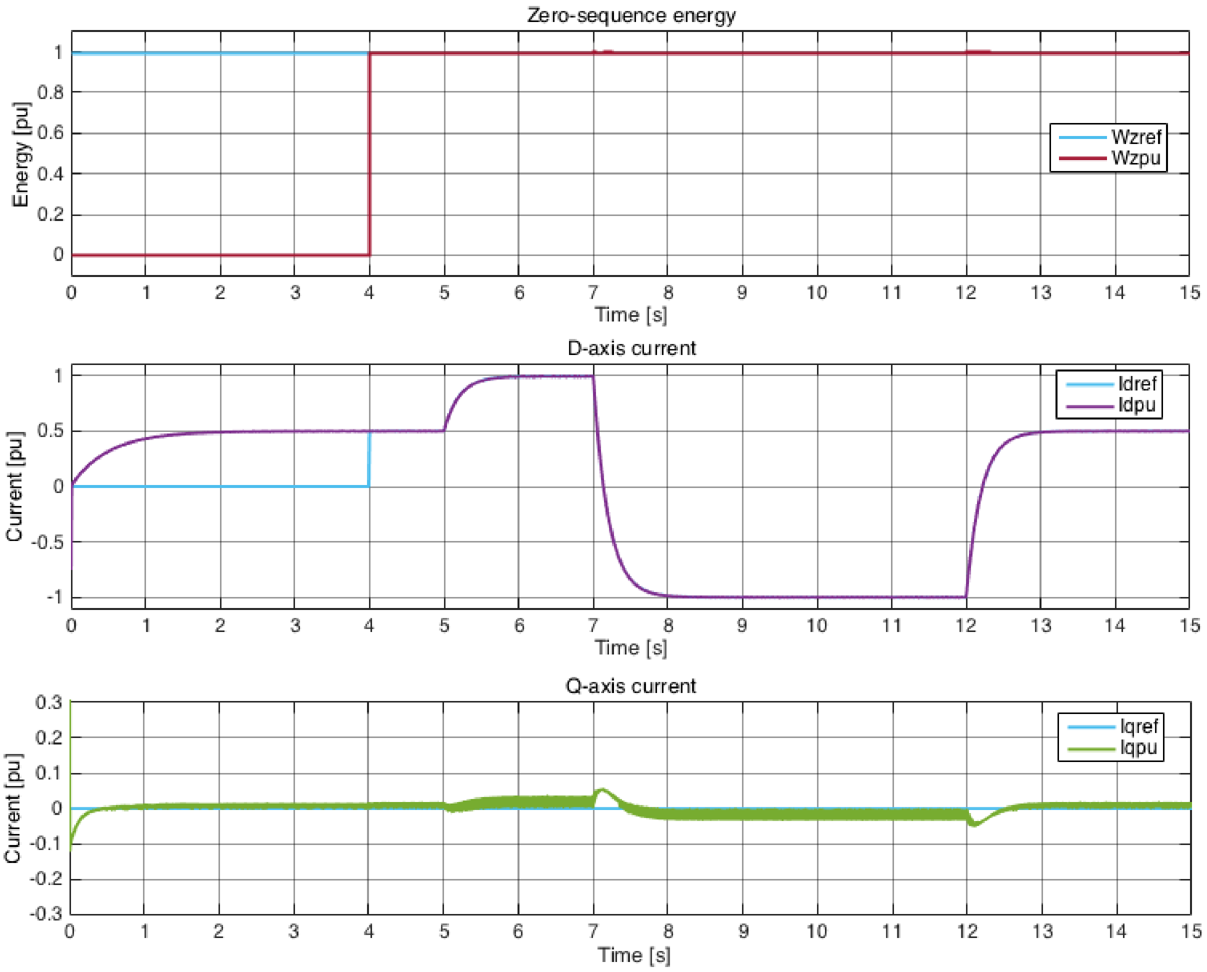

Figure 6.12: Per-unit energy, d-axis and q-axis currents of the stand alone simplified AVM-MMC

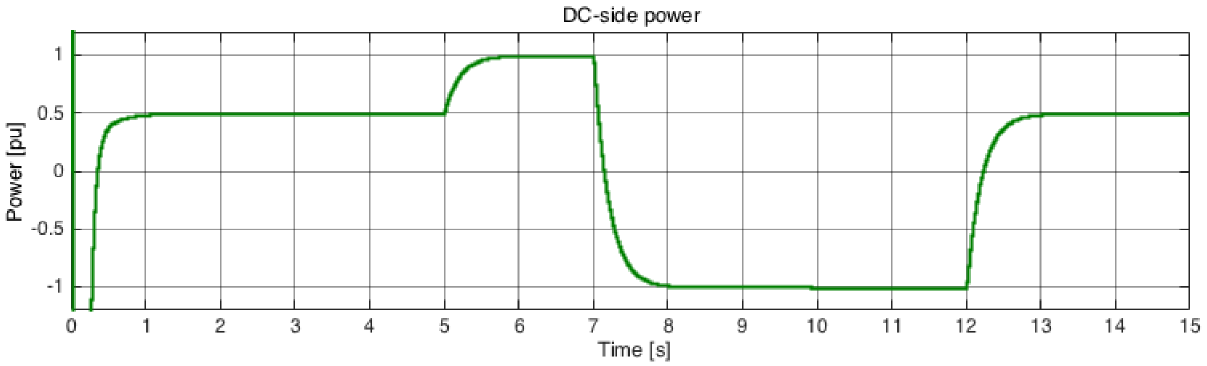

Figure 6.13: Per-unit power at the DC-side of the simplified AVM-MMC

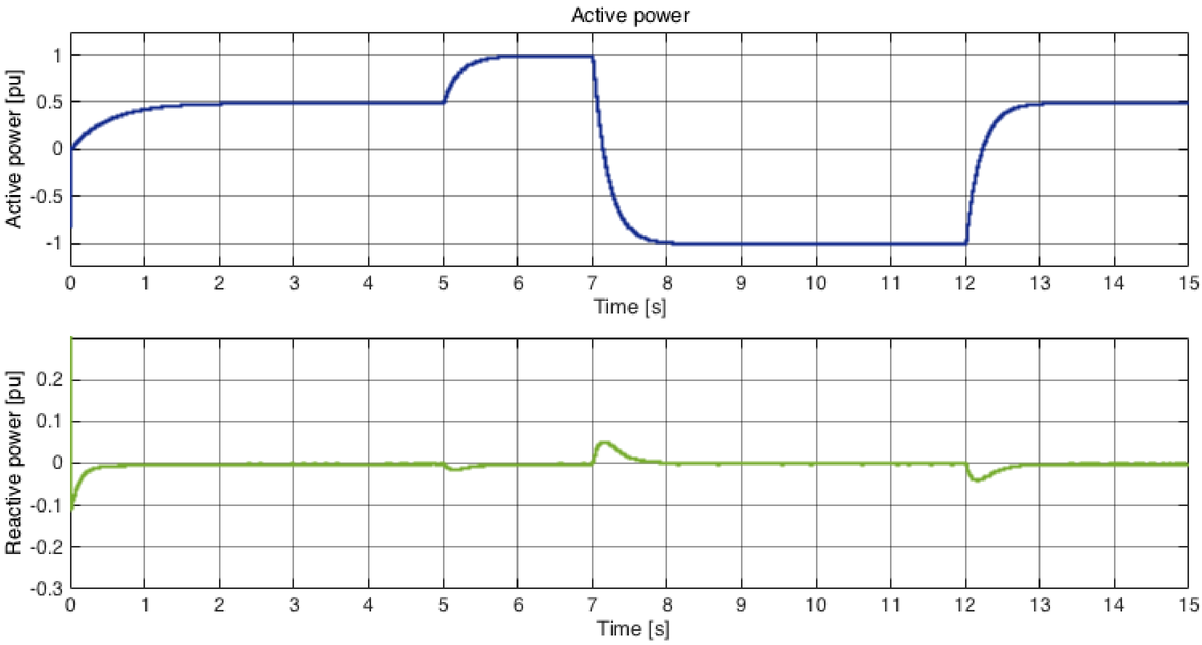

Figure 6.14: Per-unit active and reactive power at the AC-side of the simplified AVM-MMC

6.3 Coupling transformer

The Simulink model of the coupling transformer used in this project is a simplified version of the transformer described in the design part in chapter 5. The simplification includes not modeling the transformer as a medium frequency transformer, but modeling a transformer that operates at 50 Hz. If a medium frequency transformer was to be used, the operating frequency must be changed in the converters that the transformer is coupled between since then the operating frequency of the transformer would be different than the operating frequency of the AC-sides of the HVDC system, which is 50 Hz. For the MMC this would require an extra control loop. Also, since the modeling of the transformer is not the main objective in this thesis, and since the chosen transformer model does not affect the results to a large extent when the case of interest is to study how the battery storage can provide grid support in the system, a simplified transformer model is chosen. A simpler transformer design also leads to less complex simulation models and a faster running models, which is also a motivation to use a simple model of the transformer.

The Simulink model of the transformer is shown in figure D.4 and the MATLAB script used to set the parameters of the model is shown in Appendix C.2. As shown in the figure, the built-in three-phase two winding transformer block in Simulink is used to represent the transformer. The windings are grounded and star-connected (Y), and the parameters used in the simulations are provided in table 6.6. The magnetizing resistance and inductance are set to a high value to avoid core active and reactive losses. The resistance and inductance of the windings are set according to the values discussed in chapter 5. However, the built-in Simulink transformer block has a structure shown in figure 6.15 while the values of R_T and L_T in chapter 5 were based on a model of a transformer with an equivalent impedance. Since the magnetizing resistance and inductance are chosen to be very high, the transformer can be modelled as an ideal transformer with an equal impedance on the primary side which accounts for the losses in the windings, as shown in figure 6.16. Therefore, in the Simulink model, $R_1 = R_T$ and $L_1 = L_T$ while $R_2 = L_2 = 0$.

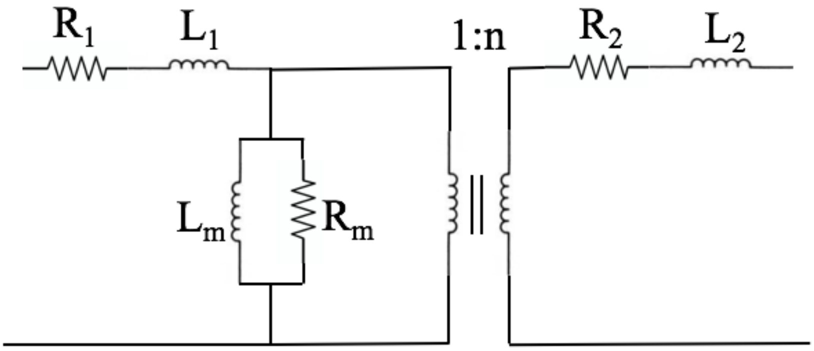

Figure 6.15: Structure of the built-in transformer in the Simulink

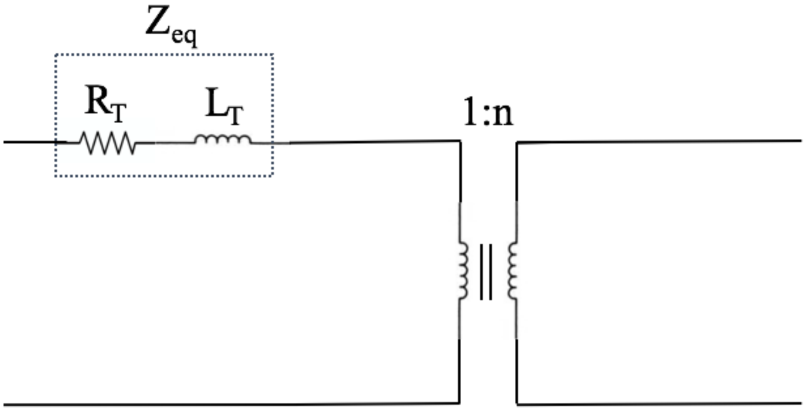

Figure 6.16: Simplified structure of the transformer used in the simulations

When the transformer is modeled as a stand alone model, a three-phase AC source without impedance that is star (Y)-connected to an internally grounded neutral is connected to the primary side of the transformer, while the secondary side is connected to a resistor with value R_{trafo}, as shown in figure D.4. R_{trafo} is calculated using equation (6.29)

$$R_{trafo} = \frac{v_{b,s}^2}{S_b} \tag{6.29}$$

where $v_{b,s}$ is the voltage at the secondary side of the transformer and S_b is the apparent power of the transformer. Since the transformer is connected to a resistive load on this side, the only power flowing on this side is active, and therefore the apparent power only consist of active power. The voltage of the AC source is set to the AC base voltage on the primary side of the transformer and the resistor on the secondary side is included to be able to measure the voltages and currents on the secondary side of the transformer.

Table 6.6: Parameters of the coupling transformer

Parameter	**Value**
Base active power, P_b	180 MW
Power factor, pf	0.95
Base apparent power, S_b	189.47 MVA
AC base phase voltage primary side, $v_{b,p}$	230 kV
AC base phase voltage secondary side, $v_{b,s}$	76.98 kV
Turns ratio, $1 : n$	1:3
Operating frequency, f_t	50 Hz
Resistance, R_T	0.005 pu
Inductance, L_T	0.15 pu
R_{trafo}	32.9281 Ω
Magnetizing resistance	500 pu
Magnetizing inductance	500 pu

6.3.1 Verification of the simulation model of the coupling transformer

To verify the model of the transformer, the model described in the previous subsection is implemented and through the simulation, the voltages and currents on the primary and secondary sides of the transformer are measured and compared. The results are shown in figures 6.17 and 6.18. They show a zoomed in view for a short time interval of the simulation. The amplitude and frequency of the signal are however equal to what is presented here for the whole simulation. Figures 6.19 and 6.20 show the measured active and reactive power at the primary and secondary sides of the transformer.

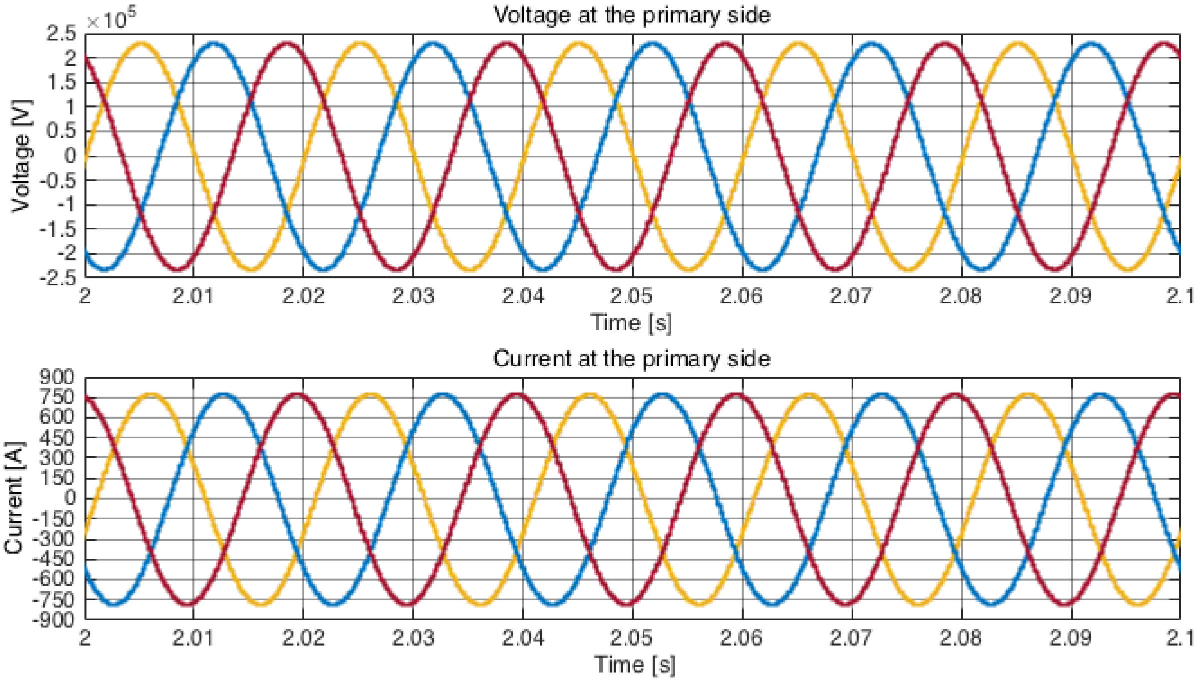

Figure 6.17: Voltage and current waveforms at the primary side of the transformer

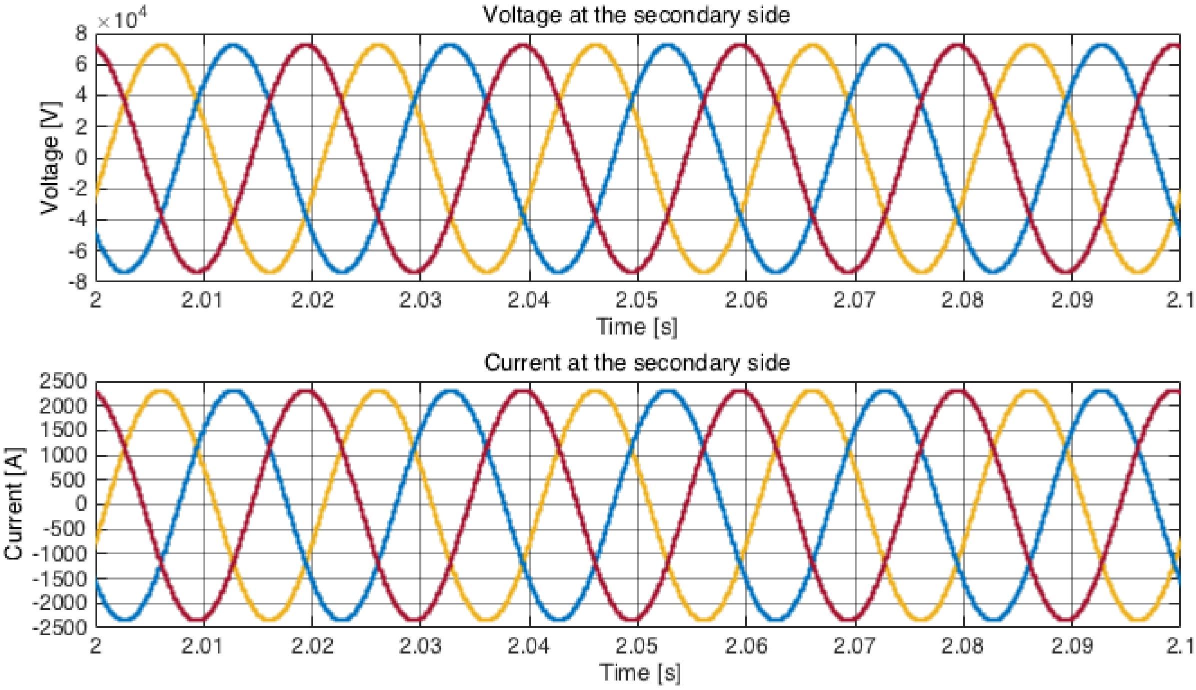

Figure 6.18: Voltage and current waveforms at the secondary side of the transformer

The results show that the voltages are stepped down by approximately $\frac{1}{3}$ from the primary to the secondary side while the current is stepped up with the same amount since the power is constant. Figure 6.20 shows that, as expected, there is only active power flow on the secondary side due to the resistive load. The active power flow at the secondary side is not equal to the active power flow on the primary side since the there is also reactive power flow on that side and also due to the losses in the windings of the transformer.

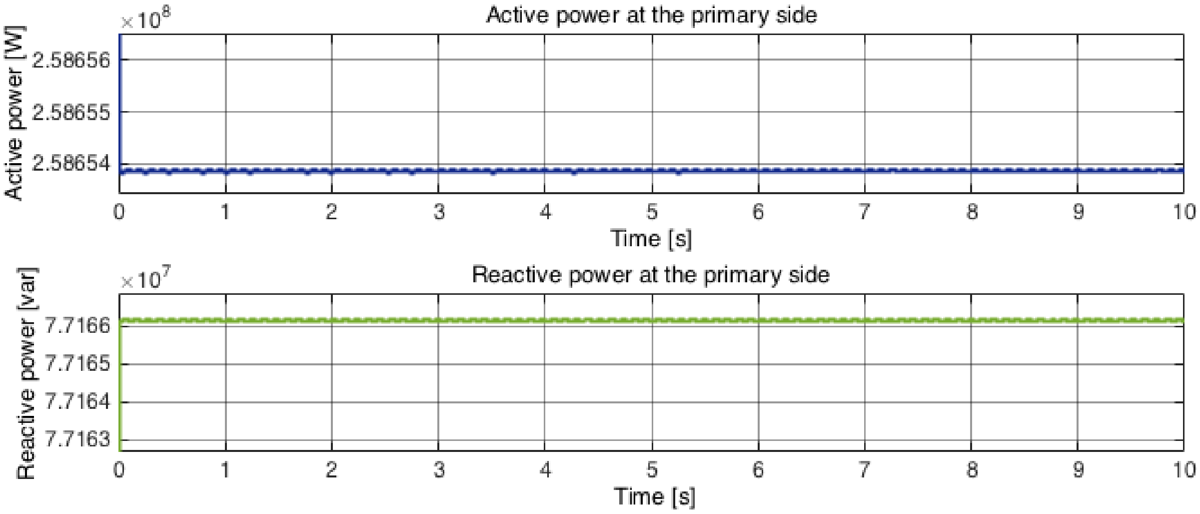

Figure 6.19: Active and reactive power at the primary side of the transformer

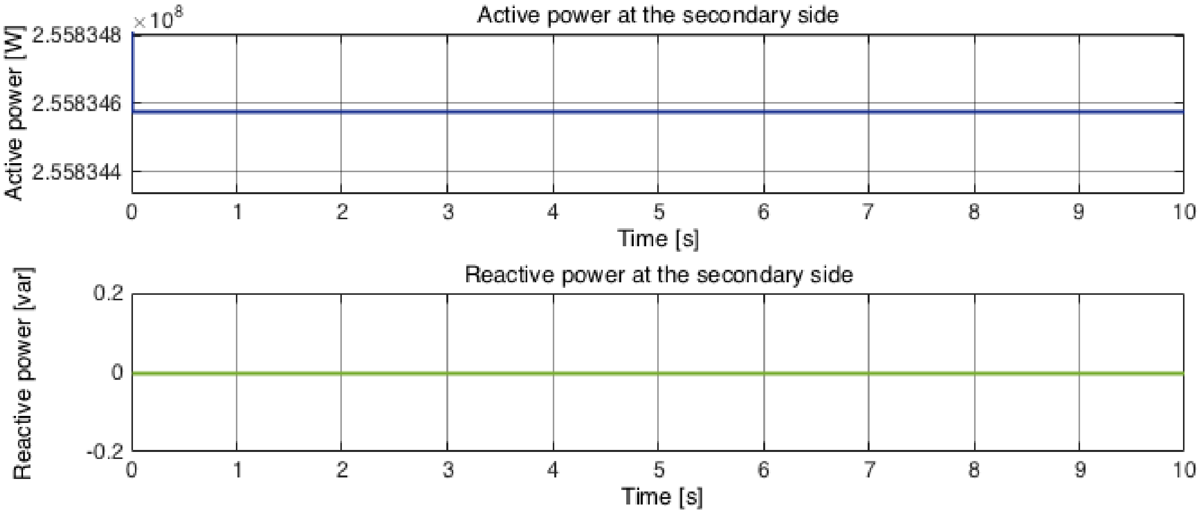

Figure 6.20: Active and reactive power at the secondary side of the transformer

6.4 2L-VSC model

The Simulink model used for the 2L-VSC at the secondary side of the coupling transformer in the DC/DC converter in this project is based on the 2L-VSC used in the HVDC system. The reasons why this model can be used in this project is the same as discussed in the HVDC system modeling part in chapter 6.1. The circuits are identical but the controllers are different. This 2L-VSC is controlled by controlling the AC-side voltage by creating a control signal based on phase shifted sinusoidal waveforms with predefined frequency and amplitude, while the currents and voltages of the 2L-VSCs discussed in subchapter 6.1 are controlled using PI-controllers to create the control signals.

A figure of the 2L-VSC as a stand-alone model is shown in figure D.5. As shown, the DC-side of the converter is connected to a battery which is modeled by a DC voltage source in series with a small resistor. The modeling of the battery is discussed further in subchapter 6.5. The AC-side of the 2L-VSC is connected to a resistor in this stand alone model, and the value of the resistor is given by equation (6.30):

$$R_1 = \frac{v_b^2}{S_b} \tag{6.30}$$

where v_b is the base value of the AC-side voltage and S_b is the base value of the apparent power. This is used for the same reason as described for the transformer in the previous subchapter; with a resistive load on the AC-side, only active power will flow there. The other parameters used in the circuit, R, L and C_{DC} are calculated similarly to the 2L-VSC parameters used in the 2L-VSCs of the HVDC system. The calculation of the parameters are provided in the MATLAB script in Appendix C.2, and the results are shown in table 6.7.

When it comes to control of this converter, it is very simple and it is based on square wave operation of the converter, described in chapter 3.5.2. Since the MMC controls the current, it is desirable to control the voltage of the 2L-VSC to be constant so that the power flow can be controlled by controlling the current. This is done by creating a three-phase signal out of three sinusoidal waves with amplitude of 1, which are 120° phase shifted. The frequency of these signals are set to 50 Hz since it was decided that the transformer operating frequency is set to 50 Hz in the simulations of this project. However, if the transformer was to be operated at a different frequency, it would be set in these signals. The signals are multiplied with a gain, controlling the pu value of AC-side voltage. In this project it is set to 1 since it is desirable to have the voltage constant at 1 pu since then the power flow of the converters can be changed by changing the reference values of the current controllers only. The signals of this controller are shown in figure 6.21 where the lower graph shows the three-phase signal used as the Cmd signal in the universal bridge block. This figure is zoomed in to a small time interval of the simulation to show the waveforms, but the amplitude and waveforms of the signals are equal to this for the whole simulation time.

Table 6.7: Parameters of the 2L-VSC

Parameter	Value
Base active power, P_b	180 MW
Power factor, pf	0.95
Base apparent power, S_b	189.47 MVA
AC base phase voltage, v_b	76.98 kV
Small resistance in series with the battery, R_o	0.001 Ω
Resistance the AC-side, R_1	32.9218 Ω
AC-side resistance, R	0.4691 Ω
AC-side inductance, L	0.0381 H
DC-side capacitance, C_{DC}	0.00047961 F

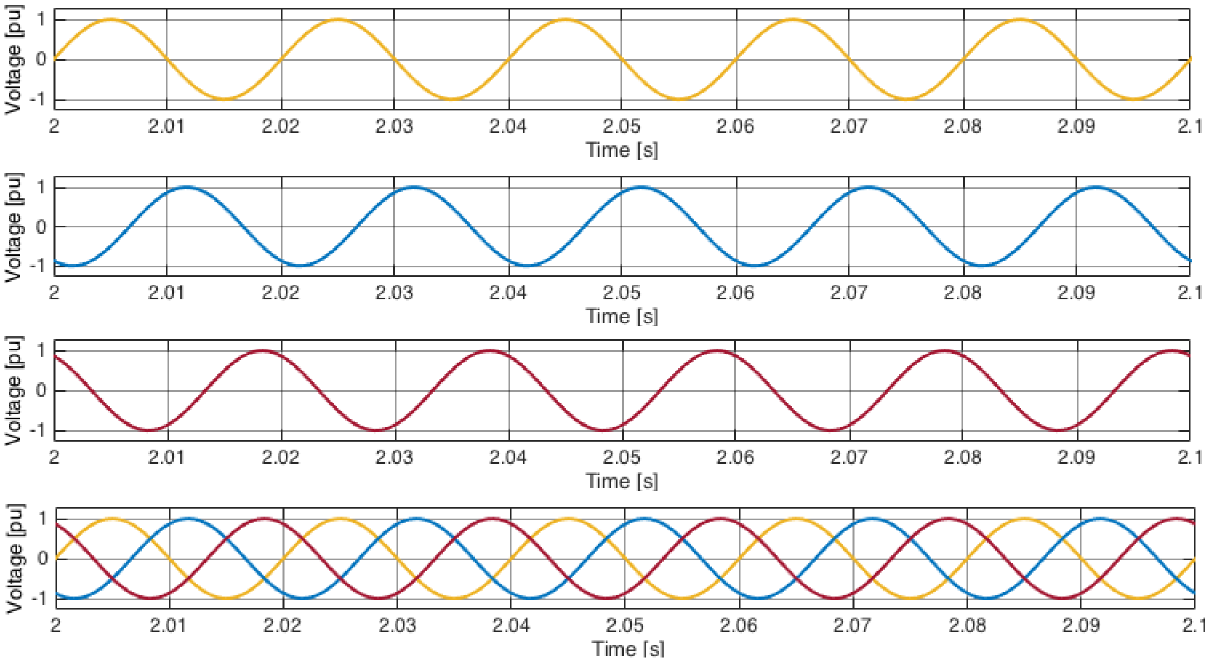

Figure 6.21: Signals to control the AC-voltage in the 2L-VSC

6.5 Battery

The simulation model of the battery is very simplified in this project. It is represented by an ideal DC voltage source in series with a small resistor, as shown in figure D.5 where it is connected to the DC-side of the 2L-VSC. The purpose of the resistor in this case is the same as for the resistor at the DC-side of the MMC model; it is included to make the model run. Also here the value of the resistor is very low in order to not influence the results of the simulation. Due to this simplified model the type of battery chosen for the project is not taken into considerations in the simulations part, and neither is the design of the battery in terms of series and parallel connections of battery modules.

The reason for this very simplified implementation of the battery in the simulation part is the same reason as for the simplifications of the other components of the system; due to the objective of power system related studies and simulation cases regarding the ”bigger picture”. The main objective is not to optimize the battery storage system in terms of efficiency, losses, lifetime, etc., but to show that there can be a bidirectional power flow to/from the battery. In addition, a more complex implementation of the battery would lead to a more complex and slow-running model of the whole system. Therefore a simplified implementation of the battery is chosen in order to keep the simulations as simple as possible whilst still having simulations that represents the system and that does not affect the results.

The parameters used for the battery model in the simulations are provided in table 6.8.

Table 6.8: Battery parameters

Parameter	Value
Power rating	180 MW
Battery voltage	108.87 kV
Battery current	1653 A
Resistance in series with the ideal DC voltage source	0.001 Ω

In order to make a model of the battery and run simulations to show that it can be charged and discharged, the state of charge (SOC) of the battery is an important parameter to consider. The SOC gives information about the quantity of energy stored in the battery at a given time [116]. When it is 100 %, the battery is fully charged and when it is 0 %, the battery is fully discharged. In [117] the SOC is defined as

$$SOC = 100(1 + \frac{\int i_b dt}{Q}) \tag{6.31}$$

where i_b is the battery charging current and Q is the battery capacity in ampere hours [Ah].

As discussed in chapter 5, not much information regarding the battery current of the EssPro^{TM} Grid modules are provided in the brochure. However, as also discussed in chapter 5, the battery capacity in terms of power is 180 MW and the discharge time is 15 minutes for this project. Hence, the an SOC equation based on power and energy instead of current and capacity in [Ah] has been deduced based on [117], to be used for the battery modeling in this project. The SOC is implemented on a per unit basis, as shown in figure D.5 so that the SOC can be plotted in the same graph as the voltage, current and power at the DC-side of the 2L-VSC for easy comparisons. The pu-modeling also simplifies the model. Equation (6.31) based on power and energy in per unit becomes:

$$SOC = 100(1 + \frac{\int P_{pu} dt}{Q_{pu}}) \tag{6.32}$$

Where Q_{pu} is the per unit energy capacity of the battery:

$$Q_{pu} = \frac{Q}{Q_{base}} = \frac{E}{E_{base}} \tag{6.33}$$

where E and E_{base} are defined as

$$E = P_{base} \cdot \frac{0.25}{60} \cdot 3600 \tag{6.34}$$

$$E_{base} = P_{base} \cdot w_{base} \tag{6.35}$$

where P_{base} is the base power of the battery and w_{base} is the base rotational frequency which is the base value for time in this model. In the simulation part of this project the base power is set to 180 MW, as shown in the script used for calculating the parameters used for the simulation models in this project, which is provided in Appendix C.2. The multiplication by 3600 in equation (6.34) is to get the capacity in [Ws] instead of [Wh] since dt in equation (6.34) is defined for seconds and not hours. In addition it is multiplied by $\frac{0.25}{60}$ and this is to scale the model to the simulation time. The model was defined to have a discharge time of 15 minutes, but the simulation time is only for 15 seconds (i.e 0.25 minutes or $\frac{0.25}{60}$ hours).

The SOC model is implemented at the DC-side of the 2L-VSC as shown in figure D.5 and the parameters required to run this model are calculated based on the equations discussed above and they are included in the script provided in Appendix C.2. As shown in the figure, the voltage and current at the DC-side are measured and converted into pu-values before they are multiplied in order to get the pu-value of the DC-side power. This power is then integrated according to equation (6.32) and multiplied with the gain as shown in the figure. Next a constant of 1 is added and the sum is multiplied by a gain of 100, indicating that the assumed battery SOC at the beginning of the simulation is 100 %, i.e the battery is fully charged. A verification of the 2L-VSC with the battery and the SOC model are provided in the next subsection.

6.5.1 Verification of the 2L-VSC and battery system

To verify this model the models described in the two previous subchapters are implemented and connected, and through the simulation the AC-side and DC-side currents and voltages are measured and compared. In addition, the power is measured at each side of the converter. For the DC-side also the SOC of the battery is measured and plotted. Figure 6.22 shows the per unit DC-side results of the whole simulation time while figure 6.23 shows the per unit AC-side results zoomed in at a small time interval to show the waveforms properly.

The results show that the DC-side voltage is constant at 1 pu, while the DC-side current has a negative pu-value with absolute value of more than 1. This shows that the current is flowing from the DC-side to the AC-side of the converter, and that the resistive load at the AC-side consumes more than the full current capability of the converter. By zooming in at the results it can be found that the AC-side current has a peak value of 1.383 pu while the DC-side current has an absolute value of 1.294 pu. Equation (6.19) describes the ratio between DC-side base current and AC-side base current, and it is $\frac{3}{4} = 0.75$. By comparing the values of the AC- and DC-currents described above, it is found that the ratio is $\frac{1.294}{1.383} = 0.9356$. The reason for the deviation is losses, which are described further in the next section.

As expected, the AC-side reactive power is 0 since a resitive load is connected. Comparing the active power of the AC-side to the power of the DC-side it can be seen that they are not equal. This is due to the losses in the filter resistor of the converter, R. Also the resistor connected in series will affect the results and provide some losses, but this resistance was chosen low in order not to influence the results to a large extent. In addition, the filter is required in the AC-side of the 2L-VSC in order to smooth the current and its values are based on the Cigre test grid, and hence it is assumed that the losses explained in this section can be reasonable to have for this converter. This model will be used further as a part of the final model of the whole system.

The results also shows that this converter converts AC quantities into DC, and vice versa, which is the purpose of this converter since it is included to connect the battery, which operates at DC, to a three-phase transformer, operating at AC. Hence, it can be concluded that the operation

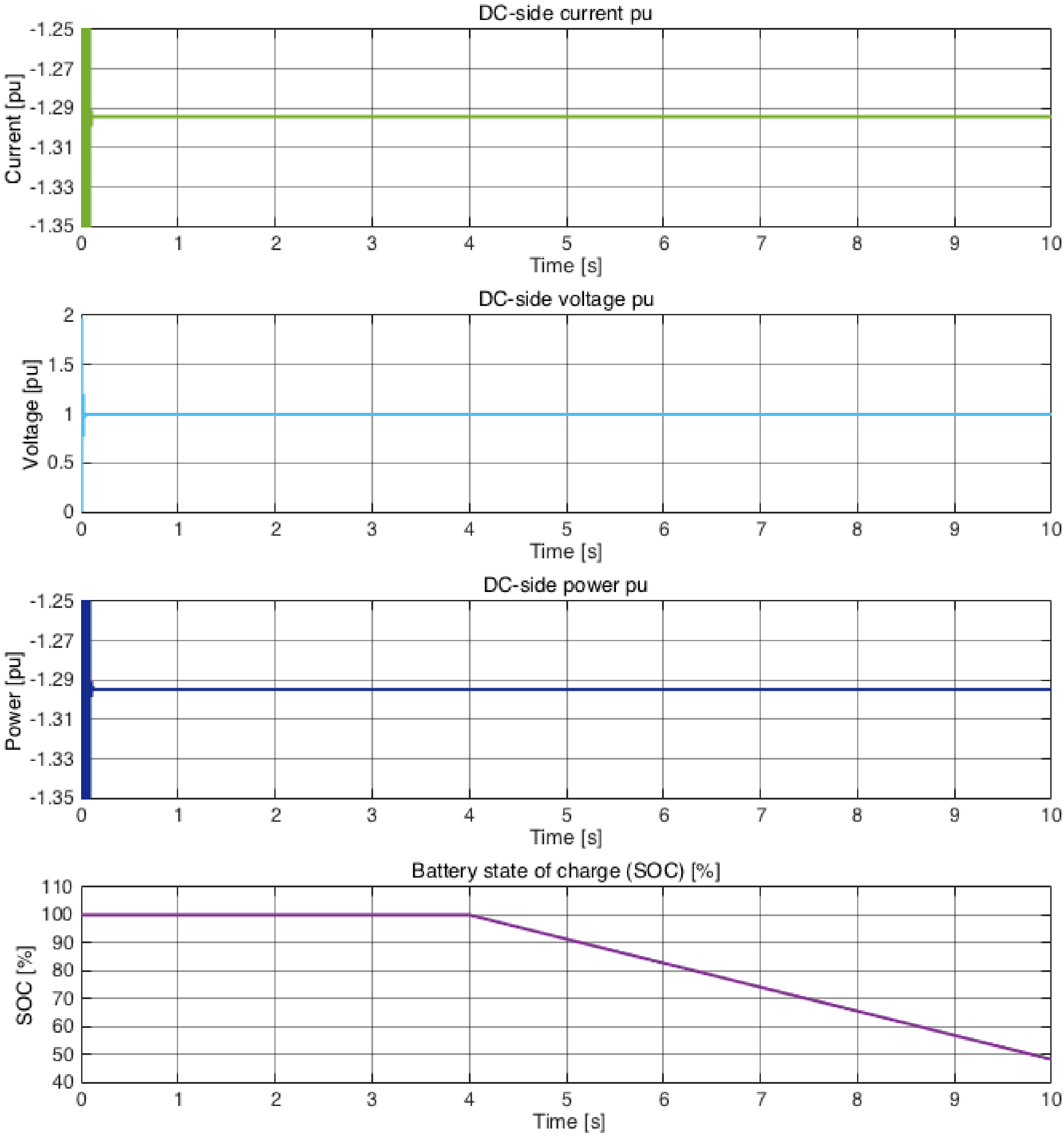

Figure 6.22: DC-side current, voltage, power and battery SOC of the stand-alone model of the 2L-VSC and the battery

of this converter is verified and that this converter works.

6.6 The final system

In the final system used for the simulation cases in this project the different parts of the system are connected. The Simulink model of the final system is shown in figure D.6 in Appendix C, and a closer look at the different parts of the system are shown in the following figures in the same Appendix. The MATLAB script used to calculate the parameters of the Simulink model

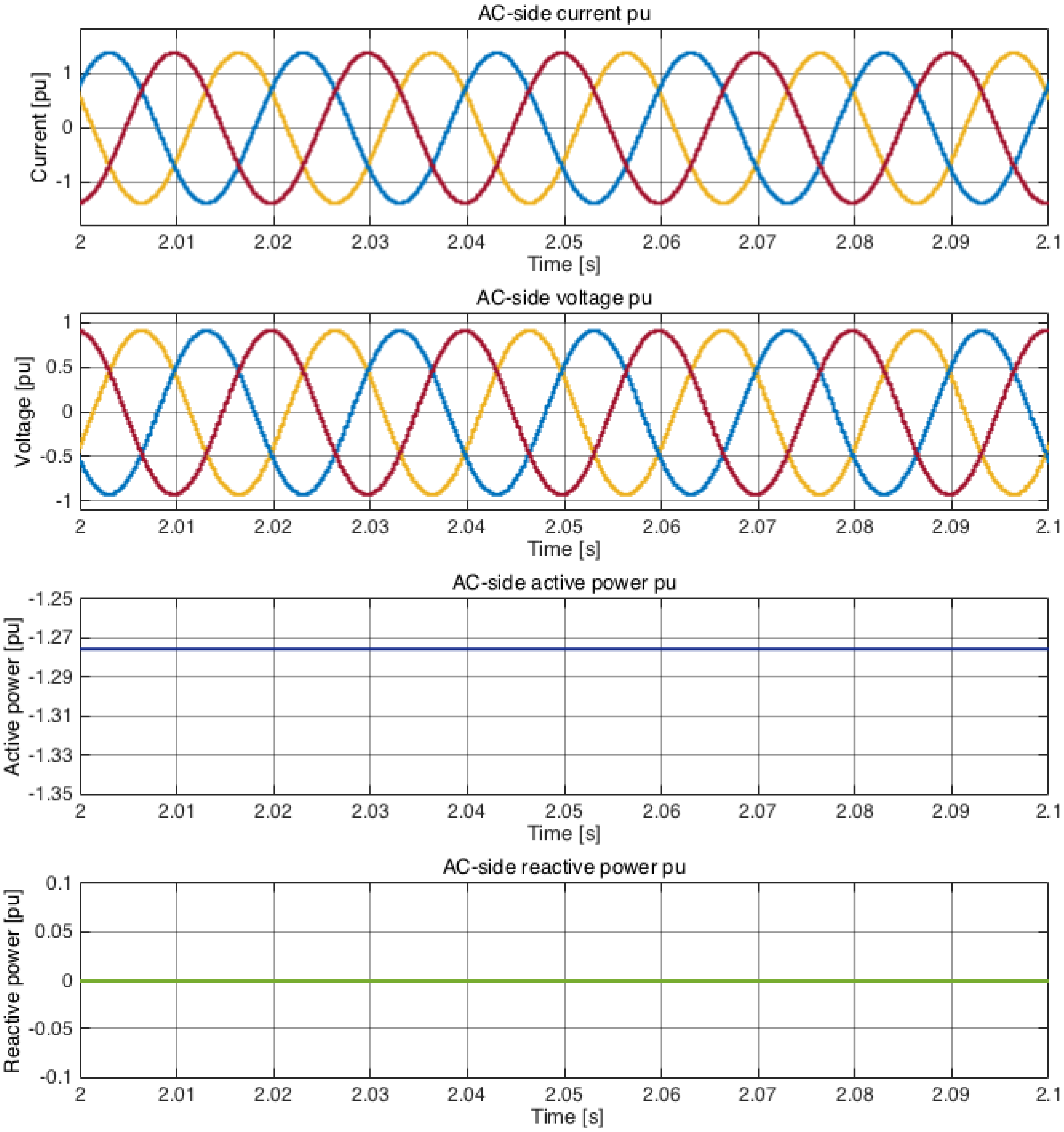

Figure 6.23: AC-side current, voltage, active and reactive power of the stand-alone model of the 2L-VSC and the battery

is provided in Appendix C.2. The HVDC system has the same model as described in 6.1. At the DC-side of the MMC, the DC voltage source in series with the small resistors is removed and the DC-side is connected to the DC-link of the HVDC system though a line PI model as shown in figure D.6. The parameters of the PI line model are calculated in the MATLAB script in Appendix C.2. At the AC-side of the MMC, the AC source is removed and a large resistor is connect in parallel to ground as shown in figure D.15. This is because the primary side of the transformer, which is grounded, is connected to the AC-side of the MMC and the resistor is included to make sure that all currents are flowing through the transformer (and not to ground). When connecting the transformer, the AC source at the primary side is removed and it is directly connected to the AC-side of the MMC. At the secondary side of the transformer the resistor is removed and the secondary side of the transformer is directly connected to the AC-side of the 2L-VSC, as shown in figure D.21. At the AC-side of the 2L-VSC the resistor is removed so that the AC-side is directly connected to the secondary side of the transformer, as shown in figure D.22. The DC-side of the 2L-VSC remains the same as it was in chapter 6.5; connected to the battery, consisting of a DC voltage source in series with a resistor.

Chapter 7

Simulations and results

7.1 Simulation cases

The test cases that the simulations are based on are described in this subchapter.

7.1.1 Case 1: Charging and discharging of the battery

The first case is to simulate that the battery can be charged and discharged. This is an important aspect to verify in this project since the purpose of the integration of battery storage in the system is that the battery can charge and discharge in order to support and stabilize the grid. This is done by verifying that the DC/DC converter connecting the battery to the DC-link of the HVDC system can provide bidirectional power flow so that the battery can charge and discharge, depending on the SOC. The charging and discharging of the battery can be verified by measuring the SOC of the battery. The SOC is modeled in the same way as for the 2L-VSC connected to the battery in chapter 6, so it is assumed that the battery is fully charged in the start of the simulation.

In this simulation case the Simulink system in figure D.23 is used, consisting of the MMC, the coupling transformer, the 2L-VSC and the battery. It is the same as the system in figure D.6 but the DC-side of the MMC is disconnected from the PI line model and connected to an ideal DC-voltage source in series with a resistor. The resistor is included to make the model run, for the same reason as described in the case of the stand-alone MMC model in chapter 6.2.4. The parameters used when running this simulation model are calculated using the script provided in Appendix C.2.

The charging and discharging of the battery is controlled by controlling the current of the DC/DC converter. This is done using the current controller of the MMC by defining the step functions that create $i_{dc,ref}$ in the DC current controller in the MMC as shown in figure D.14. The current direction of the MMC is defined such that positive DC-current signals indicate current flowing from the DC- to the AC-side of the MMC. The AC-side of the MMC is connected to the transformer, which is further connected to the 2L-VSC and the battery, so a current flow in this direction indicates that the current is flowing in the direction of the battery so that the battery can charge, depending in the SOC. In the same manner, a negative DC-current reference signal indicates that the current is flowing from the AC- to the DC-side, so that the battery can discharge, depending on the SOC.

As explained in chapter 6.2.4, the controllers of the MMC depend on each other and the output of one controller is the input to another. The only controller that have reference values that are set externally is the current controller described above. However, in this system there is also a controller of the 2L-VSC which is controlled externally and that is the voltage controller. It is described in chapter 6.4, and also for this test case the gain of the signals used to control the voltage, as shown in figure D.22, is set to 1. This indicates, as described before, that the modulation index is set to 1, indicating the the AC-side voltage is controlled to its maximum value.

Since the SOC of the battery is assumed to be 100 % at the start of the simulation, the step functions used to create the reference signal for this case are chosen so that the resulting signal will be negative first, so that the battery can discharge, and later the reference signal becomes positive so that the battery can charge. The step functions used to control the current in this test case are described in table 7.1. As described earlier, the step functions are added and a transfer function is used to create the resulting current reference signal, which is shown in figure 7.1.

Table 7.1: Step functions to control the current in case 1

Time [s]	Step from [pu]	Step to [pu]
5	0.00	-1.00
9	-1.00	1.00
13	1.00	-0.50

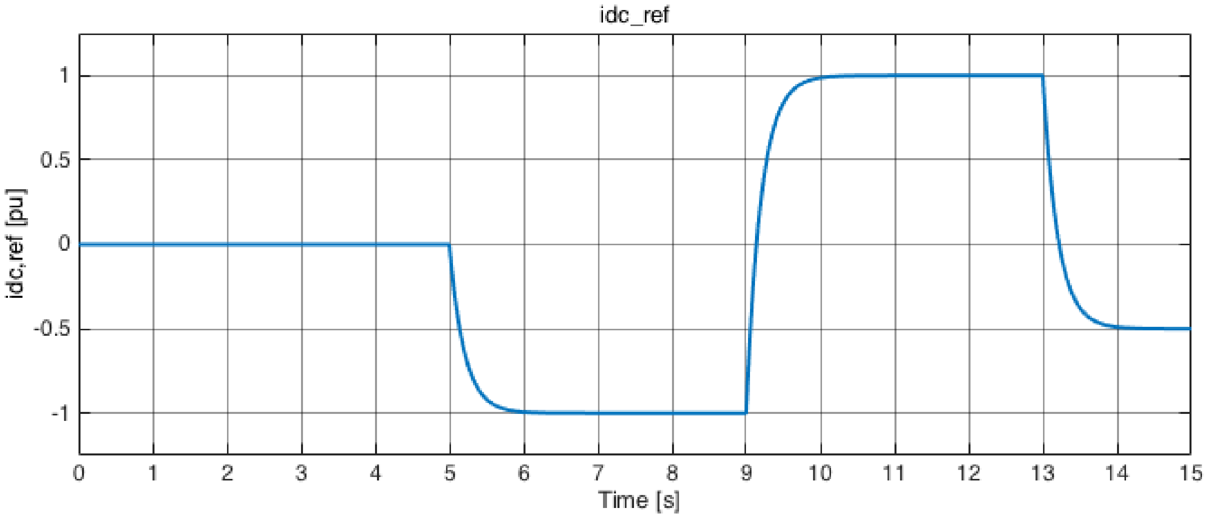

Figure 7.1: Reference current for the MMC DC-current controller, used to control the current of the DC/DC converter

As shown in figure 7.1 the current reference is initially set to 0 pu, which indicates that no current flows in the converters or battery to start with. At 5 seconds the DC-current of the MMC is controlled to -1 pu, indicating that the maximum possible current that the converters can tolerate is flowing in the direction from the battery towards the MMC. Depending on the SOC of the battery, the battery can discharge in the time interval between 5 and 9 seconds where the DC-current reference has this value. At 9 seconds the current reference is reversed to 1 pu, indicating that the maximum current is flowing in the opposite direction. In this time interval between 9 and 13 seconds, when the DC-current reference has this value, the battery can charge depending on its SOC. As shown by the reference in figure 7.1, this test case can be used to verify bidirectional power flow on the converters, and by considering the battery SOC, the ability of the battery to charge and discharge can also be verified.

The results of the simulation of this test case are provided in subsection 7.2.1.

7.1.2 Case 2: Battery providing grid support when the wind farm generation changes

In this case the model of the whole system, which is shown in figure D.6, is used in the simulation. The purpose of this simulation case is to verify that the battery can provide grid support and stabilize the grid during variable power generation due to implementation of large scale offshore wind power into the grid. Again, this is an important case to verify since the purpose of the battery storage integration in this project is to support and stabilize the grid.

It is assumed that the consumption onshore is constant, so in order to provide constant power flow to the grid onshore the battery must charge during times when the wind power generation is increased above a predefined level, and it must discharge during times when the wind power generation is decreased below the same level. Since the power capacity of the battery is set to be 18 % of the wind farm power capacity, it is assumed that the chosen level of constant power flow that must be supplied to the onshore grid is 82 %. This means that if the wind farm power output is higher than 82 %, the battery must be controlled to charge and draw an amount of $P_{windfarm,output} - 0.82$ from the DC-link. Hence, the maximum charging case is when the wind farm produces 100 % of its capacity because then the battery must draw 18 % of the power in the DC-link, i.e. the full capacity of the battery, in order to decrease the power delivered to the onshore grid to 0.82 pu. In the opposite case the wind farm produces less than 82 % of its capacity and then the battery must supply the remaining power to the DC-link in order to have a power flow of 0.82 pu delivered to the grid onshore.

The power flow in the HVDC-link is controlled by the controllers in the slave and master 2L-VSCs. As described in chapter 6.1, the power flow is controlled by controlling the current. The current controller at the slave 2L-VSC of the HVDC system is used to control the wind farm production. As also described in chapter 6.1, the q-axis current is controlled to follow its reference of 0 pu, while the d-axis current is controlled to follow its reference signal which is set by three step functions. Since the level of constant power to be supplied to the onshore grid is 0.82, the initial value of the step functions are set to 0.82, and when the step functions increase or decrease the current above or below this level, the power flow on the DC-link will increase or decrease. In the slave and master 2L-VSCs the current direction is defined such that a positive DC-current indicates current flowing from the DC-side of the converter to the AC-side of the converter. Hence a positive DC current at the slave converter indicates power flow from the wind farm to the DC-link, and a negative DC current at the master converter indicates that the power flows from the DC-link to the AC-grid onshore. Therefore, the step functions at the slave converter are controlled so that the power flow will always be in the direction of the DC-link since it is not of interest to look at the power flow in the opposite direction in this project. The step functions used to control the current in the DC-link are presented in table 7.2 and the resulting reference current is shown in figure 7.2

Table 7.2: Step functions to control the current in the DC-link in case 2

Time [s]	Step from [pu]	Step to [pu]
7	0.82	0.72
10	0.72	0.82
13	0.82	0.92

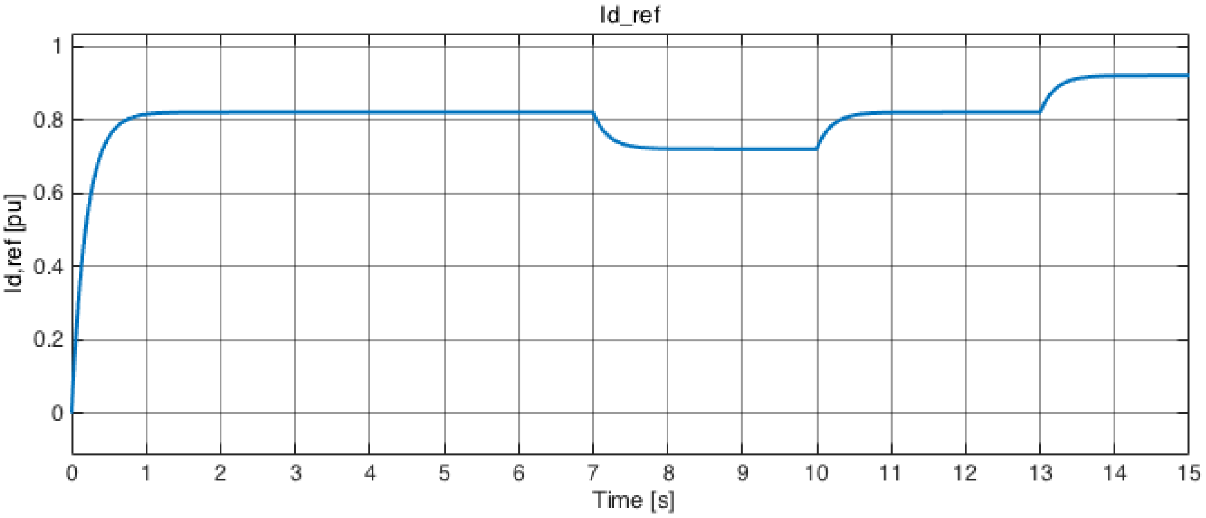

Figure 7.2: Reference current for the HVDC slave 2L-VSC current controller, used to control the power flow on the DC-link

Looking at figure 7.2 it is clear that the battery must discharge in the time interval between 7 and 10 seconds, and that it must charge between 13 and 15 seconds, in order to have a constant power flow of 0.82 pu delivered to the onshore AC grid. As described in case 1, the DC-current controller of the MMC is used to control the power flow of the converters and the battery connected to the HVDC-link. Since the current direction of the MMC is defined such that a positive $i_{dc,ref}$ indicates current flowing in the direction towards the battery, depending on the SOC of the battery, the battery can charge if $i_{dc,ref}$ is controlled to a positive value. In the same manner, depending on the SOC of the battery, it can discharge when $i_{dc,ref}$ is controlled to a negative value. As discussed, the battery must charge or discharge the remaining power that is required to be drawn or supplied to the DC-link in order for the system to constantly supply 0.82 pu of power to the onshore grid. Since the HVDC-system and MMC are based on different pu-systems, $i_{dc,ref}$ is multiplied with a gain of $\frac{Idcbase}{i_{dcb}}$, where $Idcbase$ is the base value of DC-current in the HVDC system and i_{dcb} is the base value of the DC-current in the MMC, so that the current of the MMC is controlled according to pu-system of the HVDC system. This is done because the resulting power delivered to the onshore grid is measured in the master 2L-VSC, and therefore it is important to control the currents based on the HVDC pu-system values. The step functions multiplied by this gain, used to control the current in the MMC are presented in table 7.3 and the resulting reference current after the transfer function is included, is shown in figure 7.3.

Table 7.3: Step functions to control the current in the battery in case 2

Time [s]	Step from [pu]	Step to [pu]
7	0.00	- 0.56
10	- 0.56	0.00
13	0.00	0.56

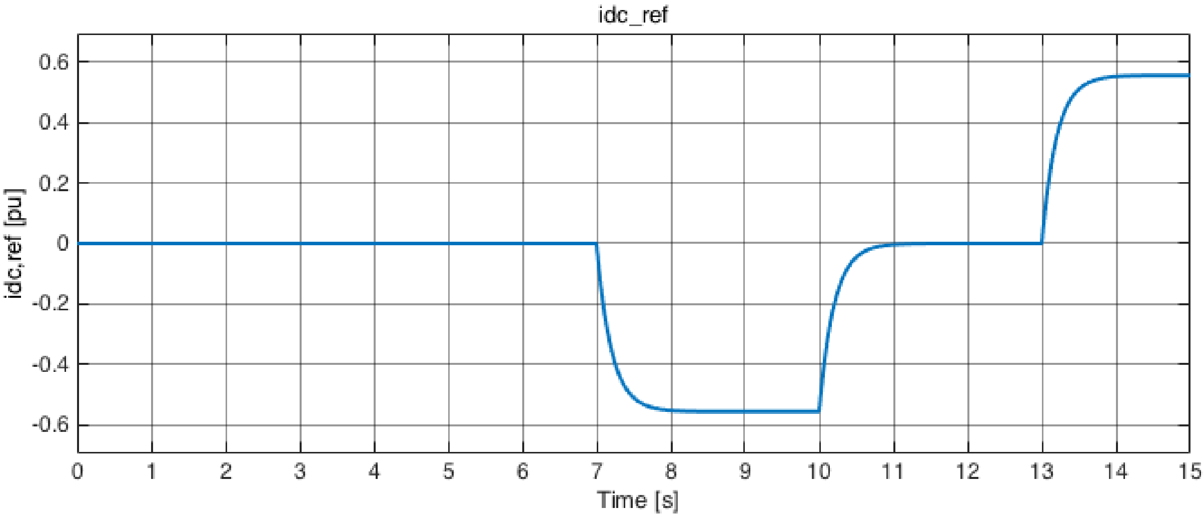

Figure 7.3: Reference current for the MMC current controller, used to control the power flow to the battery

Using this current reference as the DC-side current reference in the MMC, the battery is expected to discharge in the time interval between 7 and 10 seconds, charge between 13 and 15 seconds, and no current is supposed to flow to or from the battery during the remaining time intervals of this simulation. The simulation results are provided in subsection 7.2.2.

7.2 Results

This subchapter provides the results of the simulations. Discussions of these results are provided in chapter 8.2.

7.2.1 Results of case 1

Figure 7.4 shows the output at the scope on the DC-side of the 2L-VSC of simulation case 1. It shows the pu-values of the power, current and voltage at the DC-side of the 2L-VSC in addition to the SOC of the battery.

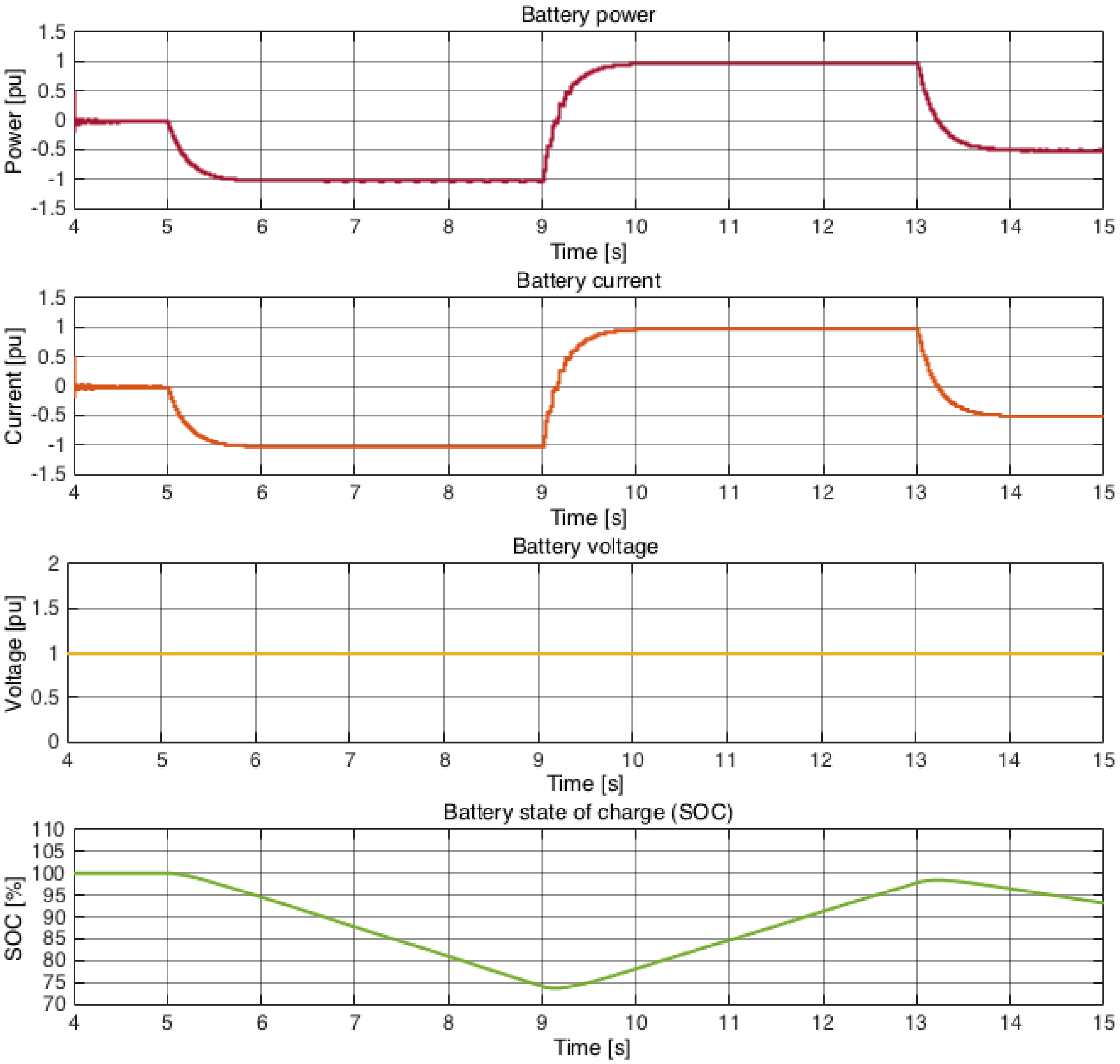

Figure 7.4: Results of case 1: Measurements at the battery side of the DC/DC converter

Figure 7.5 shows the outputs at the AC- and DC-sides of the MMC for case 1. It shows the pu-values of the zero-sequence energy, d-axis current, q-axis current and the DC-side current.

These parameters are plotted in the same graph as their reference value, shown as by light blue legends in the figure.

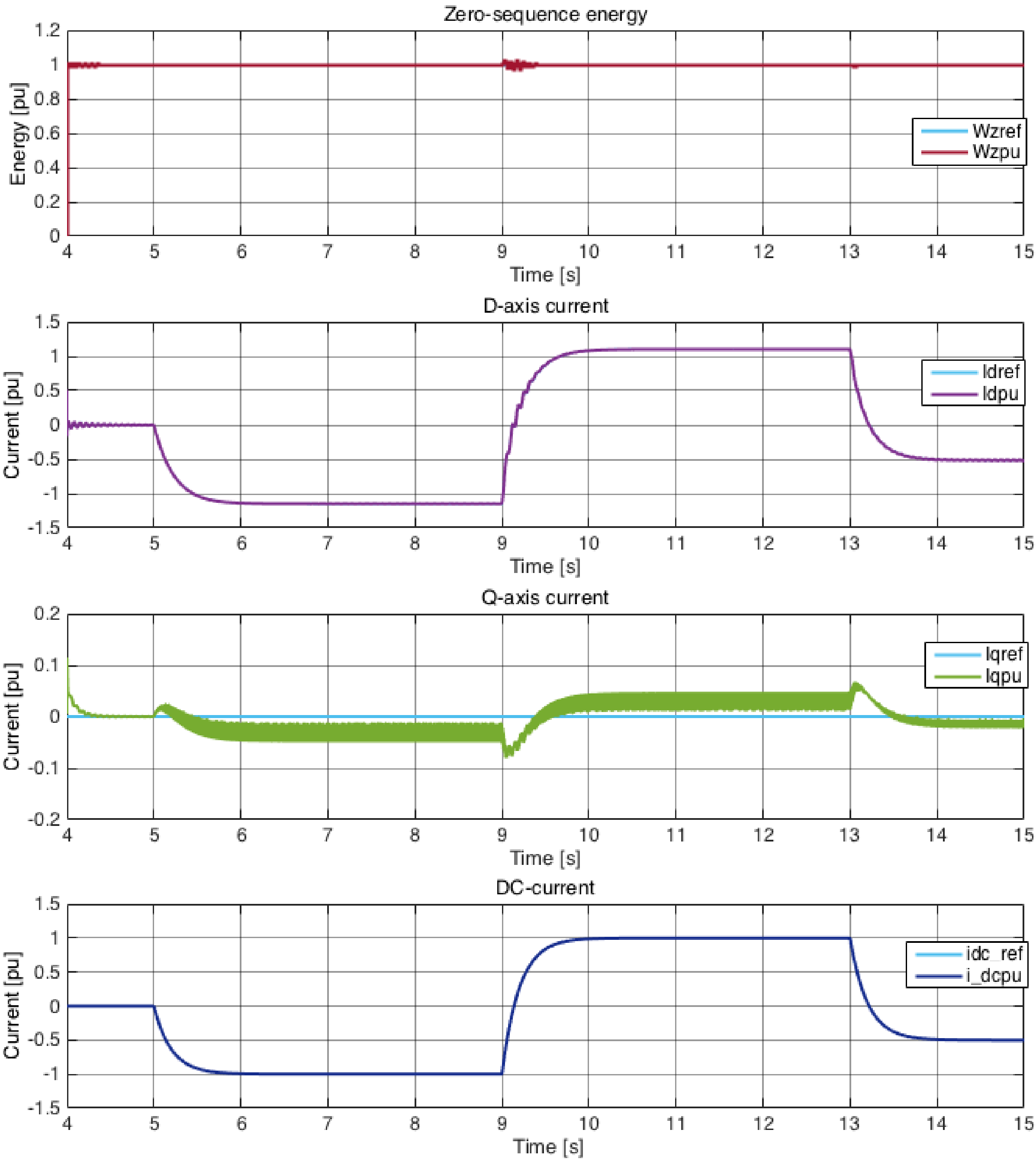

Figure 7.5: Results of case 1: Measurements of the MMC

7.2.2 Results of case 2

Figures 7.6 and 7.7 show the results of this simulation case.

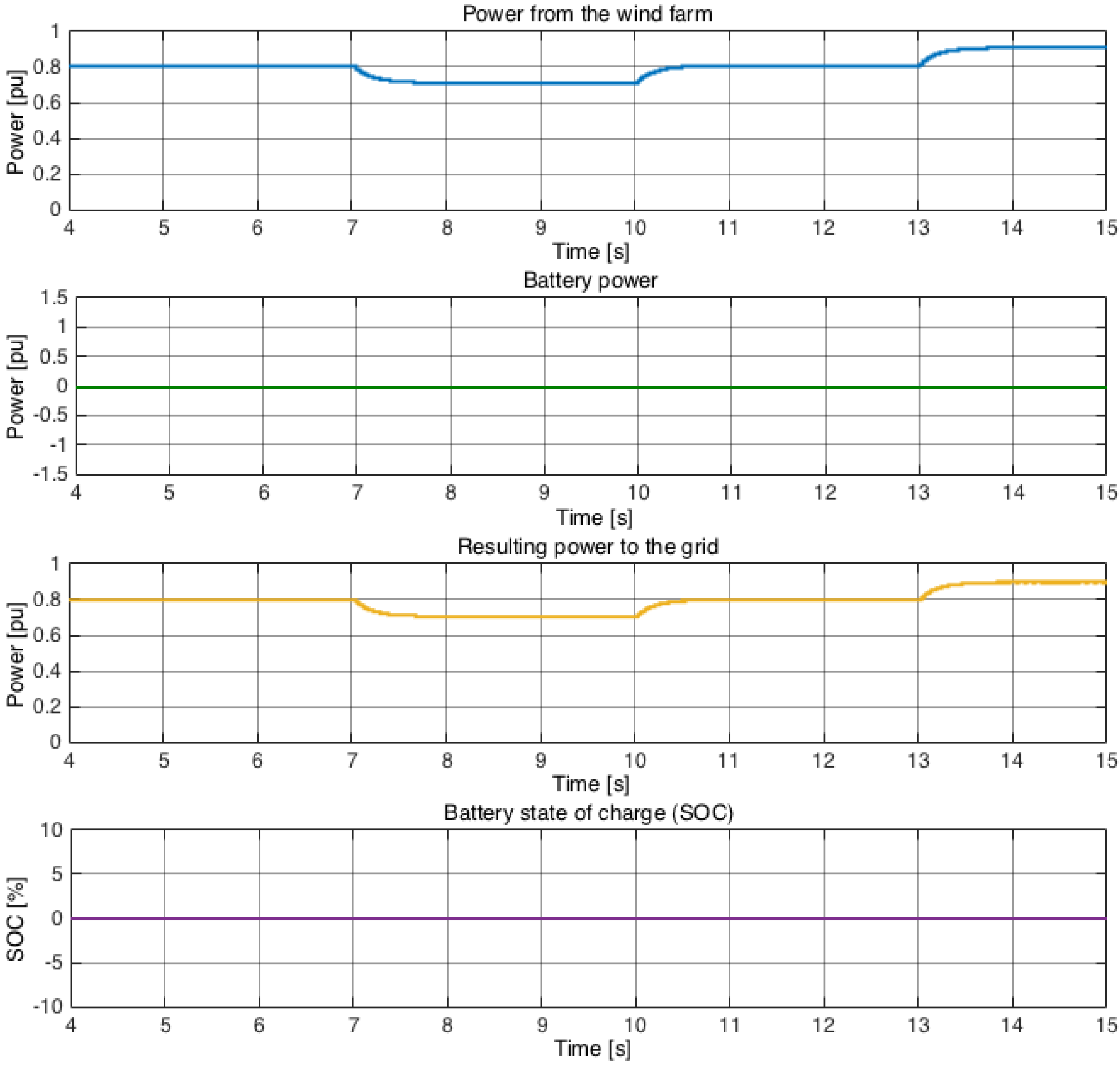

Figure 7.6: Results of case 2 without connection of the battery storage system

In both figures the upper graph shows the power output to the DC-link from the wind farm, the graph below this shows the power flow of the battery which is measured at the DC-side of the 2L-VSC, the graph below this again shows the resulting power delivered to the grid onshore, and the lower graph shows the SOC of the battery, measured at the DC-side of the master 2L-VSC of the HVDC system.

To create the two middle graphs a gain of -1 has been included to make them positive, since normally power delivered to the onshore grid would be negative due to the definition of the current direction of the two 2L-VSC converters used in the HVDC system, and the battery power would normally be positive when the battery is charging and negative when the battery is discharging, due to the definition of the current direction in the MMC. They are reversed so that the results can be more easily understood. Figure 7.6 shows the results of the simulation when the battery is disconnected from the HVDC-link, while figure 7.7 shows the results when the battery is connected and helps stabilizing the grid.

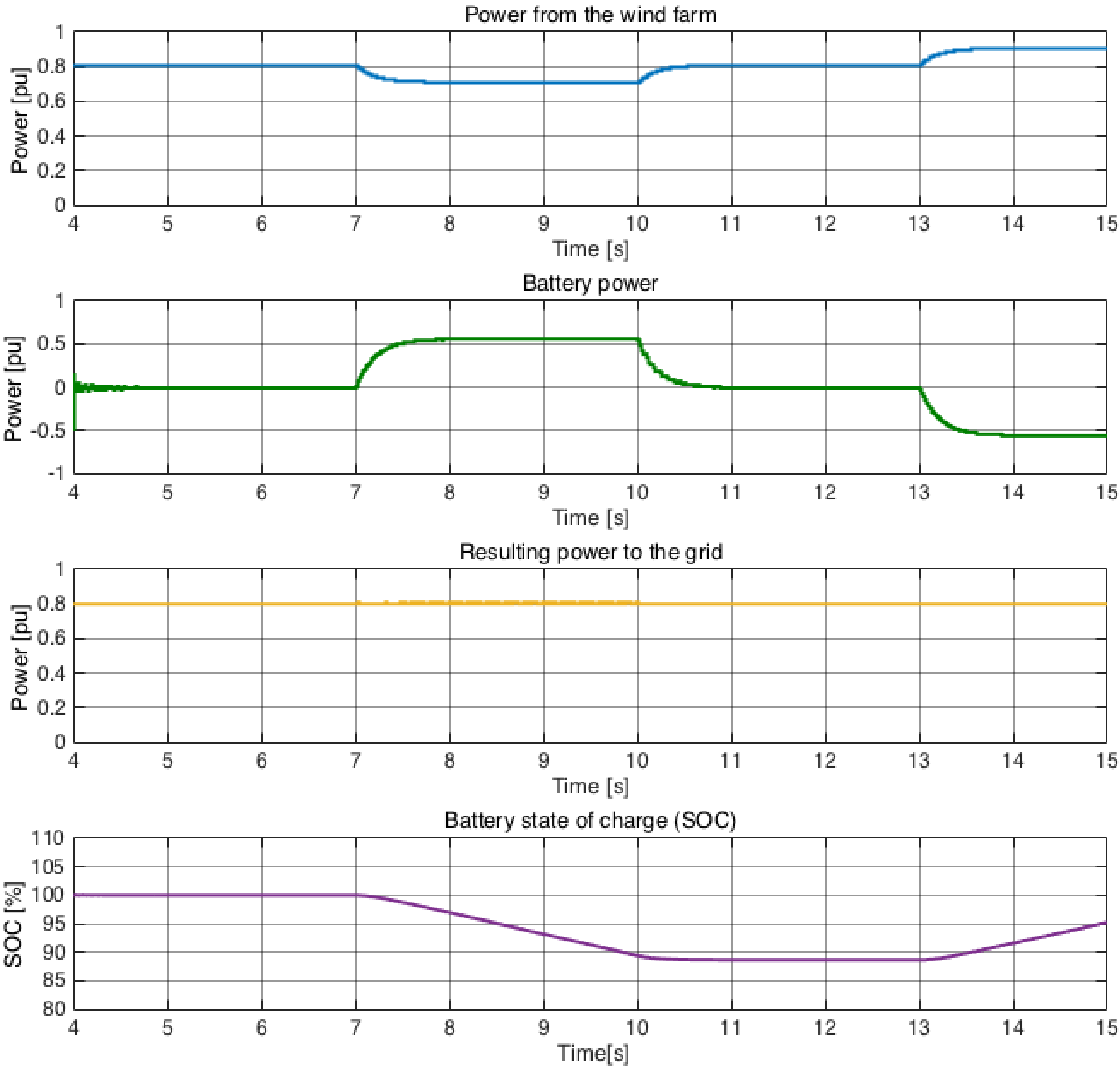

Figure 7.7: Results of case 2: Battery storage supporting the grid by ensuring stable resulting power delivered to the grid

Figure 7.8 shows the outputs at the AC- and DC-sides of the MMC for case 2. As for case 1, this figure shows the pu-values of the zero-sequence energy, d-axis current, q-axis current and the DC-side current. These parameters are plotted in the same graph as their reference value, shown as by light blue legends in the figure.

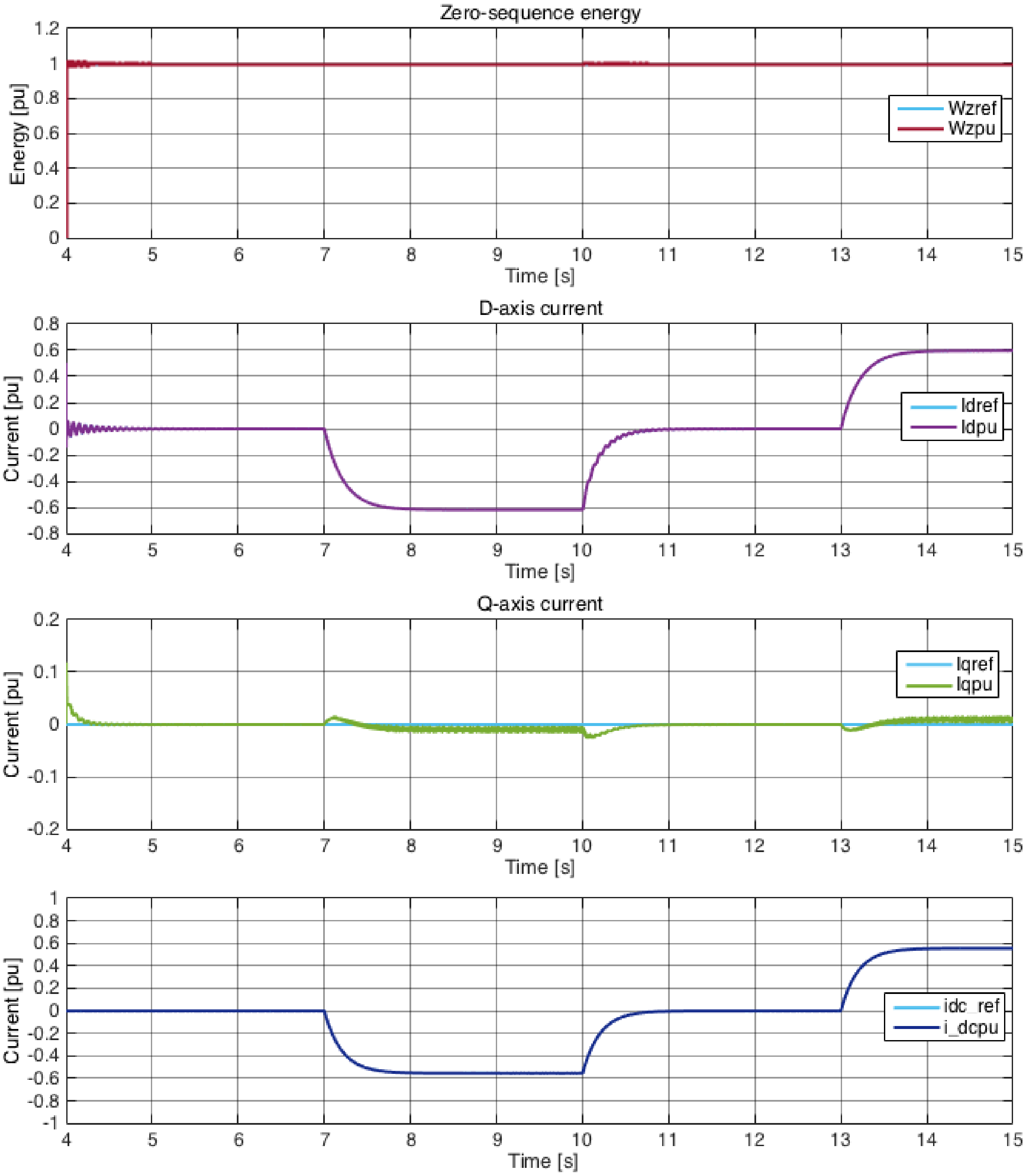

Figure 7.8: Results of case 2: Measurements of the MMC

Chapter 8

Discussion

In this chapter the results of the two main parts of the project will be discussed, namely the system design and the results of the simulations. The models used for the simulations are assumed to be sufficient for the scope of this project. However, there are weaknesses with the models and potential for improvement. This is discussed briefly in the end of this chapter.

8.1 System design

The system design was discussed in chapter 5. However, this thesis is structured to include a separate discussion chapter since this is desired if the reader wishes to jump right to the discussions of the results of the project. Therefore this subchapter will contain a summary of the discussion of system design.

The choice of using a HVDC transmission system in this project is based on the long transmission distance and the fact that subsea transmission cables have to be used since the wind farm is placed offshore. As mentioned in chapter 2, HVDC is cheaper than HVAC above the critical distance, and for HVAC the reactive power flow limits the transmission distance. Hence, for long distance transmission, HVDC will be both cheaper and have less transmission losses than HVAC, and for long enough transmission distances HVDC will actually be the only possible solution. In this project the transmission distance is 200 km, which is above the critical distance of subsea cables. Therefore HVDC is the best solution with lower costs and less transmission losses, compared to HVAC.

The DC-link voltage of 320 kV was chosen since this is the highest voltage level available for HVDC cables in use in industry today. The other voltage levels in the system were calculated based on this and using equation (5.1) to calculate the corresponding AC-side voltage and using the step ratio of the transformer to calculate the voltage level of the LV-side converter of the DC/DC converter and the battery. The power rating of the battery system was chosen based on the fact that the battery must provide services of primary and secondary reserves to the grid for up to 15 minutes in order to support and stabilize the grid in times of variable wind power generation. The wind farm power capacity was given to be 1 GW and it was discussed in chapter

5 that having a battery system with a power capacity of 180 MW, i.e 18 % of the total wind farm capacity, is considered appropriate to provide the services of primary and secondary reserves for the required time period before other slower-acting reserves can take over as tertiary control.

The DC/DC converter in this project consists of two front-to-front connected VSCs, coupled by a transformer. In the specialization project it was found that the optimal VSCs to use in terms of performances like low losses, was soft-switched DAB converters. However, these type of converters are not commercialized and used in industry yet. It can be argued that choosing a commercialized converter topology can be a safer and cheaper choice, and therefore the MMC was chosen for this project since it was the second choice of optimal converter topology based on performances.

In chapter 2 it was discussed whether both VSCs in the DC/DC converter should be MMCs or if another type of commercialized VSC could be used at the LV-side of the DC/DC converter since the transformer provides voltage matching and hence the voltage level of this LV-side VSC will be lower. The HV-side converter must be an MMC due to the high voltage level. As discussed above, the voltage level of the DC-link where the MMC is to be connected to is 320 kV, implying an AC-voltage of around 400 kV. In chapter 2 it was discussed that a 2L-VSC should only be used for voltages up to 200 kV, and hence the MMC is a better choice. Having an MMC also on the LV-side provides advantages in terms of better performance of the converter and since the battery is placed here, the battery cells can be placed inside the SMs of the MMC as distributed batteries which is better for the batteries in terms of lifetime and in case of faults.

On the other hand, the MMC is a complex and expensive converter, and taking this into consideration it can be argued that having a DC/DC converter consisting of two MMC will be too expensive. By basing the choice of LV-side VSC on a trade-off between cost and losses, the optimal choice of DC/DC converter will most likely not consist of two MMCs. In addition, due to the time limitation of this project and since the objectives of the simulations were not to study losses in detail, but rather to show that the battery system could provide grid support, a 2L-VSC was chosen for the LV-side converter in the DC/DC converter in this project.

In terms of design of the DC/DC converter, the choice of semiconductor devices is important since it affects the losses and the costs of the total system. The converters in this project require a large amount of semiconductor devices due to the high voltage levels and high power ratings of the converters. In the MMC half-bridge submoules are series connected in each arm of the converter to achieve the desired voltage level of the converter, while for the 2L-VSC semiconductor devices are series connected to achieve the desired voltage level. The choice of semiconductor devices is based on the current capability of the converter in addition to the voltage level.

For the MMC, the current that the semiconductor devices must be able to handle must be higher than the arm current of the MMC. In chapter 5 it was discussed that higher current capabilities of the semiconductor devices are related to higher costs and larger conducting areas, i.e. larger size. Therefore it is desired to base the choice of semiconductor device on the current capability by choosing a device with as low current capability as possible. In addition, the voltage level should also be considered. If a semiconductor device with a high blocking voltage capability is chosen, fewer semiconductor devices are required in order to achieve the desired voltage level of the converter and this implies lower costs of the converter. On the other hand, for the MMC, higher blocking voltages imply higher voltage steps of the converter which implies a worse performance of the converter in terms of output voltage waveform. Therefore, as argued in chapter 5, the choice of semiconductor device is made as a trade-off between cost and performances of the converter.

For the 2L-VSC, the current that the semiconductor devices must be able to handle must be higher than the phase current for half a period. The choice of semiconductor based on current capability is the same as for the MMC discussed in the previous section. However, when it comes to voltage, the 2L-VSC can only generate two voltage levels. Hence it is advantageous to choose the semiconductor device with as high blocking voltage capability as possible in order to minimize the number of semiconductors in the converter, and in that way minimize the costs.

In terms of different types of semiconductor devices, the IGBT press-pack and IGCT were compared in this project. The IGBT has been used in industry for many years and the press-pack packaging provides safe operation for high power and high voltage applications. The IGCT is also available from a few manufacturers for high voltages and currents. The main difference between the two semiconductor devices besides that they have different structures and operation since the IGBT is a transistor device wile the IGCT is a thyristor device, is in terms of losses. The IGBT has lower switching losses than the IGCT, but the IGCT has lower conduction losses than the IGBT. Since the MMC can be operated at lower switching frequencies than other 2L- and multilevel converters described in this report, the main contribution to the power losses in the MMC is the conduction losses. For the 2L-VSC on the other hand, the switching losses is the main contribution. Therefore, for the 2L-VSC, the IGBT press-pack is the obvious choice of type of semiconductor device in order to minimize the losses as much as possible. For the MMC on the other hand, both the IGCT and the IGBT press-pack can be used.

An advantage of using the IGCT is, as discussed above, that the total losses of the converter can be reduced. On the other hand, since the IGBT is more mature and a number of manufacturers offer this type of semiconductor device, it exists for a number of different rated voltages and currents, as shown in chapter 5, compared to the IGCT which is so far only produced by ABB and Mitsubishi Electric and is only offered at a few rated voltages and currents. In addition, the IGCTs that are commercially available on the market are rated for both high currents and voltages. Therefore, if both high currents and voltages are desired characteristics of the semiconductor device to be chosen, the IGCT is a good choice. In this project however, it was found that a relatively low rated current was desired, and therefore the IGBT press-pack was a better choice. The IGBT press-pack was also chosen due to the fact that the IGBT press-packs are offered at lower voltage ratings, which is an advantage in terms of output waveform of the converter.

Another component in the system that affects the total losses, size and cost is the transformer. A medium frequency transformer can be used in order to reduce the size of the transformer since the size of a transformer is inversely proportional with its operating frequency. On the other hand, increasing the operating frequency of the transformer increases the switching losses, so the choice of transformer operating frequency should be based on a trade-off between size and losses.

The turns ratio of the transformer is another part of the design that should be chosen carefully, since the choice of this parameter affects the voltage and currents in the 2L-VSC and the battery.

By choosing a high ratio, the voltage on the LV-side of the transformer, i.e at the AC-side of the 2L-VSC, will be reduced, and since the power is constant (180 MW) for all the components in the DC/DC converter plus battery system, this implies that the current increases. An increased current in the 2L-VSC implies that semiconductor devices with higher current capabilities must be used, and if semiconductor devices with high enough current capability are not available, the semiconductors can be parallel connected. Both of these options increase the cost of the converter since more expensive and/or a higher number of semiconductor devices will be required.

On the other hand, if a small turns ratio is chosen, the currents in the 2L-VSC will not be very high, so cheaper semiconductors can be used. The voltage will however be higher, so a higher number of semiconductor devices must be connected in series to achieve the desired voltage of the converter.

The last component to discuss regarding system design is the battery. The battery is built up of a number of battery modules that are connected in series and parallel in order to achieve the desired voltage level and power rating of the total battery. The number of series connections are decided by the voltage level, as shown by equation (5.12), and it can be argued that it is desirable to have as high voltage as possible per battery module in order to minimize the number of battery modules required in the system, which will also reduce the size and cost of the final system. The number of parallel connections depend on the current that the battery modules can handle, as shown by equation (5.15). On one hand it is desirable to have a large number of parallel battery strings in case of a fault in one module since then the whole string will be disconnected. If the battery consist of many parallel strings, a fault in one module may barely be noticed by the rest of the system, but in case there is only one string of batteries with a high current capability, one fault can disconnect the whole battery system. This is critical when the purpose of the battery system is to support the grid as an online reserve. In chapter 5 it is discussed that there should be at least three parallel connected strings of series connected battery modules, since if one string is disconnected due to a fault, $\frac{2}{3}$ of the battery power, i.e 12 %, will still be available for grid support. This is still within the acceptable range of battery power capacity of 10-20 % of the wind farm power capacity, in this project.

As seen from this discussion, the design of one component in the system affect another. The choices should therefore be made carefully and different options should be considered in order to find an optimal design of the system with high performances, small size and low costs.

8.2 Simulations

8.2.1 Case 1

The results of case 1 in figure 7.4 show that the battery voltage remains constant at 1 pu throughout the whole simulation and that the power is controlled by controlling the current. The voltage is constant since the battery is modeled as an ideal DC voltage source. As mentioned earlier, this is a simplification of the battery that can be used in this project since it does not affect the results of the simulation cases when the purpose is to study that the battery can charge and discharge, depending on the SOC of the battery and the power flow through the converter.

However, if the battery was to be studied more in detail, a more complex representation of the battery would be required to see how the power flows in the connections of battery modules in the battery, and in order to study performance of the battery in terms of losses, efficiency and lifetime. The ideal DC voltage source representation of the battery does not represent it in terms of losses, nor does it represent the design of the battery in terms of series and parallel connections of battery modules, and even series and battery connections of battery cells within each battery module.

The results in figure 7.4 show that, as expected, the battery discharges in the time intervals between 5 and 9 seconds and 13 and 15 seconds, and that it charges in the time interval between 9 and 13 seconds. As shown in the lower graph, the battery discharges to about 74 % of its energy capacity before the power flow is reversed at 9 seconds and it charges up to about 98% of is energy capacity. At 13 seconds the reference signal is once again reversed and the battery starts to discharge.

Figure 7.5 shows that the zero-sequence energy, d-axis current and DC-side current of the MMC perfectly follow their references throughout the simulation, while the q-axis current fails to perfectly follow its reference. As mentioned in chapter 6.2.5, this is probably due to the tuning of the PI-controller. It may not be tuned perfectly correctly and therefore the controller i probably acting slow enough so that the disturbance term, that is added after the PI-controller in the control loop, affects the results. The q-axis current controller is discussed further in the next subsection for the results of case 2.

8.2.2 Case 2

The results of case 2 in figures 7.6 and 7.7 show that when the battery system is connected to the HVDC-link, it can help stabilize the grid by supporting it in times of wind power generation that deviate from the constant onshore power consumption of 0.82 pu. The figures show that the wind power generation is decreased in the time interval between 7 and 10 seconds, so in that time interval the battery is discharging to help providing power to the grid onshore. In the time interval between 13 and 15 seconds the generation of the wind farm is increased above the limit of 0.82 pu, and hence the battery must charge in this time interval and draw power from the HVDC-link so that the remaining power flow to the onshore AC grid remains constant. The reason why the magnitude of the power that must be charged or discharged by the battery is higher than the magnitude of variation in wind power generation, is that the HVDC system is based on a pu-system with different base values than the battery system. As mentioned in chapter 7, this is accounted for by multiplying the current reference of the current controller in the MMC by a gain so that the systems are comparable at the same pu-system. As shown in the lower middle graph of figure 7.7, the resulting power to the grid remains relatively stable and constant at 0.82 pu, showing that the battery provides support to the grid in the times of variable wind power generation, and also verifying that the gain mentioned above can be used to get both systems on the HVDC pu-system.

The lower graph on figure 7.7 shows the SOC of the battery during simulation case 2 when the battery system is connected to the HVDC-link. It shows that between 7 and 10 seconds, the battery is discharging from 100 % energy capacity to around 88 %, which it remains constant at in the time interval from 10 to 13 seconds since the wind power generation is stable at 0.82 pu in this time interval, and hence no support is required from the battery. In the time interval between 13 and 15 seconds the battery is charging to around 95 % of its energy capacity.

Figure 7.8 shows that for case 2, similarly to what figure 7.5 shows for case 1, the zero-sequence energy, d-axis current and DC-side current of the MMC perfectly follow their references, while the q-axis current does not. Comparing figure 7.8 to figure 7.5 it is noticed that the magnitude of the deviation in q-axis current from its reference is larger when the magnitude of the steps for the DC-side reference current increases, since the figures show that when the DC-side current varies between -1 and 1 pu, the oscillations of the q-axis current is more visible than in figure 7.8 when the DC-side current reference only varies between approximately -0.56 and 0.56 pu. In the same manner it is shown that the oscillations around the stepping times in energy, and d- and q-axis current are more visible when the DC-current reference steps are of a larger magnitude. The oscillations around 4 seconds in both figures are due to switching transients since the energy is turned on at that time and it takes some time to stabilize the signals.

Comparing figures 7.5 and 7.8 to the zero-sequence energy and d-axis and q-axis currents of the stand-alone MMC model in figure 6.12, it is shown that the oscillations around the times where the DC-current reference changes are of smaller magnitude and duration than the oscillations in figures 7.5 and 7.8. A reason for this is probably that the results in figure 6.12 are of the stand-alone MMC model, so the only components that can affect the results are within that model. On the other hand, in figure 7.5 the transformer, 2L-VSC and battery are also included in the simulation and the 2L-VSC and transformer will affect the results since they are not implemented as ideal models. In the same manner, in figure 7.8 the same components as mentioned above will affect the results in addition to the HVDC system since that is also connected in this case.

By looking closely at the results of the MMC in terms of energy and AC-side currents, both in figure 6.12 of the verification of the stand-alone MMC model, and in figures 7.5 and 7.8 of the simulation cases, it is visible that small oscillations occur at all graphs around the times where the current reference of the MMC is changed. This is probably due to the fact that both the energy controller and the current controllers consist of PI-controllers that have a time constant T_i, and hence the signals cannot be controlled to their reference value immediately and it takes some time for the signals to stabilize.

8.2.3 Limitations of models

A weakness of the models used for the simulation cases is that there is no control of the current that is dependent on the SOC of the battery. For the simulation cases, the reference DC-current of the MMC is set externally by changing the step functions to get the desired reference signal.In the simulation cases it was chosen to set the signal in such a way that the battery would first discharge and later charge since it in the SOC model was assumed that the starting SOC of the battery was 100 %. A more realistic model of the system would inlude a control of the current dependent on the SOC of the battery as there should not be any current flow to the battery if the SOC is 100 % since it is physically impossible to charge a battery that is fully charged. In the same manner the controller should control the current so that power should only be drawn from the battery and supplied to the HVDC-link if the SOC of the battery is greater than 0 %, as it is physically impossible to discharge a battery that is fully discharged. The model used in the simulation cases in this project does not account for the aspects mentioned here, so it allows for charging the battery to more than 100 % and discharging it to less than 0 %, which is physically impossible. Implementation of a controller to solve this problem is suggested as a proposal for further work of this project in chapter 10.

Another component in the simulation models that should be discussed is the transformer. As mentioned in chaper 6, for simplicity a 50 Hz transformer was used in the simulation models of this project. Since the transformer was modelled with high magnetizing resistance and inductance in order to neglect core losses, the loss aspect in terms of using a transformer of higher frequency to reduce core losses was not visible in the simulation cases in this project. However, if the simulation models of the converters where changed to be more complex so that losses in the different components the system would be of interest to study, the transformer would also be an interesting component to study. As discussed in chapter 5, the size of the transformer can drastically be reduced if the frequency of the transformer is increased. Reduced size implies lower costs, and especially the size is an important aspect to consider in case the transformer is to be place offshore. On the other hand, the increased frequency will also increase the losses, and therefore, as discussed earlier in this chapter, the transformer should be chosen based on a trade-off between size and losses. If a transformer with a different frequency than 50 Hz were to be used in the simulations, another control loop must be added to the MMC to bring the frequency back to 50 Hz, since the MMC is connected to a HVDC system where the AC-sides of the the two 2L-VSCs that it is built up of, operate at 50 Hz, as mentioned in chapter 6. In addition, the frequency of the switching signals used to control the AC-side voltage of the 2L-VSC in the DC/DC converter must be changed to the new frequency. It is clear that this type of model would be more complex and require a longer simulation time.

Chapter 9

Connection of the battery system to the onshore AC-side of the HVDC system

9.1 Introduction

As described in the scope of this project in chapter 1, Ida Pria Reite has been working on a similar project and together we have developed the simulation model of the MMC which has been used in both projects. The difference between our projects is that in this project the battery storage is connected to the DC-link of the HVDC transmission system while in Ida's project it is connected to the onshore AC-side. In this case it is connected through a galvanically isolated DC/DC converter consisting of the MMC, a coupling transformer and a 2L-VSC. In Ida's project a transformer and the MMC is used to connect the battery storage system to the grid onshore. A one-line diagram of Ida's system is shown in figure 9.1.

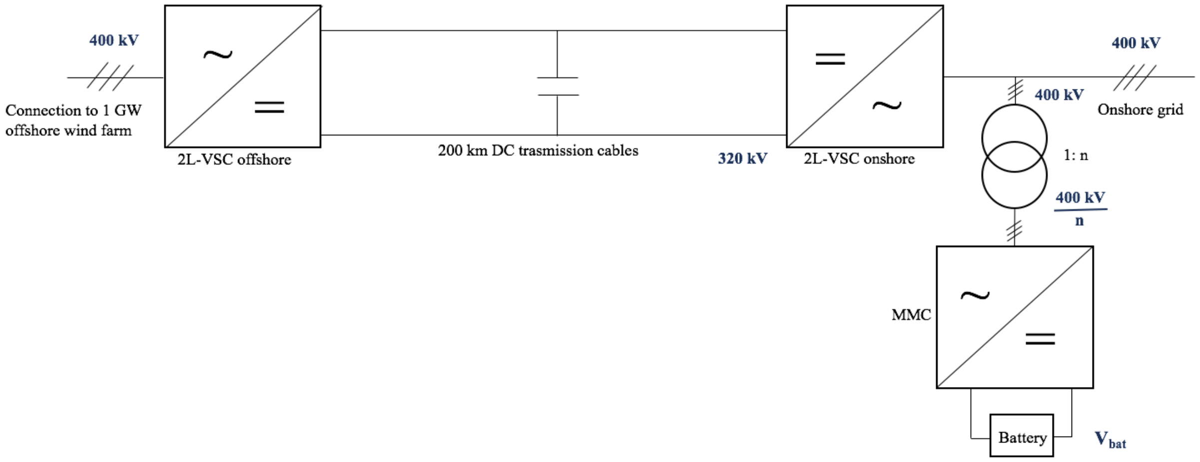

Figure 9.1: One-line diagram of the system with the battery system connected to the AC-side of the HVDC transmission system

As mentioned in chapter 1, the scope of this thesis includes a caparison of the results of simulations of the battery providing grid support when it is connected to the DC-side compared to when it is connected to the AC-side. The design of the system and the development of the simulation model regarding Ida's system are described in her Master's Thesis [19]. The results of her simulation case corresponding to simulation case 2, described in chapter 7, will be provided in this chapter and compared to the results of this project. The two simulation models are both run for case 2 the way it is described in chapter 7, with the same step functions controlling the currents at the same times. The results of both simulation models are presented in the next subchapter.

9.2 Results

Figure 9.2 shows the results of Ida's simulation while figure 9.3 shows the results of case 2, presented in chapter 7. The upper graphs show the power delivered from the wind farm. The next shows the power on the DC-side of the converter connecting the battery to the system. For the DC-side connection of the battery this corresponds to the DC-side of the 2L-VSC, while for AC-side connection it corresponds to the DC-side of the MMC. The next graph shows the resulting power delivered to the grid. For both simulation models the signal is multiplied by a gain of -1 to get a clear understanding of the results. It is however important to notice that the resulting power to the grid really has a negative pu-value since it is consumed by the onshore grid. In the same manner and for the same reason, the battery-side power of figure 9.3 is also multiplied by a gain of -1, as described in chapter 7. Figure 9.3 also shows the SOC of the battery.

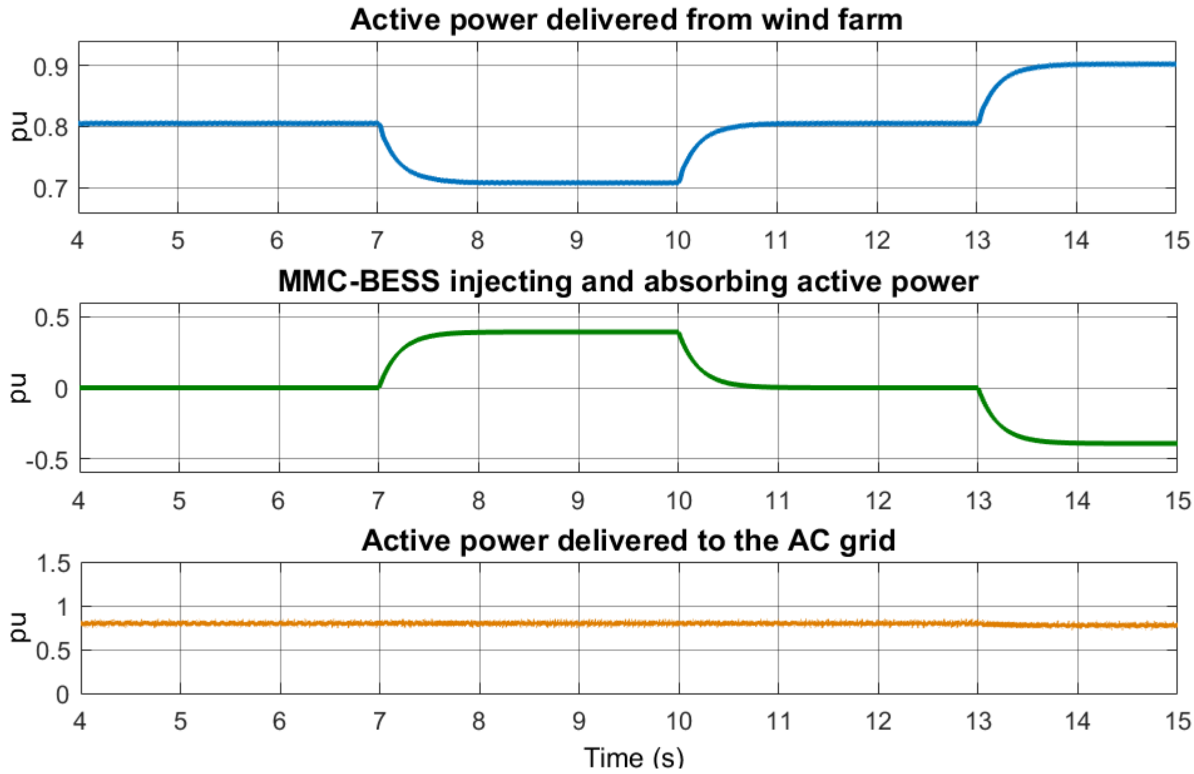

Figure 9.2: Results of case 2 when the battery is connected to the onshore AC-side of the HVDC transmission system [19]

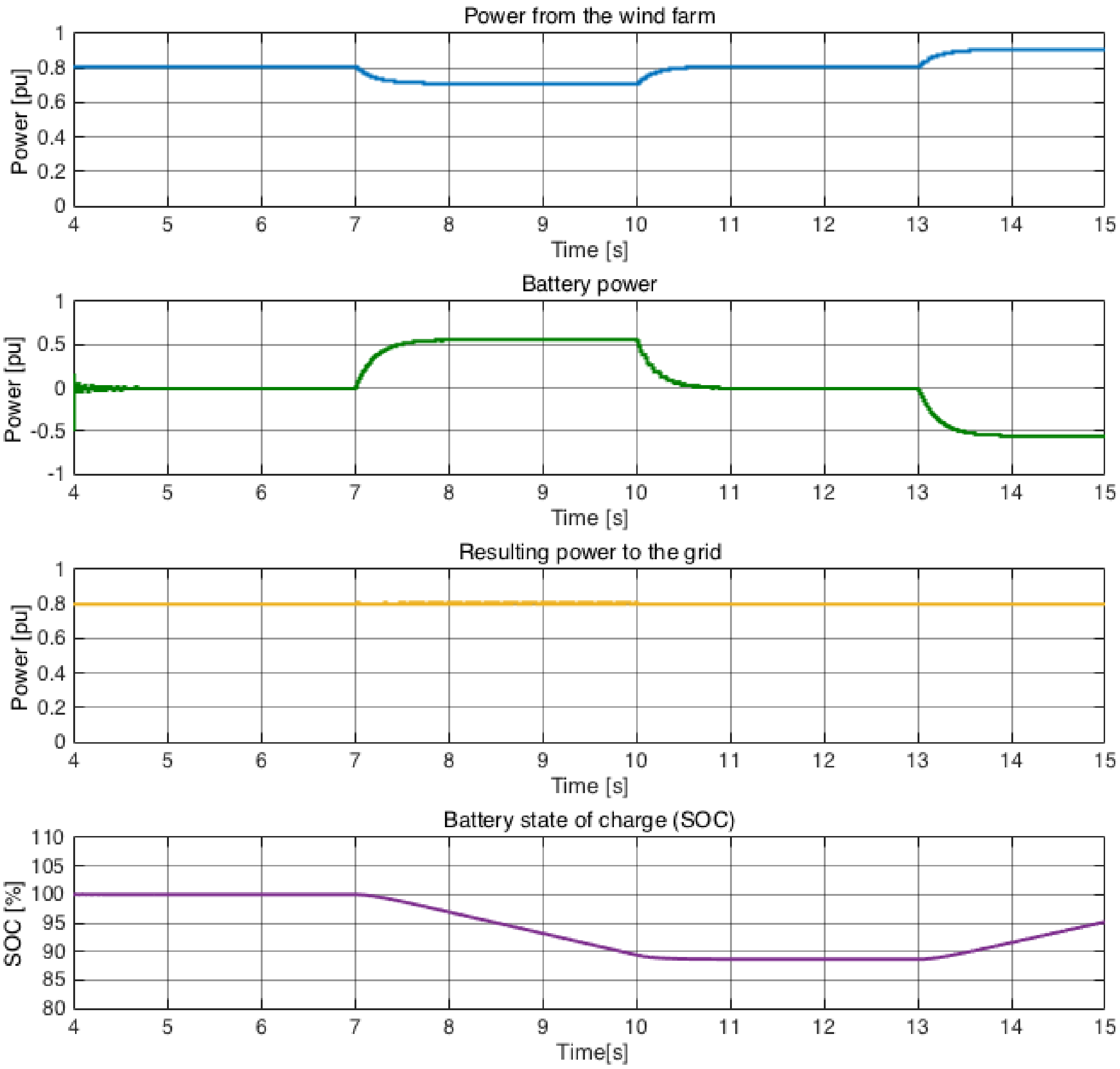

Figure 9.3: Results of case 2 with DC-side connection of the battery storage

9.3 Comparison, discussion and conclusion

The results show that both AC- and DC-connection of a battery energy storage system can be utilized to support the grid in times of variable power generation. Since the battery is connected at the DC-side of the MMC in case of AC-connection, and the current direction of the MMC is defined such that positive DC-current is flowing from the DC- to the AC-side of the MMC, the power flow at the DC-side of the MMC (the green graph in figure 9.2) is positive when the battery is discharging and negative when it is charging. The opposite yields for the DC-side connection since then the DC-side of the MMC is connected to the DC-link and the battery is connected at the DC-side of the 2L-VSC, which again is connected to the AC-side of the MMC by use of coupling transformer. Hence, for DC-side connection the battery power is negative when it is discharging and positive when it is charging. However, as mentioned in the previous subchapter a gain of -1 has been multiplied and therefore the green graph in figure 9.3 is positive when the battery is discharging (when the purple graph indicating the SOC is decreasing).

As shown by comparing the two results, the battery-side power of the two results are not equal. This is because the step functions to control the current in the MMC in both cases are multiplied by a gain in order to get the results on the same pu-system as the HVDC pu-system. The gains for the two models are not the same since the MMC is connected directly to the HVDC-link in case of DC-side connection while it it connected through a transformer for AC-side connection, and hence the turns ratio of the transformer must be considered when calculating the gain for this model.

Another difference between the two results are that figure 9.2 does not include a graph showing the SOC of the battery, and hence the results show that the battery can possibly discharge between 7 and 10 seconds, and it can possibly charge between 13 and 15 seconds, depending on the SOC of the battery. In the model of the DC-connection of the battery it is however assumed that the SOC of the battery is 100 % at the start of the simulation, and the results show that the battery discharges between 7 and 10 seconds and that it charges between 13 and 15 seconds since the SOC graph is first reduced and then it increases again at the end of the simulation time.

The results show that there are more oscillations around the times when the current step functions are changed for the DC-side connection. For the AC-side connection however, the oscillations are barely noticeable. A reason for this could be, as discussed in chapter 8, that the system for DC-side connection consist of a higher number of components and since these components are not implemented as ideal models they will affect the system with increased losses. As also discussed in chapter 8, higher steps for the DC-current of the MMC results in more oscillations, so this can also be a reason for why there are more oscillations in the results of the DC-side connection since the battery-side power, which is controlled by the DC-current of the MMC, is changed between pu-values of a larger magnitude in this case.

If a system like this were to be built, an important point of discussion in order to decide upon which system to build, is the cost. It can be argued that the system with AC-side connection might be less costly than the system with DC-side connection since this system requires more components. On the other hand, the MMC of the system with AC-side connection is included at the LV-side of the transformer, meaning that the voltage is stepped down and hence current is increased in order to keep the power constant. This implies that semiconductor devices with higher current capability are required for this converter, and as discussed in chapter 8 this implies higher cost of the semiconductor devices. However, the cost of the two systems depend on many variables as a number of different components can be chosen for the different parts that the system consist of. In addition to cost, performances and size are important parameters to consider when deciding upon a system.

The results provided in this subchapter show that both AC- and DC-side connection of battery storage is possible. To decide which configuration is better depends on a number of factors, and analysis and comparisons of different options should be considered before making a choice. A conclusion is however that both options are possible in order to connect a battery storage system to the grid to provide ancillary services and stabilize the grid.

Chapter 10

Conclusions and further work

10.1 Conclusions

The main conclusion to this Master's Thesis is that battery energy storage can be used to provide ancillary services to the grid in order to help stabilize it and support integration of intermittent renewable energy sources. This conclusion is supported by the literature review and the theoretical background in this report in addition to simulations.

A number of battery storage technologies and DC/DC converter topologies have been studied in terms of the literature review in the theory part of this report. It is concluded that the Li-ion battery technology is the most promising solution for the application in this project. When it comes to the DC/DC converter topology, which is required in order to connect the battery storage to the DC-link of the HVDC transmission system, it is concluded that a galvanically isolated bidirectional DC/DC converter consisting of two front-to-front coupled VSCs connected by a medium frequency transformer, is the optimal topology for the application in this project. It is also found that the optimal VSC technology to be used in this converter based on VSCs that are commercially available in industry today, is the MMC. However, this is a complex and expensive converter and it was discussed whether the DC/DC converter should be designed with two MMCs. It is concluded that a design consisting of an MMC on the HV-side and a 2L-VSC on the LV-side of the DC/DC converter is an optimal solution for the application in this project.

The first main part of the scope of this thesis was a design part where the design of the system was discussed. The main focus of this part was the battery and the DC/DC converter, but all components of the system were discussed and it was argued why different design choices were taken. The battery is designed based on ABB's EssPro$^{\text{TM}}$ Grid battery modules and an optimal design of the battery is proposed for the application in this project. It was found that the optimal design consist of 273 such battery modules connected in series and parallel to achieve the desired power rating and voltage level of the battery. Taking into account that the battery system will also require control systems and fault detection and protection equipment, it can be concluded that the size of the battery will be large. Considering this in addition to costs it can be concluded that it is advantageous to place the battery onshore.

For the converters the focus was on the choice of design parameters including the choice of semiconductor devices. A number of IGBT press-pack and IGCT devices from different manufacturers have been compared and based on a discussion regarding advantages and disadvantages of different choices, optimal designs for the MMC and the 2L-VSC for the application of this project is proposed. It is concluded that IGBT press-packs is the best choice of semiconductor device for both converters in this project. For the MMC it is found that 107 SMs, each consisting of two IGBT press-pack devices with $V_{CE} = 4.5kV$ and $I_C = 600A$, must be connected in series in each of the six arms of the converter in order to achieve the desired DC-voltage level of 320 kV. For the 2L-VSC it is found that 25 IGBT press-pack devices with $V_{CE} = 4.5kV$ and $I_C = 900A$ must be connected in series in each of the six semiconductor valves of the converter in order to achieve the desired DC-side voltage (i.e battery voltage) of 108.87 kV. In terms of galvanic isolation of the DC/DC converter it is found that the optimal choice for this project is to use a medium frequency transformer with a frequency of 300 Hz and a turns ratio of 1:3.

The other main part of the scope of this thesis was a simulation part. A simulation model of the HVDC transmission system based on 2L-VSCs was given for this project. Simulation models of the other parts of the system, including the MMC, the coupling transformer, the 2L-VSC and the battery have been developed in MATLAB and Simulink. Compared to the system discussed in the design part, the simulation models are simplified versions of the different components of the system. The simplifications have been argued for in chapter 6 where the simulation models are described. The simulation models were built and tested separately before they were connected to the final system, which was used for two simulation cases.

The results of the first case show that the DC/DC converter provides bidirectional power flow and it shows that by controlling the current in the MMC, the power flow of the DC/DC converter is controlled and the battery can charge and discharge, depending on its SOC. It can be concluded that the proposed DC/DC converter can be used to connect the battery storage to the DC-link of the HVDC system.

The results of the second case show that the battery supports the grid in times of variable wind power generation. It charges when the wind power generation is higher than the power consumption onshore and it discharges when the wind power generation is lower than the consumption. It is concluded that the battery storage system can be connected to the DC-link of the HVDC transmission system in order to help stabilize the grid and provide balancing services in times of variable wind power generation. Hence, it can be concluded that the battery storage can be connected to support integration of intermittent renewable energy sources, such as offshore wind power.

In the end of this thesis the results of DC-side connection of the battery system were compared to the results of the same case for AC-side connection. Based on the developed simulation models it is not possible to study losses of the system on a detailed level. Nor have the systems been analyzed and compared in terms of costs, and therefore it is hard to say that one configuration is preferred over the other. However, advantages of one over the other have been briefly discussed and from the simulation results it is concluded that both options are possible since they both provide good results.

10.2 Proposals for further work

Based on the design and modeling of the system performed in this thesis, many interesting paths for further work can be chosen. In this subchapter a number of them are discussed.

First, another simulation case that would have been interesting to study using the existing developed simulation model in this project, is to consider quicker variations of wind power generation. This is an interesting case since it corresponds to a more realistic wind profile and it would be interesting to see if the controllers of the battery system are quick enough. This would be implemented in the same way as case 2, but the step functions controlling the currents on the HVDC-link and controlling the DC-side MMC current would be changed more frequently.

In addition, it would be useful to improve the simulation model by implementing current controllers of the converters that consider the SOC of the battery, as discussed in the previous chapter. This would make the model more realistic and avoid having the limitation of the model being able to charge a fully charged battery and discharge a fully discharged battery.

Further, it would be interesting to implement protection systems to the developed model and perform fault analysis on the system. This is also an interesting case to study in order to verify that the battery system can help stabilize and provide support to the grid. A fault in a power system that disconnects a part of the system is typically a case where the frequency in the system will deviate from its nominal frequency. Therefore this is an important test case in order to show that battery system can provide ancillary services to the grid in terms of primary and secondary reserves, and in that way stabilize and restore the system frequency before slower acting rotating reserves can take over as tertiary control.

Synthetic inertia was briefly mentioned in chapter 2, and a suggestion for further work is to implement a similar controller to the controller shown in figure 2.2 to the DC/DC converter so that the DC/DC converter can provide synthetic inertia and in that way provide support to the grid. This could be interesting to implement since there is an increasing implementation of solar and wind power into the power systems that utilizes power electronics. In addition there is an increasing trend of using HVDC to connect grids, and this also adds more power electronic interfaces into the grid. As mentioned in chapter 2, the power electronic interfaces reduce the total system inertia and this is a concern. However, by adding this proposed extra control loop the power electronic interfaces, they can provide synthetic inertia which helps increase the system inertia.

It would also be interesting to implement a more complex and detailed model of the system in order to study losses and impacts of using a medium frequency transformer instead of a 50 Hz transformer. This includes implementing more detailed models of the converters where the semiconductor devices are modeled explicitly. Having such a detailed model it would also be interesting to look at the difference in terms of performance and losses of having a DC/DC converter consisting of two MMCs compared to the DC/DC converter with an MMC on the HV-side and a 2L-VSC on the LV-side, which was used in this project.

In addition to the detailed converters as described above, also the battery system could be implemented more realistically. Using an ideal DC source, which is done in the simulation models developed in this thesis, is an oversimplification of the battery system and using such a model it is not possible to study losses and performances of the battery. Neither does this model show the design of the battery in terms of series and parallel connections of battery modules. If a more detailed and realistic battery model was implemented it would have been possible to study i.e. the impact on the total system when a fault occurs in one module, leading to disconnection of a battery string. This would also require implementation of fault handling and protection systems of the battery.

Implementing more detailed models of the converters and the battery, and considering that the DC/DC converter consists of two MMCs, it would be interesting to study the performances of an MMC with distributed batteries compared to an MMC with centralized batteries.

It would also be interesting to study the AC-side versus DC-side connection of the battery more in detail. This could be done by making more complex simulation models in order to study losses of the system more in detail. In addition, a cost analysis of the two systems can be carried out since the cost is an important factor to consider regarding the choice of configuration.

Bibliography

[1] T. Toftevaag, "Lecture 1: Wind power overview and system impacts." `https://files.itslearning.com`, 2016. Lecture notes in course ELK-12 Wind power in electric power systems. Accessed: 03.02.17.

[2] J. Zhu, C. D. Booth, G. P. Adam, A. J. Roscoe, and C. G. Bright, "Inertia emulation control strategy for vsc-hvdc transmission systems," *IEEE Transactions on Power Systems*, vol. 28, no. 2, pp. 1277–1287, 2013.

[3] M. N. Hellesnes, "Use of battery storage for power balancing in a large scale HVDC-connected wind power plant," 2016. Specialization project in TET4520, Department of Electric Power Engineering at the Norwegian University of Science and Technology.

[4] United States Department of Energy's Global Energy Storage Database (DOE), "DOE Global Energy Storage Database Data Visualization." `http://www.energystorageexchange.org/projects/data_visualization`, 2016. Accessed: 31.03.17.

[5] Dr Radnya A Mukhedkar, ALTSOM, "Introduction to HVDC, LCC & VSC comparison." `http://sari-energy.org/oldsite/PageFiles/What_We_Do/activities/HVDC_Training/Presentations/Day_7/LCC_vs_VSC_ALSTOM.pdf`. Accessed: 08.02.17.

[6] C. Bajracharya, M. Molinas, J. A. Suul, T. M. Undeland, *et al.*, "Understanding of tuning techniques of converter controllers for vsc-hvdc," in *Nordic Workshop on Power and Industrial Electronics (NORPIE/2008), June 9-11, 2008, Espoo, Finland*, Helsinki University of Technology, 2008.

[7] D. Krug, M. Malinowski, and S. Bernet, "Design and comparison of medium voltage multi-level converters for industry applications," in *Industry Applications Conference, 2004. 39th IAS Annual Meeting. Conference Record of the 2004 IEEE*, vol. 2, pp. 781–790, IEEE, 2004.

[8] S. Debnath, J. Qin, B. Bahrani, M. Saeedifard, and P. Barbosa, "Operation, control, and applications of the modular multilevel converter: A review," *IEEE transactions on power electronics*, vol. 30, no. 1, pp. 37–53, 2015.

[9] H. R. Karshenas, A. Bakhshai, A. Safaee, H. Daneshpajooh, and P. Jain, *Bidirectional dc-dc converters for energy storage systems*. INTECH Open Access Publisher, 2011.

[10] A. G. Endegnanew and K. Uhlen, “Global analysis of frequency stability and inertia in ac systems interconnected through an hvdc,” in *Energy Conference (ENERGYCON), 2016 IEEE International*, pp. 1–6, IEEE, 2016.

[11] K. Padiyar, *FACTS controllers in power transmission and distribution*. New Age International, 2007.

[12] G. Wang, G. Konstantinou, C. D. Townsend, J. Pou, S. Vazquez, G. D. Demetriades, and V. G. Agelidis, “A review of power electronics for grid connection of utility-scale battery energy storage systems,” *IEEE Transactions on Sustainable Energy*, vol. 7, no. 4, pp. 1778–1790, 2016.

[13] G. B. Diaz, J. A. Suul, and S. D’Arco, “Small-signal state-space modeling of modular multilevel converters for system stability analysis,” in *Energy Conversion Congress and Exposition (ECCE), 2015 IEEE*, pp. 5822–5829, IEEE, 2015.

[14] S. Sanchez Acevedo, “Lecture 9.” `https://files.itslearning.com`, 2016. lecture notes in NTNU course ELK-23 Power Electronics in Future Power Systems, Accessed: 07.05.17.

[15] Y. Deng and R. G. Harley, “Space-vector versus nearest-level pulse width modulation for multilevel converters,” *IEEE transactions on power electronics*, vol. 30, no. 6, pp. 2962–2974, 2015.

[16] N. Hingorani and L. Gyuyi, “Understanding facts–concepts and technology of flexible ac transmission systems: Inst. elect,” 1999.

[17] ABB, “EssPro$^{\text{TM}}$ Grid - Battery energy storage systems - The power to control energy.” `https://library.e.abb.com/public/8533b9e756f84b83981150e787bc6cd5/EssPro_Grid_BR_20160527.pdf`, 2015. Accessed: 27.03.17.

[18] H. Saad, J. Peralta, S. Dennetiere, J. Mahseredjian, J. Jatskevich, J. Martinez, A. Davoudi, M. Saeedifard, V. Sood, X. Wang, *et al.*, “Dynamic averaged and simplified models for mmc-based hvdc transmission systems,” *IEEE transactions on Power delivery*, vol. 28, no. 3, pp. 1723–1730, 2013.

[19] I. P. Reite, “Battery energy storage connected to a three-phase 50 Hz grid,” 2017. Master’s Thesis, Department of Electric Power Engineering at the Norwegian University of Science and Technology.

[20] MathWorks, “Alpha-Beta-Zero to dq0, dq0 to Alpha-Beta-Zero.” `https://se.mathworks.com/help/physmod/sps/powersys/ref/alphabetazerotodq0dq0toalphabetazero.html;jsessionid=6843cf27ffd18a433489ae02582c`. Accessed: 17.05.17.

[21] X. Luo, J. Wang, M. Dooner, and J. Clarke, “Overview of current development in electrical energy storage technologies and the application potential in power system operation,” *Applied Energy*, vol. 137, pp. 511–536, 2015.

[22] A. Poullikkas, “A comparative overview of large-scale battery systems for electricity storage,” *Renewable and Sustainable Energy Reviews*, vol. 27, pp. 778–788, 2013.

[23] Rocky Mountain Insitute, Homer Energy and Cohnreznick Think Energy, “The economics

of grid defection: when and where distributed solar generation plus storage competes with traditional utility service." `http://www.homerenergy.com/pdf/RMI_Grid_Defection_Report.pdf`. Accessed: 09.03.17.

[24] G. P. Adam, I. A. Gowaid, S. J. Finney, D. Holliday, and B. W. Williams, "Review of dc–dc converters for multi-terminal HVDC transmission networks," *IET Power Electronics*, vol. 9, no. 2, pp. 281–296, 2016.

[25] C. Barker, C. Davidson, D. Trainer, and R. Whitehouse, "Requirements of DC-DC Converters to facilitate large DC Grids," *Cigre, SC B4 HVDC and Power Electronics*, 2012.

[26] H. Zhao, Q. Wu, S. Hu, H. Xu, and C. N. Rasmussen, "Review of energy storage system for wind power integration support," *Applied Energy*, vol. 137, pp. 545–553, 2015.

[27] A. Castillo and D. F. Gayme, "Grid-scale energy storage applications in renewable energy integration: A survey," *Energy Conversion and Management*, vol. 87, pp. 885–894, 2014.

[28] S. K. Kolparambath, J. A. Suul, and E. Tedeschi, "Analysis of DC/DC converters in multiterminal HVDC systems for large offshore wind farms," in *Advancements in Power and Energy (TAP Energy), 2015 International Conference on*, pp. 415–420, IEEE, 2015.

[29] International Energy Agency (IEA), "Key world energy statistics 2016." `https://www.iea.org/publications/freepublications/publication/KeyWorld2016.pdf`, 2016. Accessed: 15.02.17 .

[30] Renewable Energy Policy Network for the 21st century (REN21), "Renewables 2017 Global Status Report." `http://www.ren21.net/wp-content/uploads/2017/06/170607_GSR_2017_Full_Report.pdf`, 2017. Accessed: 11.06.17 .

[31] United Nations Framework Convention on Climate Change (UNFCCC), "Kyoto Protocol." `http://unfccc.int/kyoto_protocol/items/2830.php`. Accessed: 18.02.17.

[32] United Nations Framework Convention on Climate Change (UNFCCC), "Summary of the Paris Agreement." `http://bigpicture.unfccc.int/#content-the-paris-agreemen`, 2016. Accessed: 18.02.17.

[33] European Commission, "Renewable energy: Moving towards a low carbon economy." `https://ec.europa.eu/energy/en/topics/renewable-energy`, 2016. Accessed: 16.02.17.

[34] European Comission, "2020 climate energy package." `http://ec.europa.eu/clima/policies/strategies/2020_en`. Accessed: 16.02.17.

[35] Global Wind Energy Council, "Offshore wind power." `http://www.gwec.net/global-figures/global-offshore/`, 2016. Accessed: 16.02.17.

[36] Statnett, "Statnett's System Operations and Market Development Plan 2014-20." `http://www.statnett.no/Global/Dokumenter/Kraftsystemet/Systemtjenester/SMUP%20Overview.pdf`, 2015. Accessed: 10.05.17.

[37] United States Department of Energy's Global Energy Storage Database (DOE), "United States Department of Energy's Global Energy Storage Database." `http://www.energystorageexchange.org/`, 2016. Accessed: 31.03.17.

[38] J. F. Manwell, J. G. McGowan, and A. L. Rogers, *Wind energy explained: theory, design and application*. John Wiley & Sons, 2010.

[39] Global Wind Energy Council, "Global wind statistics 2016." `http://www.gwec.net/wp-content/uploads/vip/GWEC_PRstats2016_EN_WEB.pdf`, 2017. Accessed: 09.03.17.

[40] International Renewable Energy Agency (IRENA), "Innovation outlook: Offshore wind." `https://www.irena.org/DocumentDownloads/Publications/IRENA_Innovation_Outlook_Offshore_Wind_2016.pdf`, 2015. Accessed: 31.03.17.

[41] K. Sharifabadi, L. Harnefors, H.-P. Nee, R. Teodorescu, and S. Norrga, *Design, Control and Application of Modular Multilevel Converters for HVDC Transmission Systems*. John Wiley & Sons, 2016.

[42] A. Hansen, P. Sørensen, L. Zeni, and M. Altin, "Frequency control modelling - basics." compendium E-0103 in course 46230 Power System Balancing with Large Scale Wind power at the Department of Wind Energy at the Technical University of Denmark, 2016.

[43] O. Anaya-Lara, "Guest lecture in ELK-12 by Olimpo Anaya- Lara. Lecture 1: Grid integration of large-scale wind power plant: challenges and opportunities." `https://files.itslearning.com`, 2016. Lecture notes in course ELK-12 Wind power in electric power systems. Accessed: 04.02.17.

[44] S. Wachtel and A. Beekmann, "Contribution of wind energy converters with inertia emulation to frequency control and frequency stability in power systems," in *8th Int. Workshop on Large Scale Integration of Wind Power into Power Systems as well as on Offshore Wind Farms, Bremen, Germany*, 2009.

[45] T. Toftevaag, "ELK-12 Specialization course Wind Power in the Norwegian Energy System – Solution proposal to exam 2013." `https://files.itslearning.com`, 2013. Accessed: 04.02.17.

[46] J. Morren, S. W. De Haan, W. L. Kling, and J. Ferreira, "Wind turbines emulating inertia and supporting primary frequency control," *IEEE Transactions on Power Systems*, vol. 21, no. 1, pp. 433–434, 2006.

[47] J. Fradley, R. Preece, and M. Barnes, "Vsc-hvdc for frequency support (a review)," 2017.

[48] O. Anaya-Lara, D. Campos-Gaona, E. Moreno-Goytia, and G. Adam, *Offshore Wind Energy Generation: Control, Protection, and Integration to Electrical Systems*. John Wiley & Sons, 2014.

[49] M. Santos-Mugica, E. Robles, A. G. Endegnanew, E. Tedeschi, and J. Giebhardt, "Grid integration and power quality testing of marine energy converters: Research activities in the marinet project," in *Ecological Vehicles and Renewable Energies (EVER), 2014 Ninth International Conference on*, pp. 1–9, IEEE, 2014.

[50] International Renewable Energy Agency (IRENA), “Battery storage for renewables: market status and technology outlook.” `http://www.irena.org/documentdownloads/publications/irena_battery_storage_report_2015.pdf`, 2015. Accessed: 14.03.17.

[51] S. O. Amrouche, D. Rekioua, and T. Rekioua, “Overview of energy storage in renewable energy systems,” in *2015 3rd International Renewable and Sustainable Energy Conference (IRSEC)*, pp. 1–6, IEEE, 2015.

[52] Rocky Mountain Institute (RMI), “The economics of battery energy storage: How multi-use, customer-sited batteries deliver the most services and value to customers and the grid.” `https://rmi.org/insights/reports/economics-battery-energy-storage/`, 2015. Accessed: 20.02.17.

[53] E. Tedeschi, “Lecture 3.” `https://files.itslearning.com`, 2016. Lecture notes in NTNU course ELK-23 Power Electronics in Future Power Systems. Accessed: 20.02.17.

[54] ABB, “Technical advantages.” `http://new.abb.com/systems/hvdc/why-hvdc/technical-advantages`. Accessed: 17.02.17.

[55] C.-K. Kim, V. K. Sood, G.-S. Jang, S.-J. Lim, and S.-J. Lee, *HVDC transmission: power conversion applications in power systems*. John Wiley & Sons, 2009.

[56] E. Tedeschi, “Lecture 2.” `https://files.itslearning.com`, 2016. lecture notes in NTNU course ELK-23 Power Electronics in Future Power Systems, Accessed: 20.02.17.

[57] M. Bahrman and B. Johnson, “The ABCs of HVDC transmission technologies,” *IEEE power and energy magazine*, vol. 2, no. 5, pp. 32–44, 2007.

[58] R. Adapa, “High-wire act,” *IEEE power and energy magazine*, vol. 10, no. 6, p. 18, 2012.

[59] ABB, “Brochure introducing HVDC.” `http://www04.abb.com/global/seitp/seitp202.nsf/c71c66c1f02e6575c125711f004660e6/d8e7ec7508118cf7c1257c670040069e/FILE/Introducing+HVDC.pdf`, 2014. Accessed: 21.02.17.

[60] Siemens, “HVDC PLUS – Basics and Principle of Operation.” `https://www.energy.siemens.com/br/pool/br/transmissao-de-energia/transformadores/hvdc-plus-basics-and-principle-of-operation.pdf`, 2009. Accessed: 18.04.17.

[61] M. Barnes and A. Beddard, “Voltage source converter HVDC links–the state of the art and issues going forward,” *Energy Procedia*, vol. 24, pp. 108–122, 2012.

[62] B. Andersen, L. Xu, P. Horton, and P. Cartwright, “Topologies for vsc transmission,” *Power Engineering Journal*, vol. 16, no. 3, pp. 142–150, 2002.

[63] Y. Zhang, G. Adam, T. Lim, S. J. Finney, and B. Williams, “Voltage source converter in

high voltage applications: Multilevel versus two-level converters," in *AC and DC Power Transmission, 2010. ACDC. 9th IET International Conference on*, pp. 1–5, IET, 2010.

[64] J. Arrillaga, Y. H. Liu, N. R. Watson, and N. J. Murray, *Self-commutating converters for high power applications*. John Wiley & Sons, 2010.

[65] T. Lüth, M. M. Merlin, T. C. Green, F. Hassan, and C. D. Barker, "High-frequency operation of a dc/ac/dc system for HVDC applications," *IEEE Transactions on Power Electronics*, vol. 29, no. 8, pp. 4107–4115, 2014.

[66] G. Wang, G. Konstantinou, C. D. Townsend, J. Pou, S. Vazquez, G. D. Demetriades, and V. G. Agelidis, "A review of power electronics for grid connection of utility-scale battery energy storage systems," 2016.

[67] C. Meyer, M. Kowal, and R. W. De Doncker, "Circuit breaker concepts for future high-power DC-applications," in *Fourtieth IAS Annual Meeting. Conference Record of the 2005 Industry Applications Conference, 2005.*, vol. 2, pp. 860–866, IEEE, 2005.

[68] K. Sano and M. Takasaki, "A surgeless solid-state DC circuit breaker for voltage-source-converter-based HVDC systems," *IEEE Transactions on Industry Applications*, vol. 50, no. 4, pp. 2690–2699, 2014.

[69] S. K. Kolparambath, J. A. Suul, and E. Tedeschi, "DC/DC converters for interconnecting independent HVDC systems into multiterminal DC grids," in *2015 IEEE 13th Brazilian Power Electronics Conference and 1st Southern Power Electronics Conference (COBEP/SPEC)*, pp. 1–6, IEEE, 2015.

[70] T. M. Undeland, W. P. Robbins, and N. Mohan, "Power electronics: converters, applications, and design," 2003.

[71] S. P. Engel, M. Stieneker, N. Soltau, S. Rabiee, H. Stagge, and R. W. De Doncker, "Comparison of the modular multilevel DC converter and the dual-active bridge converter for power conversion in HVDC and MVDC grids," *IEEE Transactions on Power Electronics*, vol. 30, no. 1, pp. 124–137, 2015.

[72] C. Zhao, S. Round, and J. Kolar, "Full-order averaging modelling of zero-voltage-switching phase-shift bidirectional dc-dc converters," *IET power electronics*, vol. 3, no. 3, pp. 400–410, 2010.

[73] G. G. Oggier, G. O. Garcia, and A. R. Oliva, "Switching control strategy to minimize dual active bridge converter losses," *IEEE Transactions on Power Electronics*, vol. 24, no. 7, pp. 1826–1838, 2009.

[74] B. Zhao, Q. Song, W. Liu, and Y. Sun, "Overview of dual-active-bridge isolated bidirectional dc–dc converter for high-frequency-link power-conversion system," *IEEE Transactions on Power Electronics*, vol. 29, no. 8, pp. 4091–4106, 2014.

[75] L. Ronström, M. L. Hoffstein, R. Pajo, and M. Lahtinen, "The Estlink HVDC Light® Transmission System." `https://abblibrary.s3.amazonaws.com/public/c9f4e1c6068fb993c125731d004612b2/Estlink%20HVDC%20Light%20transmission%20system.pdf`, 2007. Accessed: 21.02.17.

[76] G. Ortiz, J. Biela, D. Bortis, and J. Kolar, "1 Megawatt, 20 kHz, isolated, bidirectional

12kV to 1.2 kV DC-DC converter for renewable energy applications," in *Power Electronics Conference (IPEC), 2010 International*, pp. 3212–3219, IEEE, 2010.

[77] Elisabetta Tedeschi, "Lecture 4." `https://files.itslearning.com`, 2016. Lecture notes in NTNU course ELK-23 Power Electronics in Future Power Systems. Accessed: 10.02.17.

[78] Elisabetta Tedeschi, "Lecture 5." `https://files.itslearning.com`, 2016. Lecture notes in NTNU course ELK-23 Power Electronics in Future Power Systems. Accessed: 10.02.17.

[79] Elisabetta Tedeschi, "Lecture 6." `https://files.itslearning.com`, 2016. Lecture notes in NTNU course ELK-23 Power Electronics in Future Power Systems. Accessed: 10.02.17.

[80] S. D'Arco, J. A. Suul, and M. Molinas, "Implementation and analysis of a control scheme for damping of oscillations in vsc-based hvdc grids," in *Power Electronics and Motion Control Conference and Exposition (PEMC), 2014 16th International*, pp. 586–593, IEEE, 2014.

[81] R. Marquardt, A. Lesnicar, and J. Hildinger, "Modulares stromrichterkonzept für netzkupplungsanwendung bei hohen spannungen," *ETG-Fachtagung, Bad Nauheim, Germany*, vol. 114, 2002.

[82] Siemens, "Siemens Debuts HVDC PLUS with San Francisco's Trans Bay Cable." `http://www.energy.siemens.com/hq/pool/hq/energy-topics/living-energy/issue-5/LivingEnergy_05_hvdc.pdf`, 2011. Accessed: 19.04.17.

[83] ABB, "HVDC Light (VSC)." `http://new.abb.com/systems/hvdc/hvdc-light`, 2016. Accessed: 03.04.17.

[84] M. Electric, "Mitsubishi Electric Develops SVC-DiamondTM Static Synchronous Compensator." `http://www.mitsubishielectric.com/news/2014/pdf/0825.pdf`, 2014. Accessed: 06.05.17.

[85] ALSTOM, "MaxSine$^{\text{TM}}$ eStorage - An innovative and efficient solution to renewable integration and grid stability." `http://www.gegridsolutions.com/alstomenergy/grid/Global/OneAlstomPlus/Grid/PDF/MaxSine%20eStorage-epslanguage=en-GB.pdf`, 2014. Accessed: 27.03.17.

[86] T. Soong and P. W. Lehn, "Evaluation of emerging modular multilevel converters for bess applications," *IEEE Transactions on Power Delivery*, vol. 29, no. 5, pp. 2086–2094, 2014.

[87] P. S. Jones and C. C. Davidson, "Calculation of power losses for mmc-based vsc hvdc stations," in *Power Electronics and Applications (EPE), 2013 15th European Conference on*, pp. 1–10, IEEE, 2013.

[88] E. N. Abildgaard and M. Molinas, "Modelling and control of the modular multilevel converter (mmc)," *Energy Procedia*, vol. 20, pp. 227–236, 2012.

[89] M. Moranchel, E. Bueno, F. Rodriguez, and I. Sanz, "Implementation of nearest level modulation for modular multilevel converter," in *Power Electronics for Distributed*

Generation Systems (PEDG), 2015 IEEE 6th International Symposium on, pp. 1–5, IEEE, 2015.

[90] W. N. James and A. R. Susan, “Electric circuits,” *Addison-1996 Wesley Publishing Company, ISBN20*, vol. 140, no. 1, pp. 00–2, 2000.

[91] M. Buschendorf, J. Weber, and S. Bernet, “Comparison of igct and igbt for the use in the modular multilevel converter for hvdc applications,” in *Systems, Signals and Devices (SSD), 2012 9th International Multi-Conference on*, pp. 1–6, IEEE, 2012.

[92] F. Filsecker, R. Alvarez, and S. Bernet, “Comparison of 4.5-kv press-pack igbts and igcts for medium-voltage converters,” *IEEE Transactions on Industrial Electronics*, vol. 60, no. 2, pp. 440–449, 2013.

[93] S. Bernet, R. Teichmann, A. Zuckerberger, and P. K. Steimer, “Comparison of high-power igbt’s and hard-driven gto’s for high-power inverters,” *IEEE Transactions on Industry Applications*, vol. 35, no. 2, pp. 487–495, 1999.

[94] Westcode, “Press-pack IGBT’s.” `http://www.westcode.com/publicity/prod_lit/pub1.pdf`. Accessed: 07.05.17.

[95] ABB, “Press-pack IGBT and diode modules.” `http://new.abb.com/semiconductors/stakpak`. Accessed: 07.05.17.

[96] Toshiba, “Press-Pack IEGTs (PPIs) and Plastic Case Module IEGTs (PMIs).” `https://toshiba.semicon-storage.com/ap-en/product/bipolar-transistor/iegt.html`. Accessed: 07.05.17.

[97] ABB, “Integrated gate-commutated thyristors (IGCT).” `http://new.abb.com/semiconductors/integrated-gate-commutated-thyristors-(igct)`. Accessed: 07.05.17.

[98] Mitsubishi Electric, “Semiconductors & devices: Thyristors.” `http://www.mitsubishielectric.com/semiconductors/php/oSearch.php?FOLDER=/product/highpwdevice/thyristor`. Accessed: 07.05.17.

[99] CIGRE, “TB 604 2014 Guide for the Development of Models for HVDC Converters in a HVDC Grid.” `http://b4.cigre.org/Publications/Technical-Brochures`. Accessed: 08.05.17.

[100] W. Shen, F. Wang, D. Boroyevich, and C. W. Tipton IV, “High-density nanocrystalline core transformer for high-power high-frequency resonant converter,” *IEEE Transactions on Industry Applications*, vol. 44, no. 1, pp. 213–222, 2008.

[101] B. Theraja, A. Theraja, U. Patel, S. Uppal, J. Panchal, B. Oza, V. Thakar, M. Patel, and R. Patel, “A textbook of electrical technology vol ii,” *Chand & Co., New Delhi*, 2005.

[102] Y. Du, S. Baek, S. Bhattacharya, and A. Q. Huang, “High-voltage high-frequency transformer design for a 7.2 kv to 120v/240v 20kva solid state transformer,” in *IECON 2010-36th Annual Conference on IEEE Industrial Electronics Society*, pp. 493–498, IEEE, 2010.

[103] M. Leibl, G. Ortiz, and J. Kolar, “Design and experimental analysis of a medium frequency transformer for solid-state transformer applications,” *IEEE Journal of Emerging and Selected Topics in Power Electronics*, 2016.

[104] P. Shuai and J. Biela, “Design and optimization of medium frequency, medium voltage transformers,” in *Power Electronics and Applications (EPE), 2013 15th European Conference on*, pp. 1–10, IEEE, 2013.

[105] I. Gowaid, G. Adam, A. M. Massoud, S. Ahmed, D. Holliday, and B. Williams, “Quasi two-level operation of modular multilevel converter for use in a high-power dc transformer with dc fault isolation capability,” *IEEE Transactions on Power Electronics*, vol. 30, no. 1, pp. 108–123, 2015.

[106] I. Gowaid, G. P. Adam, S. Ahmed, D. Holliday, and B. W. Williams, “Analysis and design of a modular multilevel converter with trapezoidal modulation for medium and high voltage dc-dc transformers,” *IEEE Transactions on Power Electronics*, vol. 30, no. 10, pp. 5439–5457, 2015.

[107] H. A. B. Siddique, S. M. Ali, and R. W. De Doncker, “Dc collector grid configurations for large photovoltaic parks,” in *Power Electronics and Applications (EPE), 2013 15th European Conference on*, pp. 1–10, IEEE, 2013.

[108] H. A. B. Siddique and R. W. De Doncker, “Evaluation of DC Collector-Grid Configurations for Large Photovoltaic Parks,” *IEEE Transactions on Power Electronics*, 2017.

[109] Conversation with Arne Nysveen regarding transformers, 24. mar 2017.

[110] A. Hassanpoor, S. Norrga, and A. Nami, “Loss evaluation for modular multilevel converters with different switching strategies,” in *Power Electronics and ECCE Asia (ICPE-ECCE Asia), 2015 9th International Conference on*, pp. 1558–1563, IEEE, 2015.

[111] Siemens, “SIESTORAGE - The modular electrical energy storage system for a reliable power supply.” `http://w3.siemens.com/powerdistribution/global/SiteCollectionDocuments/en/mv/power-supply-solutions/siestorage/siestorage_brochure_en.pdf`, 2014. Accessed: 27.03.17.

[112] T. K. Vrana, Y. Yang, D. Jovcic, S. Dennetière, J. Jardini, and H. Saad, “The cigre b4 dc grid test system,” *Electra*, vol. 270, no. 1, pp. 10–19, 2013.

[113] H. Saad, S. Dennetière, J. Mahseredjian, P. Delarue, X. Guillaud, J. Peralta, and S. Nguefeu, “Modular multilevel converter models for electromagnetic transients,” *IEEE Transactions on Power Delivery*, vol. 29, no. 3, pp. 1481–1489, 2014.

[114] Email correspondence with Kamran Sharifabadi regarding MMC modeling approaches, 20. jan 2017.

[115] S. Sanchez, G. Bergna, and E. Tedeschi, “Tuning of control loops for grid-connected modular multilevel converters under a simplified port representation for large system studies,” in *2017 Twelfth International Conference on Ecological Vehicles and Renewable Energies (EVER)*, pp. 1–7, 2017.

[116] Mattia Marinelli, “Lecture 10: Storage systems topologies, modeling and grid

applications," 2016. Lecture notes in course 31778 Emerging Energy Technologies, Technical University of Denmark (DTU). Date: 18.04.16.

[117] X. Liu, P. Wang, and P. C. Loh, "A hybrid ac/dc microgrid and its coordination control," *IEEE Transactions on Smart Grid*, vol. 2, no. 2, pp. 278–286, 2011.

[118] Battery University, "BU-808b: What causes Li-ion to die?." `http://batteryuniversity.com/learn/article/bu_808b_what_causes_li_ion_to_die`, 2016. Accessed: 04.12.16.

Appendices

Appendix **A**

Appendix A: Harmonics

The equations in this appendix are based on the equations in [38, 41].

The harmonic component of order n is described by equations A.1 and A.2. n = 1 represents the fundamental frequency.

$$V_n = a_n cos(\frac{n\pi t}{L}) + b_n sin(\frac{n\pi t}{L}) \tag{A.1}$$

or

$$V_n = c_n sin(\frac{n\pi t}{L} + \phi_n) \tag{A.2}$$

where

$$c_n = \sqrt{a_n^2 + b_n^2} \tag{A.3}$$

$$a_n = \frac{1}{L}\int_0^{2L} v(t) cos(\frac{n\pi t}{L}) dt \tag{A.4}$$

$$b_n = \frac{1}{L}\int_0^{2L} v(t) sin(\frac{n\pi t}{L}) dt \tag{A.5}$$

$$sin\phi_n = \frac{a_n}{c_n} \tag{A.6}$$

$$cos\phi_n = \frac{b_n}{c_n} \tag{A.7}$$

The function $v(t)$ is given by equation (3.51)

$$v(t) = \frac{a_0}{2} + \sum_{n=1}^{\infty} a_n cos(\frac{n\pi t}{L}) + b_n sin\frac{n\pi t}{L} \tag{A.8}$$

where a_0 represents the DC component of the current or voltage waveform.

Appendix B

Appendix B: Clarke's and Park's Transformations

The equations in this appendix are based on [20].

Clarke's transformation matrix:

$$\begin{bmatrix} x_\alpha \\ x_\beta \\ x_0 \end{bmatrix} = \frac{2}{3} \begin{bmatrix} 1 & -\frac{1}{2} & -\frac{1}{2} \\ 0 & \frac{\sqrt{3}}{2} & -\frac{\sqrt{3}}{2} \\ \frac{1}{2} & \frac{1}{2} & \frac{1}{2} \end{bmatrix} \begin{bmatrix} x_a \\ x_b \\ x_c \end{bmatrix} \tag{B.1}$$

The inverse Clarke's transformation:

$$\begin{bmatrix} x_a \\ x_b \\ x_c \end{bmatrix} = \begin{bmatrix} 1 & 0 & 1 \\ -\frac{1}{2} & \frac{\sqrt{3}}{2} & 1 \\ -\frac{1}{2} & -\frac{\sqrt{3}}{2} & 1 \end{bmatrix} \begin{bmatrix} x_\alpha \\ x_\beta \\ x_0 \end{bmatrix} \tag{B.2}$$

Park's transformation matrix:

$$\begin{bmatrix} x_q \\ x_d \\ x_0 \end{bmatrix} = \begin{bmatrix} \cos(\omega) & \sin(\omega) & 0 \\ -\sin(\omega) & \cos(\omega) & 0 \\ 0 & 0 & 1 \end{bmatrix} \begin{bmatrix} x_\alpha \\ x_\beta \\ x_0 \end{bmatrix} \tag{B.3}$$

The inverse Park's transformation:

$$\begin{bmatrix} x_\alpha \\ x_\beta \\ x_0 \end{bmatrix} = \begin{bmatrix} \cos(\omega) & -\sin(\omega) & 0 \\ \sin(\omega) & \cos(\omega) & 0 \\ 0 & 0 & 1 \end{bmatrix} \begin{bmatrix} x_q \\ x_d \\ x_0 \end{bmatrix} \tag{B.4}$$

abc to dq0-transformation matrix:

$$\begin{bmatrix} x_q \\ x_d \\ x_0 \end{bmatrix} = \frac{2}{3} \begin{bmatrix} \cos(\omega t) & \cos(\omega t - \frac{2\pi}{3}) & \cos(\omega t + \frac{2\pi}{3}) \\ \sin(\omega t) & \sin(\omega t - \frac{2\pi}{3}) & \sin(\omega t + \frac{2\pi}{3}) \\ \frac{1}{2} & \frac{1}{2} & \frac{1}{2} \end{bmatrix} \begin{bmatrix} x_a \\ x_b \\ x_c \end{bmatrix} \tag{B.5}$$

dq0 to abc-transformation matrix:

$$\begin{bmatrix} x_a \\ x_b \\ x_c \end{bmatrix} = \begin{bmatrix} \cos(\omega t) & \sin(\omega t) & 1 \\ \cos(\omega t - \frac{2\pi}{3}) & \sin(\omega t - \frac{2\pi}{3}) & 1 \\ \cos(\omega t + \frac{2\pi}{3}) & \sin(\omega t + \frac{2\pi}{3}) & 1 \end{bmatrix} \begin{bmatrix} x_q \\ x_d \\ x_0 \end{bmatrix} \tag{B.6}$$

Figure B.1 shows the relations between the abc reference frame, the fixed $\alpha\beta0$ reference frame and the rotating $dq0$ reference frame.

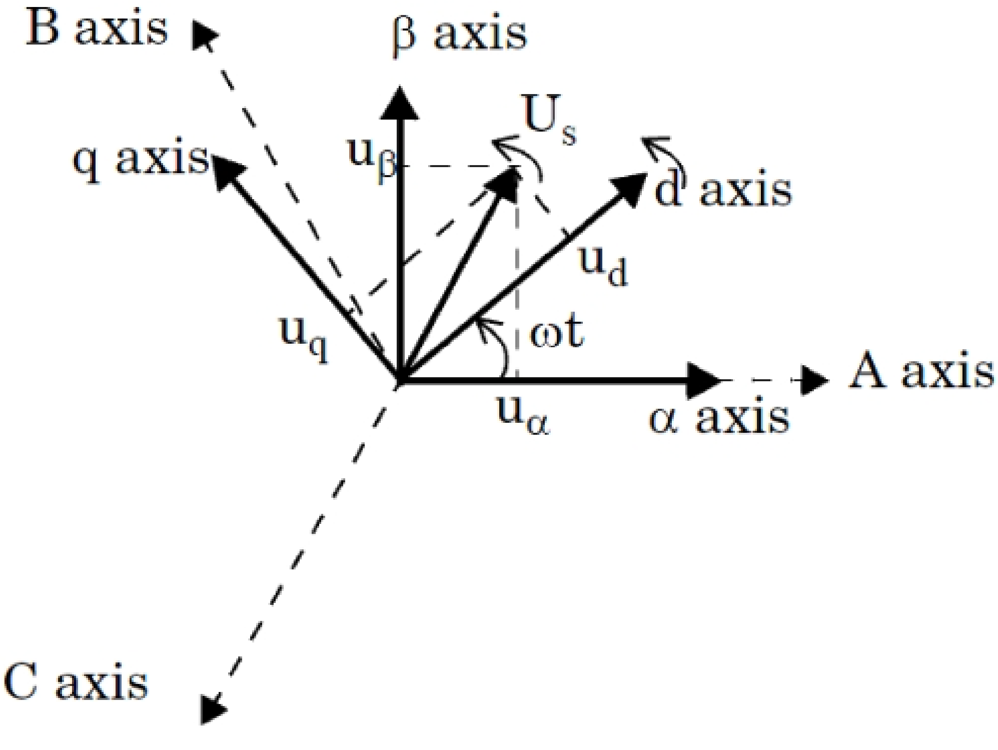

Figure B.1: abc, $\alpha\beta0$ and $dq0$ reference frames [20]

Appendix C

Appendix C: MATLAB scripts

C.1 MATLAB script for calculating the system parameters for the design part

MATLAB script used for calculating the parameters used in the design part of the report:

```
%%%%%%%%%%%%%%%%%%%%%%%%%%%%%%%%%%%%%%%%%%%%%%%%%%%%%%%%%%%%%%%
%%% Script for deciding the design parameters of the system %%%
%%%%%%%%%%%%%%%%%%%%%%%%%%%%%%%%%%%%%%%%%%%%%%%%%%%%%%%%%%%%%%%

close all
clear all
warning off

Vdc = 320e3; %DC-link voltage
Pwind = 1000e6; %Wind farm power capacity = 1 GW
fbat = 0.18; % The battery power is 10-20% of the wind farm capacity
Pbat = fbat * Pwind; %Battery power capacity
pf = 0.95; % Power factor

Vac = 400e3; %AC line RMS voltage Vac = (sqrt(3)*Vdc)/sqrt(2);
Vac_phase = Vac/sqrt(3); %AC phase RMS voltage
Sbat = Pbat/pf; %Apparent power of the battery
Swind = Pwind/pf; %Apparent power of the wind farm


%%%%%%%%%%%%%%%%%%%%%%%%%%%%%%%%%%%%%%%%%%%%%%%%%%%%%%%%%%%%%%%
%%%%%%%%%%%%%%%%%%%%%%%%%%%%% MMC %%%%%%%%%%%%%%%%%%%%%%%%%%%%%
%%%%%%%%%%%%%%%%%%%%%%%%%%%%%%%%%%%%%%%%%%%%%%%%%%%%%%%%%%%%%%%
Vmmc_dc = Vdc; %Voltage on the DC-side of the MMC
Vmmc_ac = Vac; %Voltage on the AC-side of the MMC
Vmmc_ac_phase = Vac_phase; %Phase voltage on the AC-side of the MMC
Pmmc = Pbat;
Immc_dc = Pmmc/Vmmc_dc; %DC-side current of the MMC
Smmc = Pmmc/pf; %Apparent power of the MMC
Immc_ac = (Smmc)/(3*Vmmc_ac_phase); %AC-side phase RMS current of the MMC
fc = 0.15; %Margin to acount for the circulating current
```

```
Immc_arm = (Immc_dc/3)+(Immc_ac/2)+(fc*Immc_ac); %MMC arm current that the semicondutors in the submodules must be able to withstand

%%%%%%%%%%%%%%%%%%%%%%%%%%%%%%%%%%%%%%%%%%%%%%%%%%%%%%%%%%%%%%%%%%%%%%%%
%==================================================================%
V_ce = 4500; %Collector-emitter voltage of the IGBT press-pack T0600TB45A from Westcode with Ic = 600 A.
%==================================================================%
%%%%%%%%%%%%%%%%%%%%%%%%%%%%%%%%%%%%%%%%%%%%%%%%%%%%%%%%%%%%%%%%%%%%%%%%

fsm = 0.67; %Safety margin of 33% since over-voltages are assumed due to the hard-switched PWM modulation
N = ceil(Vmmc_dc/(fsm*V_ce)); %Number of submodules in each arm of the MMC
aph = 2; %Number of arms per phase in the MMC
ph = 3; % Number of phases in the MMC
arms = aph*ph; %Total number of arms in the MMC
Ntot = arms * N; %Total number of submodules in the MMC


%%%%%%%%%%%%%%%%%%%%%%%%%%%%%%%%%%%%%%%%%%%%%%%%%%%%%%%%%%%%%%%%%%%%%%%%
%%%%%%%%%%%%%%%%%%%% Medium frequency transformer %%%%%%%%%%%%%%%%%%
%%%%%%%%%%%%%%%%%%%%%%%%%%%%%%%%%%%%%%%%%%%%%%%%%%%%%%%%%%%%%%%%%%%%%%%%
V_primary = Vmmc_ac; %Primary voltage of the transformer
n = 3; %Number of turns
Vsecondary = V_primary/n; %Secondary voltage of the transformer
ft = 300; %Operating frequency of the transformer, chosen to be < 1kHz
Pt = Pmmc; %Power capability
St = Pt/pf; %Apparent power capability


%%%%%%%%%%%%%%%%%%%%%%%%%%%%%%%%%%%%%%%%%%%%%%%%%%%%%%%%%%%%%%%%%%%%%%%%
%%%%%%%%%%%%%%%%%%%%%%%%%% 2L-VSC and battery %%%%%%%%%%%%%%%%%%%%%%%%
%%%%%%%%%%%%%%%%%%%%%%%%%%%%%%%%%%%%%%%%%%%%%%%%%%%%%%%%%%%%%%%%%%%%%%%%
V2L_ac = Vsecondary; %Line RMS voltage on the AC-side of the 2L-VSC
V2L_ac_phase = V2L_ac/sqrt(3); %Phase RMS voltage on the AC-side of the 2L-VSC
V2L_dc = sqrt(2)*V2L_ac/sqrt(3); %DC-volatge on the battery side
P2L = Pt; %Power rating of the 2L-VSC
S2L = P2L/pf; %Apparent power
I2L_dc = P2L/V2L_dc; %DC-side current of the 2L-VSC
I2L_ac = (S2L)/(3*V2L_ac_phase); %AC-side phase RMS current of the 2L-VSC. This is the current that the semiconductors must be able to withstand for half a period
Vbat = V2L_dc; %Battery voltage
Ibat = I2L_dc; %Battery current
%%%%%%%%%%%%%%%%%%%%%%%%%%%%%%%%%%%%%%%%%%%%%%%%%%%%%%%%%%%%%%%%%%%%%%%%
%==================================================================%
V_ce_2L = 6.5e3; %Blocking voltage of the IGBT: Westcode's Press-pack IGBT T0900DF65A with V_ce = 6500 V and I_c = 900 A
%==================================================================%
%%%%%%%%%%%%%%%%%%%%%%%%%%%%%%%%%%%%%%%%%%%%%%%%%%%%%%%%%%%%%%%%%%%%%%%%
f_marg = 0.67; %Safety margin of 33% since over-voltages are assumed due to the hard-switched PWM modulation
M = ceil(Vbat/(f_marg*V_ce_2L)); %Number of series-connections of IGBTs in each valve of the 2L-VSC for it to be able to block V_ce_2L
semiconductor_valves = 6; %Number of semiconductor valves in the 2L-VSC
```

```
Mtot = semiconductor_valves * M; %Total number of semiconductors used in the 2L–VSC

Vmodule = 1.2e3; %ABB EssPro Grid max battery module voltage
N_bat_parallel = 3; %Number of parallel battery strings in the battery
N_bat_series = ceil(Vbat/Vmodule); % Number of series connections of battery modules in order to get the desired battery voltage Vbat
Istring = Ibat/N_bat_parallel; %Current in each battery string
Pstring = Istring*Vbat; %Power of each battery string
Pmodule = Pstring/N_bat_series; %Power of each EssPro Grid battery module
t_discharge = 0.25; %Discharge time of the battery = 15 min
Emodule = Pmodule*t_discharge; %Energy per EssPro Grid module
N_bat_tot = N_bat_parallel*N_bat_series; %Total number of EssPro Grid battery modules used to create the battery system
```

C.2 MATLAB script for the total system

MATLAB script used for calculating the parameters used in the Simulink model of the whole system:

```
close all
clear all
warning off

%%%%%%%%%%%%%%%%%%%%%%%%%%%%%%%%%%%%%%%%%%%%%%%%%%%%%%%%%%%%%%%%%%%%%%%%%%%%%%%%
%%%%%%%%%%%%%%%%%%%%%%%%%%%%%%%% HVDC %%%%%%%%%%%%%%%%%%%%%%%%%%%%%%%%%%%%%%%%%
%%%%%%%%%%%%%%%%%%%%%%%%%%%%%%%%%%%%%%%%%%%%%%%%%%%%%%%%%%%%%%%%%%%%%%%%%%%%%%%%
Pbase=1000e6; %Base active power
pf=0.95; %Power factor
Sbase=Pbase/pf; %Base apparent power
Vbase=400e3/sqrt(3); %Base phase voltage % peak value
Ibase=2*Sbase/(3*Vbase); %Base current %peak
Vdcbase=2*Vbase; %DC base phase voltage def.
Idcbase=Sbase/Vdcbase;%Base DC current %or Idcbase = (3/2)*Ibase;
fbase=50; %Base frequency
wbase=2*pi*fbase; %Base rotational frequency
Zbase=Vbase/Ibase; %Base impedance
Zdcbase=Vdcbase/Idcbase; %Base DC impedance
Xlbase=Zbase; %Base reactance
Lbase=Xlbase/wbase; %Base AC inductance
Ldcbase=Zdcbase/wbase; %Base DC inductance
Cdcbase=1/(Zdcbase*wbase); %Base DC capacitance
fsw=2.5e3; %Switching frequency
Ts=100e-6; %Sampling time

%%% DESIGN OF THE VSC PARAMETERS L,R,C %%%
[Cvsc,Lvsc,Rvsc,kpvsc,kivsc,kpIout,kiIout,wbase,poles,Ta]= VSCpu(Vbase,
    Ibase,fsw);
%Cvsc: DC capacitor link vsc
%Lvsc: inductor AC vsc
%Rvsc: resistor AC vsc
%kpvsc: PI current Proportional gain, PI type: kp+ki/s
%kivsc: PI current integral gain
%kpIout: PI voltage Proportional gain, PI type: kp+ki/s
%kiIout: PI voltage integral gain
%wbase: base rotational speed
%poles:Information about the controllers and the current and voltage
%systems
%Ta: time constant of the sensor and PWM.
%%Frequency domain analysis controllers and RL system
figure
nyquist(tf(1,[Lvsc,Rvsc]),poles(1).Gci,poles(1).Gcv)
grid on
legend(['RL ';'Gci';'Gcv'])
figure
bode(tf(1,[Lvsc,Rvsc]),poles(1).Gci,poles(1).Gcv)
grid on
legend(['RL ';'Gci';'Gcv'])
%%%%%%%%%%%%%%%%%%%%%%%%%%%%%%%%%%%%%%%%%%%%%%%%%%%%%%%%%%%%%%%%%%%%%%%%%%%%%%%%
%%% Line design %%%
%Line between the two VSCs in the HVDC system
```

```
dist=200; %km
Cline_mtdc=dist*(0.1906e-6)/2; %in uF/km
Gline_mtdc=dist*(0.048e-6)/2;  %in uS/km
Lline_mtdc=dist*2.1120e-3; %in mH/km
Rline_mtdc=dist*0.0095;     %in ohm/km
%Line between the MMC and the DC-link
dist2=1.3; %km
Cline2_mtdc=dist2*(0.1906e-6)/2; %in uF/km
Gline2_mtdc=dist2*(0.048e-6)/2;  %in uS/km
Lline2_mtdc=dist2*2.1120e-3; %in mH/km
Rline2_mtdc=dist2*0.0095;     %in ohm/km
%%%%%%%%%%%%%%%%%%%%%%%%%%%%%%%%%%%%%%%%%%%%%%%%%%%%%%%%%%%%%%%%

%%%%%%%%%%%%%%%%%%%%%%%%%%%%%%%%%%%%%%%%%%%%%%%%%%%%%%%%%%%%%%%%
%%%%%%%%%%%%%%%%%%%%%%%%%%%%%% MMC %%%%%%%%%%%%%%%%%%%%%%%%%%%%%%
%%%%%%%%%%%%%%%%%%%%%%%%%%%%%%%%%%%%%%%%%%%%%%%%%%%%%%%%%%%%%%%%
% Paper used for the MMC model [1]: "Tuning of Control Loops for Grid-Connected Modular Multilevel Converters under a simplified Port Representation for Large System Studies", Santiago Sanchez, Gilbert Bergna, Elisabetta Tedeschi, 2017

Pb = 180e6; %Base active power
pf=0.95; %Power factor
Sb=Pb/pf; %Base apparent power
v_b=400e3/sqrt(3); %Base phase voltage % peak value
i_b=2*Sb/(3*v_b); %Base current %peak
v_dcb=2*v_b; %DC base voltage def.
i_dcb=Sb/v_dcb; %Base DC current %or Idcbase = (3/2)*Ibase;
fb=50; %Base frequency
wb=2*pi*fb; %Base rotational frequency
Zb=v_b/i_b; %Base impedance
Zdcb=v_dcb/i_dcb; %Base DC impedance
Lb=Zb/wb; %Base inductance
Cb = 1/Zb; %Base capacitance to get Cpu in [ms]
Ldcb=Zdcb/wb; %Base DC-side inductance
Cdcb=1/(Zdcb*wb); %Base DC-side capacitance
fco=2e3; %Cut-off requency, defines the bandwith of the controllers. fo=2000Hz is used in the paper [1]
Tfi = 1/(2*pi*fco);
R_DC=0.001; %Small resistance in series to the DC-voltage soure on the DC-side of the MMC the stand alone-model and in the model used for case 1

%Parameters in pu-values based on the pu-values obtained with the model in
%the paper by Santiago and Gilbert using vb=400kV and Sb=1200MVA
Ceqpu=0.0042;
Rpu=0.0047;
Lpu=0.1469;
Rdcpu=7.5212e-4;
Ldcpu=0.0120;

%SI-values of these parameters calculated based on equations defined in [1]
Rdc=Rdcpu*Zdcb;
Ra=(3/2)*Rdc;
Ldc=Ldcpu*Ldcb;
La=(3/2)*Ldc;
R=Rpu*Zb;
```

```
L=Lpu*Lb;
Rf=R-(Ra/2);
Lf=L-(La/2);
Ceq=Ceqpu*Cb;

Narms=2;%Number of arms per phase leg
Wref=2*Narms*Ceq*(v_b)^2; %Energy reference

%%%%% AC-side PI controller gains %%%%%
k = 1/Rpu;
T = Lpu/(wb*Rpu);
Tf = Tfi;
Kpac = T/(2*Tf*k);
Ti = T;
Kiac = Kpac/Ti;
%%%%% DC-side PI controller gains %%%%%
k = 1/Rdcpu;
Tdc = Ldcpu/(wb*Rdcpu);
Tf = Tfi;
Kpdc = Tdc/(2*Tf*k);
Ti = Tdc;
Kidc = Kpdc/Ti;
%%%%% Energy balance PI controller gains %%%%%
Ta = Tfi;
Teq = 2*Ta;
b = wb/(8*Ceqpu);
p = 1/Teq;
alpha = 6;
phiw=asin((alpha-1)/(alpha+1));
z = p/alpha;
wm = sqrt(z*p);
kpw = wm/b;
kiw = kpw*z;

%%% Real internal AC loop %%%
tau = Lpu/(Rpu*wb);
Hpi = tf(1/Rpu,[tau,1])*tf(1,[Tfi,1]);%System
Hci = tf([Kpac,Kiac],[1,0]);%Controller
Holac = Hpi*Hci;%Open loop transfer function
Hclac = feedback(Holac,1);%Closed loop transfer function
%%% Real internal DC loop %%%
taudc = Ldcpu/(Rdcpu*wb);
Hpidc = tf(1/Rdcpu,[taudc,1])*tf(1,[Tfi,1]);
Hcidc = tf([Kpdc,Kidc],[1,0]);
Holdc = Hpidc*Hcidc;
Hcldc = feedback(Holdc,1);
%%%% Transfer functions of the energy balancing part %%%%
Hin = tf(1,[Teq,1]); %Equivalent inner system
Hout = tf(b,[1,0]); %Energy transfer function
Hc = tf([kpw,kiw],[1,0]); %Controller transfer function
Hol = Hin*Hout*Hc; %Open loop transfer function
HclW = feedback(Hol,1); %Closed loop transfer function

figure
bode(Hclac,Hcldc,HclW)
grid on
```

```

%%%%%%%%%%%%%%%%%%%%%%%%%%%%%%%%%%%%%%%%%%%%%%%%%%%%%%%%%%%%%%%%%%%%%%%%%%%%%
%%%%%%%%%%%%%%% Medium frequency transformer %%%%%%%%%%%%%%%%%%%%%
%%%%%%%%%%%%%%%%%%%%%%%%%%%%%%%%%%%%%%%%%%%%%%%%%%%%%%%%%%%%%%%%%%%%%%%%%%%%%
Vbaset=400e3/sqrt(3); %Base AC phase voltage (peak voltage)
Pbaset=180e6; %Base active power
Sbaset=Pbaset/pf; %Base apparent power
Ibaset=2*Sbaset/(3*Vbaset); %Base current %peak
ft=50; %Operating freqency for the transformer
n=3; %Turns ratio
Vbasets=Vbaset/n; %Base AC phase voltage (peak voltage) on the secondary
Ibasets=Ibaset/n;
R_trafo = (Vbasets)^2/Sbaset; %Resistance on the secondary side for the stand-alone model of the transformer

%%%%%%%%%%%%%%%%%%%%%%%%%%%%%%%%%%%%%%%%%%%%%%%%%%%%%%%%%%%%%%%%%%%%%%%%%%%%%
%%%%%%%%%%%%%%%%%%%%%%%%%%%%%%%% 2L-VSC %%%%%%%%%%%%%%%%%%%%%%%%%%%%%%%
%%%%%%%%%%%%%%%%%%%%%%%%%%%%%%%%%%%%%%%%%%%%%%%%%%%%%%%%%%%%%%%%%%%%%%%%%%%%%
Pbase2L=180e6; %Base active power = Battery power
pf=0.95; %Power factor
Sbase2L=Pbase2L/pf; %Base aparent power
Vbase2L=Vbasets; %Base phase voltage % peak value on the AC-side of the 2L converter = voltage on the secondary of the transformer
Ibase2L=2*Sbase2L/(3*Vbase2L); %Base current %peak on the AC-side
Vdcbase2L=2*Vbase2L; %DC base voltage def. %This is the battery voltage
Idcbase2L=Sbase2L/Vdcbase2L; %Battery current % Base DC current = (3/2)*Ibase;
fbase2L=50; %Base frequency
wbase2L=2*pi*fbase2L; %Base rotational frequency
Zbase2L=Vbase2L/Ibase2L; %Base impedance
Zdcbase2L=Vdcbase2L/Idcbase2L; %Base DC impedance
Xlbase2L=Zbase2L; %Base reactance
Lbase2L=Xlbase2L/wbase2L; %Base inductance
Ldcbase2L=Zdcbase2L/wbase2L; %Base DC inductance
Cdcbase2L=1/(Zdcbase2L*wbase2L); %Base DC capacitance
%fsw=2.5e3; % Switching frequency
Ro = 0.001; %Small resistor in parallel with the Battery (ideal DC voltage soure) in order to make the model run
R1 =(Vbase2L^2)/Sbase2L; %Resitor at the three-phase side of the 2L-VSC when testing the stand-alone 2L-VSC
amplitude = 1.0; %Amplitude of the sinusoidal signals to control the AC-side voltage of the 2L-VSC
Ebase=Pbase2L*wb; %Energy base
Qpu=Pbase2L*(0.25/60)*3600/Ebase; %Battery capacity in terms of power and energy in pu, used in the battery SOC model

%%% DESIGN OF THE VSC PARAMETERS L,R,C %%%
%%%% Parameter calculations %%%%

%Values from Cigre B4 HVDC:
rpu2L=0.01; %filter resistance %pu resistor from Cigre B4 HVDC
Lpu2L=0.255; %PU inductor AC from Cigre B4 HVDC
Cpu2L=60e-3; %DC capacitor design PU from Cigre B4 HVDC in ms

%Rvsc: resistor AC vsc
Rvsc2L=rpu2L*Zbase2L;  %SI-value resistance
```

```

%Lvsc: inductor AC vsc
Lvsc2L=Lpu2L*Lbase2L; %SI-value inductance

%Cvsc: DC-link capacitor vsc
Cvsc2L=Cpu2L/Zdcbase2L; %SI-value DC-capacitance
```

C.3 MATLAB script for the calculation of the pu-values of the parameters

This MATLAB script is used to calculate the pu-values of the parameters of the MMC that is used in the script in section C.2. The calculations are based on the model and the values used in [115]:

```
%%% Calculation of pu-values of parameters for the MMC based on the SI-values used in the paper [1] and the base values Vb=400kV and Sb=1200MVA %%%

%%%%%%%%%%%%%%%%%%%%%%%%%%%%%%%%%%%%%%%%%%%%%%%%%%%%%%%%%%%%%%%%%%%%%%%%%%%%%%%%%%%%%%%%%%
% Paper used for the MMC model [1]: "Tuning of Control Loops for Grid-Connected Modular Multilevel Converters under a simplified Port Representation for Large System Studies", Santiago Sanchez, Gilbert Bergna, Elisabetta Tedeschi, 2017
%%%%%%%%%%%%%%%%%%%%%%%%%%%%%%%%%%%%%%%%%%%%%%%%%%%%%%%%%%%%%%%%%%%%%%%%%%%%%%%%%%%%%%%%%%

close all
clear all
warning off

%%% Base values used in the paper %%%
Sb=1200e6; %Base apparent power
v_b=400e3;%Base phase voltage % peak value

%%% Definitions %%%
i_b=2*Sb/(3*v_b); %Base current %peak
v_dcb=2*v_b; %DC base voltage def.
i_dcb=Sb/v_dcb;%(3/2)*Ibase; %Base DC current
fb=50; %Base frequency
wb=2*pi*fb; %Base rotational frequency
Zb=v_b/i_b; %Base impedance
Zdcb=v_dcb/i_dcb; %Base DC impedance
Lb=Zb/wb; %Base inductance
Cb = 1/(Zb); %Base capacitance to get Ceqpu in [ms]
Ldcb=Zdcb/wb; % Base DC inductance
Cdcb=1/(Zdcb*wb); %Base DC capacitance

%%% Parameters %%%
Ra = 0.6017;% Value from the CIGRE-guide for HVDC grids
La = 30.6e-3;% Value from the CIGRE-guide for HVDC grids
Rf = 0.6438;% Value from the CIGRE-guide for HVDC grids
Lf = 78.2e-3;% Value from the CIGRE-guide for HVDC grids
Ceq = 21.16e-6;% Value from the CIGRE-guide for HVDC grids

%%% Definitions %%%
R = Rf+(Ra/2); %AC-side resistance
L = Lf+(La/2); %AC-side inductance
Rdc = (2/3)*Ra; %DC-side resistance
Ldc = (2/3)*La; %DC-side inductance

%%% Calculation of pu-values %%%
Ceqpu = Ceq/Cb;
Rpu = R/Zb;
```

```
Lpu = L/Lb;
Rdcpu = Rdc/Zdcb;
Ldcpu = Ldc/Ldcb;
```

C.4 VSCpu function

This function is used in the script in section C.2.

```
%%%%%%%%%%%%%%%%%%%%%%%%%%%%%%%%%%%%%%%%%%%%%%%%%%%%%%%%%%%%%%%%%%%%%%%%
%%%%%%%%%%%%%%%%%%%%%%%Design VSC PU
function [Cvsc,Lvsc,Rvsc,kpvsc,kivsc,kpIout,kiIout,wbase,poles,Ta]= VSCpu(
    Vbase,Ibase,fsw)
Vllbase=Vbase*sqrt(3/2); % Line-to-line RIM-value
Vdcbase=2*Vbase; %DC base voltage
Zbase=Vbase/Ibase; %Zbase AC
Sbase=3*Ibase*Vbase/2; %AC base apparent power
wbase=2*pi*50; %AC base rotational speed
Idcbase=Sbase/Vdcbase; %Idc base current
Deltai=0.15*Ibase; %Maximum ripple of the current
%%%%%%%%%
Lbase=Zbase/wbase; %Base inductance
rpu=0.01; %Filter resistance %pu resistor from Cigre B4 HVDC
R2=rpu*Zbase;  %Resistance in SI-value
Lpu=0.255; %Inductance in pu-value, AC from Cigre B4 HVDC
L2=Lpu*Lbase; %Inductane in SI-value
Cbase=1/(Zbase*wbase);  %AC base capacitance
%%%%%%%%%%%%%%%%%%%%%%%%%%%%%%%%%%%%%%%%%%%%%%%%%%%%%%%%%
%%%%%%%%%%%%%%%%%%%%%%%%%%%%%%%%%%%%%%%%%%%%%%%%%%%%%%%%%%
%%%%%%%%%%%%%%%%% Capacitor DC design  %%%%%%%%%%%%%%%%%%%%%
Zdcbase=Vdcbase/Idcbase; %DC base impedance
Cdcbase=1/(wbase*Zdcbase); %DC base capacitance
a=1; %If a=-1 is martas paper Cpu and a=1 is normal Cpu
Cpu=60e-3; %DC capacitor design PU from Cigre B4 HVDC in ms
C2=Cpu/Zdcbase; %DC-side capacitance in SI-units
Cpudc=Cpu;  %DC capacitance i pu
%%%%%%%%%%%%%%%%%%%%%%%%%%%%%%%%%%%%%%%%%%%%%%%%%%%%%%%%%%
%%%%%%%%%%%%%%%%%%%%%%%%%%%%%%%%%%%%%%%%%%%%%%%%%%%%%%%%%%
%%%%%%%%%%%%%%%%%%%%%%%%%%%%%%%%%%%%%%%%%%%%%%%%%%%%%%%%%
%%%%%%%%%%%%%%%%%Control design %%%%%%%%%%%%%%%%%%%%%%%%%%%%
%%%%%%%%%%%%%%%%%%%%%%%%%%%%%%%%%%%%%%%%%%%%%%%%%%%%%%%%%%
%%%%%%%%Inner loop modulus optimum
taupu=Lpu/rpu; %Tao without wbase
Ta=1.5/(fsw);  %PWM and analog sensors approximation
%%%Kp=(1/2)*(taupu*rpu/(wbase*Ta))
kpvsc=(1/2)*(taupu*rpu/(wbase*Ta)); %Proportional gain
%%%%Ti=taupu/wbase %Integrator time
Tivsc=taupu/wbase; %Integrator time
kivsc=kpvsc/Tivsc;% %Integrator gain
%%%%Closed loop inner system
wo=1/(sqrt(2)*Ta); %Control freq
ro=Ta*wo; %Ro optimal approx=0.707
%%%%%%%%%%%%%%%%%
%%%%%%%%%%%%%%%%%%%%%%%%%%%%%%%%%%%%%%%%%%%%%%%%%%%%%%%%%%%%%%%%
%%%%%%%%%%DC voltage controller design
%%Outer loop  Controller with the lead compensator network design
Teq=2*Ta;  %equivalent time constant inner loop
p=1/Teq; %pole of the inner loop
alpha=6; %gain to obtain the z smaller than p
phi=asin((alpha-1)/(alpha+1)); %phase margin defined by alpha
z=p/alpha; %zero for the control design
```

```
wcut=sqrt(z*p); %Freq for max peak phase margin
if a==-1 % if a=-1 as Paper Understanding PI controller VSC
     b=1/(Cpudc*wbase);
     Kvv=b*wcut;
else %normal pu for Cdc
     Kvv=(Cpudc/wbase)*wcut;
end
kpIout=Kvv;%%PI voltage proportional gain
kiIout=Kvv*z; %%PI voltage integral gain

%%%%%%%%%%%%%%%%%%%%%%%%%%%%%%%%%%%%%%%%%%%%%%%%%%%%%%%%%%%%%%%%%%%%%%%
Lvsc=L2; Rvsc=R2; Cvsc=C2; %parameters to return
%%%%%%%%%%%%%%%%%%%%%%%%%%%%%%%%%%%%%%%%%%%%%%%%%%%%%%%%%%%%%%%%%%
%%%%Controllers analysis inner and outer
%%%poles analysis
kk=wbase/Lpu;
if a==-1
     kc=wbase*Cpudc;
else
     kc=wbase/Cpudc;
end

poles(1).RL=-Rvsc/Lvsc;
poles(1).I=roots([1,kk*kpvsc,kk*kivsc]);
poles(1).V=roots([1,kc*kpIout,kc*kiIout]);
wo2=sqrt(kc*kiIout);%/wbase
wo=sqrt(kk*kivsc);%/wbase
poles(1).w=[wo,wo2];
poles(1).RLtf=tf(1,[Lvsc,Rvsc]);
poles(1).Gci=tf([kk*kpvsc,kk*kivsc],[1,kk*kpvsc,kk*kivsc]);
poles(1).Gcv=tf([kc*kpIout,kc*kiIout],[1,kc*kpIout,kc*kiIout]);
return
```

Appendix **D**

Appendix D: Simulink models

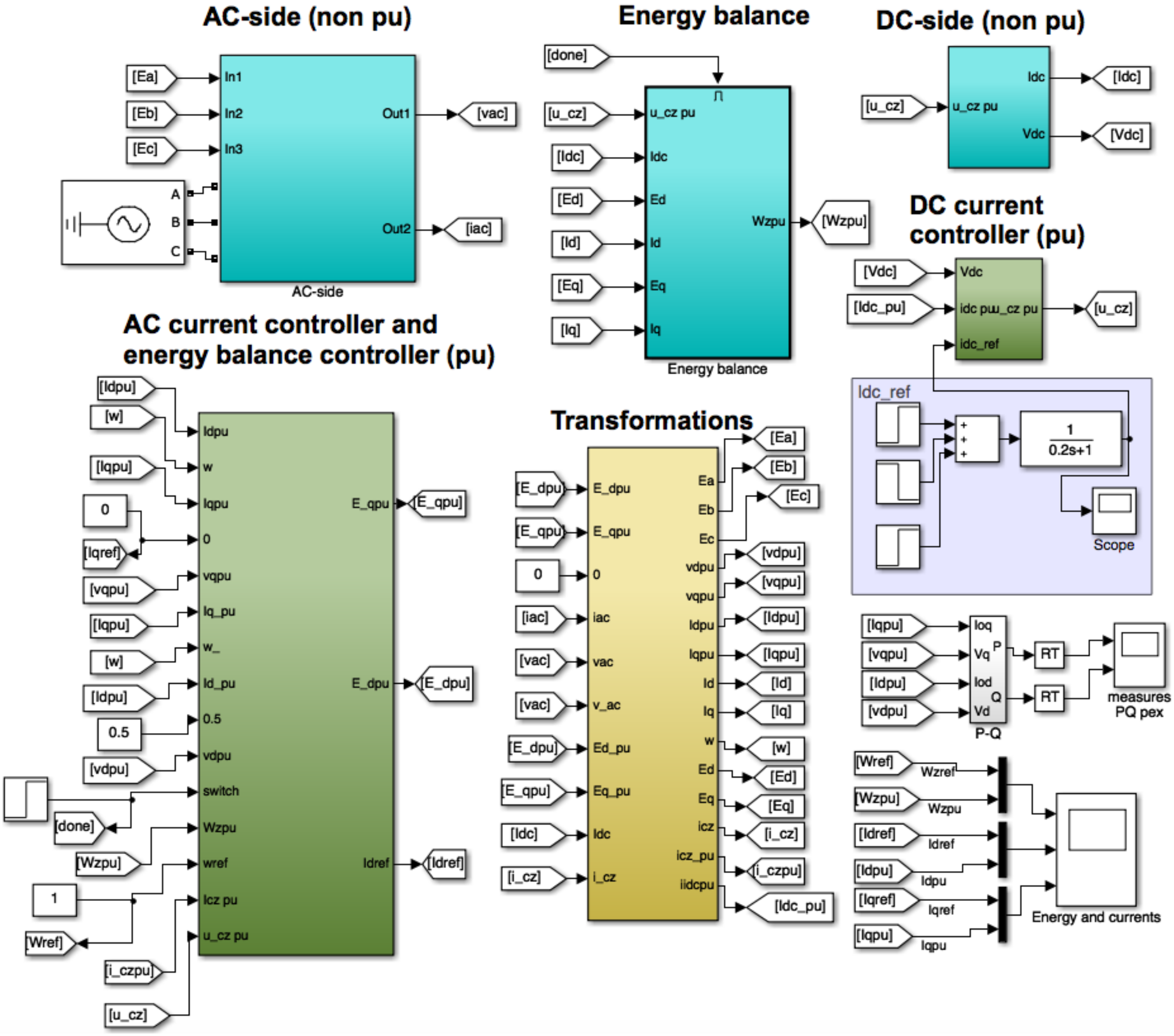

Figure D.1: Simulink model of the stand alone simplified AVM-MMC model

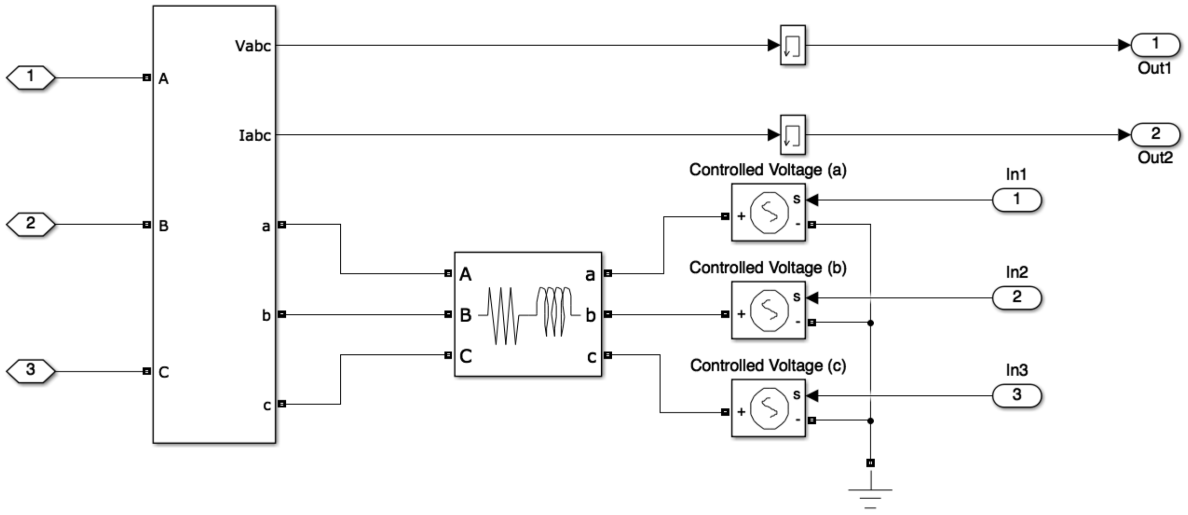

Figure D.2: Simulink model of the AC-side of the stand alone simplified AVM-MMC model

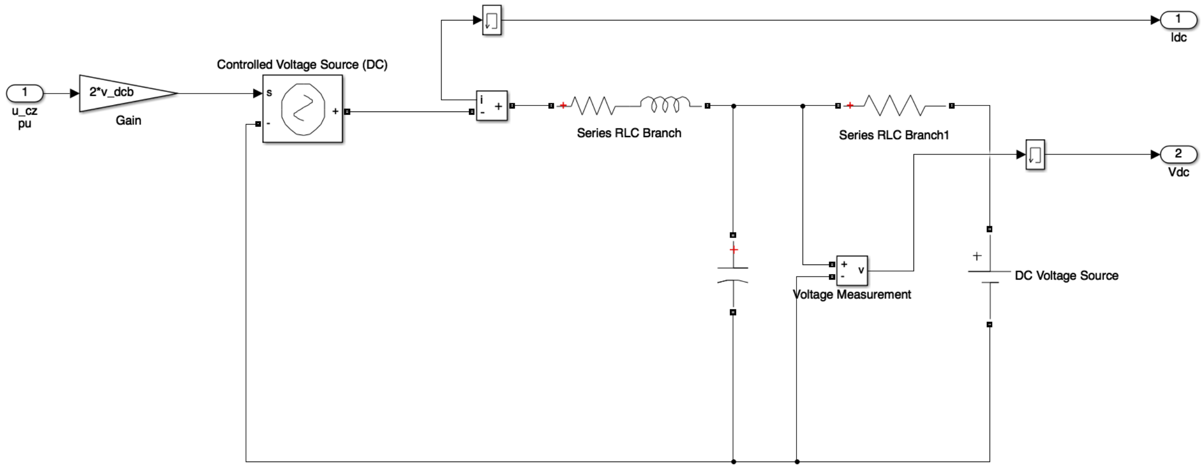

Figure D.3: Simulink model of the DC-side of the stand alone simplified AVM-MMC model

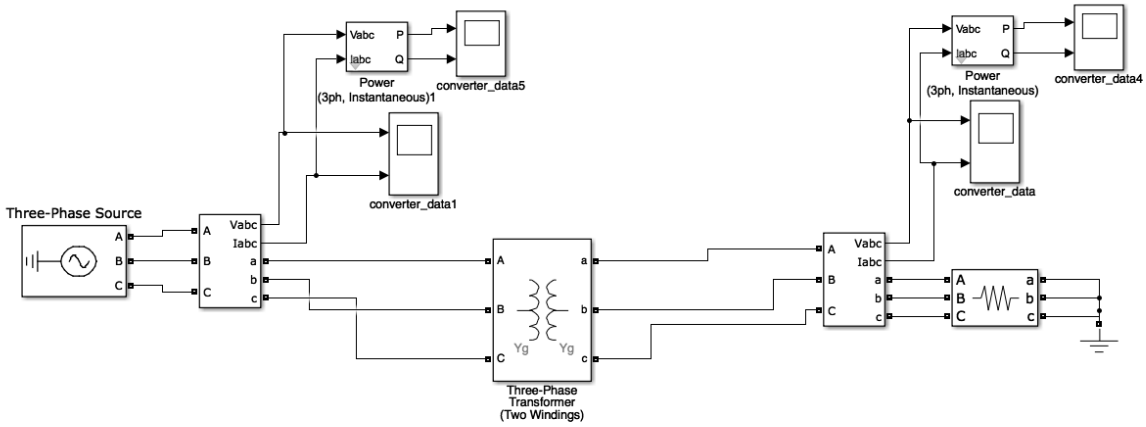

Figure D.4: Simulink model of the stand-alone coupling transformer model

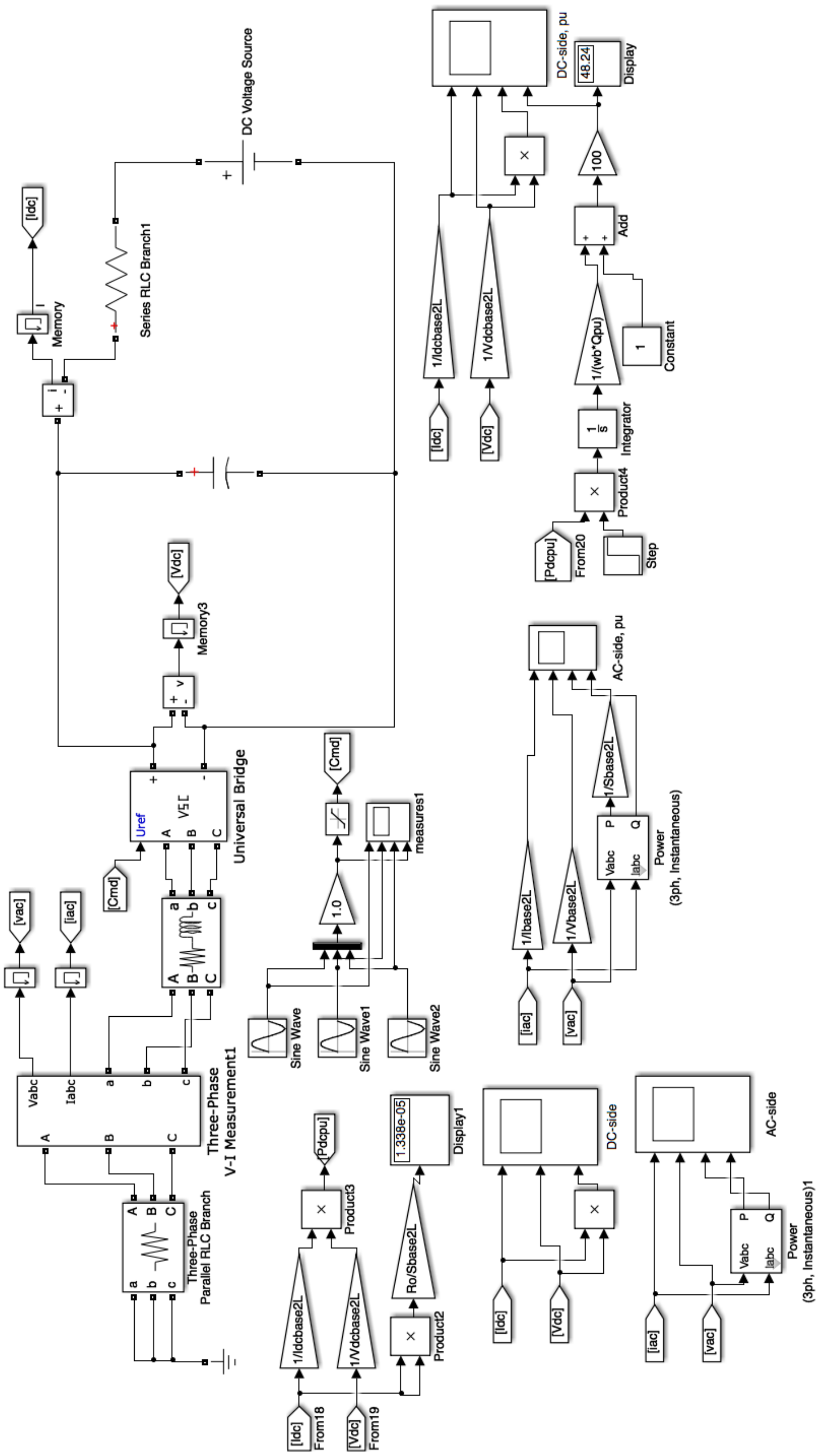

Figure D.5: Simulink model of the stand-alone 2L-VSC connected to the battery

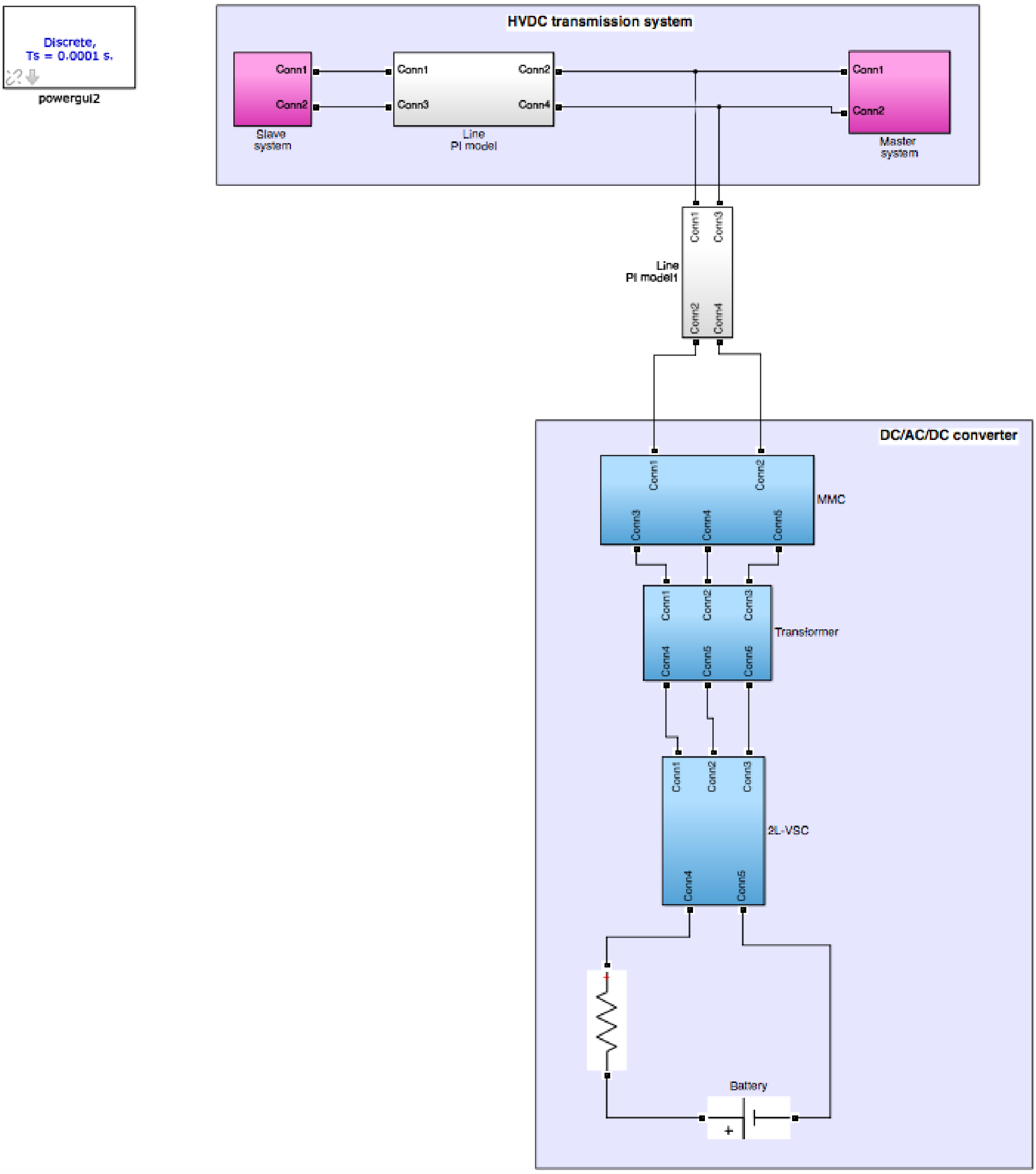

Figure D.6: Simulink model of the system

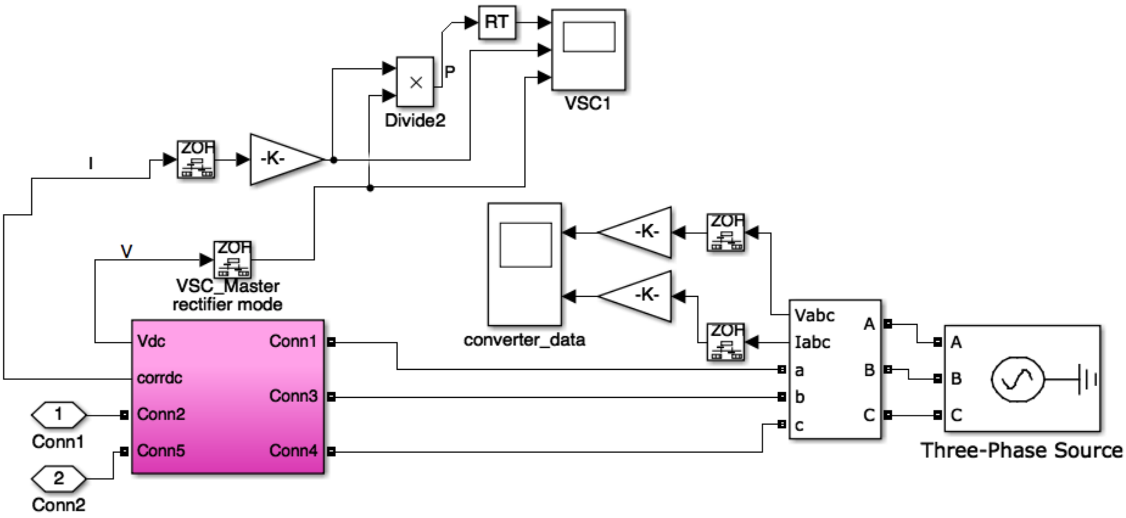

Figure D.7: Simulink model of the 2L-VSCs of the HVDC system

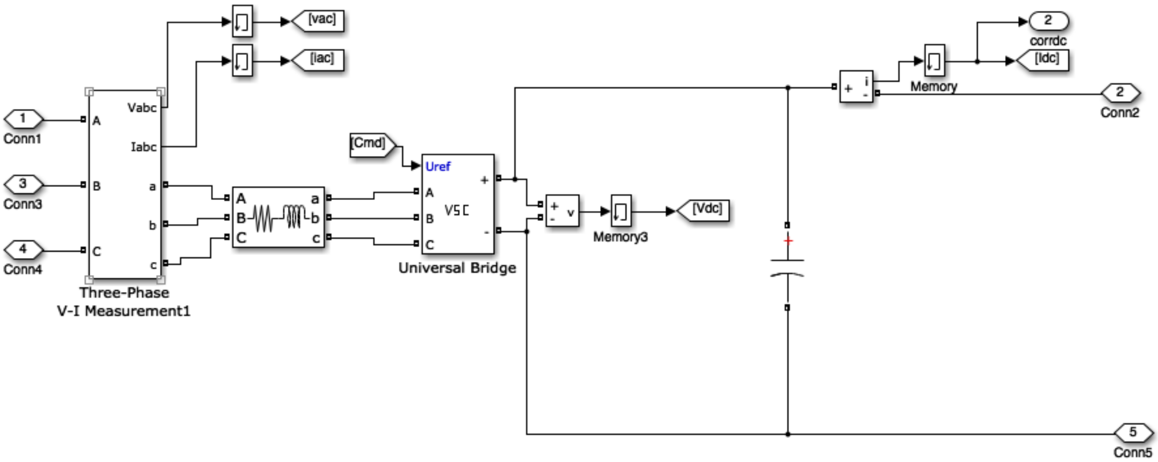

Figure D.8: The circuit of the 2L-VSCs of the HVDC system

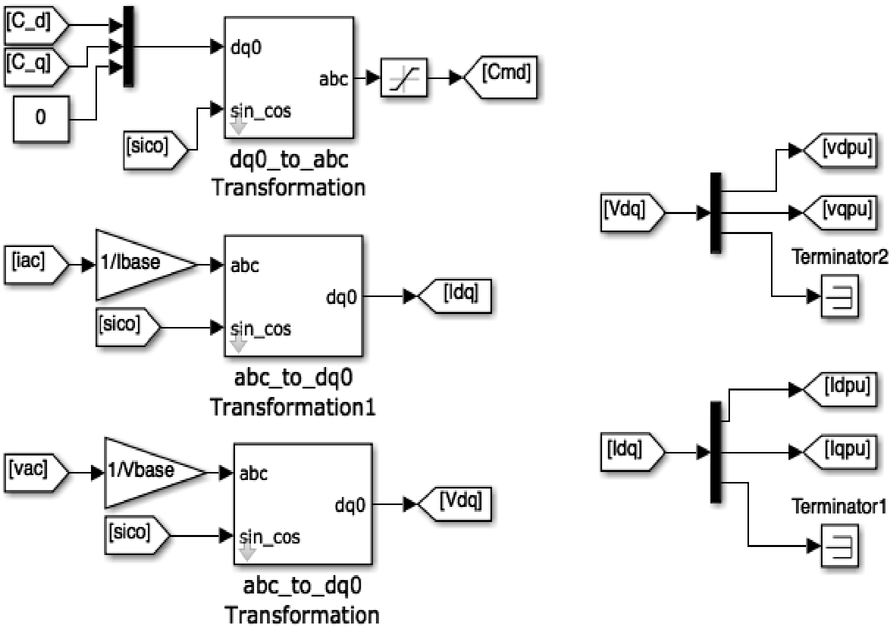

Figure D.9: Transformations used in the 2L-VSCs of the HVDC system

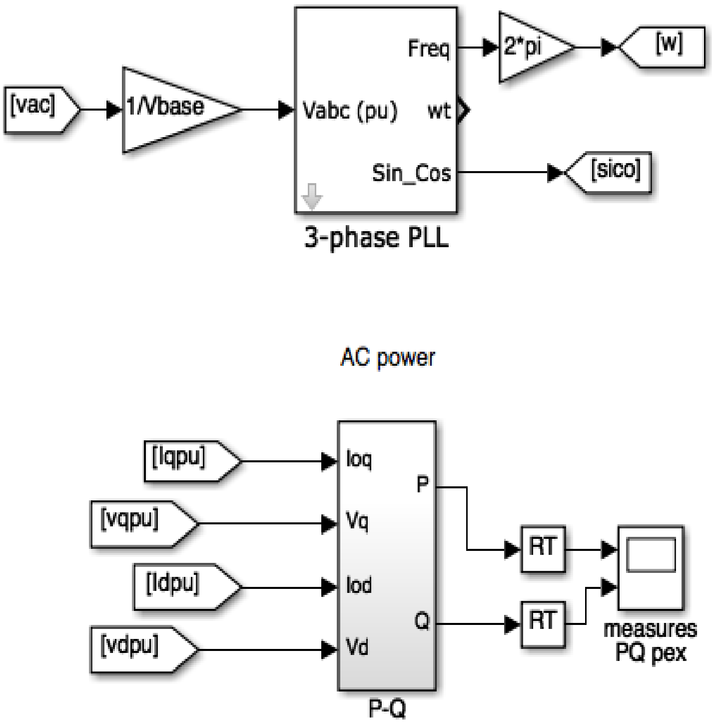

Figure D.10: PLL used in the 2L VSCs of the HVDC system and power output

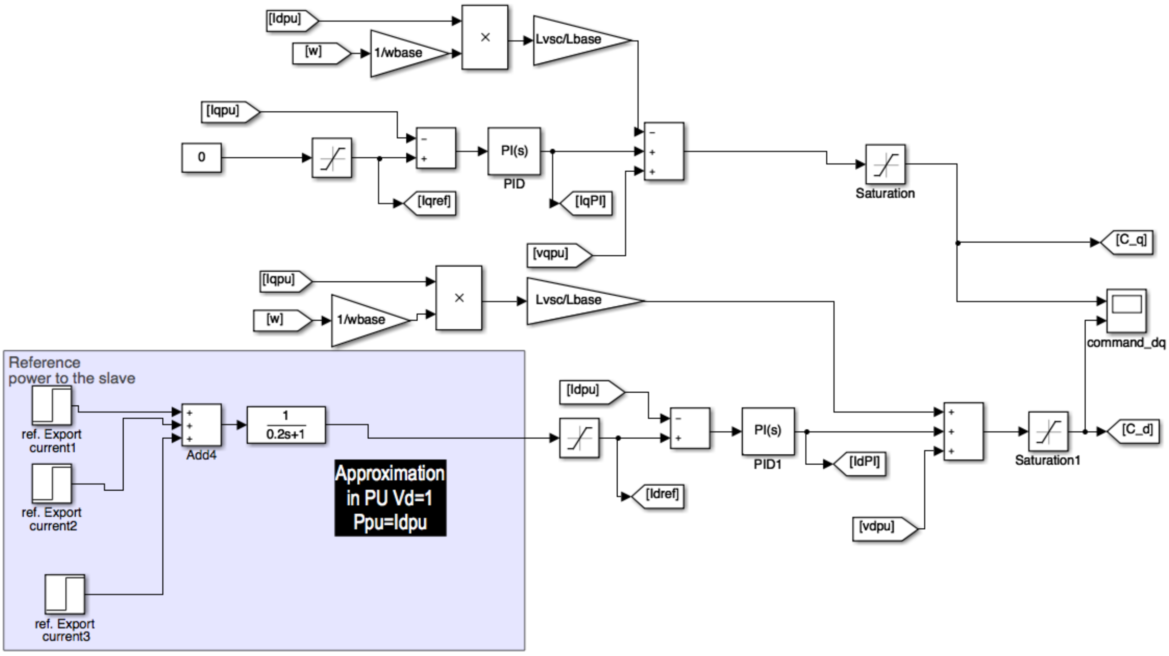

Figure D.11: Current controller on the 2L slave of the HVDC system

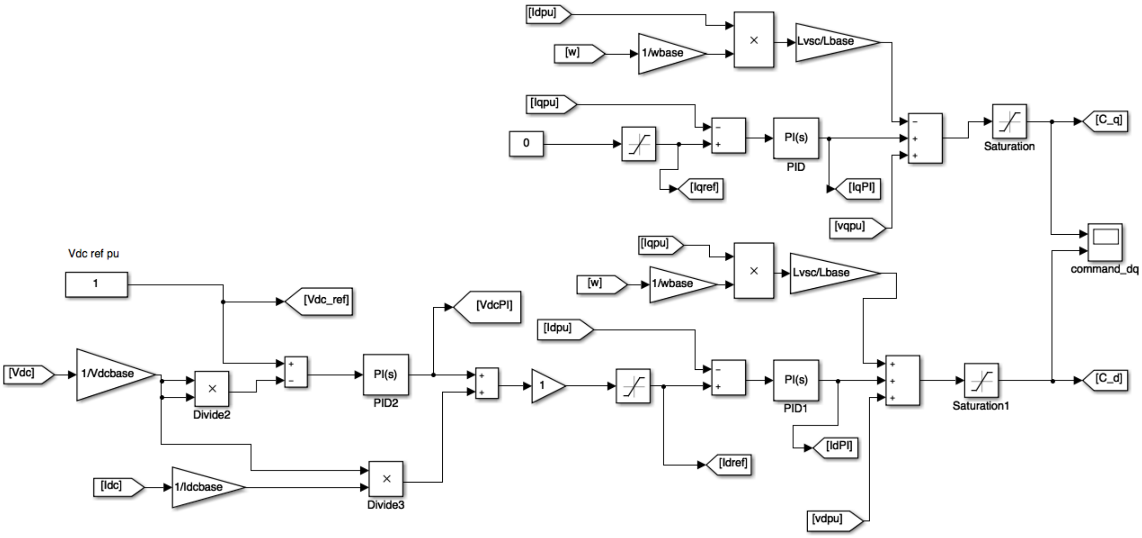

Figure D.12: Current and voltage controller on the 2L master of the HVDC system

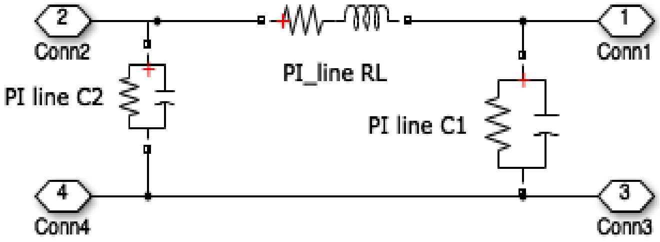

Figure D.13: Simulink model of the transmission lines

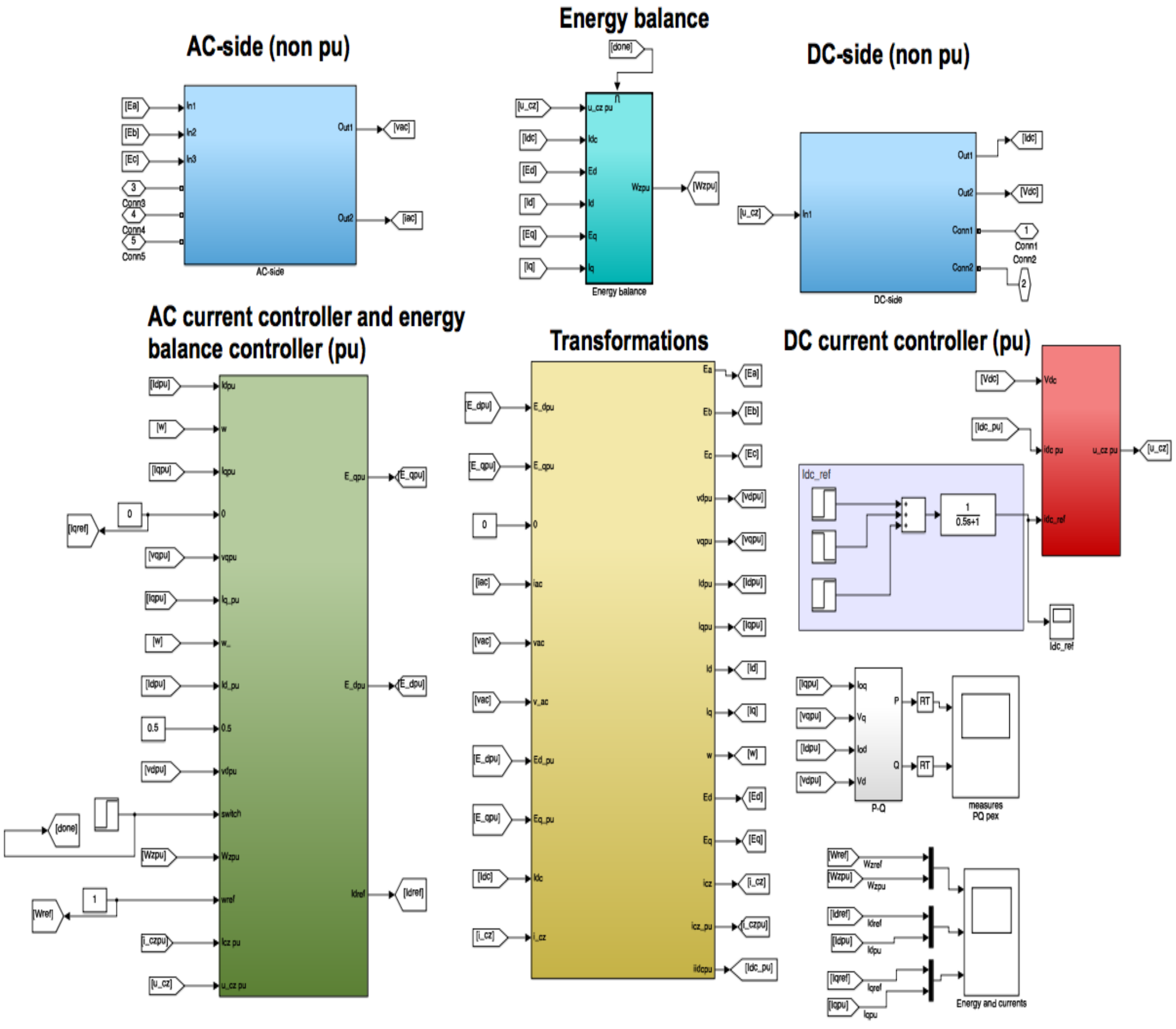

Figure D.14: Overview of the MMC model and controllers

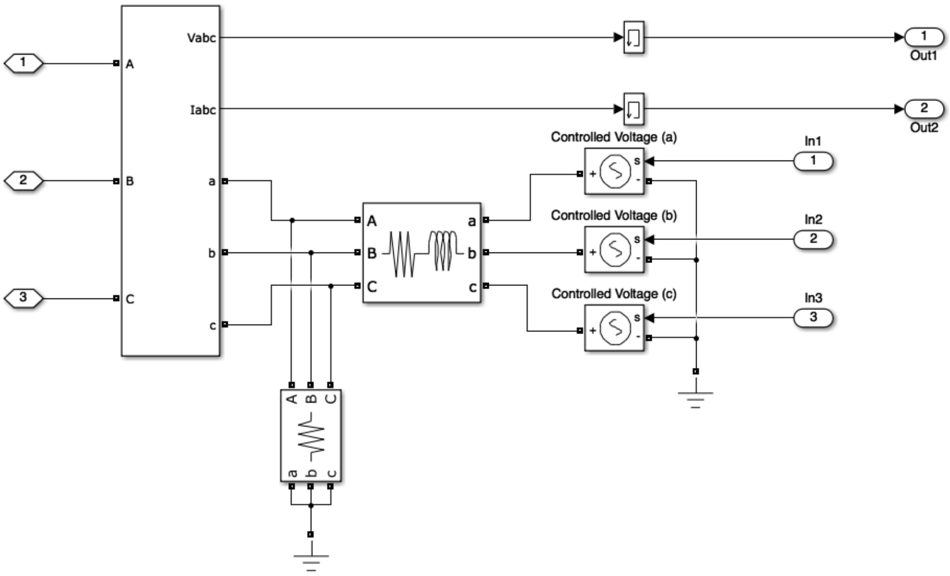

Figure D.15: MMC AC-side circuit

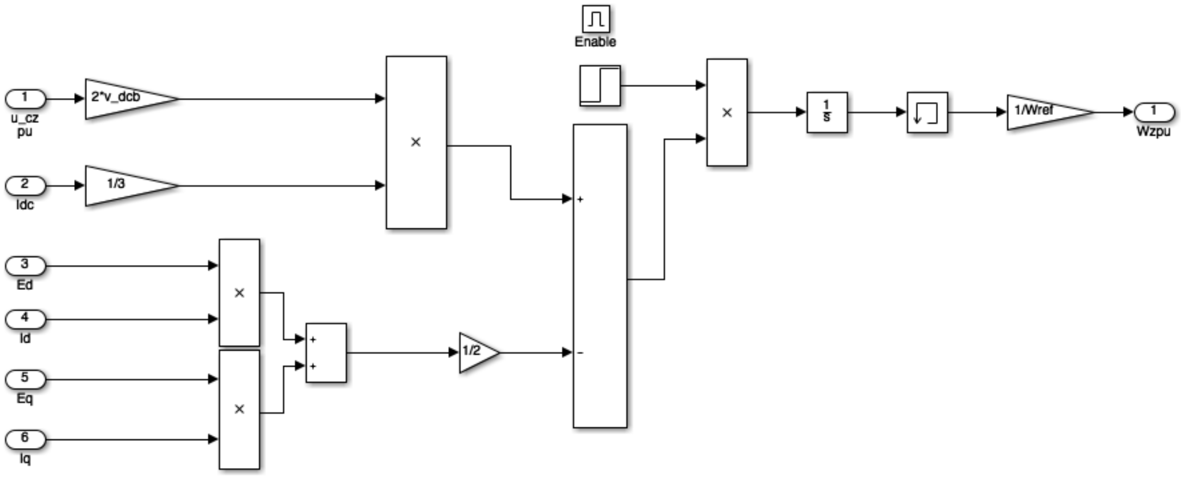

Figure D.16: MMC energy balance

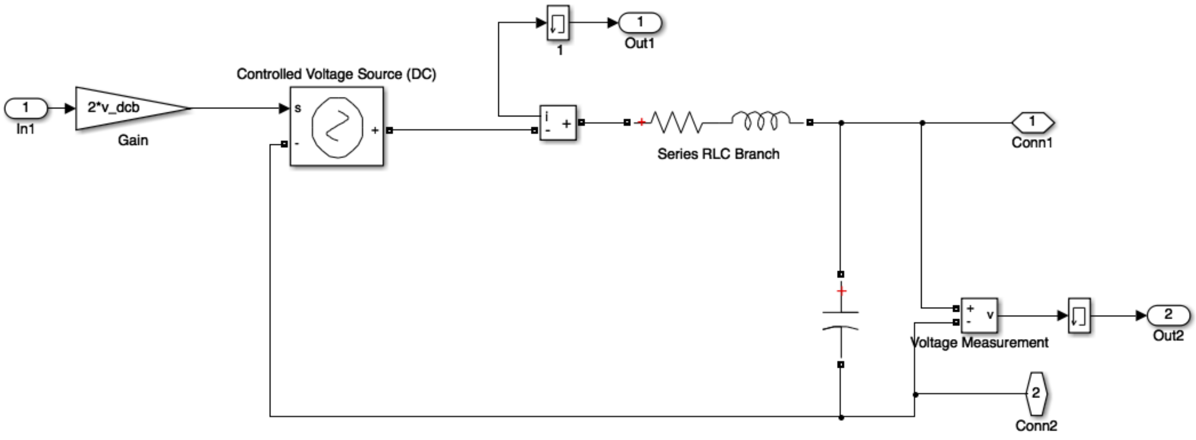

Figure D.17: MMC DC-side circuit

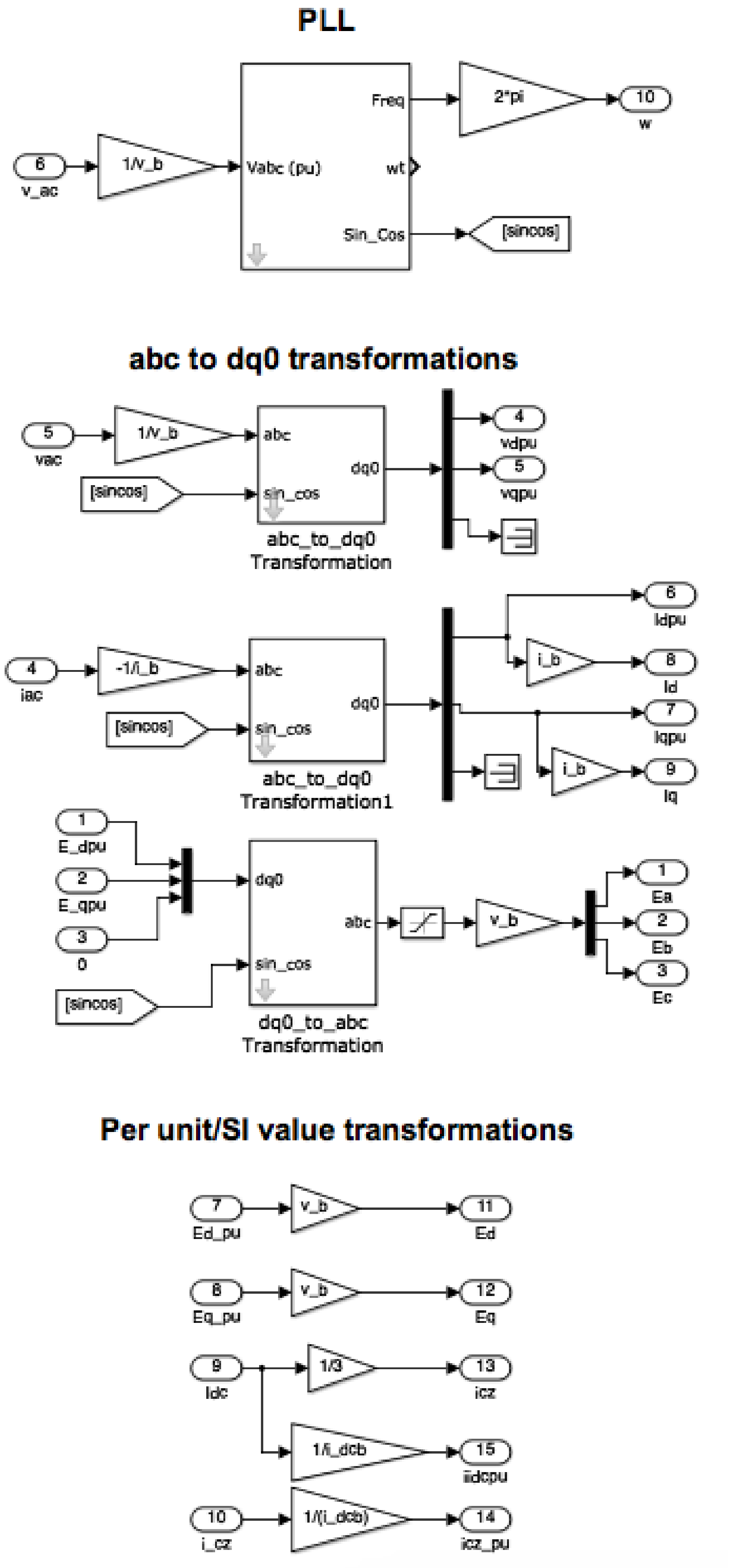

Figure D.18: Transformations used in the MMC model

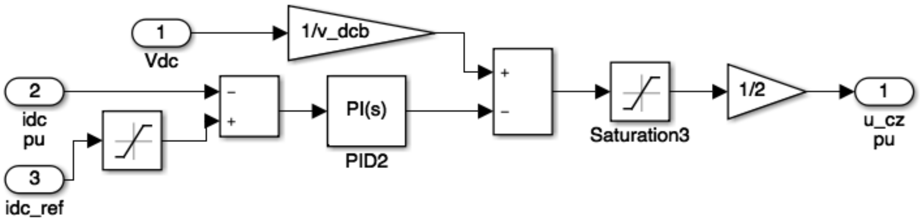

Figure D.19: MMC DC-side controller

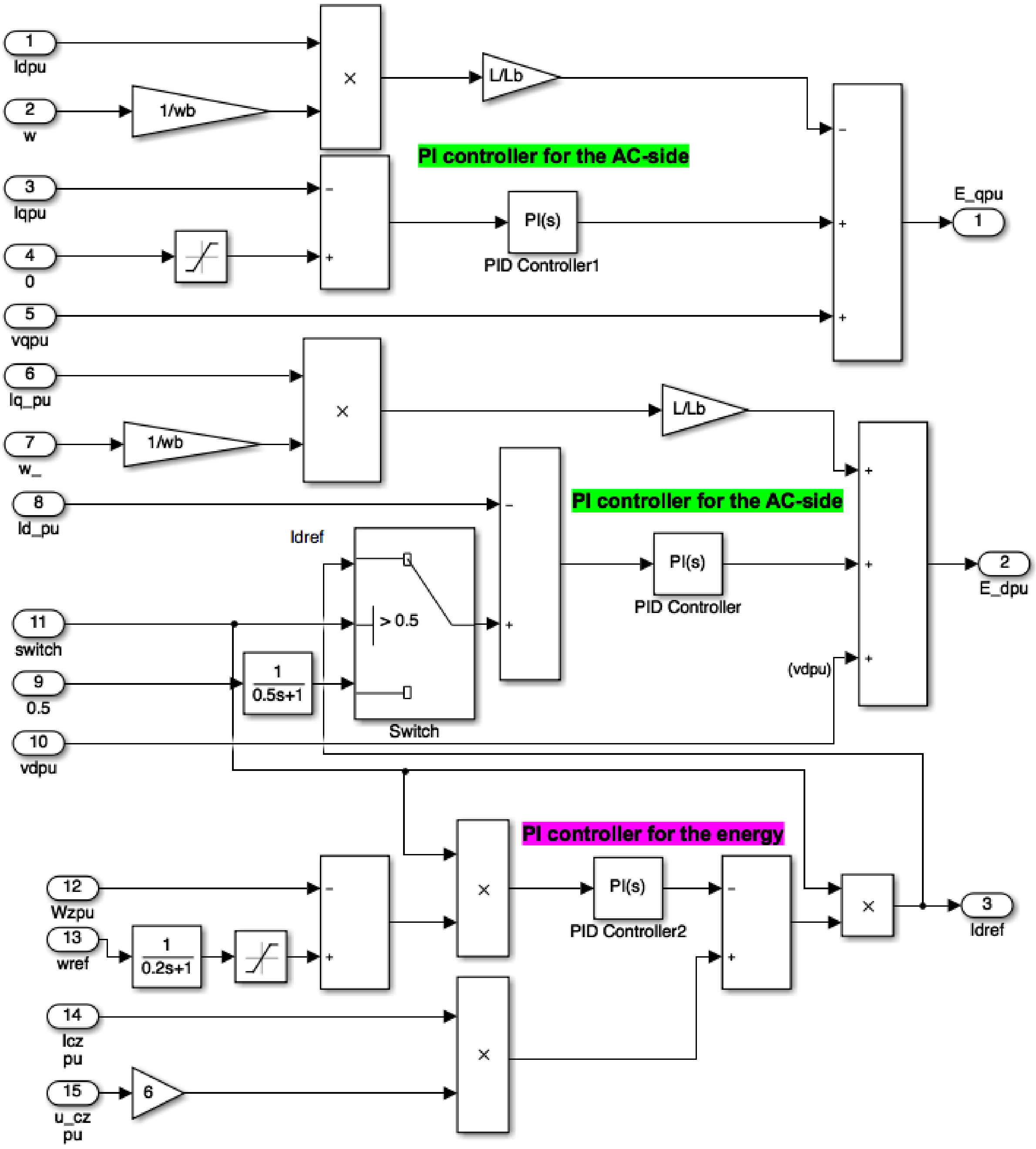

Figure D.20: MMC AC-side and energy balance controllers

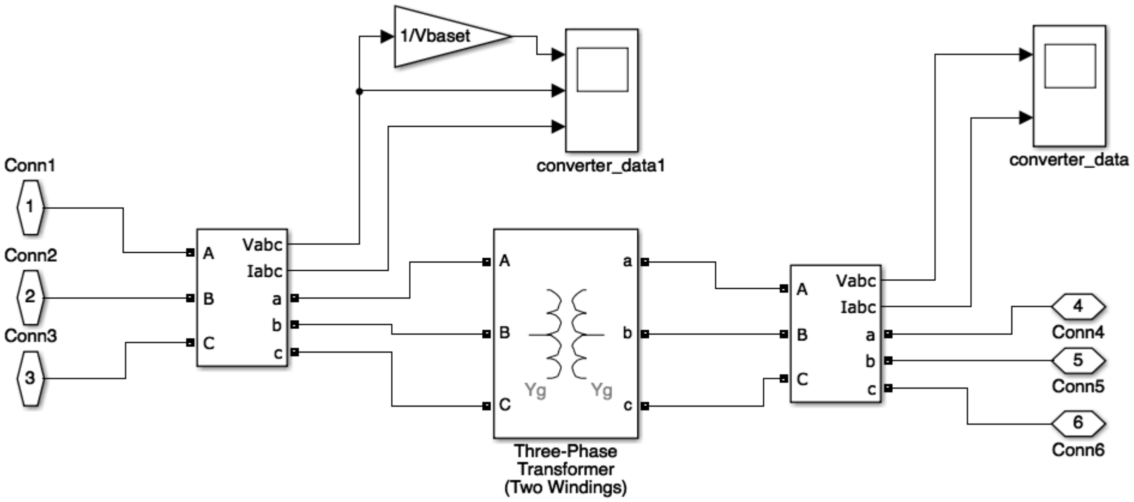

Figure D.21: Transformer

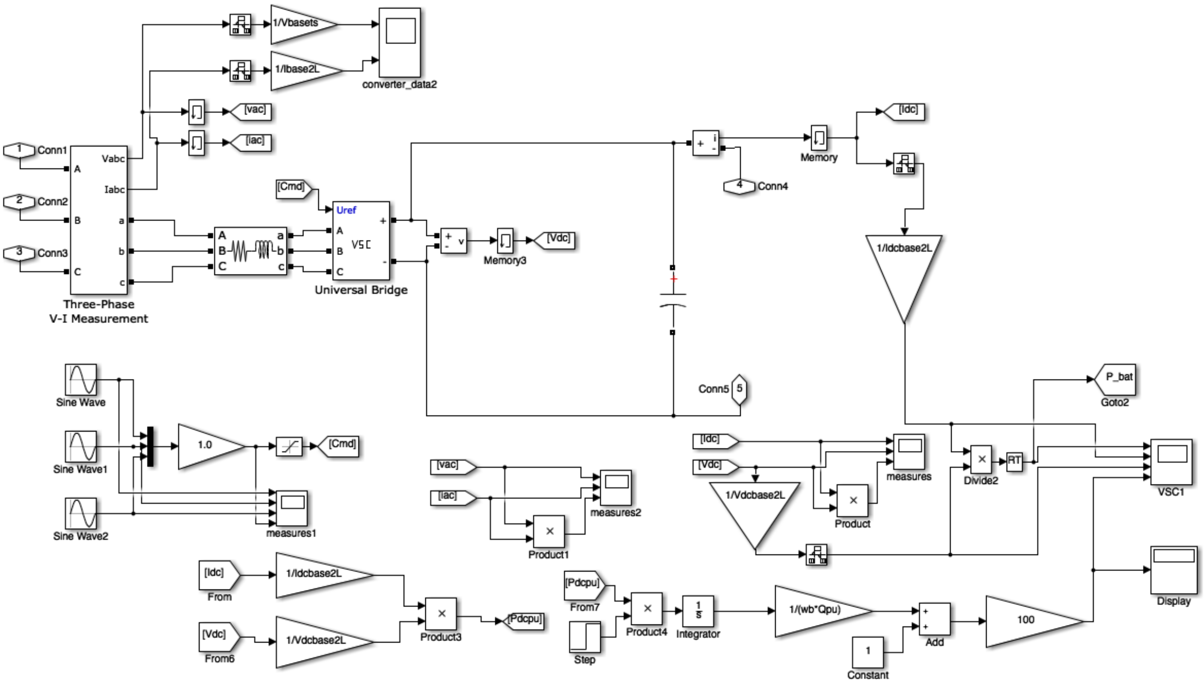

Figure D.22: 2L-VSC connected to the battery and its control

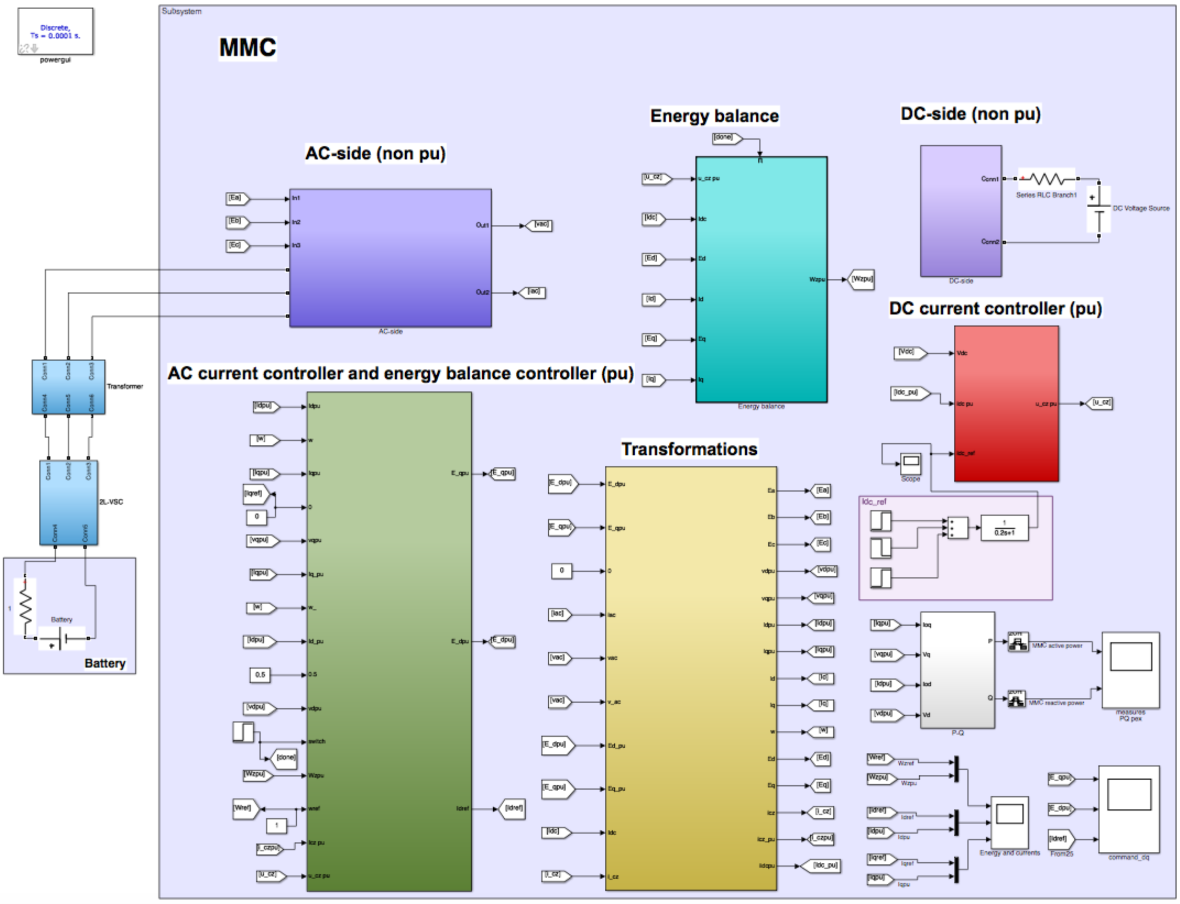

Figure D.23: Simulink model of the system used for test case 1

Appendix **E**

Appendix E: Battery storage technologies

This appendix contains an excerpt from the battery energy storage chapter in the specialization project [3]

E.1 Battery energy storage systems

When it comes to energy storage systems for wind power integration support, which is the objective of this specialization project, H. Zhao et. al. [26] refers to pumped hydro storage (PHS), compressed air energy storage (CAES), flywheel energy storage (FES), battery energy storage systems (BESSs), superconducting magnetic energy storage (SMES) and super-capacitors (SCs) as technologies that are commonly used for this application. Tables E.1, E.2 and E.3 lists technical features of these ESS technologies.

Table E.1: Capacity, power rating, energy density and power density for ESS technologies for wind power integration [21, 26, 27]

Technology	Capacity [kWh]	Power rating [MW]	Energy density [Wh/kg]	Power density [W/L]
PHS	≥ 150	100-5000	0.2-2	0.1-0.2
CAES	≥ 10	5-300	2-6	0.2-0.6
FES	1-25	0-0.25	20-80	5000
LA	≤ 100	0-20	50-80	90-700
Li-ion	≤ 10	0.005-50	200-400	1500-10,000
NaS	≤ 100	0.05-8	150-300	140-180
VRB	20-50	0.03-3	25-35	0.5-2
SC	≤ 10	0-0.3	10-20	100,000+
SMES	≤ 10	0.1-10	6	2600

Table E.2: Discharge duration, self-discharge per day and response time for ESS technologies for wind power integration [21, 26, 27]

Technology	Discharge duration	Self-discharge per day [%]	Response time
PHS	several hours	very small	minutes
CAES	hours	small	minutes
FES	seconds-minutes	100	milliseconds
LA	hours	0.1-0.3	milliseconds
Li-ion	minutes-hours	0.1-0.3	milliseconds
NaS	hours	almost zero	milliseconds
VRB	2-8 hours	very low	seconds
SC	seconds	20-40	milliseconds
SMES	hours	10-15	milliseconds

This project will look at the electro-chemical batteries type of energy storage for offshore wind power application. A description of different electro-chemical battery technologies will be provided in the next sub chapters. In the end of this chapter, the important technical features when it comes to support of offshore wind power integration will be compared, and based on that a battery technology will be chosen for the simulations part of this project.

Table E.3: Lifetime, cycle efficiency and capital cost for ESS technologies for wind power integration [21, 26, 27]

Technology	Lifetime [cycles]	Lifetime [years]	Cycle efficiency [%]	Capital cost [$/kWh]
PHS	10,000-30,000	40+	75-85	5-100
CAES	8000-12,000	20+	45-60	2-50
FES	20,000+	20	90-95	1000-5000
LA	200-1800	5-15	70-80	200-400
Li-ion	1000-10,000	10-15	90-97	600-2500
NaS	2500-4500	10-15	75-90	300-500
VRB	12,000+	5-20	75-85	150-1000
SC	50,000+	5-20	90-97	300-2000
SMES	20,000+	20+	95-98	1000-10,000

Since batteries are made of chemicals there are some conditions that especially affect their performance, lifetime and costs [50]:

- **Depth of discharge (DoD):** This describes the used amount of the capacity of the battery and it is expressed as a percentage of the battery's full capacity. A deep DoD is defined as 80 % or more and it means that 80 % of the full capacity of the battery is utilized. The DoD depends on the chemicals the battery consists of and the type of battery (conventional batteries are affected by the DoD to a greater extend than flow batteries).
- **Ambient temperature:** High ambient temperatures can cause internal reactions in the battery which can decrease the capacity of the battery and reduce its lifetime. It can also cause creation of gases due to corrosion which in addition to decreasing the capacity and lifetime of the battery, will require ventilation which will affect the cost. Low temperatures, on the other hand, can cause slow reactions and the electrolyte may freeze. Too high or too low ambient temperatures will affect the performance of the battery in a negative manner and some batteries therefore require integrated temperature management to ensure safe and optimal operation.
- **Cycle lifetime:** This is the number of charge- and discharge cycles the battery can complete without losing considerable performance. It depends on the the temperature and the DoD of the battery as well as on the size of the installation and the application.
- **Cycle efficiency:** This is the efficiency of one charging and discharging cycle of the battery. It is also known as the Coloumbic efficiency (CE), which is defined as the completeness of the transferring of electrons in the battery during charge and discharge [118]. Namely, the ratio of electrons extracted during discharge compared to the number of electrons being able to enter the battery during charge. A high efficiency implies that there is little stress on the battery, and the lifetime of the batery is expected to be longer. The CE vary with temperature and self-discharge of the battery.

In addition to the factors mentioned above, other factors that also should be taken into account when choosing a battery technology include: safety, power, grid requirements, costs (both capital/investment costs and maintenance costs), performance requirements, response time, and footprint/size [50].

E.1.1 Battery energy storage (BES)

A BES system is built up of electrochemical cells connected in series and parallel to achieve the desired voltage and power level. The system produces electricity from electrochemical reactions in the cells. These reactions are bi-directional, so the cell can produce electricity from chemical energy and it can produce chemical energy from electricity. Each cell consists of two electrodes, one anode and one cathode, separated by an electrolyte. Figure E.1 shows a schematic of the operation of a BES system. The battery is charged by applying an external voltage source to the two electrodes. During discharge, electrochemical reactions occur at the two electrodes simultaneously, and electrons are provided from the anode to the cathode.

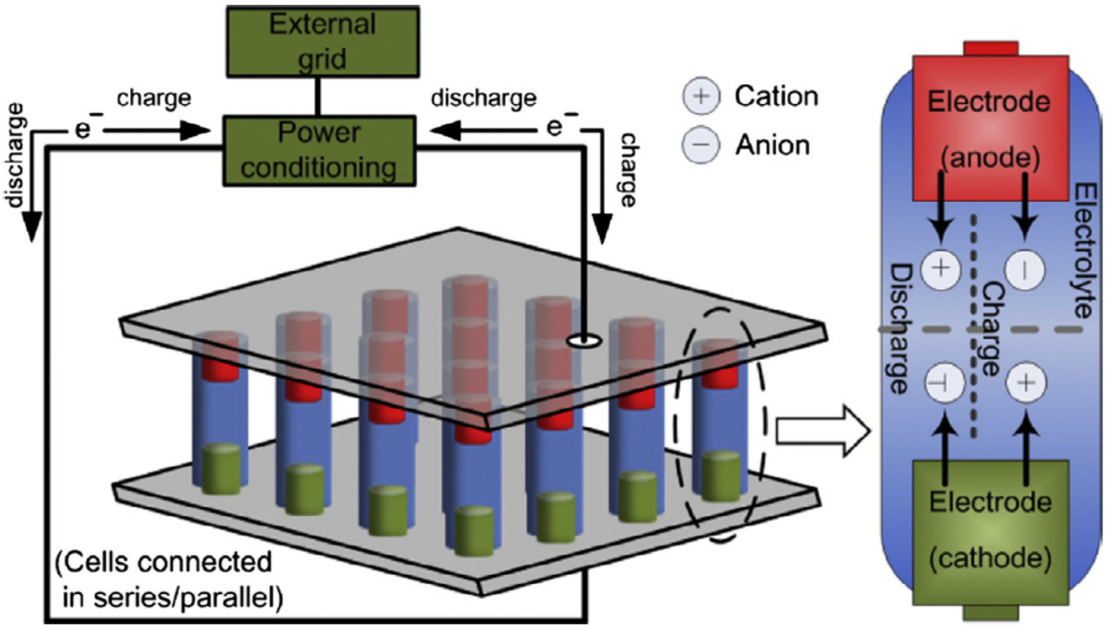

Figure E.1: Schematic of operation of a BES system [21]

Lead-acid (LA)

The LA battery is the most widely used rechargeable battery [21]. In this battery, the cathode is made of PbO_2, the anode is made of Pb and the electrolyte is liquid sulfuric acid. Advantages of this technology are fast response times, low capital costs, small daily self-discharge and relatively high cycle efficiency, as can be seen in tables E.1, E.2 and E.3. Disadvantages that limit the use of this technology for utility-scale BES are short lifetime, low energy density and low specific energy. In addition, the battery cannot be fully discharged and the materials used in this battery are toxic and can cause environmental hazards [21, 22, 51].

To overcome some of these disadvantages, modifications can be made to the electrodes. One modification mentioned in literature [22, 51] is to use lead-carbon electrodes. In this modification, carbon is added to the negative electrode to increase specific power and to reduce the incidence of sulfation during charging cycles. This technology has longer lifetimes and better performances than the traditional LA batteries.

Lithium-ion (Li-ion)

Li-ion batteries are also a widely used battery technology. The cathode is made of lithium metal oxide, the anode is made of graphitic carbon and the electrolyte consists of lithium salts dissolved in organic carbonates [51]. According to X. Luo et. al.[21], this battery technology is a good candidate for applications where small dimension and weight of the equipment is important as well as fast response time, as this technology has advantages of fast response time and high power and energy densities. The main disadvantage with this battery technology has for a long time been its high costs compared to other battery technologies, but according to the International Renewable Energy Agency, IRENA[50] the cost of this technology has decreased drastically over the last years, and it is now a good competitor to the other technologies also when it comes to costs.

Sodium-sulfur (NaS)
In this battery, the electrodes are made of molten sodium and molten sulfur, and the electrolyte consists of solid beta alumina, which is a fast ion conductor material. This is a high temperature battery since a high operation temperature of 574-624 K is required to ensure that the electrodes are in liquid state [21, 22]. The temperature requirement adds to the cost, and a disadvantage of this technology is that it is costly. On the other hand, this battery has many advantages, including high capacity, high energy density and almost zero daily self-discharge. According to X. Luo et. al.[21], this battery technology is one of the most promising for high power energy storage applications.

Nickel-cadmium (NiCd)
The electrodes in the NiCd battery consist of nickel hydroxide and metallic cadmium and the electrolyte is an aqueous alkali solution. Advantages of this battery is that it is has low maintenance requirements and it has a low per-cycle cost. However, there are several disadvantages with this technology which makes it a less preferred solution when it comes to large scale energy storage. It consists of toxic materials which can cause environmental hazards and it suffers from the memory effect. This means that the maximum capacity can be drastically decreased if the battery is repeated recharged after only being partially discharged.

According to A. Poullikkas[22], this battery technology has become popular as storage for solar generation due to its ability to withstand high temperatures. On the other hand, this technology is avoided for energy management application as it does not perform well during peak shaving applications, and according to X. Luo et. al.[21], this technology will most likely not be used for future large-scale EES projects.

Nickel-metal hybrid (NiMH)
This battery is similar to the NiCd, but in this battery the Cd-electrode is replaced by a hydrogen-absorbing alloy [21]. Compared to the NiCd battery, the energy density and the specific energy is improved, making this battery a better choice when it comes to small size and weight of the battery. In addition, the memory effect is reduced, making the lifetime of the battery longer. Another advantage of this battery is that it is more environmental friendly than the NiCd since the toxic cadmium is removed. A disadvantage of this battery, which makes it challenging for long time storage, is its high rate of self-discharge.

Sodium nickel chloride (ZEBRA)
The ZEBRA battery is similar to the NaS battery and this technology also requires high operating temperatures. The negative electrode consists of liquid sodium and the positive electrode consists of an insoluble metal chloride.This battery uses two electrolytes, a ceramic one and one consisting of molten sodium tetrachloroaluminate [22]. Advantages of this battery is that it has a high cell voltage, very little self-discharge, long lifetime, and it has safe reaction products. In addition to the high operating temperature, another disadvantage of this battery according to X. Luo et. al.[21] and A. Poullikkas[22], is that only a few companies have been involved in the development of this type of battery, and that may limit its potential.

E.1.2 Flow battery energy storage (FBES)

In a flow battery, an electrolyte containing one or more dissolved electro-active species flows through an electrochemical cell to produce electricity from chemical reactions [22]. Figure E.2 shows the schematic of a flow battery. The battery stores energy in two redox couples which are placed in external liquid electrolyte tanks (the catholtye and anolyte receivers on the figure). The electrolytes are pumped into the cell stack which consists of two electrolyte flow compartments separated by ion selective membranes. Then one electrolyte is oxidized (at the anode during charging and at the cathode during discharging) while the other is reduced. The battery is charged by applying an external voltage source. During discharge the chemical redox reactions produce electricity.

An advantage of the FBES technology is that its power is independent of its storage capacity as the power is determined by the number of cells in the stack and the size of the electrodes, while the storage capacity is determined based on the electrolyte and its concentration [21]. In addition, the self-discharge of this type of battery is small since the electrolytes are stored in separate sealed tanks and flow batteries have long cycle lifetimes because there are no solid-solid phase changes in the reactions. There are also some drawbacks with this technology, including high costs and low performance due to reactant mass transfer limitation and non-uniform pressure drops. In addition, these batteries are quite complicated compared to traditional electrochemical batteries as they might require extra control systems, pumps and sensors, and compared to the traditional electrochemical batteries, the flow batteries overall have lower energy densities.

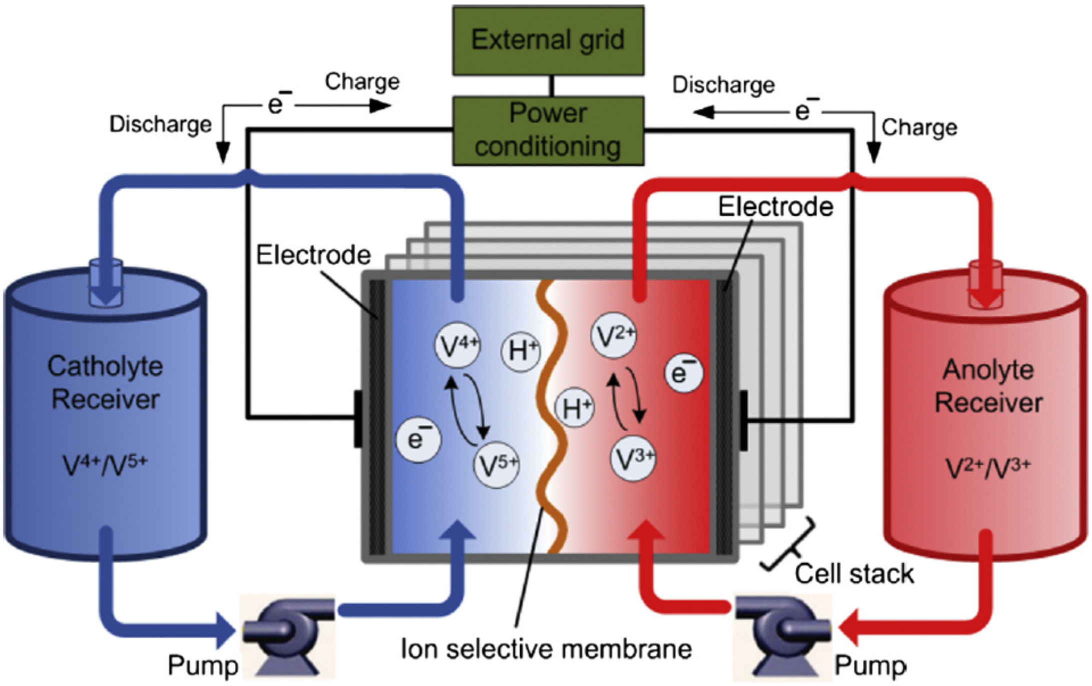

Figure E.2: Schematic of a Vanadium Redox Flow Battery (VBR) [21]

Flow batteries can be divided into two categories depending on how well the electroactive components can be dissolved in the electrolyte [22, 51]:

1. **Redox flow batteries:** In this type of flow battery all electroactive components are dissolved in the electrolyte.
2. **Hybrid flow batteries:** In this battery there is one fuel cell electrode and one battery electrode which makes up the electrochemical cell. This means that only one solution is stored in the external tank while the other one always is kept in the electrochemical cell.

The vanadium redox flow battery, the zinc bromine flow battery and the polysulfide bromine flow battery are three types of flow batteries that are mentioned in literature [21, 22, 26, 27, 51]. They will be discussed in the next sections.

Vanadium Redox Flow Battery (VBR)

The principle of the VBR flow battery is shown in figure E.2. This is a type of redox flow battery which uses vanadium in four oxidation states (V^{2+}, V^{3+}, V^{4+} and V^{5+}) to store chemical potential energy in two electrolyte tanks. During charge and discharge, H^+-ions are exchanged through the ion selective membrane.

Disadvantages of this technology include high costs, low energy density and low efficiency due to a high rate of self-discharge. On the other hand, the VBR has many advantages including long lifetime, it is based on a clean technology using just one electro-active element, it can offer large capacities and it can be left discharged for longer periods without ill effects. According to A. Poulikkas[22] the VBR flow battery is well suited for large storage applications such as contributing to a smoother power generation of highly variable energy sources such as wind, due to the fact that it can provide extremely large capacities.

Zinc Bromine flow battery (ZnBr)

This is a type of hybrid flow battery and figure E.3 shows the principle of this technology. It consists of two external tanks and a cell stack which consists of carbon-plastic composite electrodes. The two tanks store the two electrolyte solutions which contain the reactive components of zinc and bromine. During charge the electrolytes are pumped through the cell stack and back into the tanks and metallic zinc is electroplated onto the negative electrode surfaces while bromide is converted to bromine at the positive electrode surfaces. During discharge the reverse process occurs where zinc and bromine react electrochemically and produce electricity.

Advantages of the ZnBr flow battery include long lifetime, deep discharge capability and scalable capacities from 3kW to 500kW. Disadvantages include material corrosion and relatively low efficiency compared to traditional electrochemical batteries. X. Luo et. al. [21] mentions some projects where this type of battery is in use today for grid support. The utility BESS application of this battery is still in the early stage of demonstration, and the power range of the projects mentioned in the article is from 3 kW up to testing at around 2 MW.

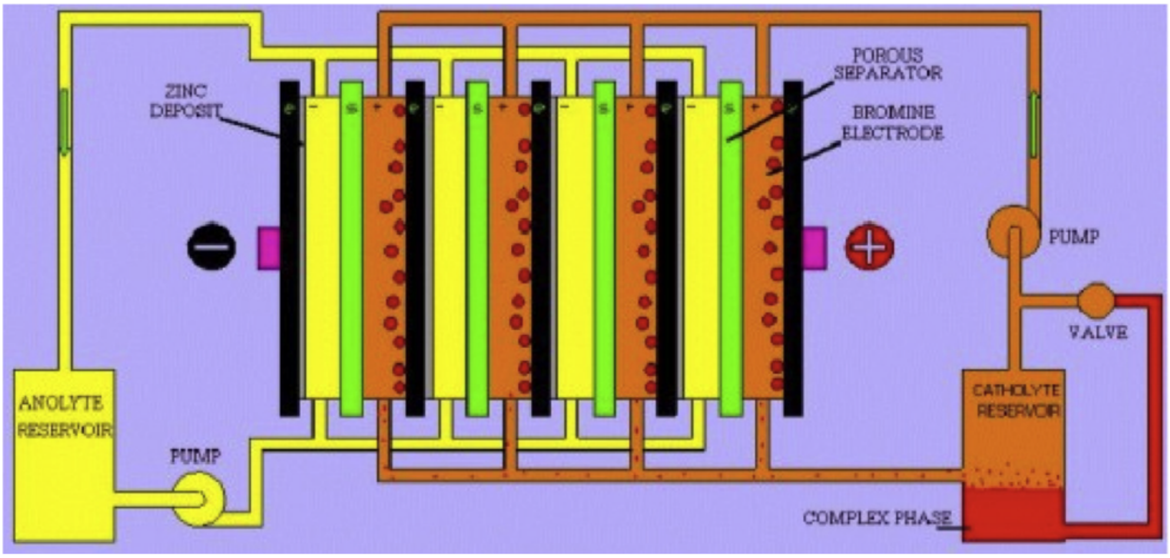

Figure E.3: Schematic of a Zinc-Bromine Flow Battery (ZnBr) [22]

Polysulfide Bromide flow battery (PSB)
This is also a type of redox flow battery, and the electrolytes of this battery consist of sodium bromide and sodium polysulphide. Advantages of this technology include cost-effective materials and fast response time. On the other hand, a disadvantage is that environmentally hazarding bromine and sodium sulfate crystals are produced during the reactions. Due to the fast response time, this technology is well suited for frequency and voltage control of power systems. According to X. Luo et. al.[21], the PSB technology have so far just been used for demonstration testing at multi-kV scales. The article mentions two projects that were planned based on this technology, but they could not be constructed due to financial constraints and engineering difficulties.

Table E.4 shows the technical characteristics of the battery technologies discussed in this chapter. The table is based on numbers found in [21, 26, 27, 51]. The information provided in this table will be used as the basis for choosing a battery technology for the project, later in this chapter. Most of the information is found in [21], but the information provided in this reference is from a number of references, so for each characteristic as far as it was possible, the same reference has been used for different battery technologies for the information provided to be comparable. The footnotes in the table describe where the information for each of the characteristics is found.

Table E.4: Characteristics of different battery storage technologies

	LA	**Li-ion**	**NaS**	**NiCd**	**NiMH**	**ZEBRA**	**VRB**	**ZnBr**	**PBS**
Power rating [MW][i]	0-20	0.005-50	0.05-8	0-40	-	-	0.03-3	0.05-2	1-15
Energy density [Wh/L][i]	50-80	200-400	150-300	60-150	170-420	150	25-35	30-65	20-30
Power density [W/L][i]	90-700	1500-10,000	140-180	80-600	-	-	0.5-2	25	2
Specific energy [Wh/kg][i]	30-50	75-200	150-240	50-75	70-100	94-120	10-30	30-50	15-30
Specific power [W/kg][i]	75-300	150-315	150-230	150-300	-	150-170	166	100	-
Unit voltage [V][i]	2.0	3.7	2.08	1.0-1.3	1.0-1.3	2.58	1.4	1.8	1.5
Response time[ii]	ms	ms	ms	ms	-	-	ms	1/4 cycle	ms
Lifetime [cycles][i]	200-1800	1000-10,000	2500-4500	2000-2500	-	-	12,000+	2000	-
Daily self-discharge [%][i]	0.1-0.3	0.1-0.3	~ 0	0.03-0.6	5-20	-	very low	low	~ 0
Cycle efficiency [%][iii]	70-80	90-97	75-90	60-83	-	90	75-85	65-75	60-75
Capital cost [$/kWh][iv]	200-400	600-2500	300-500	800-1500	-	-	150-1000	150-1000	-
O&M costs [$/kWh/year][i]	50	-	80	20	-	-	70	-	-

When it comes to battery technologies, the market for power sector battery storage was earlier dominated by NaS batteries [50]. During the recent years this trend has shifted and now Li-ion batteries are dominating due to the many advantages when it comes to performances in terms of efficiency and lifetime as well as safety. The shift of the trend towards Li-ion is mainly due to a decrease in battery costs of this technology over the last years as well as improved performances of this technology. The decrease in costs of Li-ion batteries over the last years is shown in figure E.4. The red, yellow and blue legends represent price projections based on data from three different datasets, and the green legend shows the averaged price projection. More information regarding the price projections and the datasets used can be found in [23] which is the report by Rocky Mountain Institute, Homer Energy and Cohnreznick Think Energy, where the figure is taken from.

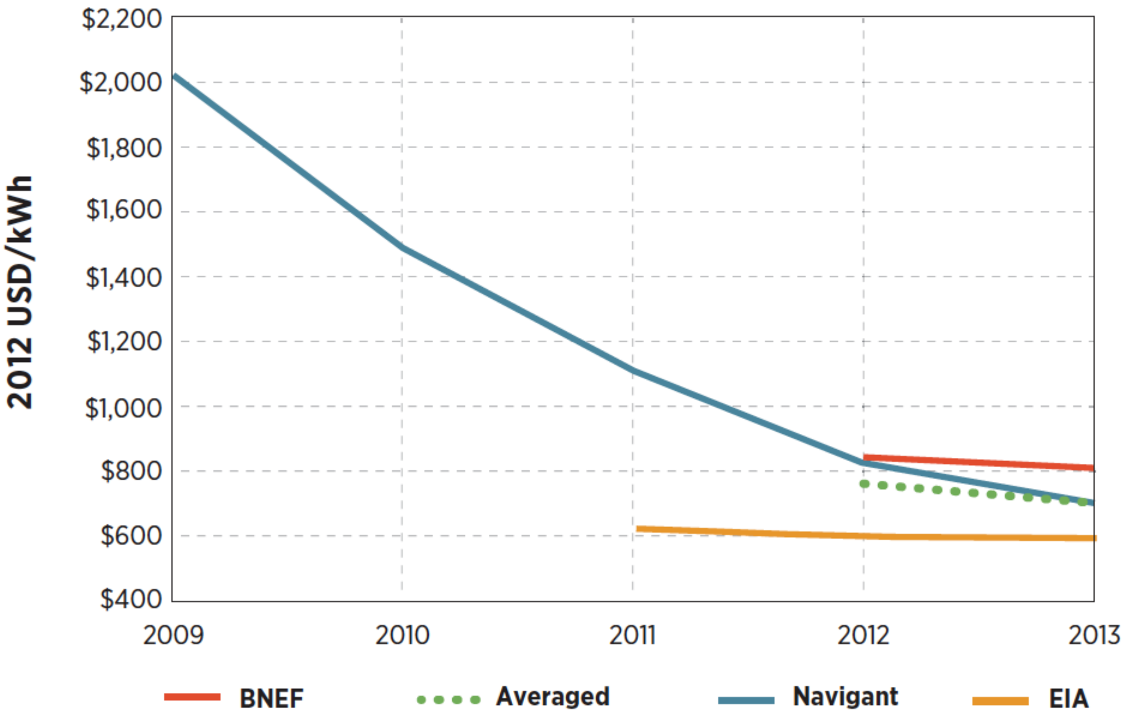

Figure E.4: Costs of Li-ion batteries [23]

E.2 Discussion: choice of battery technology for this project

The battery used in this project should have a rated power of about 10-20 % of the rated power of the wind farm, meaning around 200 MW. As can be seen in table E.4, the power rating of one battery cell for each of the battery technologies discussed in section E.1, is in general quite low

---

[i] Power rating, energy density, power density, specific energy, specific power, unit voltage, lifetime, daily self-discharge and operation and maintenance cost characteristics found in [21]

[ii] Response time characteristics found in [21, 27]

[iii] Cycle efficiency characteristics found in [21, 51]

[iv] Capital cost characteristics found in [26]

compared to the power rating that is needed for the battery of this project. Several batteries must therefore be connected in series and parallel to achieve the desired power rating of 200 MW.

As mentioned earlier, several factors should be taken into account when choosing a battery technology. When choosing a battery technology for this project, some aspects should particularly be taken into account:

1. **Quick response time:** The application of the battery in the project is to provide services of primary and secondary reserves in case of short imbalances in the AC grid. It should be used to maintain power balance in the system as well as to regulate frequency and control voltage during an imbalance. The battery must therefore have a very quick response time in order to provide these services in case of a sudden imbalance.
2. **Size:** The size of the battery is also an important aspect. Especially if the battery is to be connected offshore, extra weight will add to the costs. Hence, the specific power and energy should be as high as possible to get a high power output but with a battery that is small in size and weight.
3. **Lifetime:** Lifetime is another important aspect. It is preferred to have a long lifetime to reduce the need for frequent maintenance or replacement of the battery, which will add to the cost. In addition, it might increase the environmental impact in case the battery consist of toxic materials.
4. **Cost:** The cost should be low for this technology to be a preferred solution over more mature energy storage technologies.
5. **Efficiency:** The efficiency should be as high as possible for the battery to perform well.
6. **Environmental friendly technology:** The environmental hazards should be kept to the minimum as one of the main drivers of using energy storage for this application is to reduce the use of high-emission non-renewable generation for this application.

By comparing the technical features of the batteries discussed in section E.1 with the aspects mentioned above, especially LA, Li-ion, NaS and VBR are good alternatives when it comes to high efficiencies and quick response times. In terms of lifetime, Li-ion and VBR are the best alternatives. A disadvantage of the flow batteries is that the energy and power densities and also the specific power and energy rates are lower than for the conventional batteries. Hence, when considering size, a flow battery is not a good alternative.

When it comes to costs, the LA battery is the cheapest one of the conventional batteries. An important note that should be taken into account when it comes to the technical features in table E.4, is that that table is based on references from 2013-2015, but the numbers used in the references are cited all the way back to early 2000's. As have been seen in this chapter, the battery technologies have grown rapidly during the last decade. Hence, the numbers in 4.2 might not fully represent the state of the art of all technologies anymore even though it gives a good indication on how the different technologies perform compared to each other. As mentioned in section D.1, the Li-ion has improved in terms of performance and cost in the recent years, and hence this will be a better choice than the LA battery since Li-ion has longer lifetime, higher specific power and energy and higher efficiency. The NaS technology has also been mentioned as a good alternative so far, but a disadvantage with this technology is its high operating temperatures, which will require extra equipment for heating and cooling, and that will add to the cost. As a conclusion, the Li-ion battery is the best technology for the purpose of this project and this is the technology that will be used in the simulation later.

Appendix F

Appendix F: DC/DC converters

This appendix contains an excerpt from the DC/DC converter chapter in the specialization project [3]

F.1 Dedicated converters

Two-quadrant converter (2Q)
The structure of the dedicated 2Q DC/DC converter is shown in figure F.1 (a). The presence of the inductor L is to smooth the current ripple on the low voltage side, and this is advantageous to the battery as smoother charging and discharging current will result in longer lifetime and higher efficiency of the battery [9]. The capacitors C1 and C2 smooth the output and input voltages, respectively. Smooth currents and voltages are important to maintain the desired power quality level of the system.

As the name of the converter implies, this converter can operate in two quadrants of the V-I curve. It operates in boost or step-up mode when the current direction is from the battery or the low voltage (LV) side to the grid or high voltage (HV) side. In this mode, switch S1 and diode D2 are always off, while the current alternates between flowing through the switch S2 while it is on and the diode D1 when S2 is off. In buck or step-down mode, the current flows from the HV side to the LV side and in this mode it is the switch S1 that is turned on and off and the diode D2 that is forward biased when S1 is off.One drawback with the use of this converter is that it can only step the voltage up in one direction and step it down in the other, so it can only be used for applications where the voltage at one side of the converter always is lower than the voltage at the other side of the converter. However, this is not a problem for the application in this project as the battery will always have a lower voltage than the grid. Another disadvantage with this topology is that the structure becomes impractical for larger voltage ratios [9].

Four-quadrant converter (4Q)
Figure F.1 (b) shows the structure of the 4Q converter. This converter also has as inductor and two capacitors, for the same purposes as the 2Q converter. As its name implies, this converter can operate in all four quadrants of the V-I curve. Table E.1 shows the operating states of the

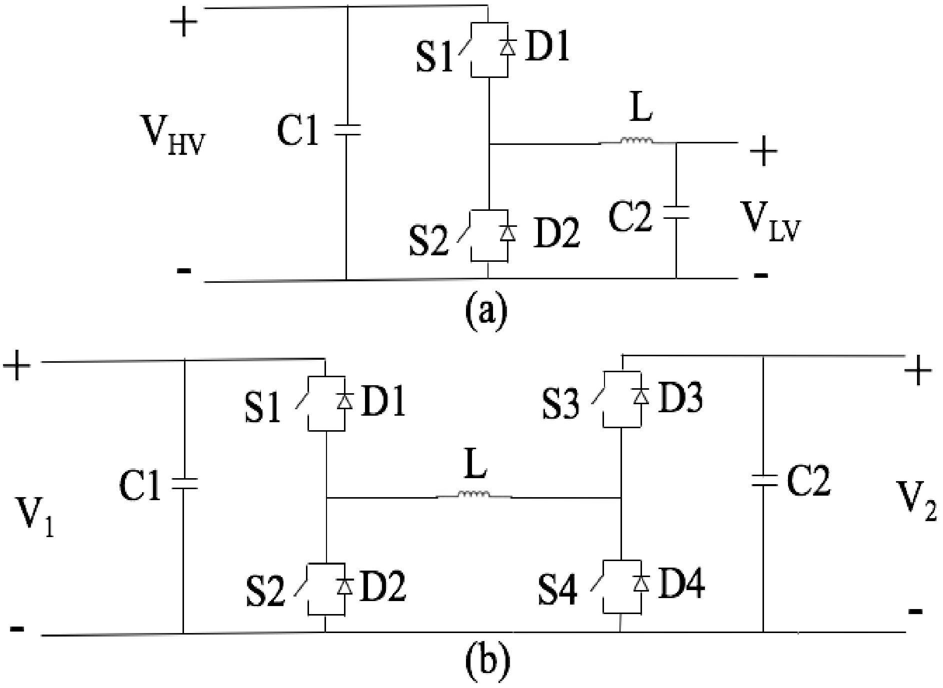

Figure F.1: (a) Dedicated 2Q DC/DC converter (b) Dedicated 4Q DC/DC converter

switches and diodes in this converter, where A indicates active, 1 indicates on and 0 indicates off.

Table F.1: Operating states of switches and diodes in the 4Q DC/DC converter [28]

Voltage	Power direction	Mode	S1	S2	S3	S4	D1	D2	D3	D4
$V_1 > V_2$	$1 \to 2$	Buck	A	0	0	0	0	A	1	0
$V_1 < V_2$	$2 \to 1$	Buck	0	0	A	0	1	0	0	A
$V_1 < V_2$	$1 \to 2$	Boost	1	0	0	A	0	0	A	0
$V_1 > V_2$	$2 \to 1$	Boost	0	A	1	0	A	0	0	0

Compared to the 2Q converter, the 4Q topology has a wider range of operating voltage ratios and it can operate as a step-up and a step-down converter in both directions [9]. On the other hand, this converter requires more semiconductor devices, so the size will be larger and the cost will be higher compared to the 2Q converter.

F.2 Dual Active Bridge (DAB) converters

G. P. Adam et. al.[24] compares different types of DAB converters for HVDC application, including DAB converters based on 2L, MMC, controlled transition bridge converter (CTB), transition arm multilevel converter (TAC), alternative arm MMC and hybrid cascaded 2L. The structure of the mentioned converter technologies are shown in figures F.2-F.7.

The structure of the 2L based DAB is the same as for a front-to-front connected 2L converter, and the difference in the DAB converter is the operation of the converter. The control is based on selective harmonic elimination (SHE) where the power flow in the AC link is controlled using the magnitudes of the voltages at the terminals of the two converters and by controlling the phase shift between the AC voltages of the two converters [24]. This is the same control operation as described for the single-phase DAB above. The voltage stress, dv/dt increases with an increasing operating DC voltage, and this voltage stress is impressed upon the transformer in the converter. Voltage stress higher than a certain value will be intolerable for the transformer, and this restricts the applications of this converter to low power and low DC voltages of up to ±200 kV [24].

Similarly, the MMC based DAB has the same structure as a front-to-front connected MMC converter, and the difference is the operation of the converter. The paper [24] discusses two types of operation of the MMC-DAB; the operation with sinusoidal voltage and currents in the AC link and the quasi-two-level operation. The former is similar to the operation of a MMC used in a VSC-HVDC grid and the latter is operating the MMC as a 2L converter. The MMC based DAB converter has lower switching losses and lower voltage stress than to the 2L based DAB, and this converter topology is a more promising solution for higher operating DC voltages [24].

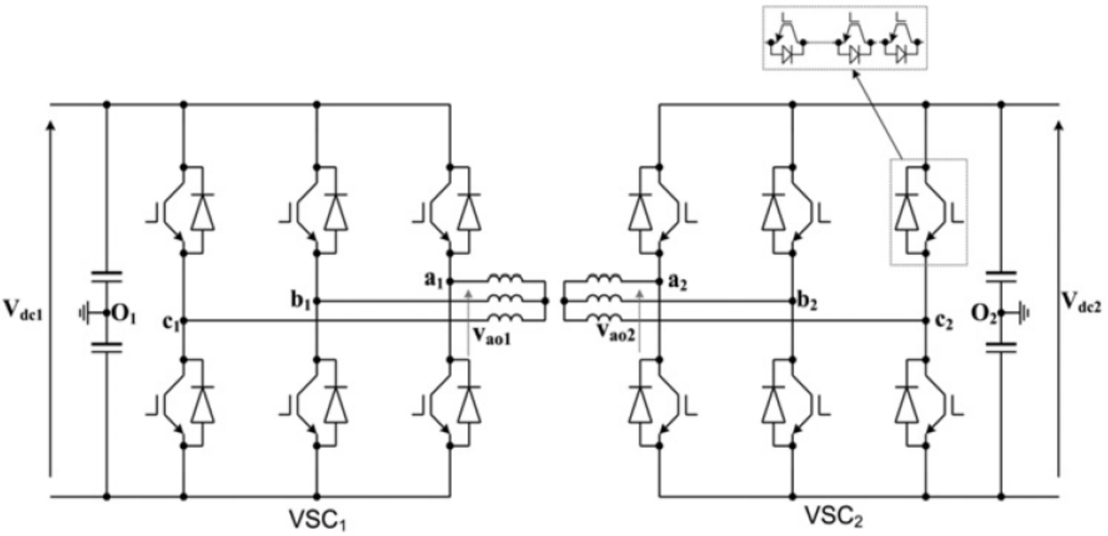

Figure F.2: 2L based DAB converter [24]

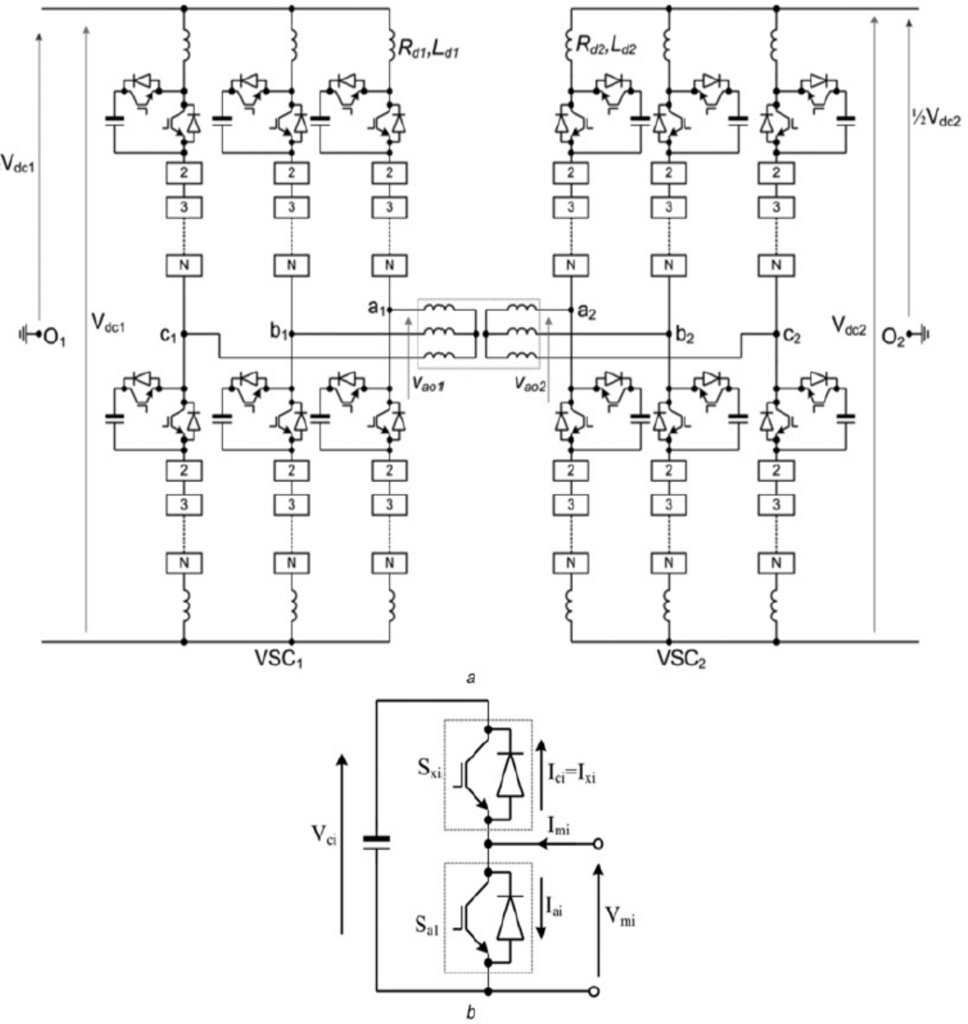

Figure F.3: MMC based DAB converter [24]

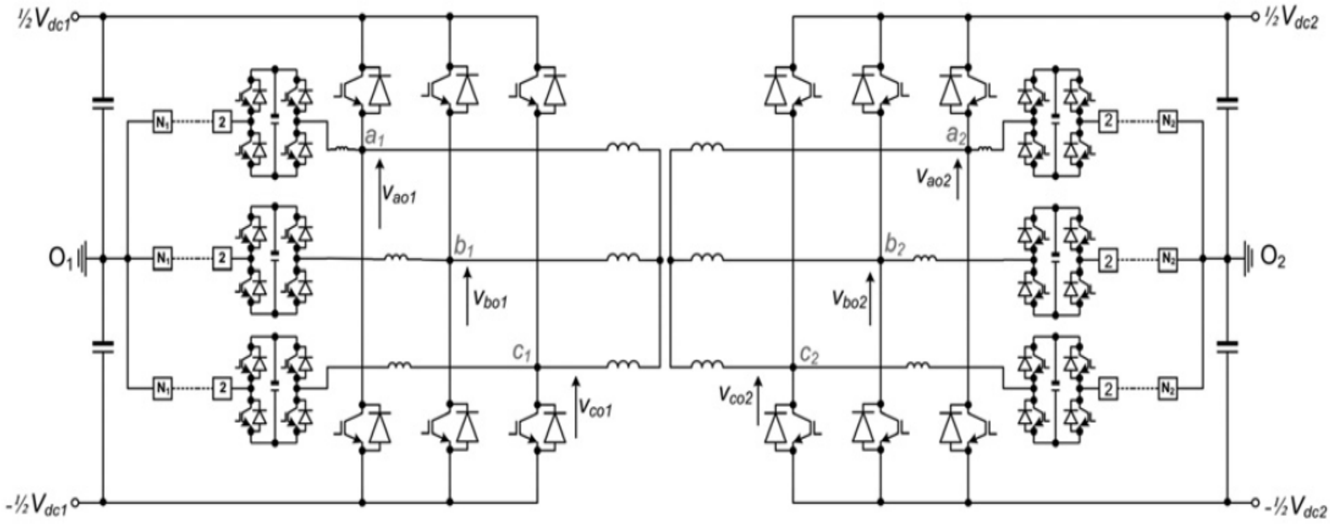

Figure F.4: Two-level CTB based DAB converter [24]

The CTB based DAB in figure F.4 is based on a three-phase controlled transition bridge multilevel converter and it is operated using established modulation strategies, i.e. quasi-two-level SHE [24]. Compared to the two previously discussed DAB converter topologies, the CTB offers advantages in terms of smaller footprint, lower semiconductor losses and low voltage stress.

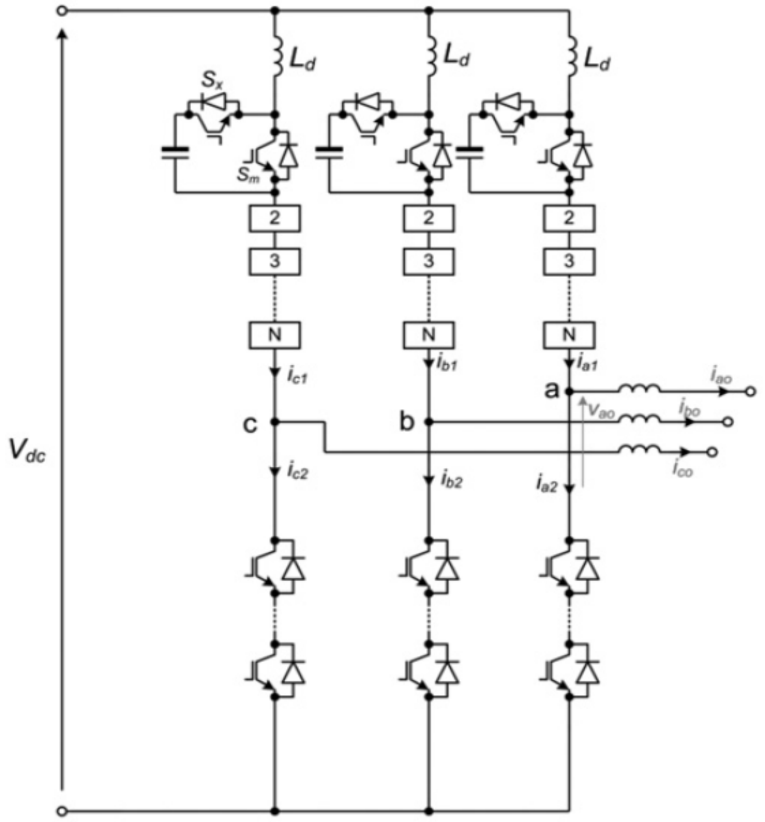

Figure F.5: TAC based DAB converter [24]

The TAC based DAB consists of half-bridge submodules like in a typical MMC configuration in the upper (or lower) arms, while the typical MMC structure of sub-modeles in the lower (or upper) arms are replaced with switches, i.e. series connected IGBTs like in the typical 2L configuration. In the TAC, only the upper arms (if these are the ones with MMC structure) are used to create the stepped transitions between the negative and positive DC rails, while the lower arms only are used when the output voltage of -$\frac{1}{2}V_{DC}$ needs to be synthesised at the AC output poles [24]. This operation of the TAC based DAB provides a gradually built voltage stress and small arm inductance compared to the similar quasi-two-level operated MMC.

The alternative arm MMC based DAB is also similar to the MMC based DAB, but this configuration has a reduced number of full-bridge submodules, which reduces the footprint of the converter [24]. The structure of the converter is shown in figure F.6. The operation of the converter, which is based on alternating 180° operation of the arms, reduces the semiconductor losses of the converter compared to the full-bridge MMC and hybrid cascaded 2L converter. Similarly to the MMC DAB, this converter can also be operated in the quasi-two-level operation mode and this reduces the footprint even further. However, the efficiency in this operation mode is lower compared to the same operation of the regular MMC DAB due to the fact that this operation mode of the TAC based DAB inserts a large number of semiconductor devices in the conduction path.

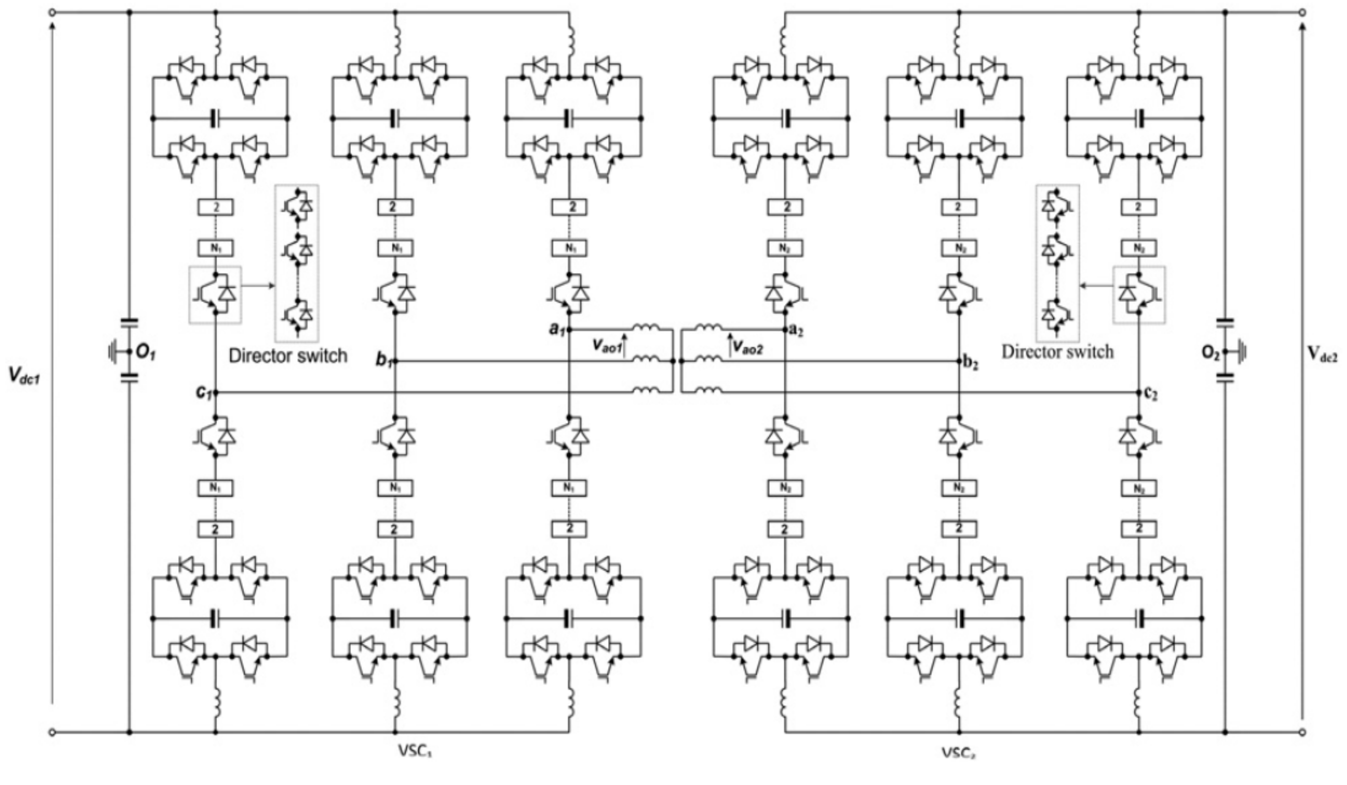

Figure F.6: Alternative arm MMC based DAB converter [24]

The structure of the hybrid cascaded 2L DAB is shown in figure F.7. This converter is similar to the CTB based DAB since they have the same number of switching devices and capacitors[24]. However, this converter has the advantage of offering reverse blocking capability during a DC fault. On the other hand, this converter topology has higher switching losses compared to the similar operation of the CTB based DAB due to the fact that it has a large number of switching devices in its conduction path. The paper[24] concludes that this converter topology is unlikely to be used for high-voltage DC/DC converters.

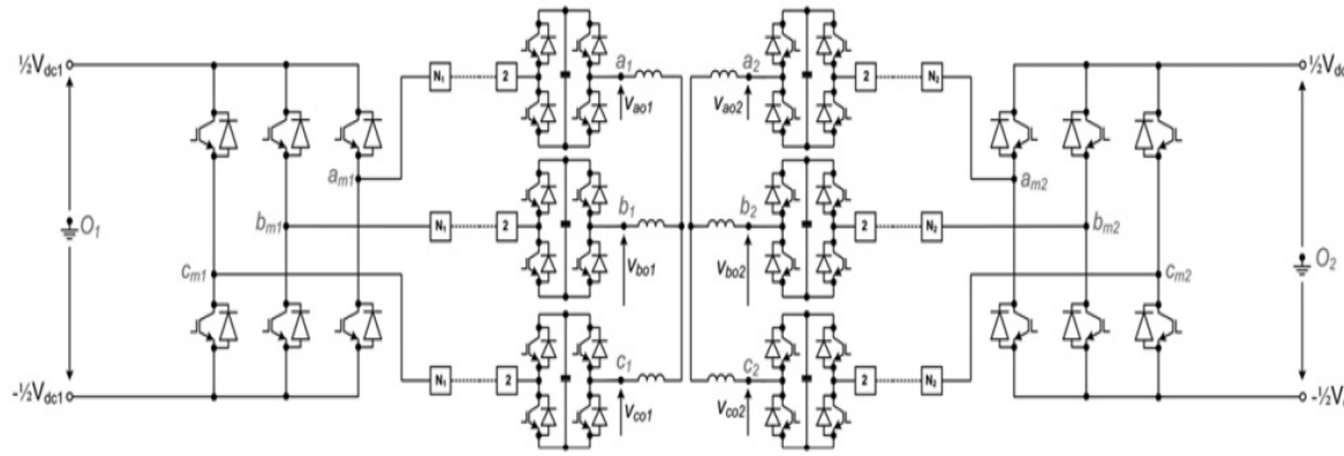

Figure F.7: Hybrid cascaded 2L based DAB converter [24]

According to the paper, voltage matching, voltage control, fault prevention and voltage stress (dv/dt) control of the switching devices, passive components and transformer, are the most desirable features for high voltage DC/DC converters [24]. The paper concludes that based on these features, the CTB-DAB is the best choice. In addition, it mentions the MMC and TAC based DAB converters as good alternatives due to their low losses and reduced footprints. It also concludes that the 2L DAB due to its low voltage levels, and the alternative arm MMC and hybrid cascaded 2L based DABs due to their high semiconductor losses and current stresses, are not the best choices for high-voltage DC/DC converters.

S. P. Engel et. al. [71] compares the MMC converter and the DAB converter for four different scenarios in terms of efficiency, magnetic components, number of semiconductor devices and expense on capacitive storage. The MMC converter is of the type push-pull M2DC where the submodules are either half-bridge or full-bridge, and the DAB converter is MMC based and consists of two full-bridge converters and a medium frequency transformer. The four scenarios are:

A Connection of grid at voltage V = $\pm 5kV$ to an HVDC link of V_{HVDC} = $\pm 150kV$ at power $P = 15MW$.

B Connection of offshore wind farms with grid collector voltage V = $\pm 10kV$ to and HVDC link of V_{HVDC} = $\pm 150kV$ at power $P = 1.2GW$.

C Interconnection of two HVDC grids, both at voltage V_{HVDC} = $\pm 150kV$ at power $P = 15MW$, where voltage variations of $\pm 10\%$ must be tolerated and black start capability is required.

D Interconnection of two HVDC grids at voltages V_{HVDC1} = $\pm 300kV$ and V_{HVDC2} = $\pm 150kV$ at power $P = 15MW$, where voltage variations of $\pm 10\%$ must be tolerated and black start capability is required.

Optimal designs for the two types of converters are found for the different scenarios, and in the end of the paper, they are compared [71]. It is found that the DAB converter has lower switching losses since that converter is based on a soft-switched operating mode, while the MMC is based on hard-switched PWM modulation. The results show that in terms of efficiency, the DAB performs, in almost all cases, better than the M2DC. It is only in scenario A for low-load conditions and in scenario C with balanced voltages that the M2DC is competitive and show better results than the DAB. In scenario C, the best efficiency is obtained for the M2DC, exceeding 99.5%. In general, the DAB features efficiencies between 98.9% and 99.2%, which is considered very good. The results also show that for higher loading conditions in scenario A and in scenario D, the M2DC preforms bad as it only provides efficiencies of 92.9% and 96.46%, for scenario A and D respectively.

The paper [71] also includes an economic evaluation of the converters for the different scenarios. The results show that the cost mainly depends on the cost of the power electronics. The DAB can be designed with a significantly lower amount of semiconductor devices, and therefore, as the results also show, the costs of the DAB are much lower than M2DC for all scenarios.

F.3 Discussion: choice of DC-DC converter technology for this project

The voltage ratio for this project is high as the DC-link has a voltage of 320 kV while the battery voltage is 1.2 kV. The battery in this project is providing services to the grid in terms of primary and secondary reserves in order to support integration of large scale offshore wind power into the grid. The power rating of the battery is around 10-20 % of the power rating of the wind farm, and hence a DC/DC converter with power rating of 100-200 MW is required in this project. In appendix D it was found that the power rating of the battery to be used in this project is 180 MW. Therefore, the power rating of the DC/DC converter is classified as medium power.

As mentioned earlier, several factors should be taken into account when choosing a DC/DC converter topology. When choosing a DC/DC converter for this project, some aspects should particularly be taken into account:

1. **Bidirectional power flow:** As mentioned earlier in this chapter, it is important that the converter provides bidirectional power flow capability so that the power can flow in both directions between the battery and the DC-link so that the battery can provide the services that it is implemented for.

2. **Voltage ratio and voltage level:** It is important that the converter can operate for the voltage levels and voltage ratio required in this project. It is found that the voltage ratio is high and that the battery voltage is 1.2 kV while the DC link voltage is 320 kV. Therefore, the converter must be able to operate under these conditions.

3. **Power rating:** It is found that the power rating in this project is 180 MW, so it is important that the converter can operate at this medium power level.

4. **Fault tolerance:** As have been mentioned earlier in this report, DC faults are critical in HVDC systems, and in chapter 3.5 it was seen that especially in multiterminal DC grids, DC circuit breakers are required to tolerate faults. Since the HVDC system in this project is a point-to-point HVDC system, the AC circuit breakers can be used. However, when it comes to fault transfer between the battery and the DC-link, faults can only be prevented in case a DC/DC converter with galvanic isolation is used, and DC faults are critical for the battery. In this chapter it is seen that the transformer used as galvanic isolation in DC/DC converters not only provides isolation of faults, but also voltage matching. This is an advantage in this project since the voltage ratio is high. In this chapter it is also found that DC/DC converters without galvanic isolation is best suited for low voltage ratios where the transformer may not be required to prevent faults from being transferred from one DC-system to the next. Therefore, since the voltage ratio is high, a DC/DC converter with galvanic isolation is the preferred solution in this project.

5. **Converter losses:** It is desirable to have as low losses as possible in order to minimize the total losses of the system.

6. **Complexity of converter and its control:** It has been seen in this chapter that the complexity of converter topologies and their control systems vary from converter topology to converter topology. Complexity might add to the cost, so this should be taken into consideration when choosing a converter topology.

7. **Cost:** The cost should be as low as possible for a solution which is able to operate under the other conditions mentioned here. As have been seen in this report, the costs for battery technologies and HVDC transmission systems for a project of this size and power level, are high. A low total cost can give an incentive to go ahead with the project and this is an advantage when it comes to implementing this relatively new technology and in reaching the goals of implementing more renewables into the power system.

Table F.2 provides information about the important characteristics to consider for this project for the different DC/DC converter topologies discussed in this chapter. It was not possible to find comparable numerical characteristics for all converter topologies, so therefore some of the characteristics are described in terms of high/medium/low or yes/no. A line (–) means that it has not succeed finding information about that characteristic for the given converter topology. The footnotes provide further information regarding the characteristics and explain where the information is found if that is not stated by a [reference] in the table. The information in this table along with the information given in this chapter will be used to come up with a proposal for an optimal DC/DC converter for this project.

When it comes to the first aspect which is bidirectional power flow, it can be seen from the table that all converter topologies discussed in this chapter provides this characteristic. However, when it comes to the next aspect of voltage ratio and voltage levels, the table shows that the 2Q, 4Q and DHB converter topologies are not very well suited for this project as the two former has low voltage ratio, and since they all operate at low voltage levels. Therefore, the decision is to be made between the 2L, 3L, MMC and DAB converters.

In terms of fault prevention, all of the remaining topologies can be constructed with a transformer providing galvanic isolation and it has been seen that this is the preferred solution. The differences between the remaining solutions are their structure, number of components, switching frequencies, converter losses, controls and costs. It has been seen that when it comes to switching frequency, a lower frequency is better in terms of reducing the switching losses and to reduce the harmonics, and hence the need for filters, which again reduces the total cost. Therefore the 3L solution is preferred over the 2L solution, and the MMC solution is preferred over both the 2L and 3L solutions in terms of losses and harmonic content. In terms of costs of these three solutions it can be seen that the costs depend on the number of components in the converter and its control. Assuming that the MMC has more than three levels or that its submodules are based on full bridges, the MMC will be the most expensive solution out of the three. However, the extra cost of the converter should be compared to the losses of choosing a converter topology that performs worse, and a trade-off between acceptable losses and acceptable costs for the specific project should be used to choose an optimal DC/DC converter topology for the project.

DHB and DAB converters are most common in the field of research and academia. The DAB converter is relatively new, and even though research shows that most of its structures provide better performances than the corresponding, ”regular” 2L, 3L and MMC topologies, it has not succeed to find reference projects using the DAB topologies in this project. A reason for this could be that the ”regular” 2L, 3L and MMC topologies have been used in a number of HVDC projects in the recent years, and they could therefore be looked at as more mature technologies and safer choices. Choosing a topology that is relatively simple and that have been tested and used in other projects, and that has been improved over the last years, can be looked at as a safer choice, and therefore the choice of DC/DC converter topology in this project will be made among the ”regular” 2L, 3L and MMC topologies.

The purpose of the DC/DC converter in this project is to connect battery storage to the DC-link of an HVDC transmission system. The MMC provides an advantage of placing the battery storage inside the submodules, so this is another reason for the MMC topology being a good choice. In addition, it provides the lowest losses compared to the other topologies. This implies that the costs of filters can be reduced or neglected for this topology due to reduced or no need for harmonic filters. In addition maintenance of this converter topology is easy due to its modularity and scalability, and therefore it can be assumed that maintenance costs can be reduced compared to other topologies where maybe the whole converter needs to be replaced in case of maintenance operations due to i.e. a fault. This means that costs in terms of maintenance and harmonic filters can be reduced in this topology.

Table F.2: Characteristics of different DC/DC converter topologies

Topology	2Q	4Q	2L	3L	MMC	DHB	DAB
Switching frequency [Hz]	–[i]	–[i]	1950[61], 1150[75][ii]	1350[61][iii] 1500[61][iv]	150[61], 89-765[71][v]	–[i]	Depends[vi]
Converter losses [%] (at power)[vii]	–[i]	–[i]	3[61]	1.8-2.2[61]	1(1000MW) [61][viii]	–[i]	0.8-1.01(1.2GW)[71]
Scalability	–	–	–	–	Easy	–	Easy
Complexity of controller	Low	Low	Low	Medium	High	Low	Low
Fault tolerance	No	No	If isolated	If isolated	If isolated	Yes	Yes
Voltage ratio	Low	Low	Low-High[ix]	Low-High[ix]	Low-High[ix]	High	High
Voltage level [V]	Low	Low[x]	±200000[xi]	High	High	10s-100s[xii]	Depends[24][xiii]
Number of valves[xiv]	2	4	6	12	12n[xv] 24n[xvi]	2[xvii]	Depends[xviii]
Number of extra components[xix]	0	0	0	6[xx] 3[xxi]	Depends[xxii]	0	Depends[xxii]
Cost[xxiii]	Low	Low	Medium, $13,260 [7]	Medium, $15,499[xxiv]or $16,311[xxv]	High	Low	Depends[xxvi]
Bidirectional power flow	Yes[xxvii]	Yes	Yes	Yes	Yes	Yes	Yes

In terms of performance and efficiency, the 3L-NPC is also a good alternative if this choice reduces the costs significantly. As a conclusion, the DAB converter will ideally be the optimal choice, but when choosing among the converter topologies that are in use in industry today, the MMC topology is by far the converter that performs best in most of the criteria for this project. Therefore the MMC will be chosen as the DC/DC converter topology for this project.

---

[i] Numerical values for switching frequency was not found for the 2Q, 4Q or DHB converter. Based on the structure of these converters it can be assumed that the 2Q and DHB will have similar characteristics in terms of switching frequencies and converter losses, and that the 4Q and the DAB converters will have similar characteristics in terms of switching frequencies and converter losses.

[ii] Switching frequency for the 350 MW 2L optimal pulse-width modulation (OPWM) switched converter used in the Estlink HVDC Light® Transmission System

[iii] For the 3L active NPC [61]

[iv] For the 3L diode NPC [61]

[v] Different switching frequencies for the upper and lower arms for different operating scenarios of the MMC described in [71]

[vi] According to [76] the switching frequency is 20 000 Hz for a power of 1 MW, and for increasing power, the switching frequency decreases. The paper does not say anything about power levels as high as 200 MW, but for 5 MW the switching frequency is 1000 Hz. According to [71], a switching frequency of 1000 Hz is used for powers of 15 MW and 1.2 GW

[vii] Typical losses per converter. This includes both switching losses and conduction losses

[viii] Close to 1 % losses per station for converter stations of up to 1000 MW [60]

[ix] Low for 2L/3L/MMC based front-to-front DC/DC converter without galvanic isolation and and higher voltage ratios for 2L/3L/MMCs with transformer/galvanic isolation if assumed that the 2L and 3L converters with galvanic isolation can operate at higher voltage ratios similarly to the MMC in [25]

[x] Higher than for the 2Q converter

[xi] Assuming that it has the same voltage level as the 2L based DAB in [24]

[xii] Characterized as: voltage level on low voltage side - voltage level on high voltage side. I.e. 10s of volts on the LV side and 100s of volts on the HV side.

[xiii] 2L based: up to ±200 kV, MMC based: higher than for the 2L based

[xiv] Number of valves per converter. The front-to-front connection of VSCs and the DHB and DAB converters consist of two converters per DC/DC converter.

[xv] For a three-phase MMC with n half-bridge submodules (2 valves per submodule)

[xvi] For a three-phase MMC with n full-bridge submodules (4 valves per submodule)

[xvii] For a single-phase DHB

[xviii] 4 for a single-phase DAB, 6 for a 2L-based DAB, 12n for a MMC based DAB with half-bridge submodules, 24n for a MMC based DAB with full-bridge submodules, 6+6n for the TAC based DAB, 6+12n for the CTB based and the hybrid cascaded 2L based DABs and 6+24n for the alternative arm MMC based DAB. n is the number of submodules.

[xix] Number of extra diodes or extra capacitors per converter. The front-to-front connection of VSCs and the DHB and DAB converters consist of two converters per DC/DC converter.

[xx] Extra diodes for the 3L-NPC, the 3L-FLC does not have any extra diodes

[xxi] Extra capacitors for the 3L-FLC, the 3L-NPC does not have any extra capacitors

[xxii] Depends on the type of sub-module used in the MMC and MMC-based configurations of the DAB.

[xxiii] According to [71], the power electronics account for a major part of the total cost of the converter. Therefore the cost to a great extent depends on the number of power electronic components that the converter consists of. For some of the converter topologies it was possible to find a numerical cost value, so then that is given in this table in addition to a cost evaluation of low, medium or high costs.

[xxiv] For the 3L-NPC from [7]

[xxv] For the 3L-FLC from [7]

[xxvi] Depends on the structure of the DAB, but in general the cost of a DAB compared to a similar MMC is lower due to the fact that the DAB consists of fewer semiconductor components [71]

[xxvii] But it can only step up the voltage in one direction and step it down in the other [9]